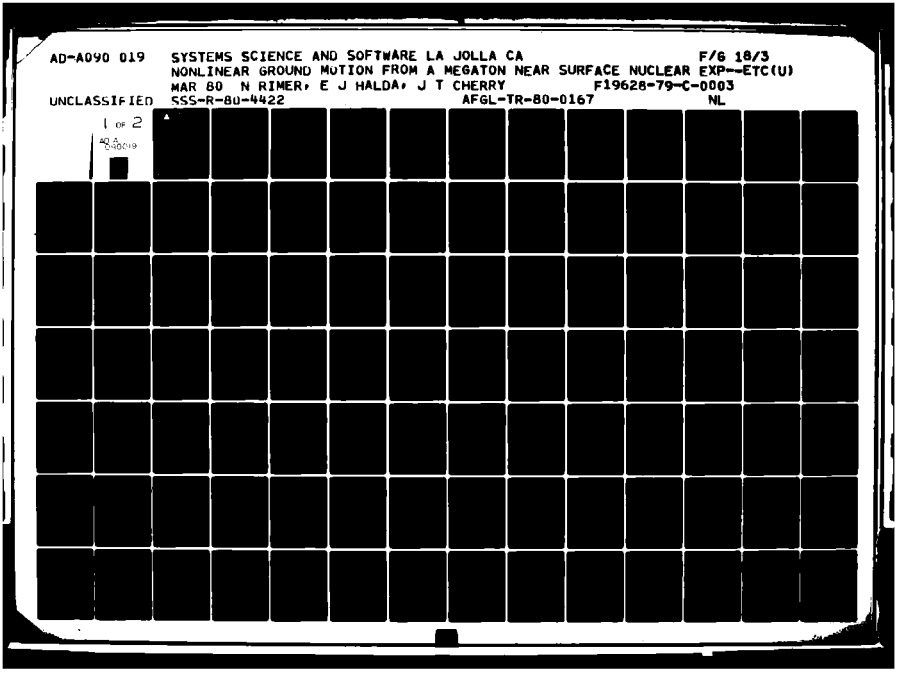
AD-A090 019
SYSTEMS SCIENCE AND SOFTWARE LA JOLLA CA
F/G 18/3
NONLINEAR GROUND MOTION FROM A MEGATON NEAR SURFACE NUCLEAR EXP--ETC(U)
MAR 80 N RIMER, E J HALDA, J T CHERRY
F19628-79-C-0003
UNCLASSIFIED
SSS-R-80-4422
AFGL-TR-80-0167
NL
1 OF 2
AD A090019

LEVEL II

12

SYSTEMS, SCIENCE AND SOFTWARE

AFGL-TR-80-0167

NONLINEAR GROUND MOTION FROM A MEGATON NEAR SURFACE NUCLEAR EXPLOSION

NORTON RIMER
ELDON J. HALDA
J. THEODORE CHERRY

SYSTEMS, SCIENCE AND SOFTWARE
P.O. BOX 1620
LA JOLLA, CALIFORNIA 90238

SCIENTIFIC REPORT No. 1

MARCH 1980

APPROVED FOR PUBLIC RELEASE; DISTRIBUTION UNLIMITED

AIR FORCE GEOPHYSICS LABORATORY
AIR FORCE SYSTEMS COMMAND
UNITED STATES AIR FORCE
HANSCOM AFB, MASSACHUSETTS 01731

P. O. BOX 1620, LA JOLLA, CALIFORNIA 92038, TELEPHONE (714) 453-0060

Unclassified

SECURITY CLASSIFICATION OF THIS PAGE (When Data Entered)

(19) REPORT DOCUMENTATION PAGE	READ INSTRUCTIONS BEFORE COMPLETING FORM
1. REPORT NUMBER (18) AFGL-TR-80-0167	2. GOVT ACCESSION NO. AD-A090 019
3. RECIPIENT'S CATALOG NUMBER	
4. TITLE (and Subtitle) (6) NONLINEAR GROUND MOTION FROM A MEGATON NEAR SURFACE NUCLEAR EXPLOSION	5. TYPE OF REPORT & PERIOD COVERED Scientific Report No. 1
	6. PERFORMING ORG. REPORT NUMBER (14) SSS-R-80-4422
7. AUTHOR(a) (4) Norton J. Rimer / Eldon F. Halda / Ted Cherry / J. Mendoza / Cherry	8. CONTRACT OR GRANT NUMBER(s) (15) F19628-79-C-0003 new
9. PERFORMING ORGANIZATION NAME AND ADDRESS Systems, Science and Software P.O. Box 1620 La Jolla, CA 92038	10. PROGRAM ELEMENT, PROJECT, TASK AREA & WORK UNIT NUMBERS 61102F (16) 2309G2 AD (17) 09 01
11. CONTROLLING OFFICE NAME AND ADDRESS (11) Air Force Geophysics Laboratory Hanscom AFB, Massachusetts 01731 Monitor/K. C. Thomson/LWH	12. REPORT DATE March 1980
	13. NUMBER OF PAGES 100
14. MONITORING AGENCY NAME & ADDRESS (if different from Controlling Office) (12) 173	15. SECURITY CLASS. (of this report) Unclassified
	15a. DECLASSIFICATION, DOWNGRADING SCHEDULE

16. DISTRIBUTION STATEMENT (of this Report)

Approved for public release; distribution unlimited.

17. DISTRIBUTION STATEMENT (of the abstract entered in Block 20, if different from Report)

18. SUPPLEMENTARY NOTES

19. KEY WORDS (Continue on reverse side if necessary and identify by block number)

Ground coupling; Airblast; Shock wave; Ground motion; Crater; Finite difference calculations; Shear failure; Tension failure.

20. ABSTRACT (Continue on reverse side if necessary and identify by block number)

Presented here are finite difference calculations of the ground motions from a one-megaton near-surface nuclear explosion over a saturated soil. These calculations are unique in that they were carried out to a time of 3.26 sec so that the motions could be computed at ranges at which the soil response was linearly elastic. Having a detailed specification of the explosion-induced ground motion on cylindrical monitoring surfaces in the elastic regime, -

DD FORM 1473 EDITION OF 1 NOV 65 IS OBSOLETE Unclassified

SECURITY CLASSIFICATION OF THIS PAGE When Data Entered

analytical techniques from elasticity will be applied to continue the ground motion through layered earth models out to ranges of 10 to 500 ~~kilometers~~ km.

The finite difference calculations were initialized at 0.8 msec using ~~the~~ results of the Source 3/5 ground coupling calculation which incorporates a detailed model of the nuclear device mass, materials and dimensions. The ground motions were computed out to 5.0 msec in an Eulerian hydrodynamic code and then transferred to the Lagrangian CRAM stress wave code containing appropriate constitutive models, shear failure, tension failure, etc. A bowl-shaped crater was calculated with a cratering efficiency of 37 ~~cubic feet~~ per ton of explosive energy, a factor of 5 or 6 smaller than given by empirical scaling formulae based on ~~the~~ Pacific nuclear tests.

(cu ft/ton)

TABLE OF CONTENTS

LIST OF ILLUSTRATIONS

LIST OF ILLUSTRATIONS (continued)

LIST OF ILLUSTRATIONS (continued)

LIST OF ILLUSTRATIONS (continued)

LIST OF TABLES

ACKNOWLEDGEMENTS

It is a pleasure to acknowledge the contributions of Doctors J. C. Baker and L. E. Bailey and Mr. J. L. Waddell in the early time Eulerian stages of the calculation. Dr. K. D. Pyatt, Jr., has been most helpful in the analysis of the crater related ground motions. The calculation from 0.8 to 5.0 msec and subsequent analyses was supported in part from funds provided by the Defense Nuclear Agency.

I. INTRODUCTION AND SUMMARY

The definition of both the near and far-field ground motion environment is a critical input to the design of land-based strategic weapons systems that are required to survive a first strike nuclear attack. In order to help this definition, we present in this report, a detailed computer calculation of the explosion induced ground motions from a 1-MT near surface burst.

The ground motions have been computed to a time of 3.26 sec. out to ranges of 800 meters where the material response is linearly elastic. An important result of the work is the output of the calculation at monitoring surfaces in the elastic regime. Analytical propagation techniques from theoretical seismology can be applied to this data so that the response of geologic and structural configurations of interest can be computed. In this sense these results will provide a resource for the community that can be used for future studies. A subsequent report will present the propagation of this data through earth models appropriate for MX valleys.

Our calculation was begun using the results of the Source 3/5 calculation as an energy source. Source 3/5 was an extensive calculation of the ground coupling from a 1-MT surface burst over wet tuff performed by S^3 for the Defense Nuclear Agency (DNA). The Source 3/5 calculation began with a highly detailed 1-MT source at a 58 cm height of burst. (The source was scaled to the correct yield from the previously reported Source 3 (Allen and Knowles, 1971; Allen and Schneyer, 1973).) The results of the Source 3/5 calculation at 800 μsec, some of which will be summarized in Section III of this report) served as the starting point for our calculation.

The Source 3/5 calculation (out to 800 μsec) used a gas equation-of-state for the ground material, allowing it to have

higher compression than would otherwise be expected. After a few one-dimensional test problems were run, it was determined that the pressures and velocities were reasonable compared to that expected from a solid equation-of-state. Since the problem was to be continued to late time where solid effects become more significant, it was decided to switch the equation-of-state to a better representation of a ground material. This was done by retaining the velocity field and pressure and specific internal energy distributions. Only material density was adjusted. Test calculations indicated this would have a small perturbation on the ground shock.

The calculation had been run to 800 μsec with radiation, at which time it was determined that radiation was no longer playing a significant role. The calculation was continued in the same code (STREAK, a two-dimensional Eulerian radiation hydrodynamic code) in a hydrodynamic-only mode to a time of 5 msec using the solid equation-of-state. At this point the calculation was transferred to CRAM, a two-dimensional Lagrangian elastic-plastic ground motion code containing constitutive models appropriate for the behavior of geologic materials over a wide range of stresses, including a linking of an effective stress law for porous and saturated materials with detailed tension and shear failure models.

As described in Melzer, et al. (1979) future MX sites lie in alluvial valleys which are filled with a variety of geological materials. The major purpose of this calculation was to study in detail the far field ground motion from a 1-MT surface burst. For this reason, rather than to calculate a particular MX site, we chose a simple geological configuration, a homogenous, fully saturated ground material having an unconfined strength of 18.75 bars. Although the constitutive model provided for a maximum strength of 100 bars, applying the effective stress concept to the saturated ground

reduced its effective maximum strength to under 20 bars. Therefore, the ground material being modeled represents a very weak saturated rock or competent soil.

At the time of overlay (5 msec) the airblast being modeled explicitly in the STREAK code was replaced by a time-dependent pressure boundary condition on the free surface in CRAM. The Brode (Brode, 1968) airblast solution for a 1-MT surface burst was used as the boundary condition up until a time of approximately 306 msec. At later times, the Needham (Needham, et. al., 1975) representation, which is slightly better at small overpressures, was used as the free surface boundary condition.

A grid from the two-dimensional linear elastic small deformation SAGE (Cherry, et. al., 1974) code was placed around the outer boundaries of the CRAM grid. This allowed us to follow the near-field ground motion to late times (several seconds) more efficiently without nonphysical reflections propagating back from grid boundaries. As a further cost saver, we have recently developed an absorbing boundary condition for SAGE boundaries which provides a momentum trap for almost all of the incoming P-waves and a good deal of the S-waves.

The finite difference calculation has been run out to 3.26 seconds. Data (time histories of stresses, velocities, and displacements) has been saved along monitoring surfaces on which the motions are linear elastic in both CRAM and SAGE in order to provide redundancy to verify our analytical continuation techniques. At 2.70 seconds, any information reflecting from the absorbing SAGE boundaries which travel at the P-wave speed of the medium (2000 m/sec) is calculated to begin arriving at the outermost monitoring surface in SAGE (a cylinder extending to a depth of 677 meters and a radial distance of 815 meters. The other two monitoring cylinders

are located approximately 100 meters (in SAGE) and 200 meters (in CRAM) closer in. If necessary, the finite difference calculation could be run without introducing much error to 4.1 sec. at which time information from the absorbing boundaries at the S-wave speed (632 m/sec) begins to arrive at the outermost monitoring surface.

Beginning at about 0.75 sec, estimates of the crater dimensions and crater volume were made from the calculation at regular intervals up to approximately 1.25 sec. Each grid element having sufficient momentum to escape from the grid was ejected ballistically in order to estimate its final location in the free surface. The estimates of crater dimensions at various time intervals differed only slightly; representative dimensions at 1.17 sec were a crater depth of approximately 90 meters and a crater radius of 105 meters. These give a crater volume of approximately 37 cubic feet per ton of explosive energy, in line with the most recent calculations of crater size. As will be discussed later, the calculated crater volumes are still smaller than empirical estimates of generic crater volumes for wet soft rock (100 ft^3/ton) and wet soil (200 ft^3/ton) based on scaling from the Pacific nuclear tests in saturated coral (Cooper, 1976).

The remainder of this report is organized in four sections. In Section II, we discuss the constitutive models and material properties used in calculating the ground motion. In Section III we summarize the results of the Source 3/5 calculation at 800 μsec., discuss in some detail the changeover to the solid equation-of-state and present results obtained using the Eulerian code out to 5 msec, the time of overlay into CRAM. Section IV begins with a description of the nonlinear CRAM calculation including the approximations (boundary conditions, regions, etc.) used. This section continues with a presentation of the ground motion results and concludes with a discussion of the crater formation.

II. CONSTITUTIVE MODELS AND MATERIAL PROPERTIES

A fairly simple geological configuration, a homogeneous fully saturated competent soil, was chosen for this calculation. This saturated, weak medium, when compared to a dry soil was expected to give less attenuation of the direct coupled ground motion as it propagated away from the source as well as less attenuation of the airblast induced ground motion. By using a completely saturated soil, we avoid the modeling approximations inherent in crushing up air-filled voids in an asymmetric environment but not at the expense of any generality in the far field solutions which are of prime interest here. A homogeneous media was chosen rather than a layered media in which reflections could obscure the main features of the propagation.

The constitutive models used to predict the nonlinear behavior of the ground material may be separated into three basic parts, an equation-of-state to describe the thermodynamic state of the material (pressure as a function of energy and density), a shear failure model to account for the material strength of the rock, and a tension failure model to account for the material strength of the rock, and a tension failure model to account for the opening and closing of tensile cracks in the rock. A complete description of these constitutive models may be found in Cherry, et. al., 1975.

2.1 EQUATION-OF-STATE

CHEST is a chemical equilibrium equation-of-state for saturated tuff which was developed at S^3 (Laird, 1976) especially for use with hydrodynamic codes to study nuclear explosion phenomenology. This tabular equation-of-state gives pressure as a function of energy and specific volume and accurately models the rock behavior in pressure regimes from tens of megabars down to a few tenths of a bar. CHEST,

plotted in Figure 2.1, coupled an elaborate chemical equilibrium treatment with steam tables and bulk modulus data to provide one consistent equation-of-state over this entire energy-specific volume space. For calculational reasons, an ambient ground energy of 1.342×10^9 ergs/gm at one atmosphere and 98 degrees Kelvin was defined as zero energy in the finite difference code. The constant energy lines shown in Figure 2.1 are labeled relative to this ambient energy.

The CHEST equation-of-state covers regions where the tuff is condensed and where it is vaporized. The curves for energy greater than 12.7×10^{10} erg/gm in Figure 2.1, for example, correspond to tuff that is vaporized and must be treated as a gas of chemically reacting constituents. For smaller energy densities, the curves lie in a region where the tuff is in mixed phase, partly vapor and partly condensed. The tuff mixed phase and tuff vapor regions are marked "I" in Figure 2.1. In the region marked "II," tuff is solid, but the free water content is part liquid, part vapor. Thus, the curve bounding region II is the steam dome for the water content of the tuff. The narrow region marked III in the figure is the domain in which the tuff is solid and water is liquid. The nearly vertical curves arising from the left boundary of the steam dome are lines of constant energy. The experimentally observed Hugoniot for wet tuff is nearly parallel to these curves up to pressures of the order of 100 kbar.

The CHEST table is designed to be used with a high speed computer interpolation routine. Figure 2.2 shows adiabatic releases computed from the CHEST Hugoniot for wet tuff. This model contained a total water content of 23.66 percent by weight (including bound water). Because of the importance of a detailed treatment of the water-rock mixed phase and vapor regions in particular, we chose to use the

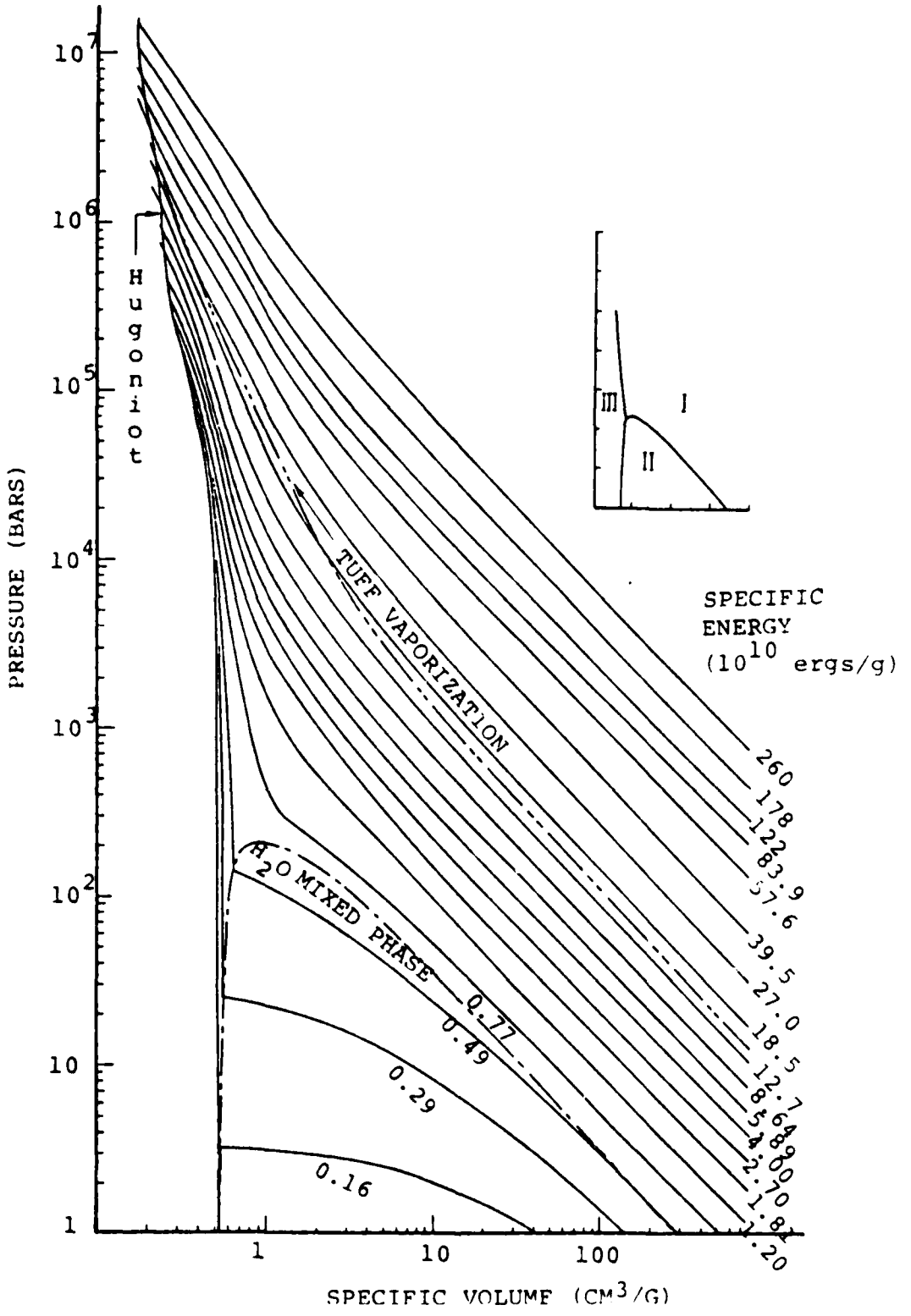

Figure 2.1 CHEST equation-of-state for saturated tuff showing constant energy lines (zero energy in the plot corresponds to an ambient ground energy of 1.342×10^9 ergs/gm).

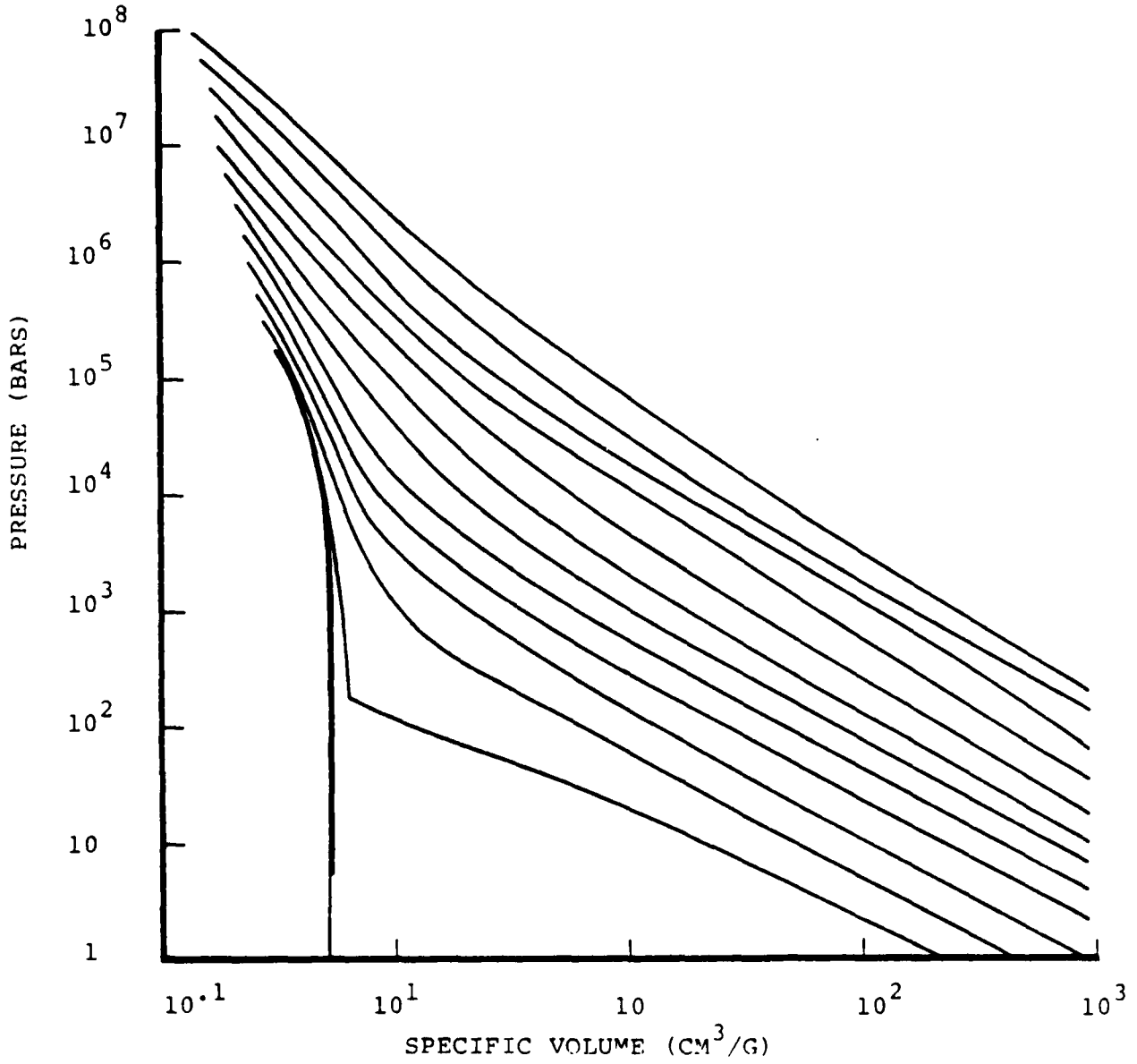

Figure 2.2 Calculated adiabatic releases from CHEST Hugoniot.

CHEST equation-of-state of Figures 2.1 and 2.2 to model our fully saturated ground material. CHEST tuff has a bulk density and a bulk modulus comparable to saturated clays or silty sands found below the water table in valleys of interest for MX sites (see Melzer, et al., 1979). Table 2.1 gives the elastic constants used in our model.

Since the finite difference calculation must be run to very late times where material behavior is elastic over most of the grid of interest, CHEST was replaced in the calculation at those times and locations by a polynomial fitted to the CHEST Hugoniot at these lower pressures.

TABLE 2.1 ELASTIC CONSTANTS

Bulk density	=	1.9445	gm/cm
Longitudinal wave speed	=	2000	m/sec
Shear wave speed	=	632	m/sec
Bulk modulus	=	67.25	kb
Shear modulus		7.76	kb
Poisson's ratio	=	0.445	

2.2 SHEAR FAILURE

Cherry and Peterson (1970) have identified the dependence of material strength on the third deviatoric invariant and shown the improvement in the definition of material strength, Y, when pressure, P, is replaced by $\bar{P}$. Y, P and $\bar{P}$ are obtained from the stress invariants, J_1, J_2', J_3' as follows:

$$Y = (3J_2')^{1/2}$$

$$\bar{P} = P - \frac{1}{2}\left(\frac{J_3'}{2}\right)^{1/3}$$

$$P = -\frac{J_1}{3} \quad .$$

Here, P is the pressure component with the overburden pressure, P_0, added. J_1, J_2' and J_3' are the first, second deviatoric and third deviatoric stress invariants. If σ_{11}, σ_{22}, σ_{33} are principal stresses, then

$$J_1 = \sigma_{11} + \sigma_{22} + \sigma_{33}$$

$$J_2' = \frac{(\sigma_{11} + P)^2 + (\sigma_{22} + P)^2 + (\sigma_{33} + P)^2}{2}$$

$$J_3' = (\sigma_{11} + P)\ (\sigma_{22} + P)\ (\sigma_{33} + P) \ .$$

Note that when the intermediate principal stress, σ_{22}, is equal to either the maximum, σ_{11}, or minimum, σ_{33}, principal stress, then

$$Y = |\sigma_{11} - \sigma_{22}|$$

and

$$\bar{P} = -\left(\frac{\sigma_{11} + \sigma_{22}}{2}\right) \quad .$$

The failure surface for the ground material in a dry state is modified to account for the presence of water using "effective stress" principles. These state that the effective stress, P_{eff}, given by

$$P_{eff} = \bar{P} - P_f$$

wnere P_f if the fluid or pore pressure, should be used in defining the dependence of material strength on the stress state. Thus our failure surface was chosen (at low temperature or internal energy) to be

$$Y = 15.0 + 0.4\ P_{eff} \text{ (bars)}$$

with a maximum strength of 100 bars.

For our fully saturated material, we assumed that the pore pressure was identically equal to the mean stress in the soil. Thus the effective stress degenerates to

$$P_{eff} = -\frac{1}{2}\left(\frac{J_3'}{2}\right)^{1/3}$$

so that the effective maximum strength is less than 20 bars.

A further modification was made to the failure surface to account for loss of strength at high temperatures (internal energy). The calculated strength Y was reduced by a multiplicative factor

$$1 - \frac{e}{e_m}$$

where e is the specific internal energy and e_m the melt energy, chosen to be 2.05×10^{10} ergs/gm. Once a material is melted it is assumed to have no strength even upon condensation.

Hooke's law is used to obtain an initial estimate of the stress deviators, i.e.,

$$\hat{S}_{ij}^{n+1} = S_{ij}^{n} + 2\mu\ \dot{e}_{ij}\ \Delta t$$

where $\hat{S}_{ij}^{n+1}$ and S_{ij}^{n} are the values of the stress deviator at time t + Δt and t, respectively.

μ is the shear modulus

$\dot{e}_{ij}$ is the strain rate deviator

Δt is the time increment.

Shear failure occurs if the material strength evaluated at $\bar{P}$ (P_{eff} in our calculation) is exceeded, i.e., if

$$J > Y(\hat{\bar{P}})$$

where

$$J = \left[\frac{3}{2}\left(\hat{S}_{11}^2 + \hat{S}_{22}^2 + \hat{S}_{33}^2\right)\right]^{1/2}$$

$$\hat{\bar{P}} = p^{n+1} - \frac{1}{2}\left(\frac{\hat{S}_{11}\hat{S}_{22}\hat{S}_{33}}{2}\right)^{1/3} .$$

p^{n+1} includes the overburden pressure and we have omitted the n+1 superscripts in $\hat{S}_{ij}$.

If $J > Y(\bar{P})$, then adjustment of the stress deviators, $\hat{S}_{ij}^{n+1}$ is required. We assume that

$$S_{ij}^{n+1} = a\hat{S}_{ij}^{n+1}$$

where S_{ij}^{n+1} is the adjusted value of the stress deviator and

$$a = \frac{Y(\bar{P}) + \frac{b}{2}\left(\frac{\hat{S}_1\hat{S}_2\hat{S}_3}{2}\right)^{1/3}}{J + \frac{b}{2}\left(\frac{\hat{S}_1\hat{S}_2\hat{S}_3}{2}\right)^{1/3}}$$

$$b = \frac{dY}{dP} \quad \text{(evaluated at } \hat{\bar{P}}) \ .$$

The equation for a is obtained by approximating the strength function at $\hat{\bar{P}}$ with a first order Taylor series and

assuming that no adjustment in P^{n+1} occurs during shear failure.

2.3 TENSION FAILURE

Tension failure is assumed to occur in the element if a principal stress is greater than zero and if shear failure has ever taken place. We then apply the tension failure model proposed by Maenchen and Sack (1964) and introduce an inelastic strain normal to the crack. This inelastic strain is just sufficient to zero the tensile stress.

For example, if $\hat{\sigma}_{11}$, $\hat{\sigma}_{22}$ and $\hat{\sigma}_{33}$ are the three principal stresses and if $\hat{\sigma}_{11}$ is greater than zero, then the adjusted stress (σ_{11}, σ_{22}, σ_{33}) are given by

$$\sigma_{11} = \hat{\sigma}_{11} - \left(k + \frac{4}{3}\mu\right)\Delta e_{11}$$

$$\sigma_{22} = \hat{\sigma}_{22} - \left(k - \frac{2}{3}\mu\right)\Delta e_{11}$$

$$\sigma_{33} = \hat{\sigma}_{33} - \left(k - \frac{2}{3}\mu\right)\Delta e_{11}$$

where

$$e_{11} = \frac{\hat{\sigma}_{11}}{k + \frac{4}{3}\mu}$$

k is the bulk modulus, μ is the shear modulus and all stresses include the overburden pressure.

If two of the principal stresses, say σ_{11} and σ_{22} are greater than zero, then the stress adjustment becomes

$$\sigma_{11} = \hat{\sigma}_{11} - \left(k - \frac{2}{3}\mu\right)\left(\Delta e_{11} + \Delta e_{22}\right) - 2\mu\Delta e_{11}$$

$$\sigma_{22} = \hat{\sigma}_{22} - \left(k - \frac{2}{3}\mu\right)\left(\Delta e_{11} + \Delta e_{22}\right) - 2\mu\Delta e_{22}$$

$$\sigma_{33} = \hat{\sigma}_{33} - \left(k - \frac{2}{3}\mu\right)\left(\Delta e_{11} + \Delta e_{22}\right)$$

$$\Delta e_{11} = \frac{\left(k + \frac{4}{3}\mu\right)\hat{\sigma}_{11} - \left(k - \frac{2}{3}\mu\right)\hat{\sigma}_{22}}{4\mu\left(k + \frac{\mu}{3}\right)}$$

$$\Delta e_{22} = \frac{\left(k + \frac{4}{3}\mu\right)\hat{\sigma}_{22} - \left(k - \frac{2}{3}\mu\right)\hat{\sigma}_{11}}{4\mu\left(k + \frac{\mu}{3}\right)} \quad .$$

All the inelastic strain increments (Δe_{11}, Δe_{22}, Δe_{33}) are accumulated on each cycle giving

$$E_{11}^{n+1} = E_{11}^{n} + \Delta e_{11}$$

$$E_{22}^{n+1} = E_{22}^{n} + \Delta e_{22}$$

$$E_{33}^{n+1} = E_{33}^{n} + \Delta e_{33} \quad .$$

These equations give the basic stress-strain adjustment during tension failure. However, they apply equally well for crack closure. If at least one of the total strains (say E_{11}^{n}) is greater than zero, then the crack will open or close depending on the sign of $\hat{\sigma}_{11}$. If $\hat{\sigma}_{11} > 0$, then

$$\Delta e_{11} > 0$$

$$E_{11}^{n+1} > E_{11}^{n}$$

and the crack width increases. The inequalities are reversed if $\hat{\sigma}_{11} < 0$ and the crack width decreases. Closure will continue until

$$E_{11}^{n} + \Delta e_{11} < 0.$$

Then

$$\Delta e_{11} = - E_{11}^{n}$$

$$E_{11}^{n+1} = 0$$

and the crack is completely closed. When this state is achieved, the element is able to support a compressive stress in the (1,0,0) direction, but is not assumed to heal.

III. THE SOURCE 3/5 GROUND COUPLING CALCULATION

In this section, we briefly describe the early time Source 3/5 calculation and detail the procedures and approximations made to continue this calculation in an Eulerian code from 800 μsec (the initial time of our ground motion calculation) out to a time of 5 msec when the calculation was transferred to a Lagrangian finite difference code.

3.1 INITIAL CONDITIONS, RESULTS AT 800 μSEC

Source 3/5, a calculation of the energy source and ground coupling out to 800 μsec from a 1-MT near surface burst (58 cm height of burst), was scaled from the Fource 3 calculation (Allen and Knowles, 1971) in which appropriate masses, materials, and dimensions were used in modeling the device. The code used in this calculation was STREAK, a two-dimensional Eulerian radiation hydrodynamic code used for numerous ground coupling calculations in the past. In this version of the 2D-Vera family of codes, the radiation treatment was grey (i.e, no multifrequency effects), nonequilibrium, time-dependent diffusion with flux limiters. The hydrodynamic treatment was Eulerian with moving material boundaries and separate material properties (density, specific internal energy, and velocity) within a mixed cell. STREAK contains the ability to package portions of the space in the calculation with vastly different grids (or zoning) and to allow each package to run at its appropriate time step. The calculation was run to 800 μsec (0.800 msec) with radiation on, at which time it was determined that radiation was no longer playing a significant role.

Figure 3.1 sketches some of the important features of the Source 3/5 solutions at 800 μsec. First note the presence at zero time of a cylindrically shaped, air-filled "room" located directly beneath the working point. This room, having 38-cm thick concrete walls, was intended to represent part of

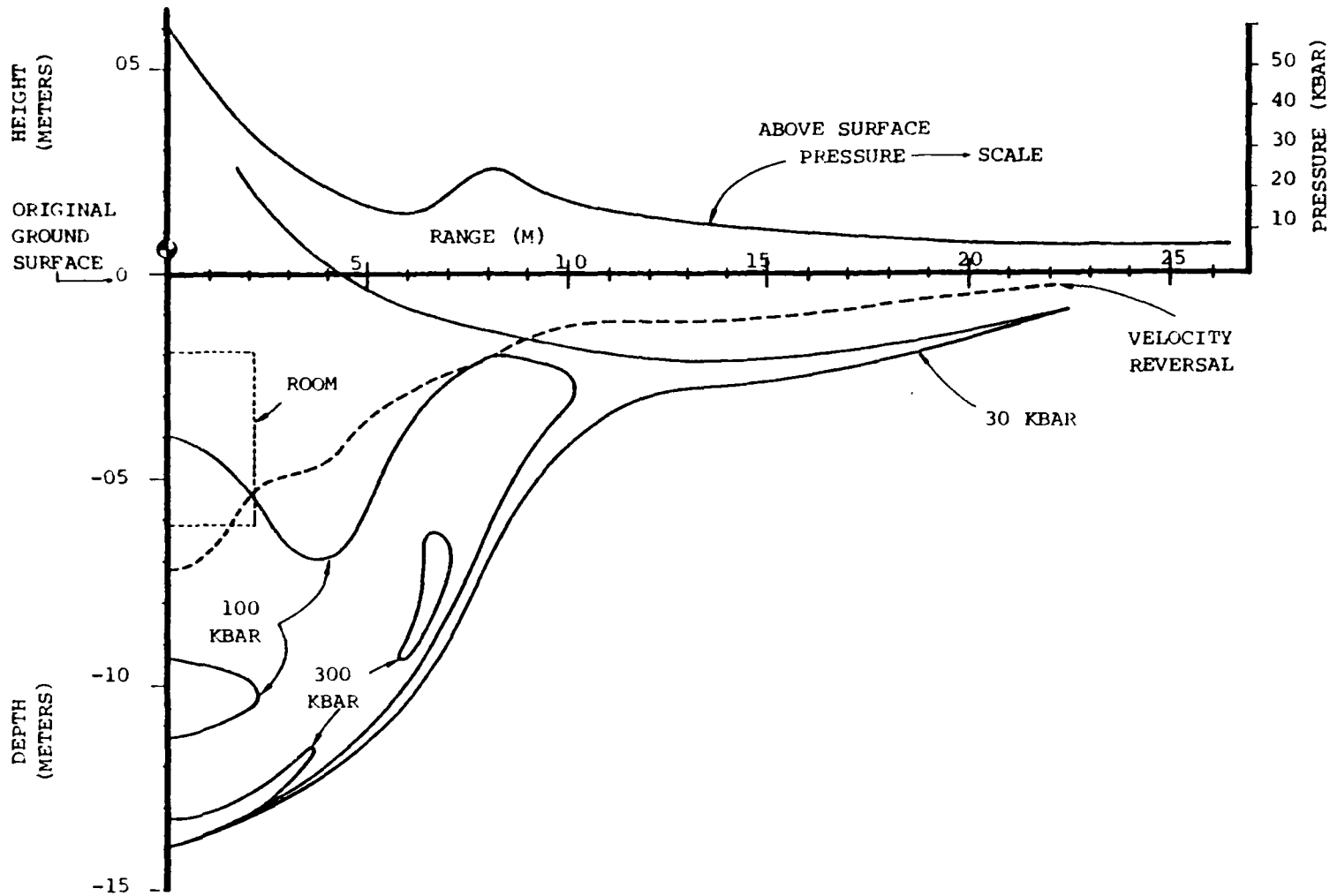

Figure 3.1. Source 3/5 phenomenology at 800 μsec.

an MX trench suffering a direct hit from a 1-MT surface burst. At 800 μsec, this air-filled room has long since been compressed by the propagating shock wave and was no longer being considered in the Source 3/5 calculation. However, the initial presence of the room has had considerable influence on the solutions, particularly on the direct induced ground motion. The expected spherical shape of the directly coupled shock wave has been altered somewhat. As shown in the equal pressure contours of Figure 3.1, the peak pressure is not constant along this shock front. Figure 3.2 gives these contours at 800 μsec in greater detail while Figure 3.3 shows the particle velocity vectors at that time indicating the disturbance to the downward directed spherical shock. We shall see that at later times, the influence of this "room" on the shock is small.

Both Figures 3.2 and 3.3 show solutions confined to Package 1 of the STREAK calculation. Three separate packages were used in the calculation; Package 1, including all of the ground material extending radially approximately 12 m (the entire direct coupled shock); Package 2, monitoring the air and fireball materials; and Package 3, extending 4 meters into the ground and containing the ground-fireball interface from 12 out to approximately 80 m. Package 3 was very finely zoned vertically (and thus sub-cycled relative to Package 1) in order to accurately model the planar downward propagating shock generated by radiation deposition in the ground. This planar shock, part of which is sketched in Figure 3.1, has a magnitude of approximately 30 kbar at 800 μsec. Not shown is the airblast front extending out to about 80 m with a shock wave peak pressure of 14 kbar, and with approximately 6 kbar pressure behind the shock. (Near the working point, fireball pressures are as high as 15 kbar.)

Figure 3.4 shows the locations at 800 μsec of the tracer particles which mark the boundary at zero time between

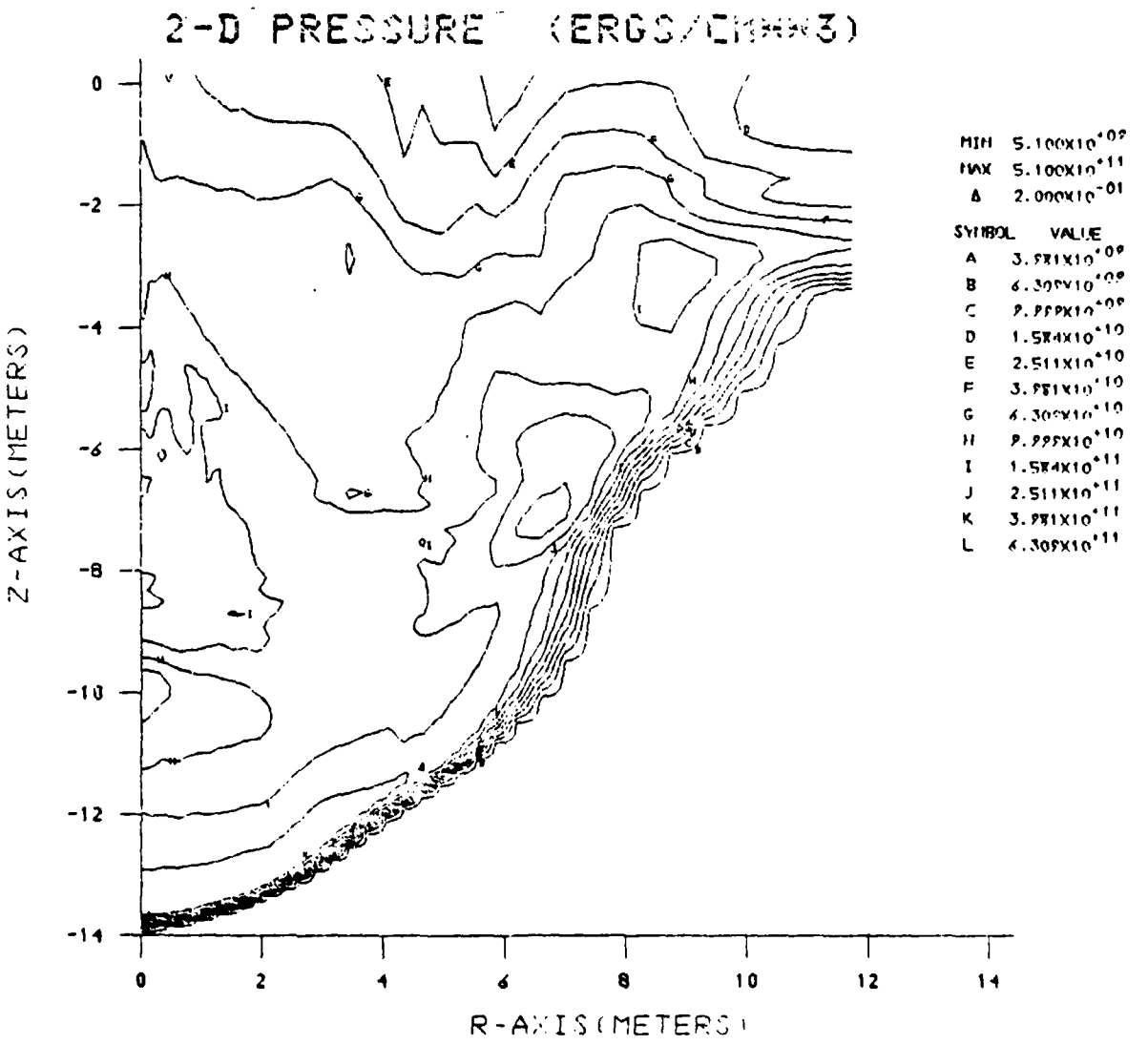

Figure 3.2 Source 3/5 pressure contours at 800 usec.

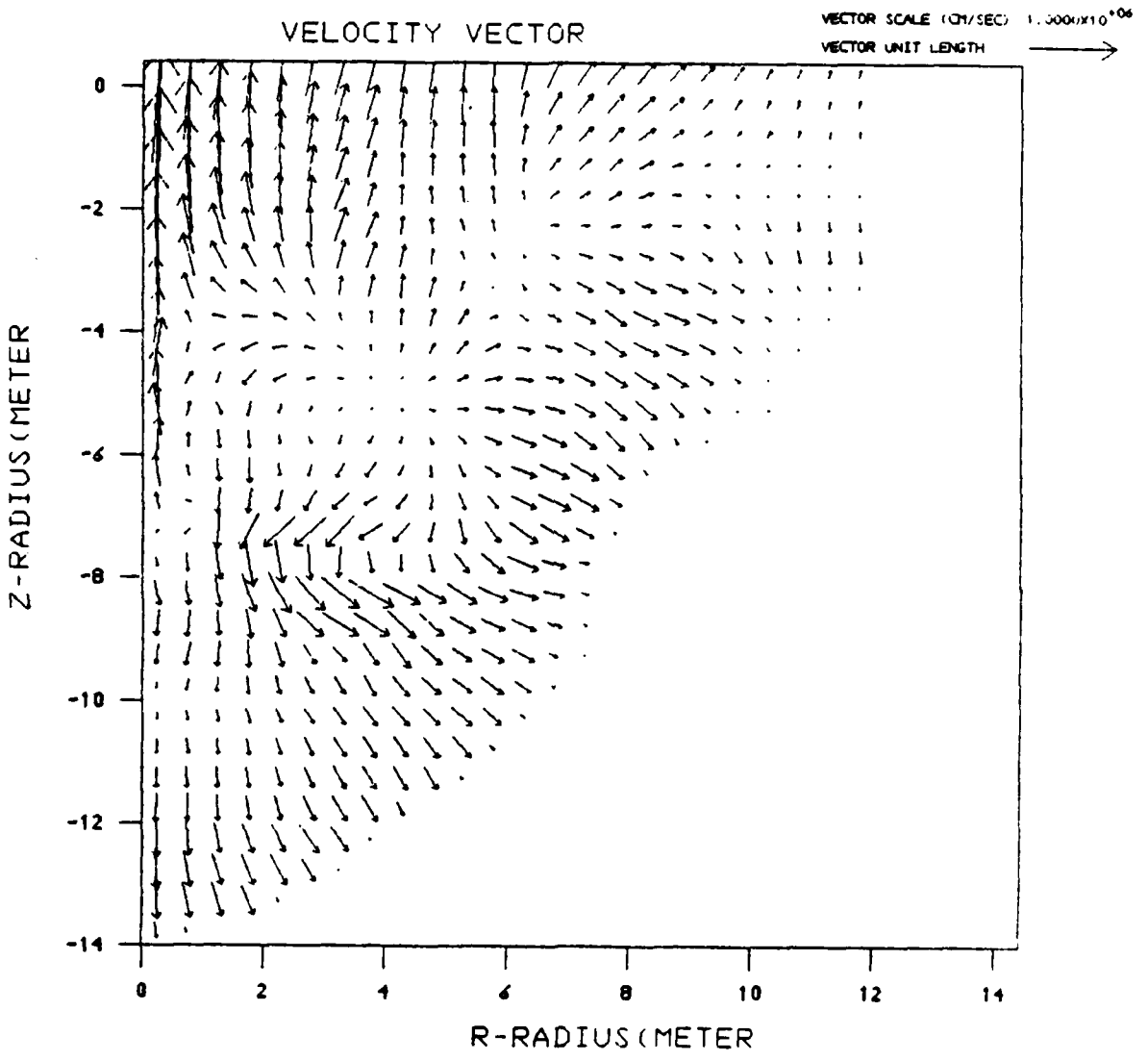

Figure 3.3 Source 3/5 velocity vectors at 800 μsec.

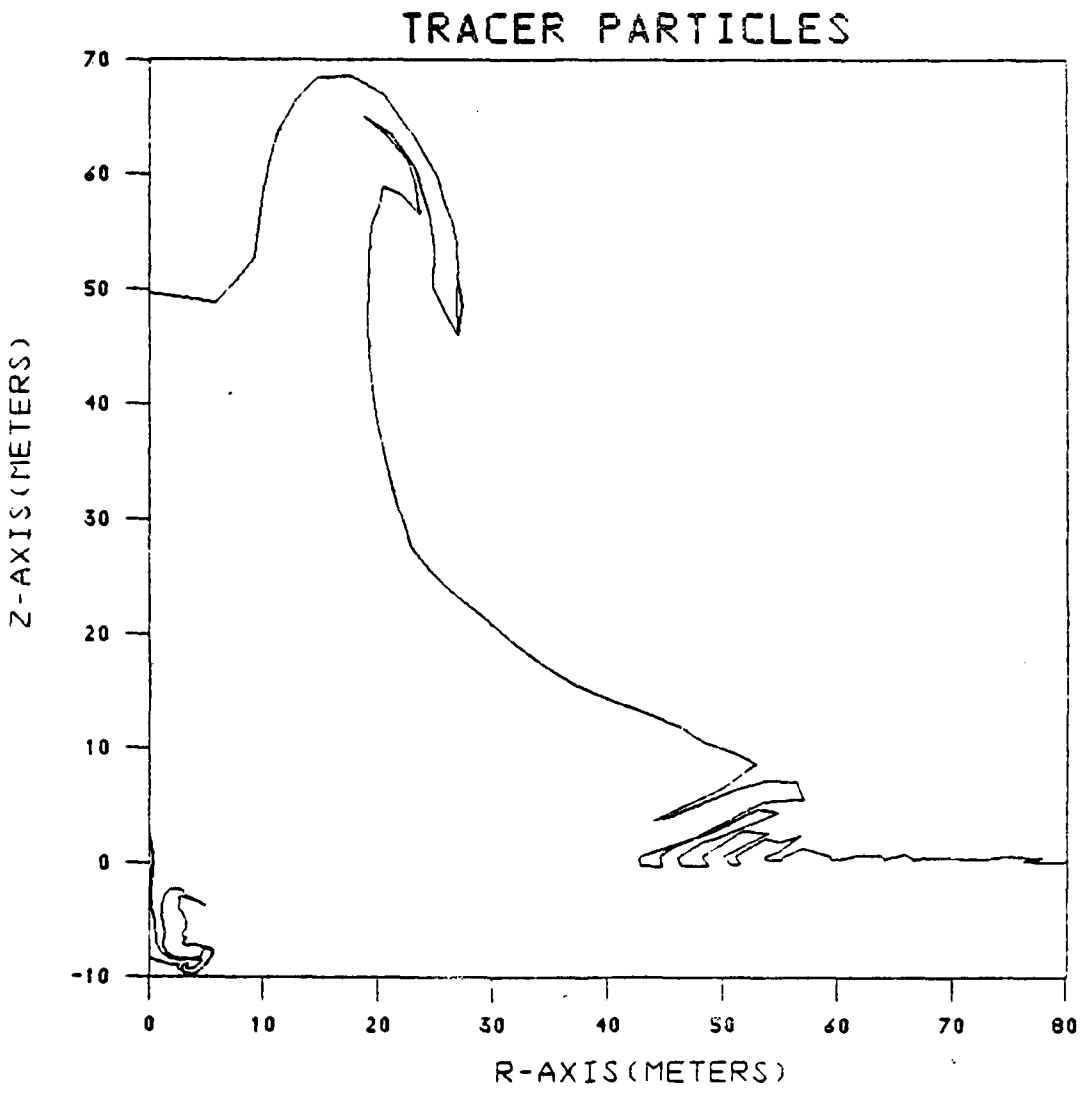

Figure 3.4 Tracer particles marking boundary at 800 μsec between air and original ground material.

the ground material and the air and fireball materials. At 800 μsec, hot ground materials directly above the source having very low densities have been blown over 50 meters out of the ground. Pressures in this material have been sketched in Figure 3.1. The sonic line at this time is approximately at the original ground surface. The velocity reversal line, defining the boundary between upward and downward moving material, is as shown in Figure 3.1 and is moving downward with time.

3.2 SOURCE 3/5 CONVERSION OF EQUATION-OF-STATE

The Source 3/5 calculation was run out to 800 μsec using the EIONX equation-of-state computer subroutines (Pyatt, 1966). EIONX assumes local thermodynamic equilibrium (LTE) involving neutral atoms, ions, and electrons in solving an extensive system of coupled nonlinear equations for the concentrations of each constituent. The assumptions made in solving these equations, as well as some more basic assumption in this gas equation-of-state, have limited validity in the shock waves calculated at 800 μsec. The EIONX equation-of-state, because of its lack of solid-like models, overcompressed material at the shock front, but modeled accurately the hot expanded blowoff materials behind the shock.

A decision was made to convert to the CHEST wet tuff equation-of-state, described in Section 2.1 before continuing the Source 3/5 calculation past 800 μsec. A series of simplified one-dimensional spherically symmetric blast wave test calculations were performed in order to evaluate different proposals for accomplishing the equation-of-state conversion. The final conversion accepted values of pressure, specific internal energy, and velocity from the calculations made with EIONX and iterated on density to get the same pressure values with CHEST. This resulted in much less energy

being present in the shock front since CHEST reduced compressed densities significantly. In the hot expanded region, densities were increased. Figure 3.5 compares the distribution of energy in downward-moving ground material (upward directed motions are not important to the calculation at this time) below the original ground surface *before* and *after* this conversion. Plotted are values of internal energy (including radiation energy) plus kinetic energy of material moving downward per unit of area in cylindrical strips of ground at the radial distances shown.

Table 3.1 gives the integrated total energies before and after the conversion. Over the entire grid, the most noticeable change was a large decrease in kinetic energy at the shock front (approximately 35 percent) which resulted in a decrease in total energy of approximately 5 percent. Behind the shock (inside of 6 meters radially) internal energy increased by about 32 percent.

We do not believe that the changes introduced into the Source 3/5 results at 0.8 msec by the conversion of equations-of-state described above have seriously affected the solutions at later times. To quantify this, two spherically symmetric blast wave calculations were made for a device yield of 100 KT. The first calculation used the CHEST equation-of-state to describe the ground material surrounding the device. The second calculation used the EIONX equation-of-state until the peak of the ground shock had reached a range of 1350 cm. (Peak pressure in the shock at that range was 300 kbars, comparable to the Source 3/5 peak pressure at 0.8 msec.) Then, EIONX was replaced by CHEST, accepting values of pressure, velocity, and internal energy as was done above, and iterating to determine mass density from the CHEST equation-of-state. This calculation was continued using CHEST out to better than twice the range of 1350 cm.

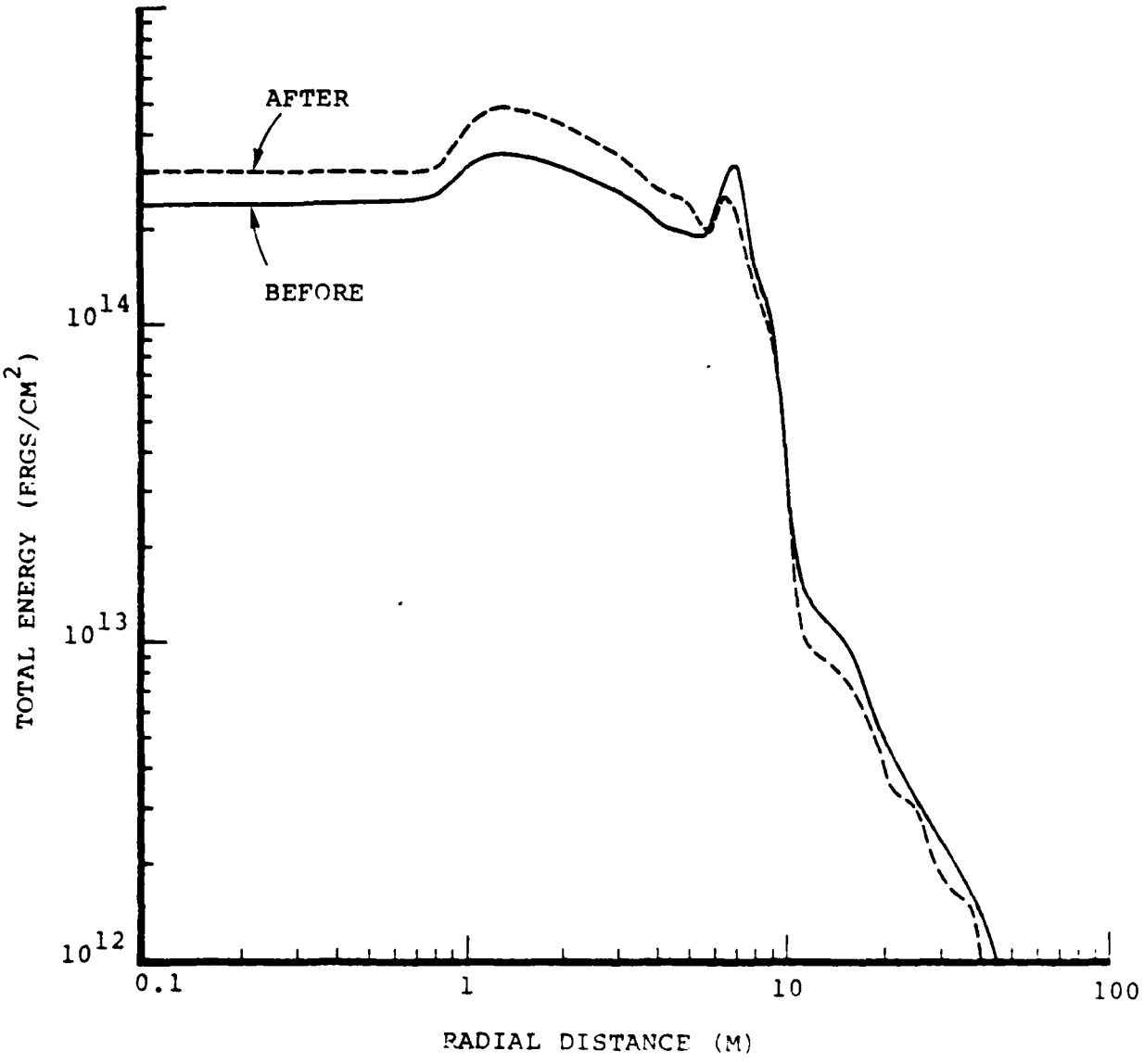

Figure 3.5 Energy (internal plus kinetic) in downward-moving ground material below original ground surface before and after equation-of-state change.

TABLE 3.1 TOTAL ENERGIES IN CALCULATION GRID AT 800 μSEC BEFORE AND AFTER EQUATION-OF-STATE CONVERSION

	Internal Energy (10^{20} ergs)	Kinetic Energy (10^{20} ergs)	Total (10^{20} ergs)
Total Grid			
Before	6.11	1.93	8.04
After	6.15	1.46	7.61
Inside 6 Meters			
Before	2.05	0.50	2.55
After	2.69	0.46	3.15

Peak pressure versus range for the two spherically symmetric test calculations are shown in Figure 3.6. The second calculation, incorporating the equation-of-state conversion, at a range of 1350 cm, gives peak pressures within 10 percent of the calculation made using CHEST from the very beginning. Figures 3.7 through 3.9 compare the flow fields (pressures, densities, and velocities) for the two calculations at a time when the shock waves have traveled out to 2700 cm, twice the range at which the equation-of-state conversion was made. The agreements between pressures and densities is outstanding as is the agreement between velocities near the shock front. However, the velocities do differ behind the shock front. This is the region in which extrapolation from the spherically symmetric calculations to the surface burst is tenuous at best. On the whole, the results of these test calculations give us a great deal of confidence in the credibility of the equation-of-state conversion over most of the active grid.

The EIONX equation-of-state was intended to be used at high temperatures and pressures. This gas equation-of-state had a ground cold pressure of approximately 3.4 kbar, which caused the ground at large radii (smaller, too, of course, but they had less time to work) to blow off. By 800 μsec the ground surface had moved up to approximately 20 cm and was moving at a velocity of 800 m/sec. To correct for this artificial blow off, the ground was put back to normal density, cold motionless values beyond a radius of 76 meters and its surface was returned to zero. The shock in the air was at a radius of $\sim$ 83 meters at this time. Thus the ground surface from 76-84 meters is not impacted with the correct airblast shock values.

Also, in the equation-of-state switch, there were a few zones at the outer edge of what was accepted in the ground which gave slightly anomalous values. Due to the

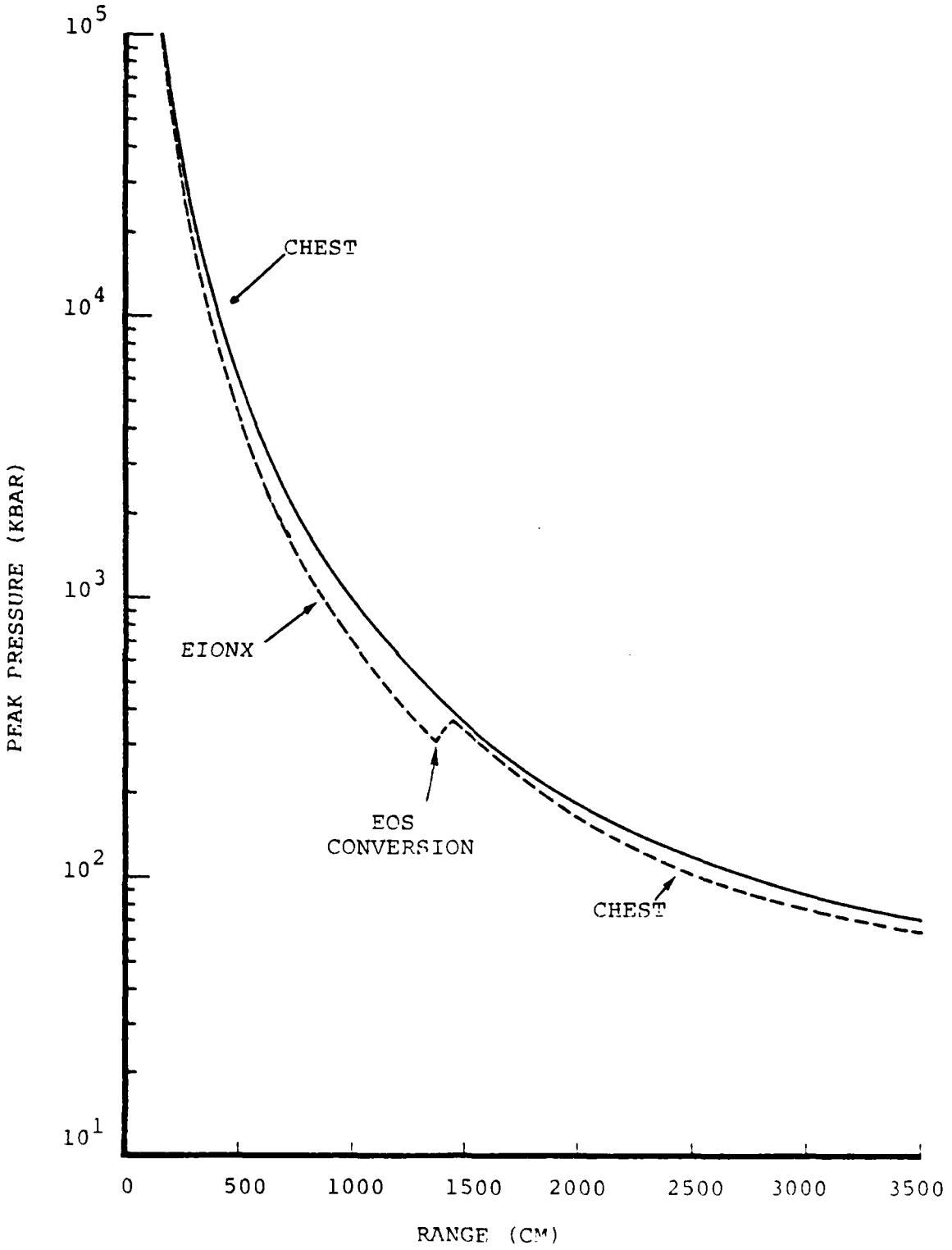

Figure 3.6. Peak pressure versus range from spherically symmetric 100 KT test calculation.

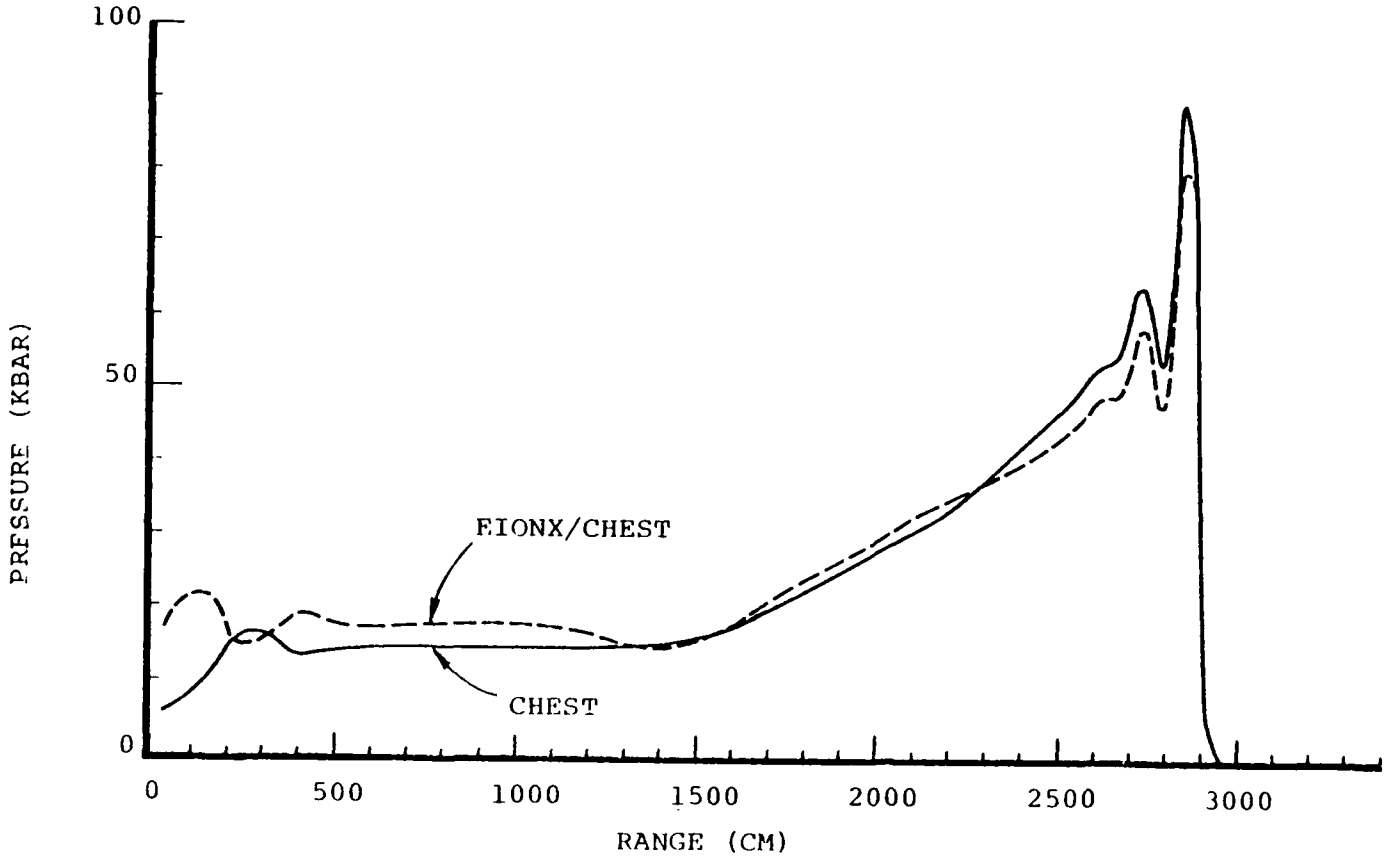

Figure 3.7 Pressures profiles for spherically symmetric test calculations.

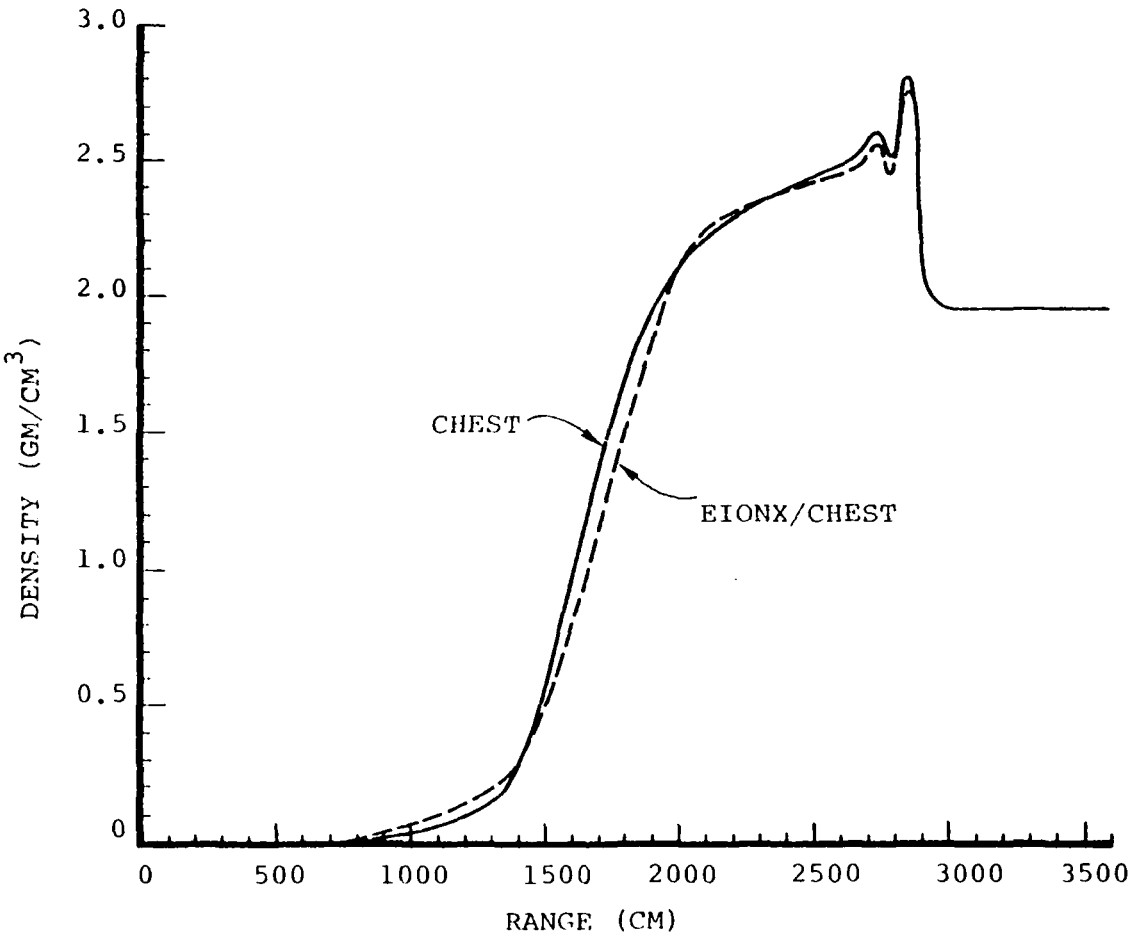

Figure 3.8 Density profiles for spherically symmetric test calculations.

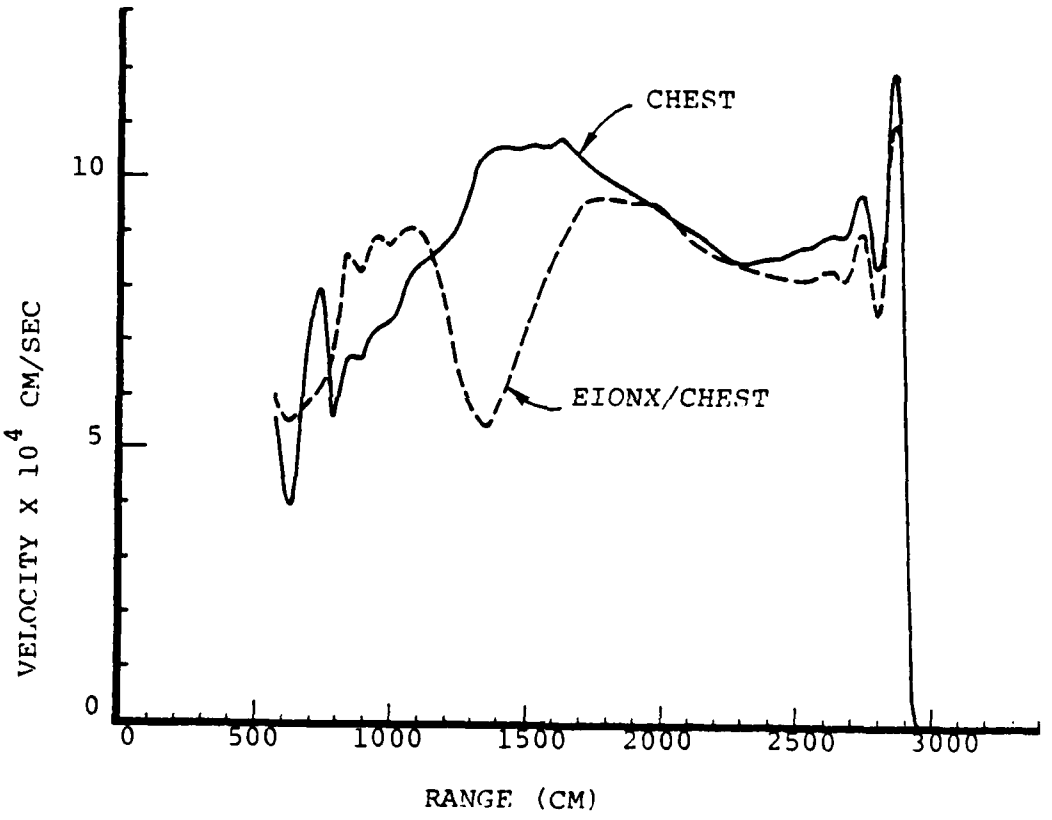

Figure 3.9 Velocity profiles for spherically symmetric test calculations.

sensitive density dependence of the CHEST equation-of-state, a few zones at radii of 70-75 meters and a few centimeters depth had pressures of one bar bracketed between zones of 10 kbar pressures. It was felt that this would not be a significant perturbation to the calculation of the crater since this is in material which should be ejected ultimately. During the course of the calculation it was also felt that much of this would be washed out in running or rezones and would not effect the far-field ground motion.

3.3 RESULTS OF THE EULERIAN CALCULATION TO 5 MSEC

After the conversion to the CHEST equation-of-state, the calculation was run out to 5 msec using the Eulerian STREAK code in hydrodynamics mode with radiation turned off. At 5 msec, the calculation was overlaid into the Lagrangian CRAM code and strength effects included for the first time. Strength effects for the first 5 msec of the calculation are negligible relative to the high pressures calculated.

Figures 3.10 and 3.11 show the locations of tracer particles at 1.87 and 5.0 msec defining the boundary of original ground material which has been blown off at very low densities. At 1.87 msec ground material has reached a height of approximately 100 meters while at 5.0 msec it extends about 150 meters into the air. The radial extent is approximately 75 meters at 5.0 msec. For comparison, at 5.0 msec the airblast has propagated out to a radial range of approximately 175 meters.

Figure 3.12 shows contours of equal internal energies in material still in the ground at 1.87 msec. Figure 3.13 shows mass density contours for the same material. The soil directly under ground zero contains the highest internal energies and has been expanded to less than one quarter of the initial density. This material is rapidly blowing out of

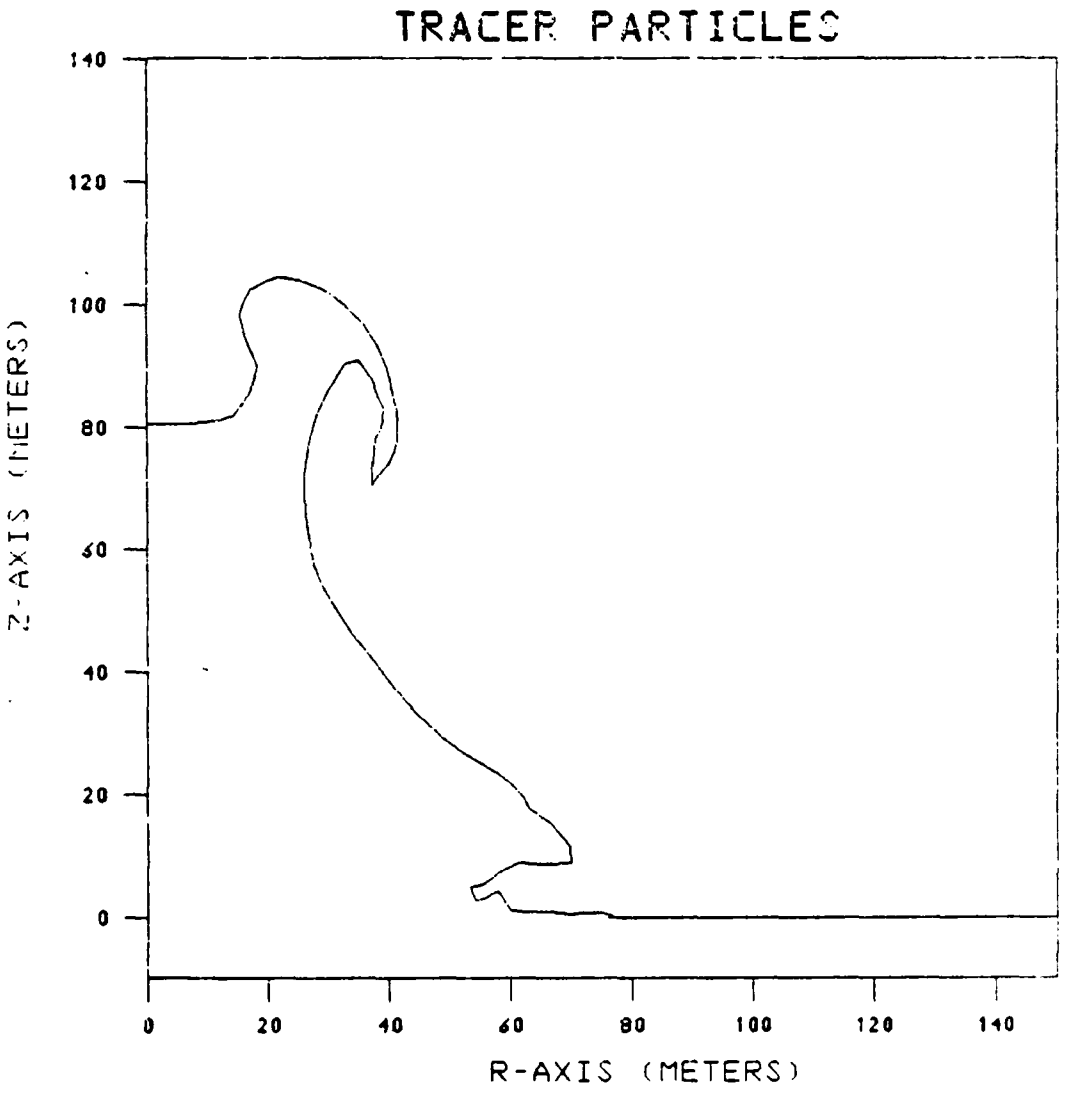

Figure 3.10 Tracer particles showing extent of blowoff of original ground material at 1.87 μsec.

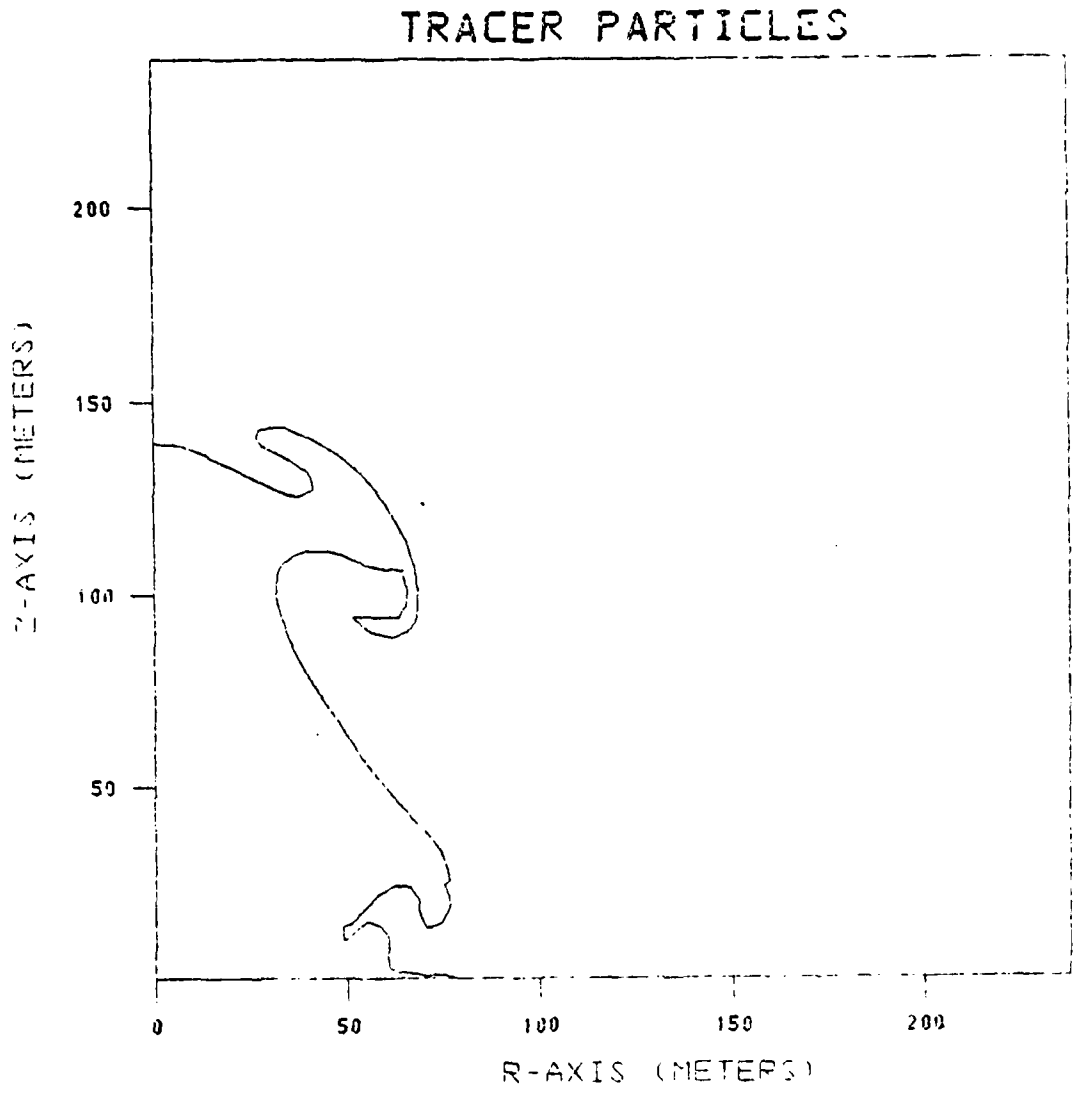

Figure 3.11 Tracer particles showing extent of blowoff of original ground material at 5.00 msec.

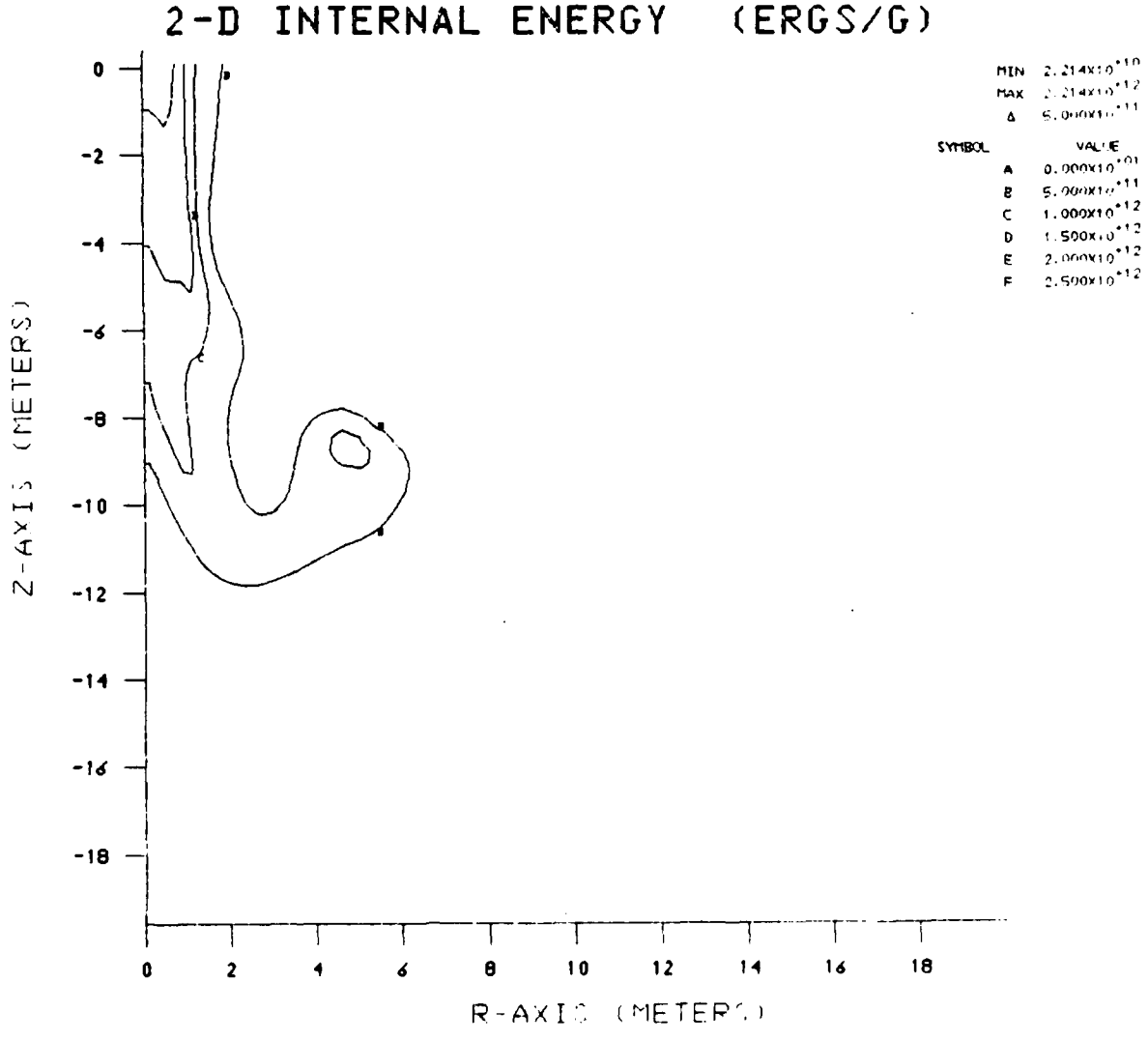

Figure 3.12 Internal energy contours in ground material at 1.87 msec.

the ground at particle velocities greater than one meter per millisecond. (See Figure 3.14 for velocity vectors at this time.) Figures 3.13 and 3.14 show the main shock wave at a spherical radius of roughly 19 meters from ground zero. The intersection of this shock and the planar fireball-induced shock lies near the free surface and at a horizontal range of approximately 16 meters. The planar shock extends out to approximately 100 meters at 1.87 msec.

Figures 3.12 through 3.14 show only the results which are included in Package 1 of the computational grid. Most of the planar fireball and airblast induced shocks have been calculated using Package 3 which is very finely zoned vertically. All computational packages have been rezoned several times in the course of these calculations. We shall see that Package 1 dimensions are increased with time to include all of the expanding spherical shock wave.

Figures 3.15 through 3.18 show peak pressure contours from Package 1 at four times from 1.87 to 5.00 msec. These show the propagation of the spherical shock front and the decay in peak pressure with time. By 5 msec, peak pressures have decreased to below 60 kbars over most of this shock front (68.6 kbar is the maximum in the grid). Figure 3.19 shows pressure contours at 5.00 msec including much of the planar airblast-induced shock out to 60 meters. (Note the change in contour scale from Figure 3.18.) Peak pressures in the planar shock wave are between 5 and 10 kbar or approximately 10 percent of the peak pressures in the main shock wave. The minimum pressure calculated was 0.44 kbar in this region. Figure 3.20 shows pressure contours in the planar shock at even larger horizontal ranges at 5.00 msec. Pressures of 0.5 kbar extend out to 160 meters (airblast peak pressures of approximately 1.5 kbar were experienced at the free surface at a range of 160 meters). Note that these pressures

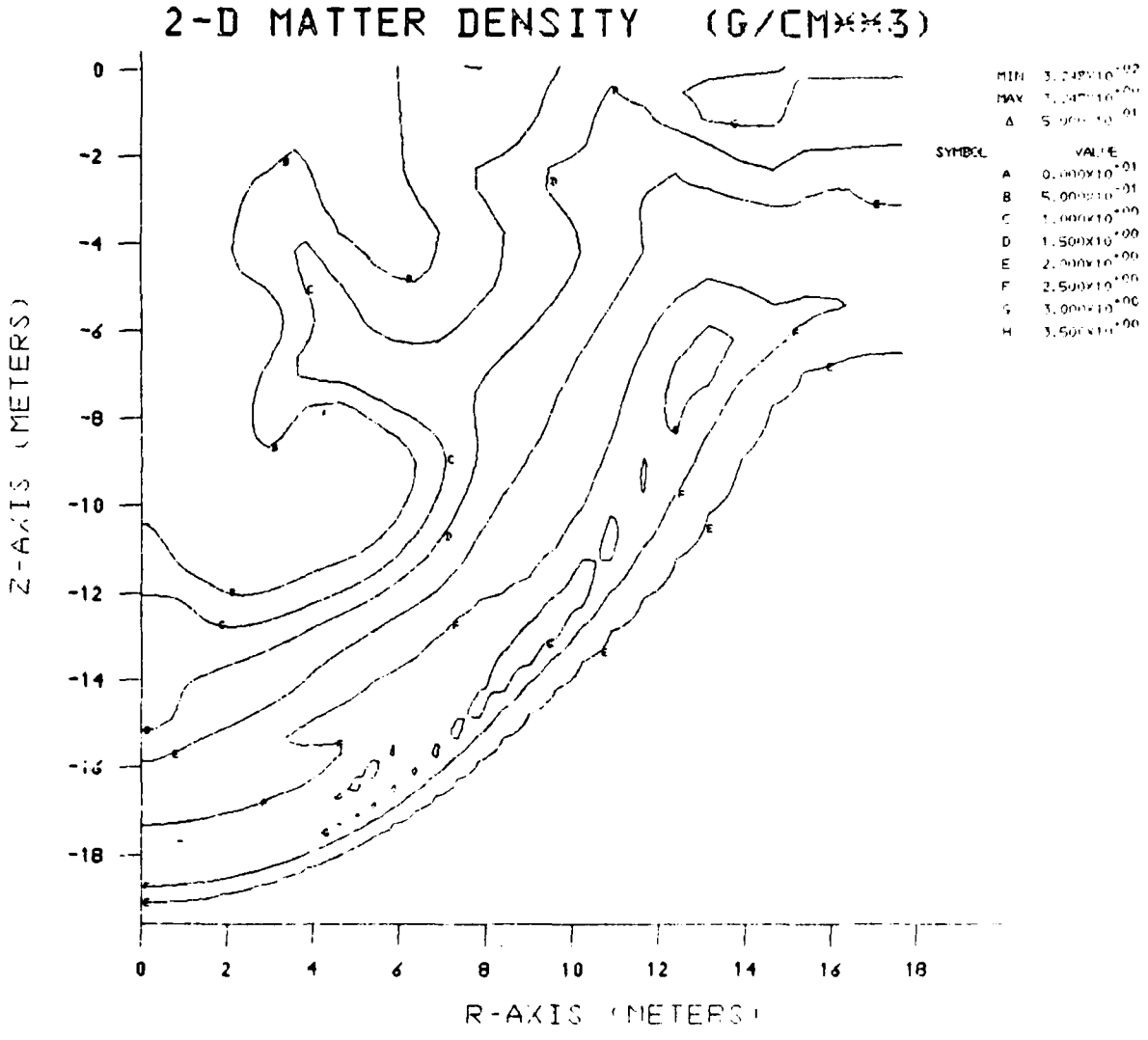

Figure 3.13 Mass density contours in ground material at 1.87 msec

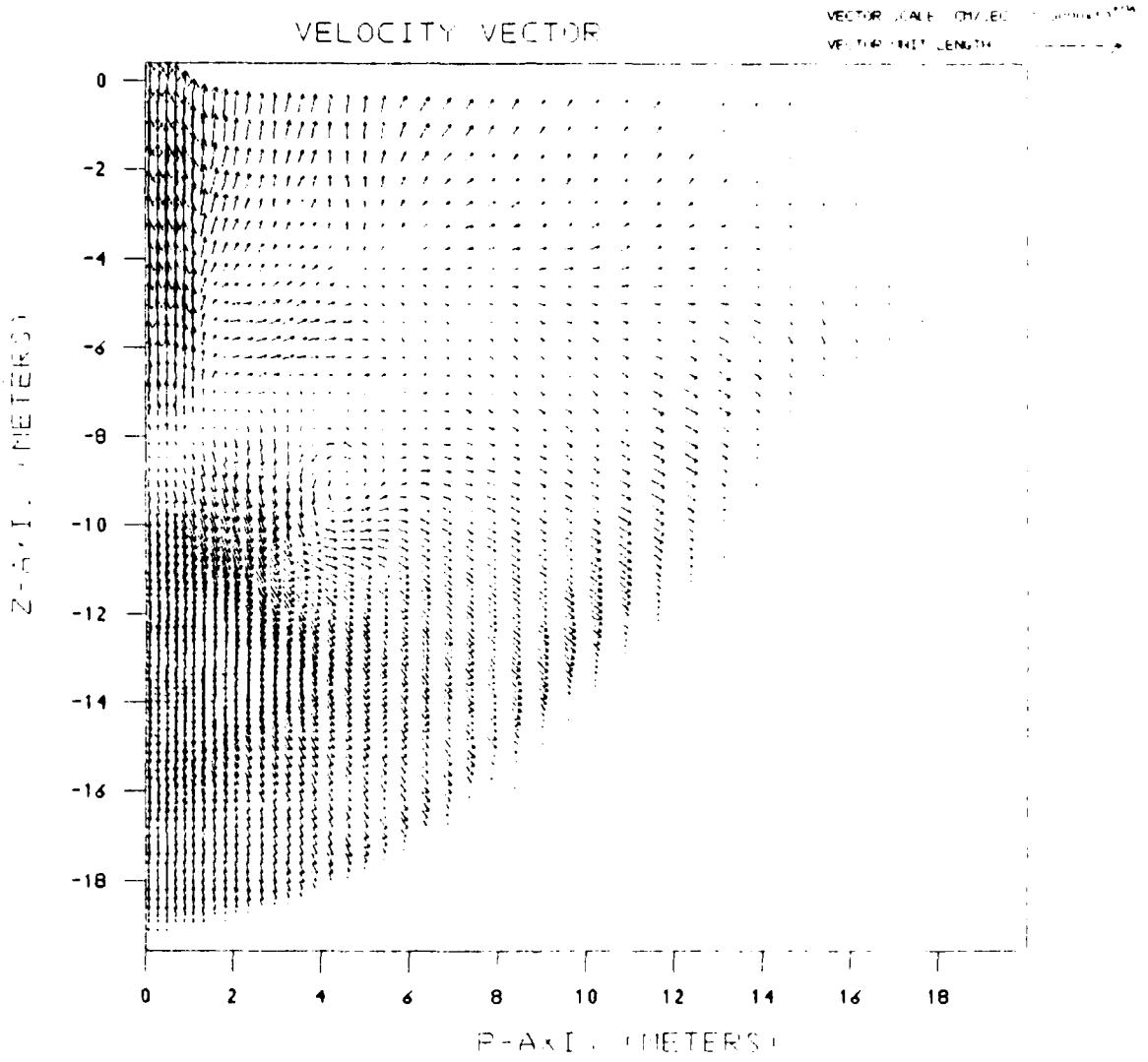

Figure 3.14 Velocity vectors at 1.87 msec.

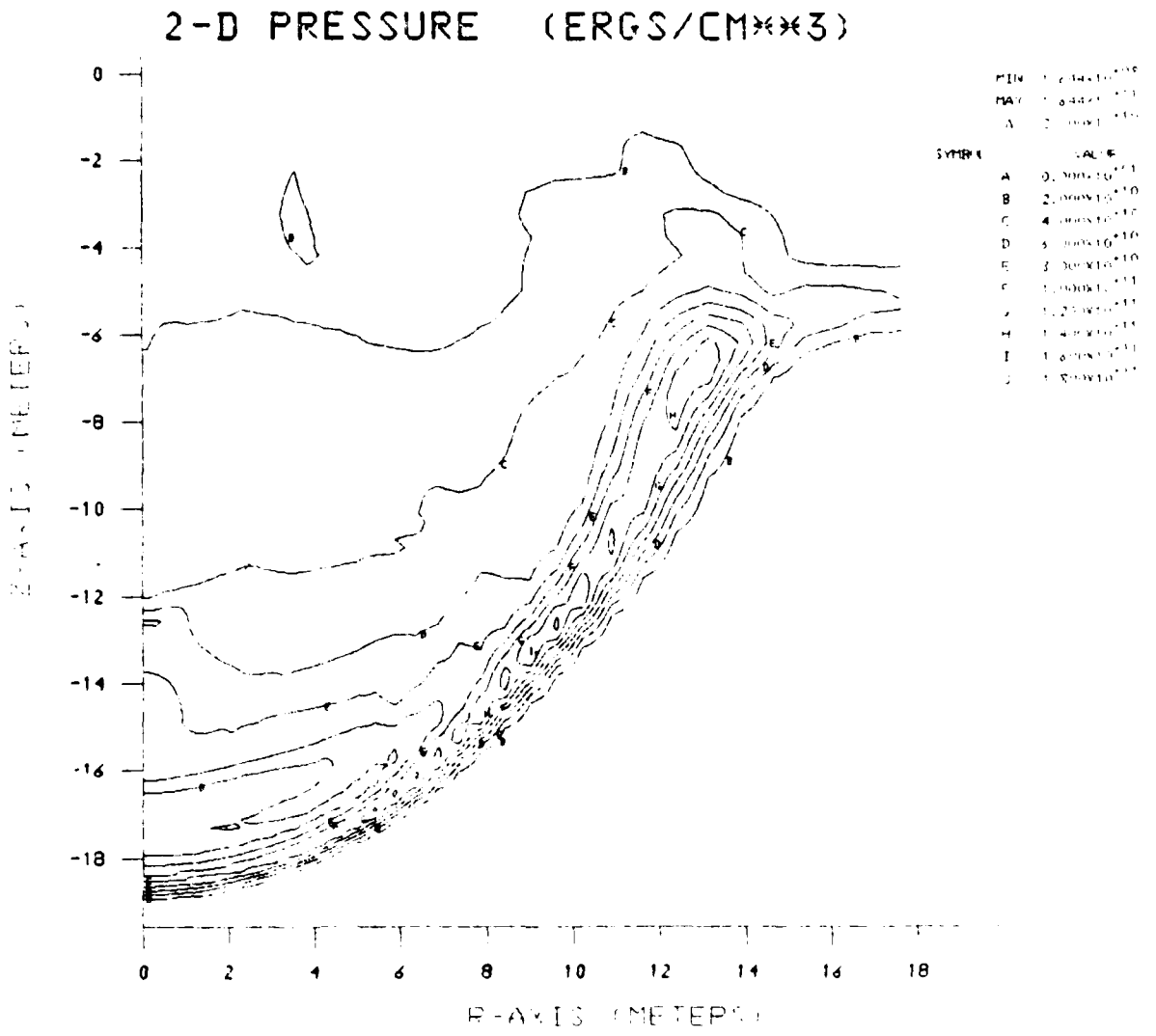

Figure 3.15 Pressure contours at 1.87 msec.

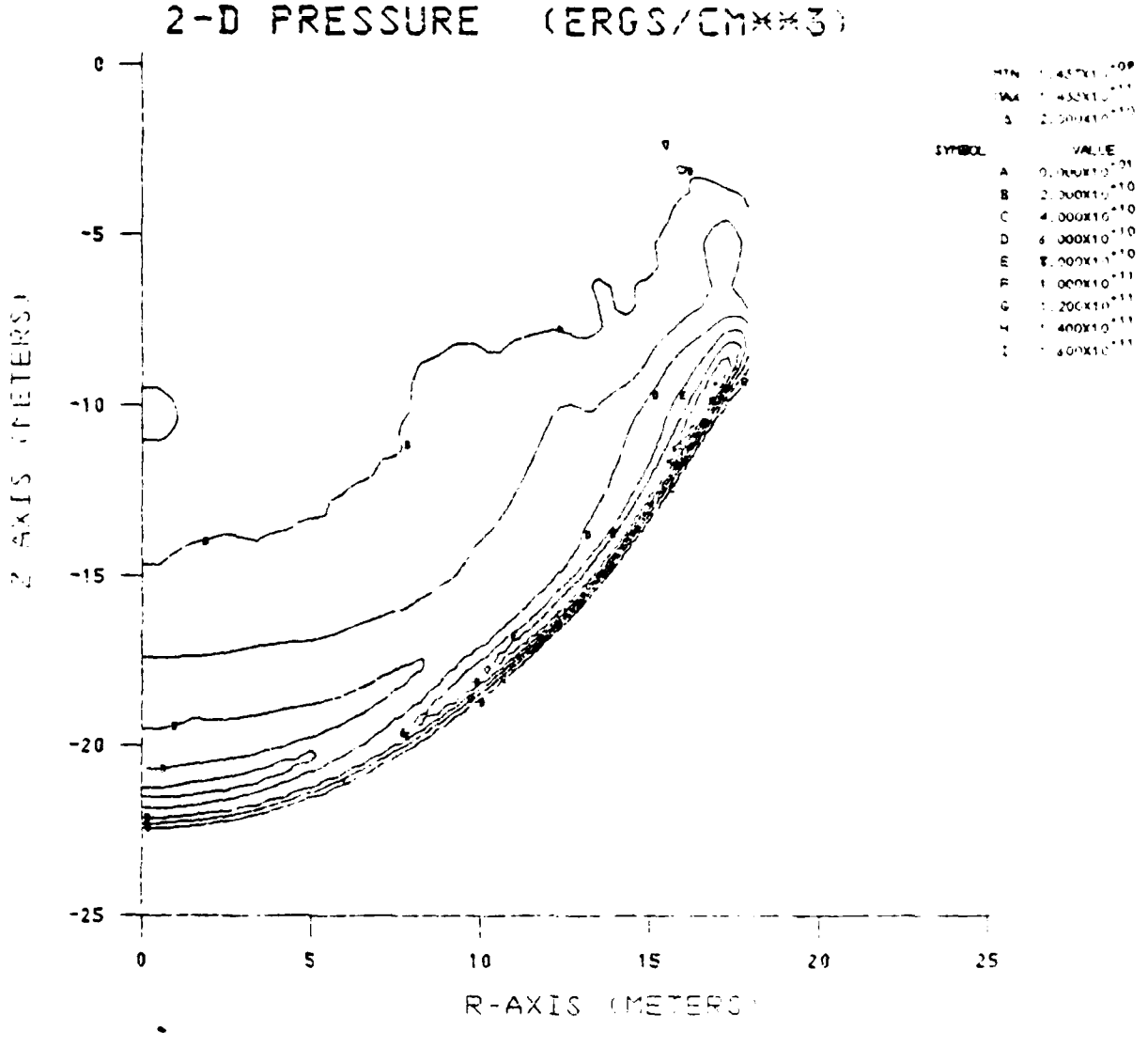

Figure 3.16 Pressure contours at 2.84 msec.

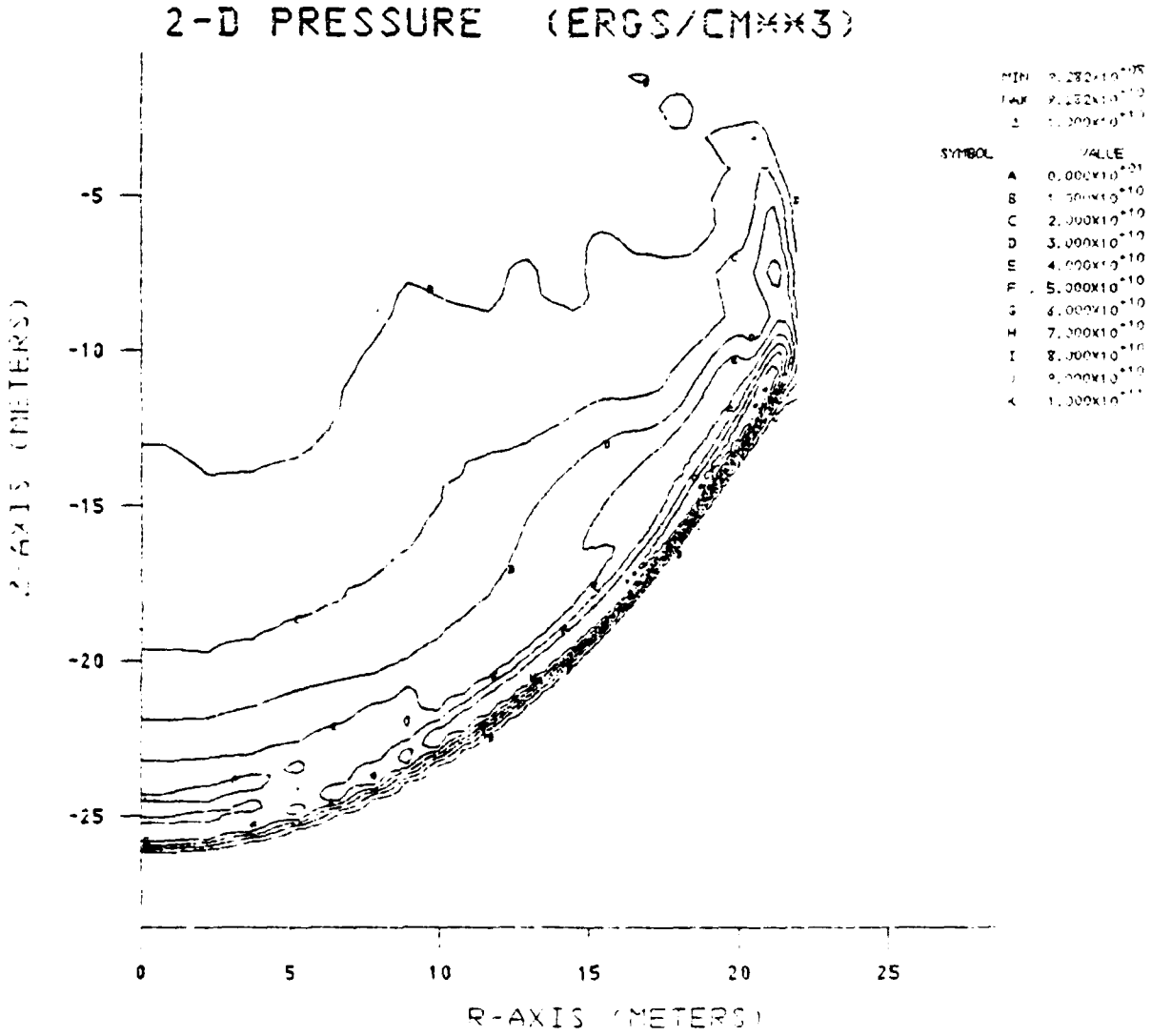

Figure 3.17 Pressure contours at 3.94 msec.

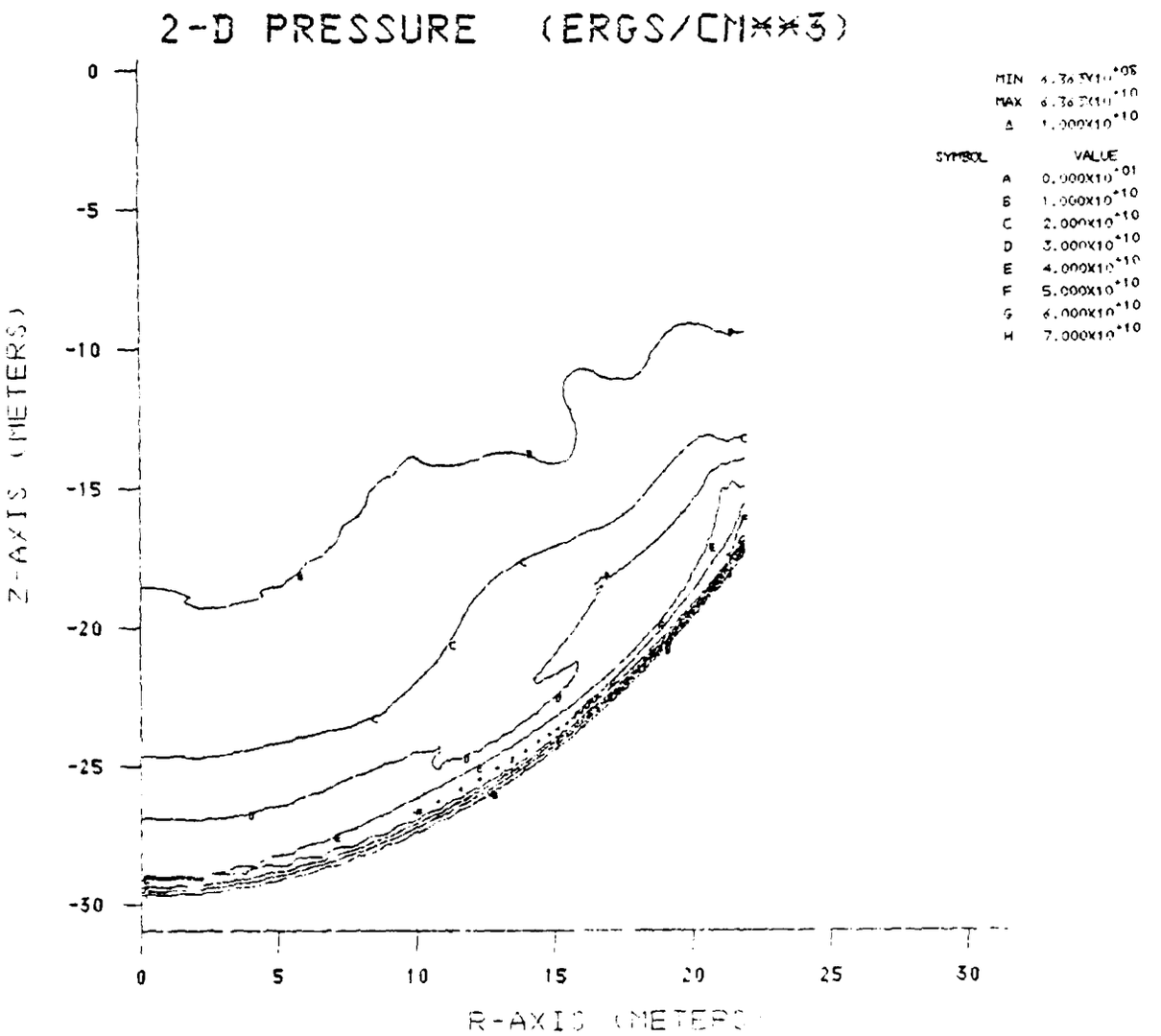

Figure 3.18 Pressure contours at 5.00 msec showing main shock.

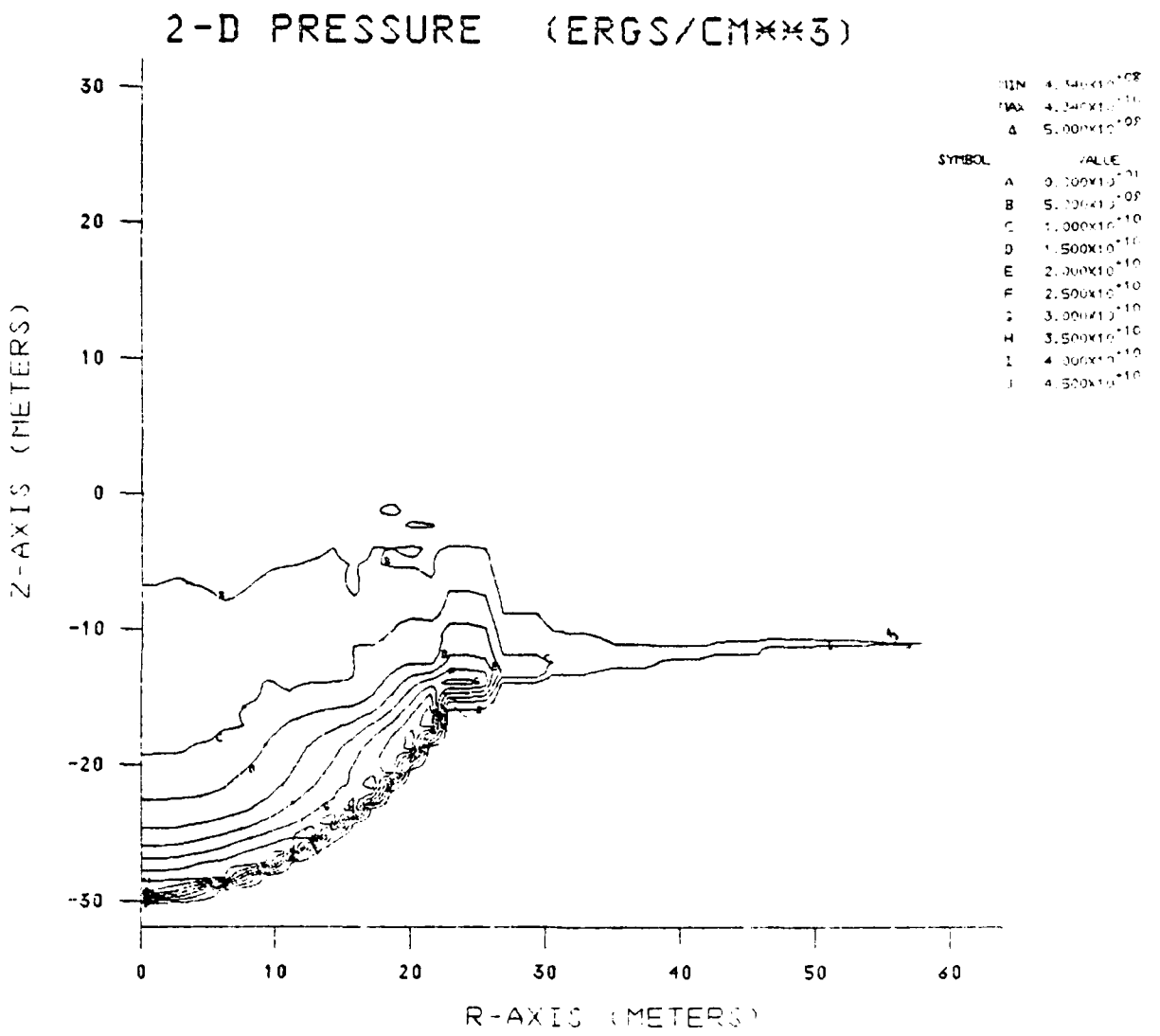

Figure 3.19 Pressure contours at 5.00 msec out to a range of 60 meters.

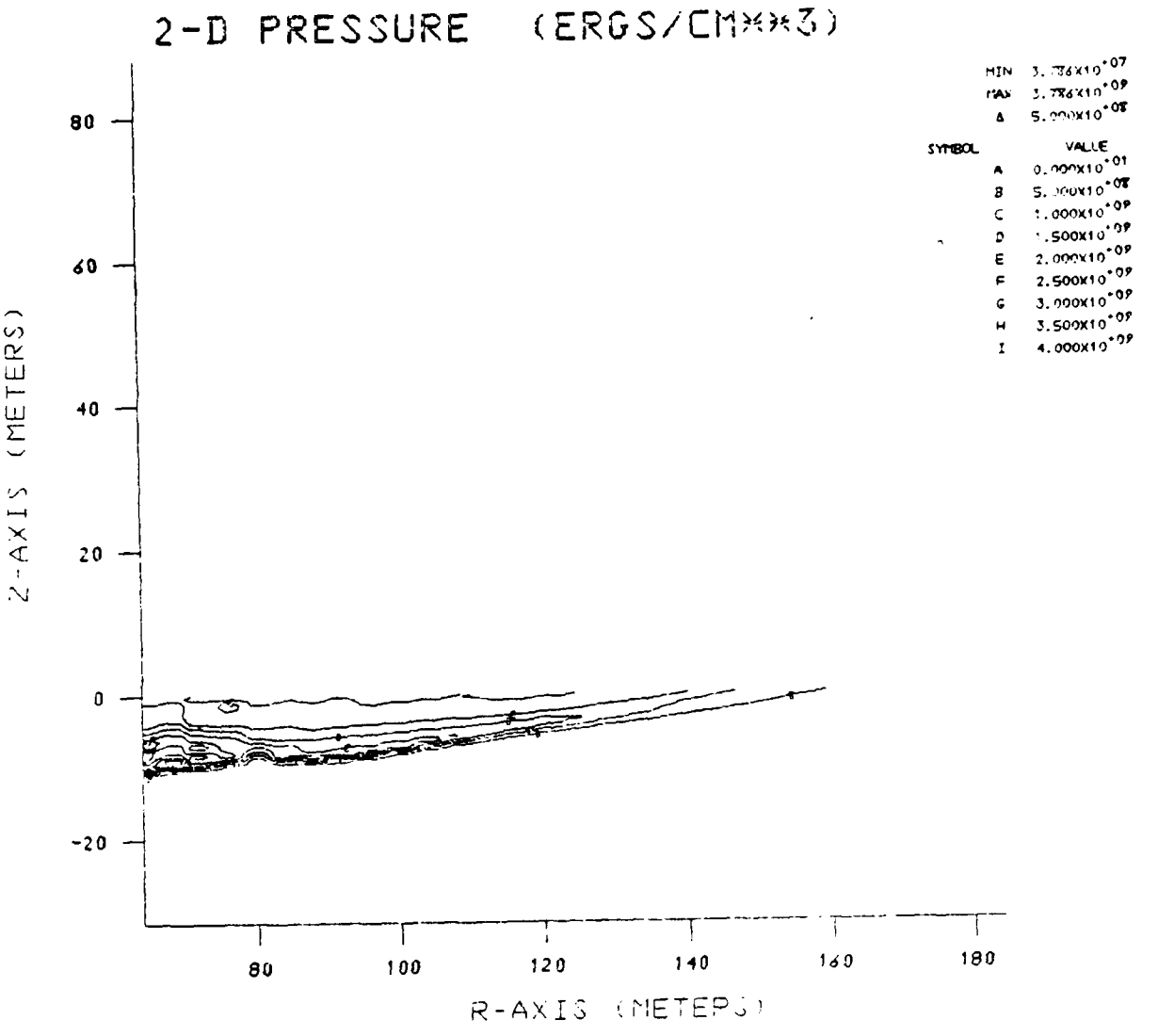

Figure 3.20 Pressure contours in ground at ranges greater than 60 meters at 5.00 msec.

are quite large when compared with an assumed shear strength of less than 20 bars for the saturated soil.

Velocity vectors at 5.00 msec are shown in Figure 3.21. The largest of these as before are directed out of the ground near the burst point. Velocities in the airblast-induced planar shock are considerably smaller than in and behind the main spherical shock.

Figure 3.22 shows mass density contours at 5.00 msec. Again, the lowest densities are in the high velocity blow off region near ground zero. All material with density less than 1.0 gm/cc is very likely to be blown off in time. Figure 3.11 gave the boundary of original ground material at 5.00 msec. This material with very low densities has not been included in Figure 3.22 and will be neglected in our calculation.

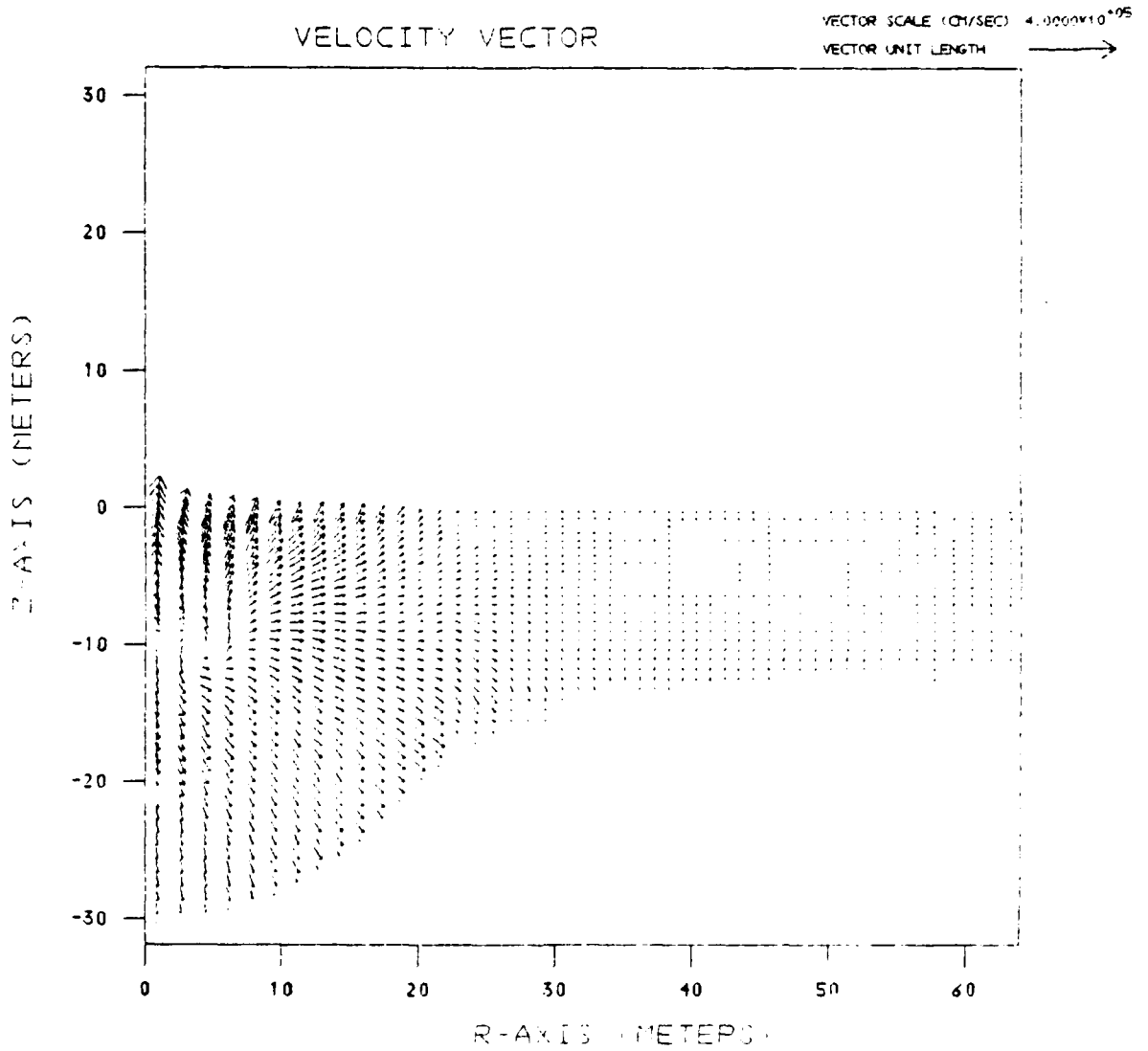

Figure 3.21 Velocity vectors at 5.00 msec.

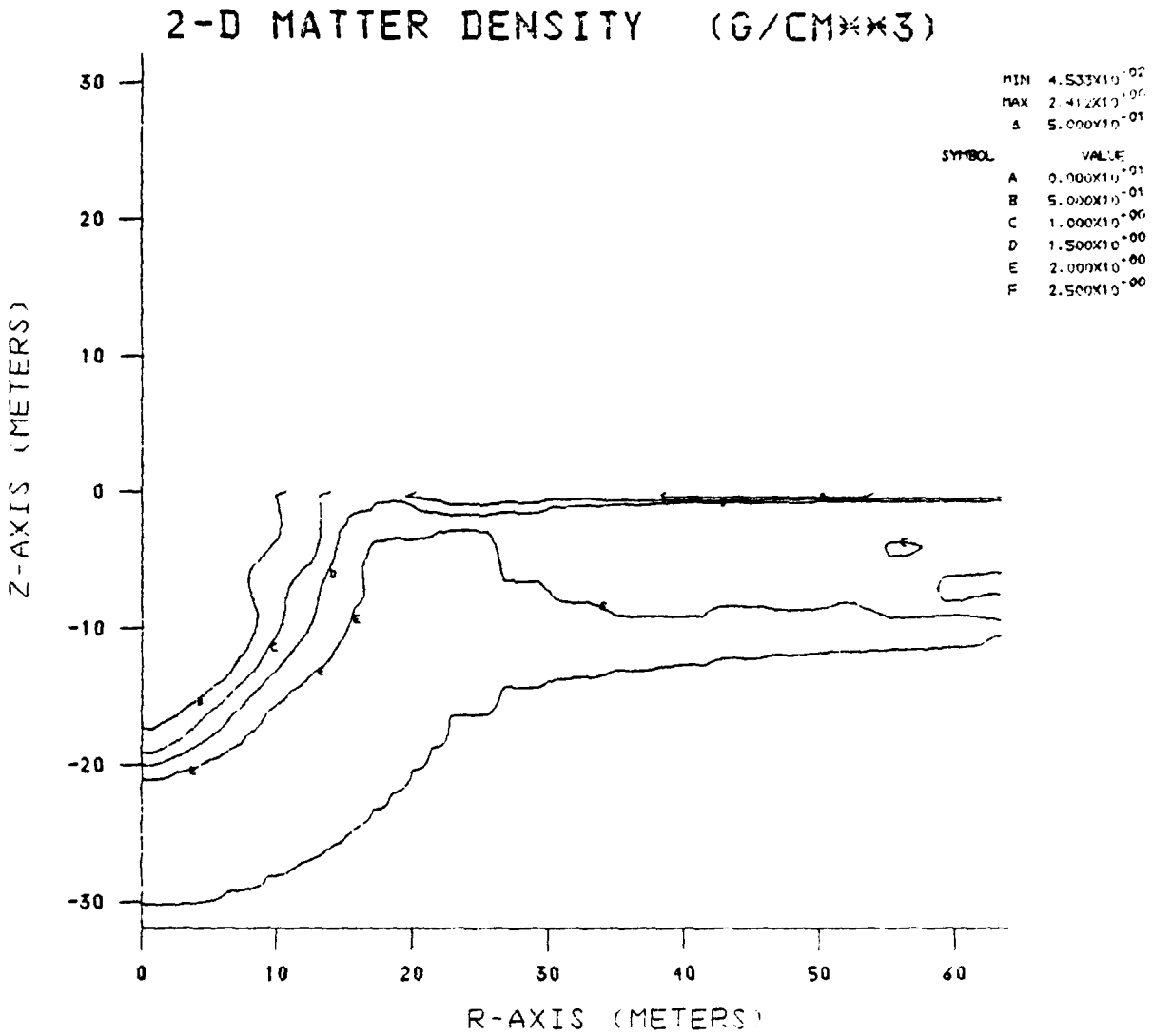

Figure 3.22 Density contours at 5.00 msec.

IV. NONLINEAR GROUND MOTION OUT TO THE ELASTIC RADIUS

The Source 3/5 ground coupling calculation out to 5.00 msec was made using the two-dimensional Eulerian hydrodynamic STREAK code. At 5 msec, this calculation was transferred to the two-dimensional Lagrangian stress wave code, CRAM, and material strength introduced into the calculation for the first time. In this section we describe the numerical procedures used and present the results of this calculation.

4.1 NUMERICAL PROCEDURES

Both Eulerian and Lagrangian computer codes have certain advantages and disadvantages for two-dimensional ground motion calculations. A Lagrangian code, because each computational cell follows the motion of a specified mass of material, gives a more accurate description of the behavior of that mass element, particularly when complex material models are needed. Since it was also necessary to follow the ground motion out to low stress ranges (a few bars), where the diffusion inherent in Eulerian codes would be likely to obscure the physical solutions, the Lagrangian CRAM code was used for our calculation.

Our greatest difficulties in the course of this calculation were in overcoming the large zone distortions inherent in the Lagrangian approach to a surface burst calculation. From the beginning, it was obvious that we would be unable to adequately treat the hot, high velocity, low density blowoff materials near ground zero which were described earlier in this report. Zone distortions would be just too large. Therefore we decided to remove these materials from consideration as they moved well above ground level. Similarly, we chose not to continue numerically modeling the mixture of hot gases, air and blowoff material above the air-ground surface.

We replaced these by using as free surface boundary conditions the airblast solutions developed by Brode (1968) and Needham (1975). The pressure as a function of range along the free surface was specified at each computational time step at first using a numerical fit to the Brode solutions. Later, at approximately 306 msec, this fit was replaced by the Needham computer subroutine which was thought to be a more accurate representation for low pressures.

The first step in our calculation was to overlay the Eulerian solutions at 5.00 msec into a Lagrangian grid suitable for continuing the simulation. Relatively fine zoning was needed in the vertical direction near the free surface in order to adequately treat the airblast induced motions. We chose a vertical mesh size of 0.5 meters at the free surface and very gradually increased mesh size with depth. Horizontal zone sizes in the cratering region were between 1 and 2 meters with the smallest mesh sizes ahead of and in the region of the propagating main shock. These mesh spacings can be considerably coarser than those in the Eulerian STREAK grid at 5.00 (0.20 to 0.60 meters both vertically and horizontally) due to the more accurate Lagrangian definition. The solutions at 5.00 msec were first rezoned into a STREAK grid identical to the proposed CRAM mesh. Thus the overlay of masses, velocities, densities, pressures, and specific internal energies from STREAK Packages 1 and 3 to CRAM was accomplished very simply on a one-to-one zone basis.

The CRAM zone boundaries as defined at 5.00 msec were identical to the STREAK tracers (see Figure 3.11) locating the ground-air interface at ranges from 76 meters outward. At 76 meters, the ground surface was displaced 0.13 m upward. In closer than 76 meters, the hot, low density blowoff materials above original ground surface were not included in the calculation. Figure 3.21 indicated that these materials are moving upward at velocities greater than several kilometers

per second. CRAM zones containing the hot melted and gaseous materials still below initial ground surface were flagged to indicate present or earlier melt. Our constitutive model did not allow deviatoric stresses in this melted material. Elsewhere, strength was included using the model defined in Section 2.2. Gravity was also included in the momentum equation for the first time and all inactive zones given a hydrostatic overburden pressure.

After a careful check of the overlay, the Lagrangian calculation was begun. Figure 4.1 is a plot of a part of the CRAM grid at a time of 10.15 msec, 100 cycles into the Lagrangian calculation. (The same plot is used to show tensile crack orientation; no cracks were open at this time). Figures 4.2 and 4.3 show velocity vectors and pressure contours over the same portion of the grid. As in earlier plots from STREAK, the positive Z direction is out of the ground. Low density soil, moving upward near ground zero at the largest velocities shown by Figure 4.2, has resulted in very large distortions in the Lagrangian grid. These distortions will become worse with time. Elsewhere the grid has not distorted greatly from the overlay time. Some distortion can be seen in Figure 4.1 marking motion at and behind the main shock wave.

The calculation at this time has been zoned only to a depth of 97 meters. To the right, zoning is in place out to almost 300 meters (not all shown in Figures 4.1 - 4.3) in order to accommodate the airblast induced ground motion. At 10.15 msec, this motion is out to approximately 220 meters horizontally More zones will be added before either the airblast arrival reaches the right of the grid or the direct induced ground motion reaches the bottom of the grid. Well before these occur, the continuing distortion of the grid near ground zero will require rezoning.

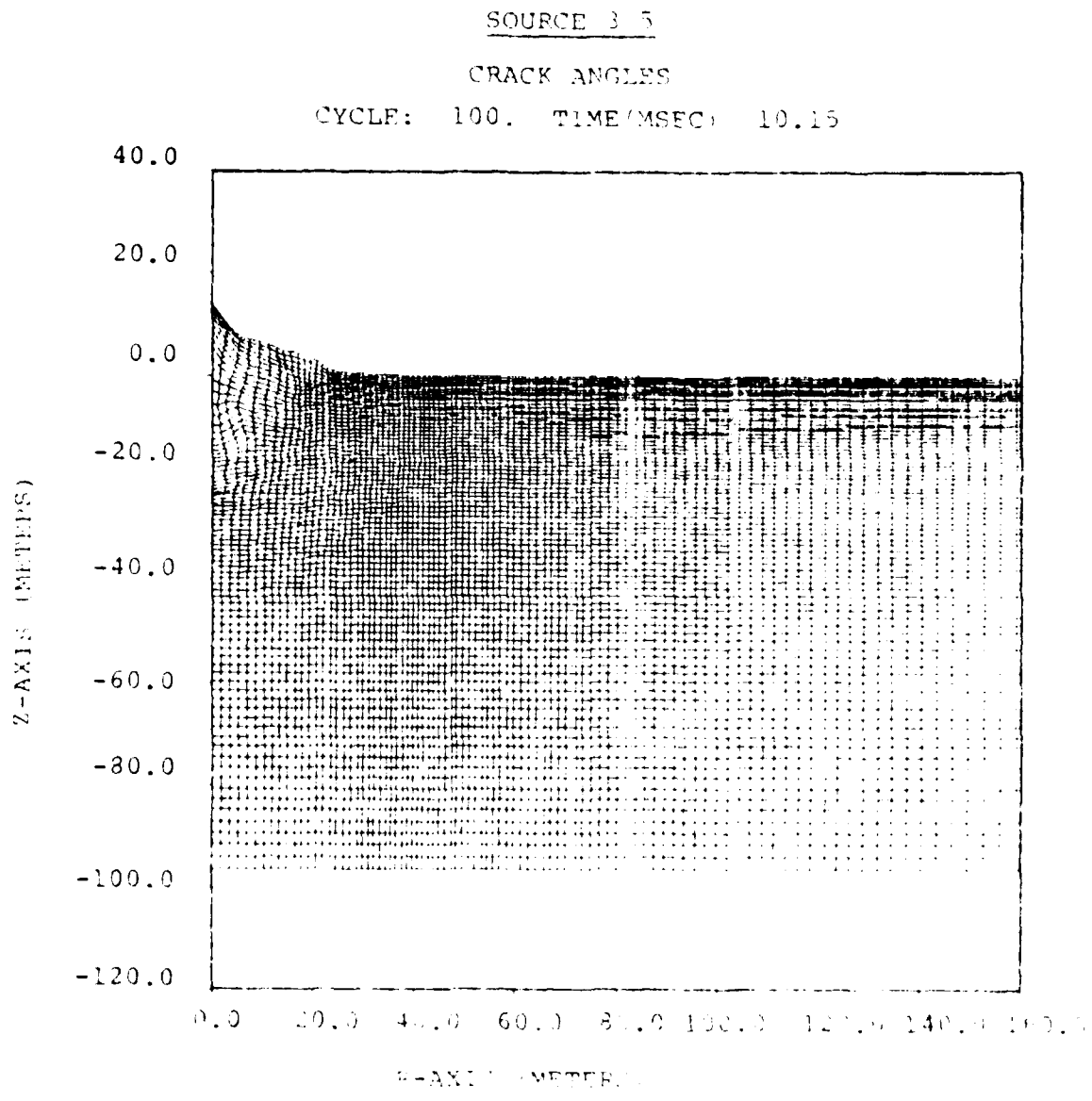
SOURCE 3 5
CRACK ANGLES
CYCLE: 100. TIME(MSEC) 10.15
40.0
20.0
0.0
-20.0
-40.0
-60.0
-80.0
-100.0
-120.0
Z-AXIS (METERS)
0.0
20.0
60.0

Figure 4.1

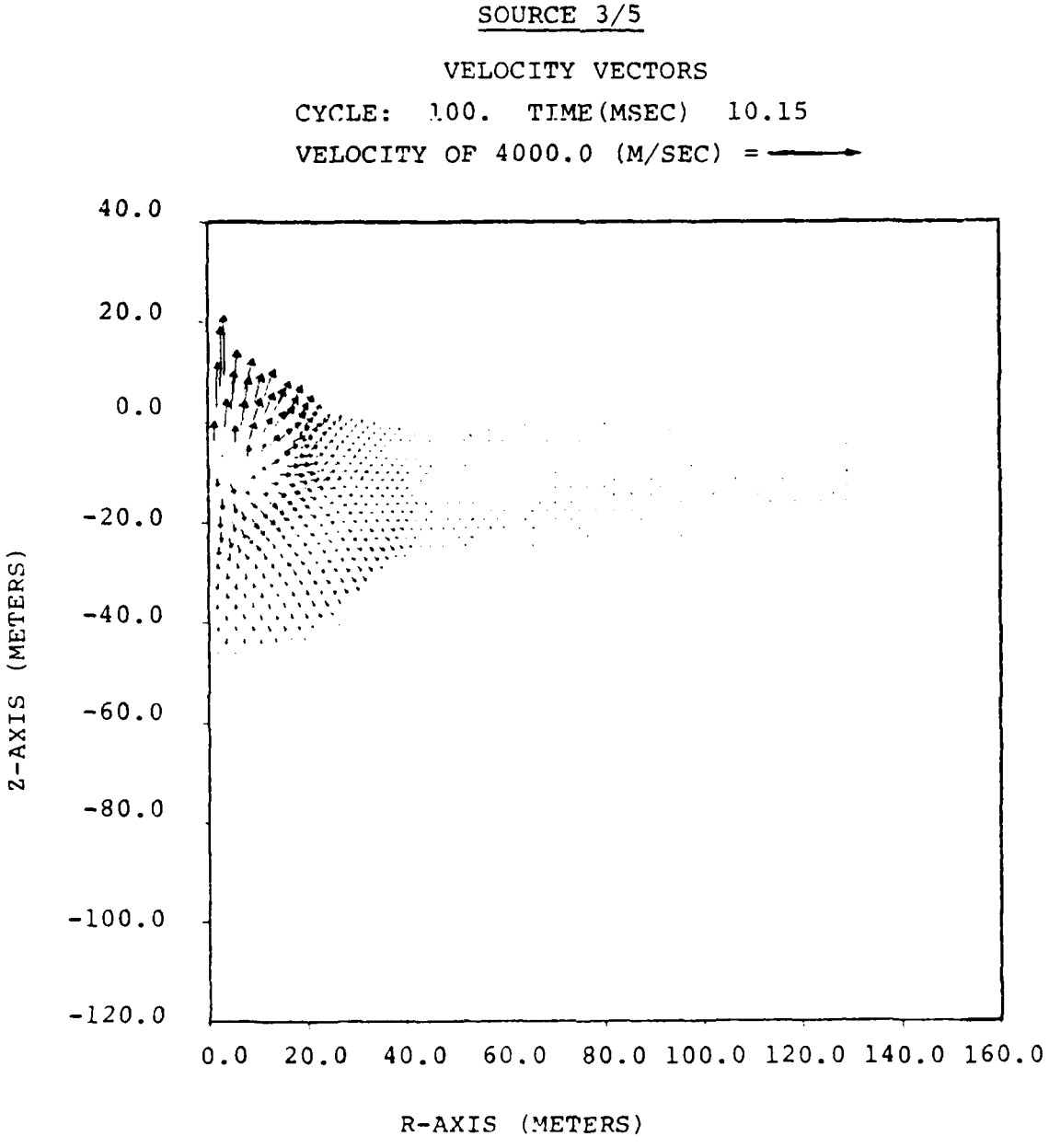

Figure 4.2. Velocity vectors at 10.15 msec.

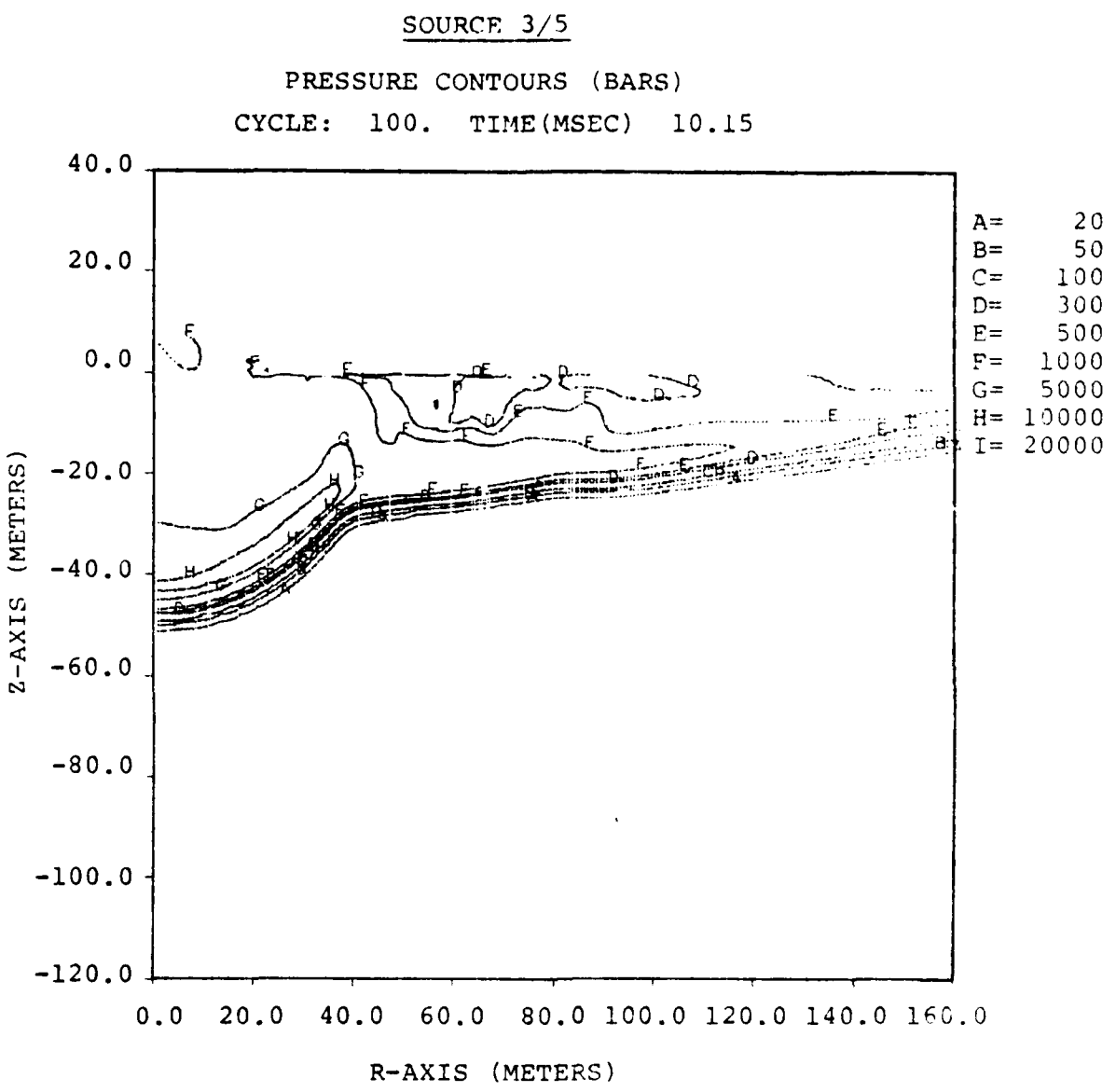

Figure 4.3. Pressure contours at 10.15 msec.

Our calculation was accomplished in several different stages, successive benchmarks in time in general being separated by a rezone of the existing grid and an overlay into a newer computational grid covering a larger area of activity. Major rezones were made at times of 18, 54, 126, 306 and 594 msec. Table 4.1 summarizes the numerical procedures applied in each stage of the calculation, listing the types of rezones used and the appropriate zone sizes in the cratering region. Note that the minimum vertical zone size in that region is also the vertical zone size elsewhere along the free surface.

Several types of rezones are available in CRAM. The most straightforward of these combines neighboring zones two for one. All zones adjacent to a specified vertical or horizontal line must be combined with their neighbors across the specified line to maintain the code algorithm. This is equivalent to removing a horizontal or vertical grid line from the mesh, thus lowering the cost of the calculation both by increasing the time step when the finer definition is no longer required and by decreasing the total number of zones to be calculated.

It is the "hand rezoning" feature of CRAM that proved most useful during this calculation. A series of computational subroutines have been developed which allow a distorted region of the mesh to be rezoned into a completely new set of regular grid lines or curves. The only limitations on this new set of lines is that they be continuous with the remainder of the old grid. We have used this feature to remove low density material which is above initial ground surface and continuing to blow out of the ground with time, thus distorting the Lagrangian grid. For example, if we had chosen to hand rezone the grid shown in Figure 4.1, we would have taken the region near ground zero out to 20 or 30 meters horizontally and down to about 25 meters vertically and set up a completely new set of grid lines each continuous with the appropriate line at the region boundary. A reasonable choice would have

TABLE 4.1 SUMMARY OF LAGRANGIAN CALCULATION

Time (msec)	Rezone Summary	New Zone Sizes in 100x100 meter cratering region	Other Features
5	Overlay from STREAK to CRAM. Zone out to R = 288 m and Z = 97 m	ΔR = 1-2 m ΔZ = 0.5-2.4 m	Addition of material strength, gravity and overburden for the first time. Brode airblast boundary condition replaces Package 2 of the STREAK computational grid.
18	1. Hand rezone of crater region and removal of blowoff material above ground zero. 2. Remove every other horizontal grid line to depth of 24 m. 3. Grid extended to R = 480 m. Z = 190 m.	ΔR = 1-3 m ΔZ = 1-2.4 m	
54	1. Same as above. 2. Remove every other horizontal from 24-55 meters. 3. Remove every other vertical line out to 72 meters. 4. Final CRAM grid dimensions reached R = 633 m, Z = 509 m.	ΔR = 2-3 m ΔZ = 1-2.4 m	
126	1. Same as above 2. General 2 to 1 rezone of CRAM grid removing every other horizontal and vertical line with a few exceptions.	ΔR - 4-5 m ΔZ - 2-4 m	Surround CRAM by SAGE grid to R = 3003 m, Z = 2856 m with absorbing boundary conditions. Monitoring stations activated in CRAM and SAGE.

TABLE 4.1 SUMMARY OF LAGRANGIAN CALCULATION (Continued)

Time (msec)	Rezone Summary	New Zone Sizes in 100x100 meter cratering region	Other Features
306	1. Same as above	ΔR = 4-5 m ΔZ = 2-4 m	Replace Brode solution by Needham subroutine. Pressure boundary condition applied directly to all melted cells.
594	1. General 2 to 1 rezone of CRAM grid.	ΔR = 8-10 m ΔZ = 4-8 m	
1730	1. Removal of a few lines which control time step	ΔR = 10 m ΔZ = 8 m	Motion frozen for $R < 140$ m, $Z < 140$ m since not enough definition left for crater region.

been to angle the free surface line up to Z = +5 meters at the axis of symmetry, throwing away the low density material above the new free surface line.

In actuality we rezoned at 18 msec when the free surface was approximately 30 meters above initial ground. Figure 4.4 is a plot of part of the new grid at 26.52 msec, showing the larger vertical zone sizes near the free surface behind the main shock (now at a depth of about 90 meters) as well as the reordered grid near ground zero. Figure 4.5 plots the grid and crack angles at 51.05 msec. (Tensile cracks can be seen at about 100 meters from the axis of symmetry. These will be discussed later.) The large zones near ground zero indicate very low density, hot material down to nearly 40 meters and out to about 30 meters. Adjacent to the free surface out to about 70 meters, zones which have had extensive radiation deposition until 0.8 msec are at a very low density. Rezoning of the grid was accomplished at 54 msec, including removing this low density material as well as some of the blowoff material near ground zero.

The calculation was run out to 126 msec, at which time another rezone was needed. At this time, the elastic radius appeared to be expanding very slowly if at all. Therefore a grid from the two-dimensional linear elastic SAGE code (Cherry and Halda, 1974) was placed around the existing CRAM grid out to a radial range of 3002 meters and a depth of 2856 meters (R = 633 m, Z = -509 m defined the CRAM-SAGE boundaries). The SAGE code contains an absorbing boundary treatment which effectively traps almost all of the incident P-wave signals and a great deal of the incident S-waves. This code is often used at S^3 to provide cheap, efficient boundary conditions for CRAM (it is an order of magnitude less expensive to calculate ground motion in SAGE rather than CRAM).

At 126 msec, monitoring stations at which velocities, displacements and stresses were to be saved were placed in

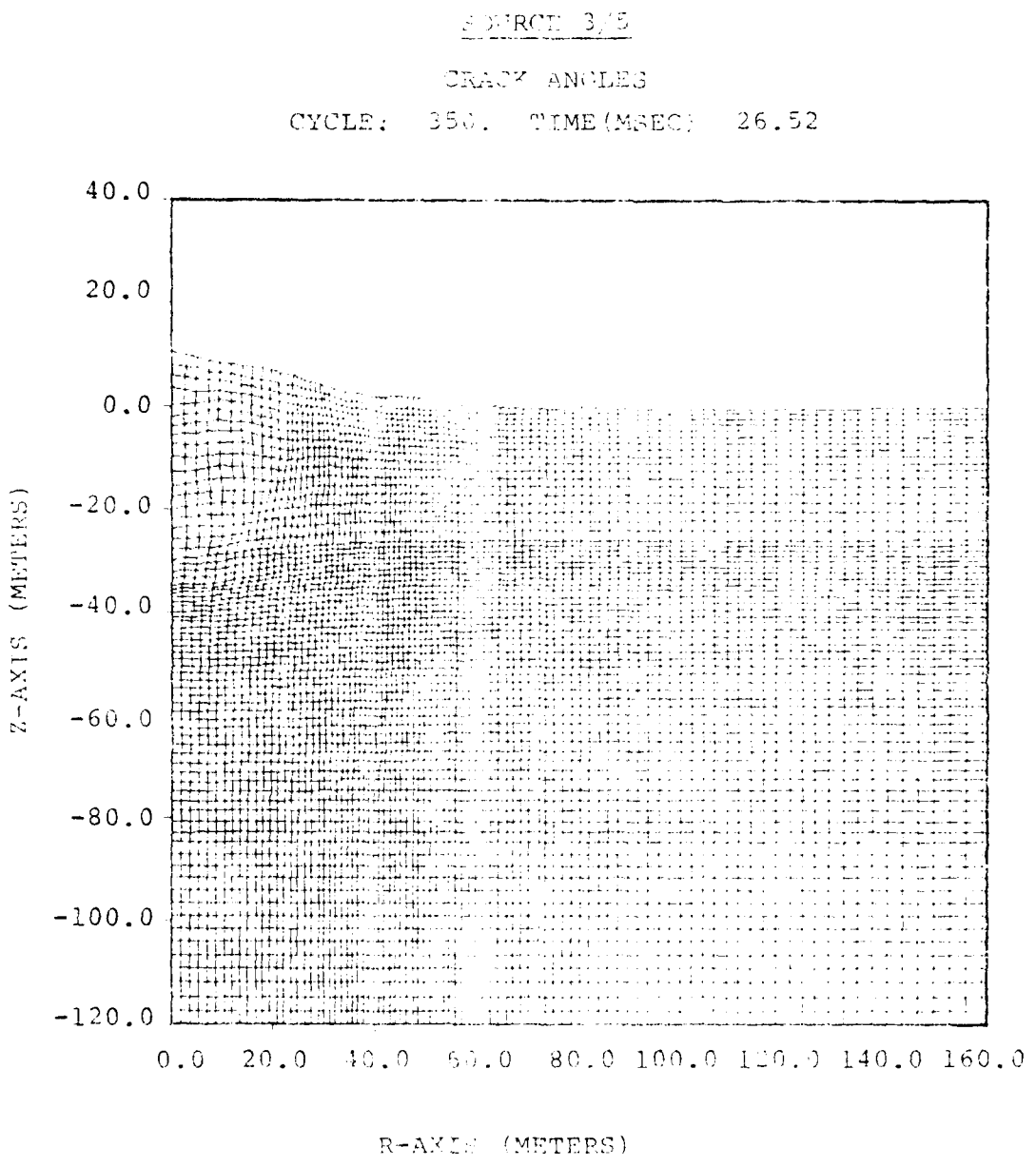

Figure 4.4. Grid and crack angles at 26.5 msec.

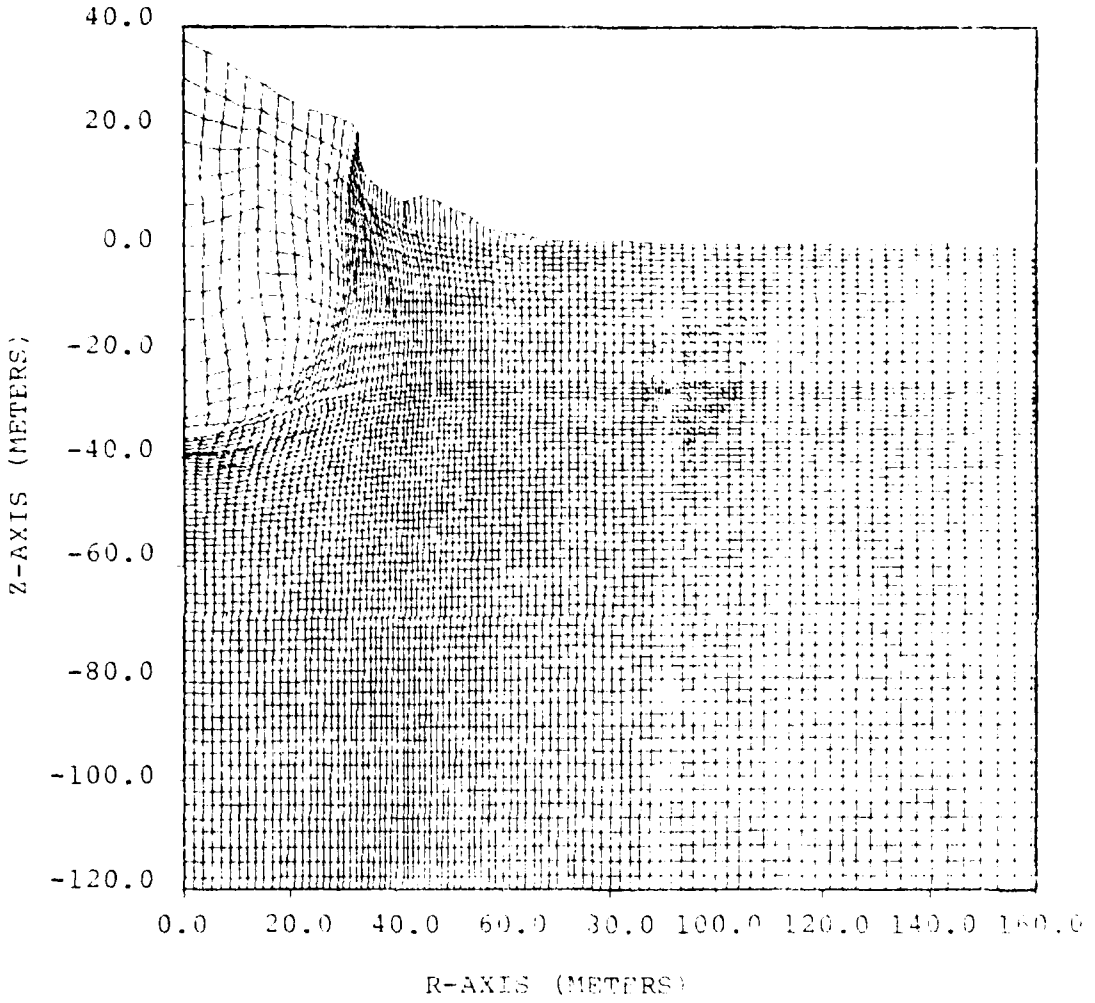

Figure 4.5. Grid and crack angles at 51.0 msec.

both CRAM and SAGE outside of the elastic radius. Figure 4.6 sketches the cylindrical monitoring surfaces, located to provide redundant surfaces with which to check out the analytical continuation methods. As a failsafe procedure to insure linear elastic behavior near the monitoring surfaces in CRAM, zones within 25 meters of these surfaces were required to behave elastically. Unfortunately our estimate of the depth of yielding was in error. CRAM cells below the mandated elastic surface at a 465-meter depth would have yielded at later times if allowed to. A careful examination of the stress deviators established that preventing plastic yielding was equivalent to the soil below 465 meters out to a horizontal range of approximately 200 meters having an effective strength of approximately 32 bars. Since realistic MX geologies would almost certainly be stronger at depth, no error has been introduced into the calculational results. Plastic flow did not occur near the vertical monitoring surface in the calculation.

The next benchmark in the calculation occurred at 306 msec. At that time, a hand rezone was again made in the cratering region. The zones inside of the melt radius (approximately 60 meters) were at extremely low densities (some at 10^{-5} gms/cc), outside of the range of the CHEST equation-of-state tables. Therefore we decided to disregard the pressures given by CHEST for these cells and to apply the airblast pressure to the boundary of the low density melt. This is equivalent to removing those cells from the computation for the rest of the calculation. At this time, the Brode airblast solution was replaced as a boundary condition by the Needham airblast solution, deemed to be more accurate at low pressures. Figure 4.7 shows the complete CRAM grid at 321.91 msec, soon after this rezone. The crater region at this time is surrounded by cells containing tensile cracks.

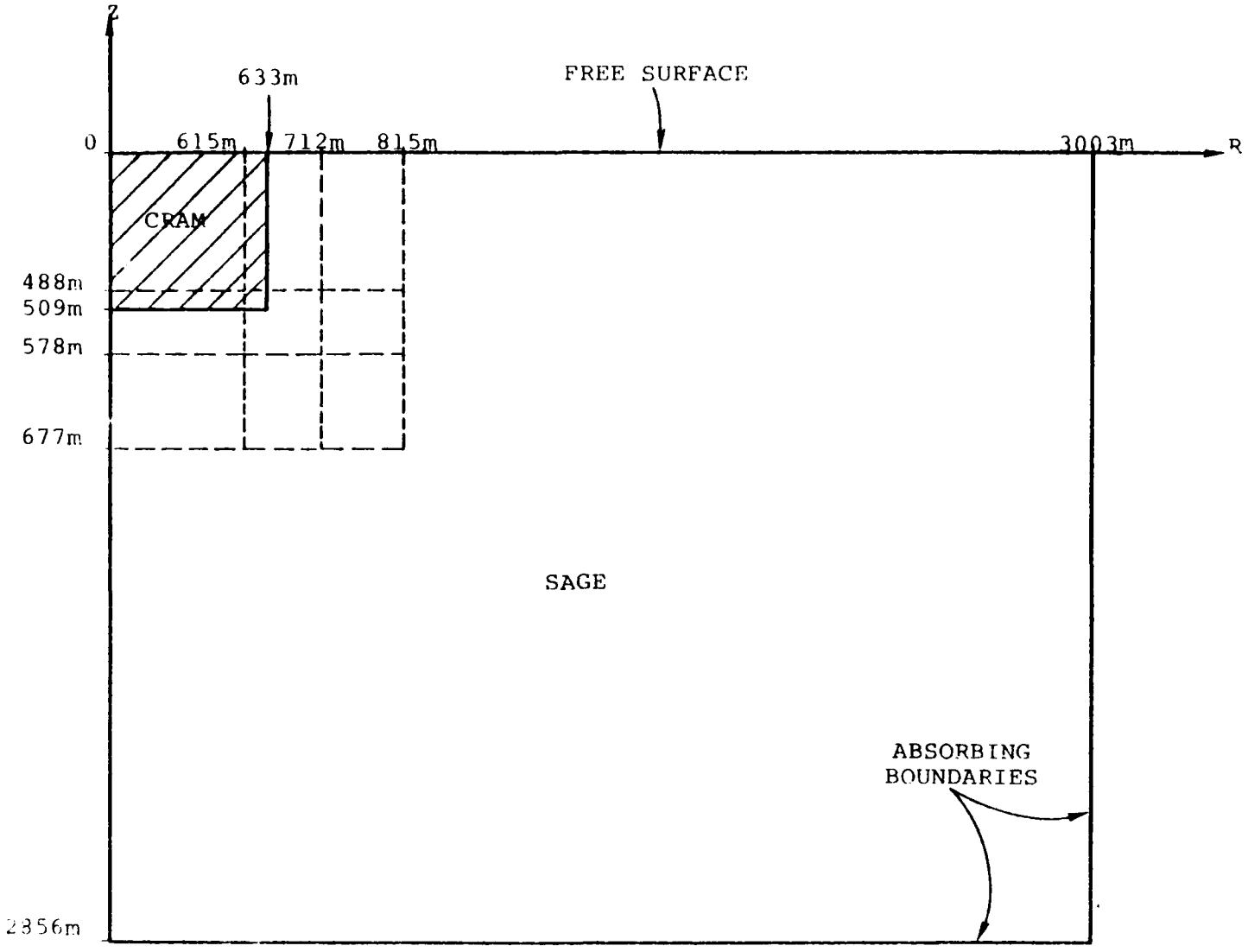

Figure 4.6 Locations of monitoring surfaces in CRAM and SAGE (not to scale).

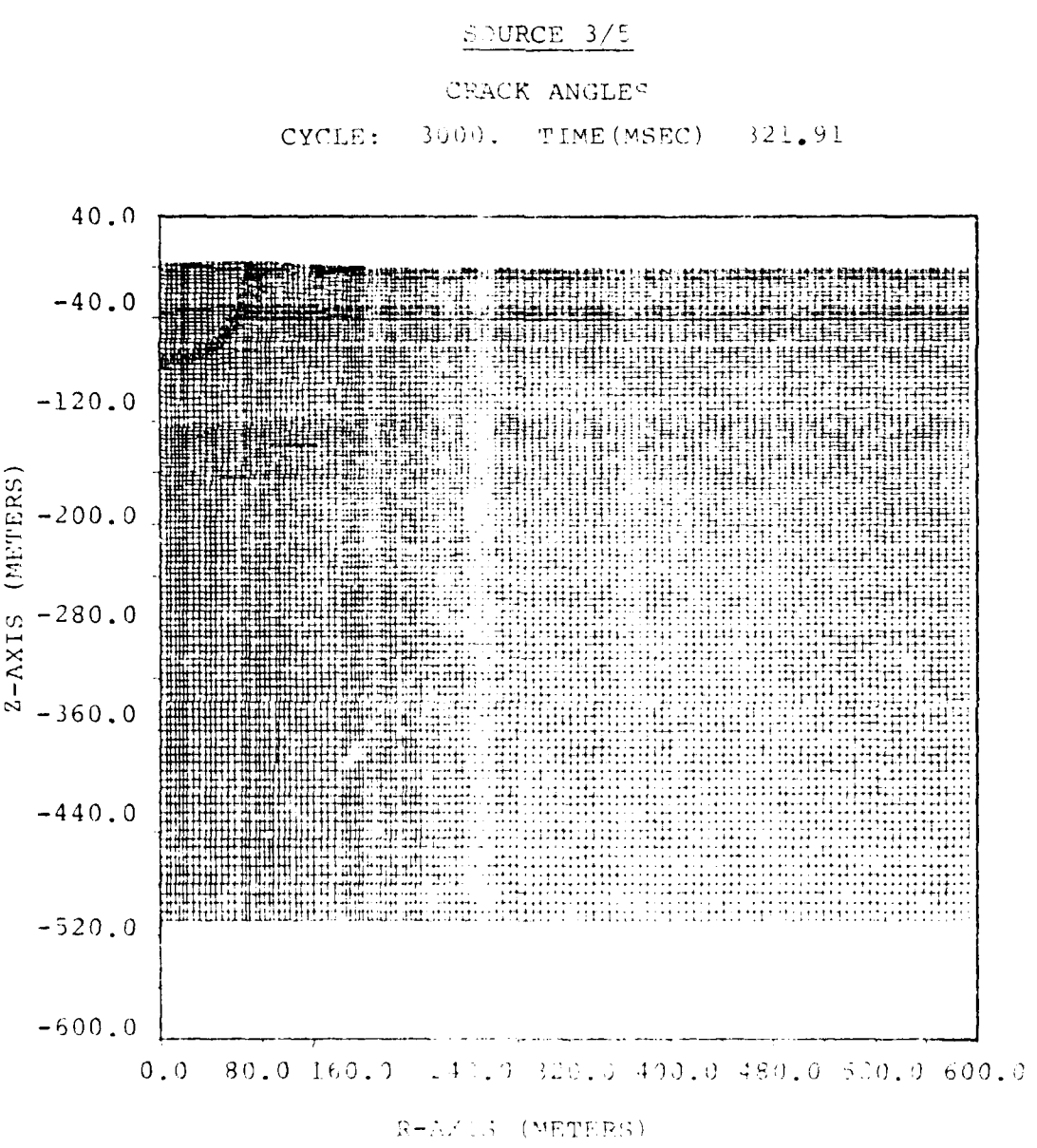

Figure 4.7. Complete "FAN" grid and crack angles at 321.91 msec.

The last major rezone was made at 594 msec. Figure 4.8 shows the rezoned grid at 647 msec. Note that the grid lines in the melted region near ground zero are completely decoupled from the rest of the grid. Only at the boundary of this melt is the motion calculated by CRAM. By 1.73 seconds, the crater calculated using ballistic trajectories has remained virtually the same for some time. Stresses and velocities are very small as well. Therefore we felt reasonably safe in freezing the motion near the crater ($R < 140$ m and $Z < 140$ m) and rezoning away the few lines controlling the time step so that the ground motions at the monitoring surfaces could be calculated to later times more cheaply. The calculation with this final grid was run out to 3.26 sec. The plots of velocities, displacements, and stresses on the monitoring surfaces presented in Appendix B show arrivals at approximately 2.5 seconds which are probably due to freezing the crater motions.

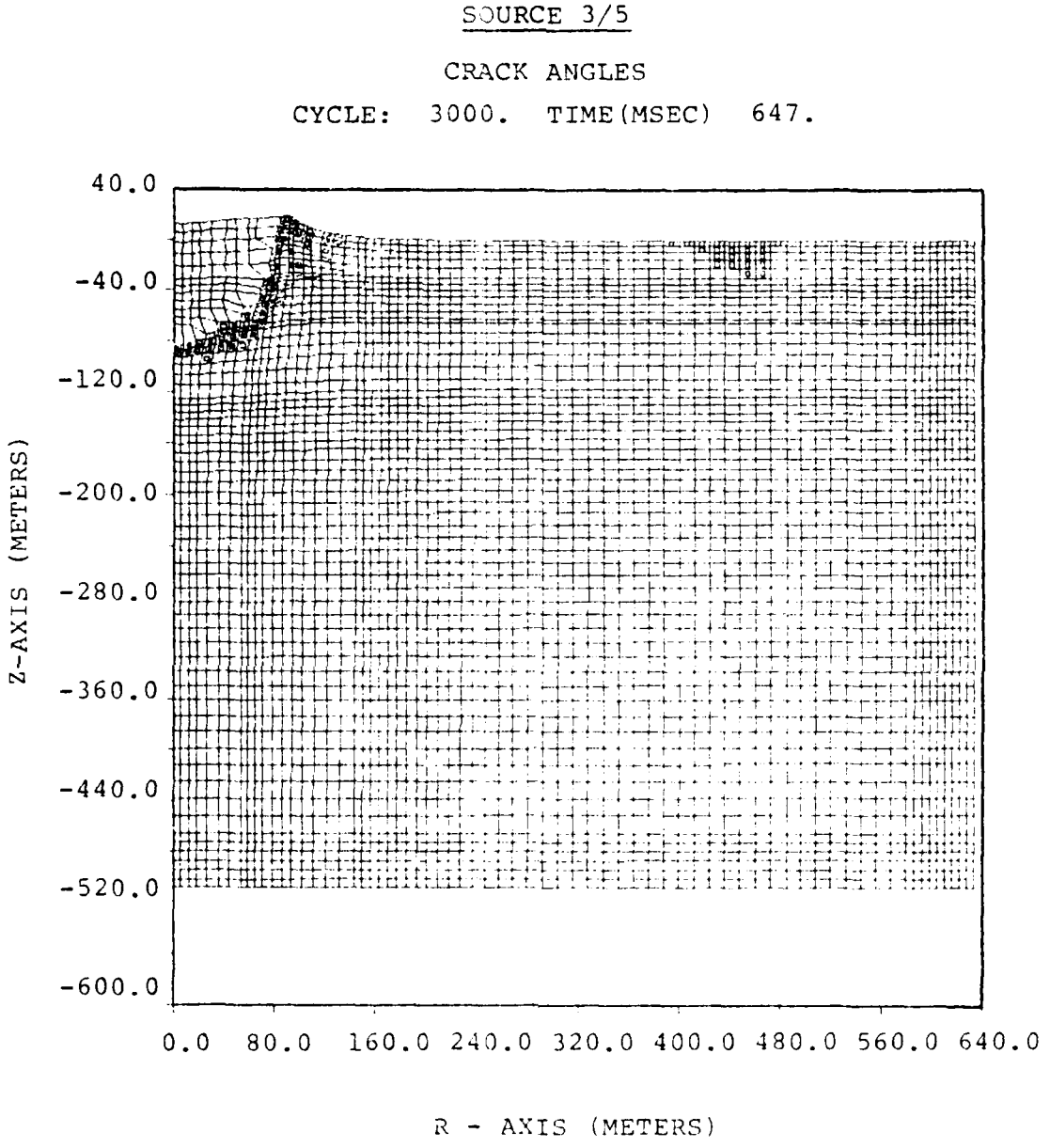

Figure 4.8. CRAM grid and crack angles at 647 msec.

4.2 GROUND MOTION RESULTS

A receiver in the ground close to the free surface tends to experience two distinct arrivals from a nearby surface burst. These correspond to the airblast induced shock, propagating downward from the free surface and the direct induced shock propagating roughly spherically from ground zero. The relative magnitudes and order of arrival of each depends upon the location of the receiver relative to both the free surface and ground zero.

Figure 4.9 shows the calculated pressure versus time monitored at 10 meters below initial ground at a horizontal range of 80 meters, Figure 4.10, the velocity at that location, and Figure 4.11, the displacement there. These plots were made after completion of the calculation by accessing the available computer dump tapes widely spaced in time compared to the time step of the calculation. This implies that where gradients are steep, peak values in pressure or velocity most likely were not sampled. Nevertheless, much useful information may be extracted from plots of this type.

The first peaks in Figures 4.9 and 4.10 at approximately 12 msec are from the airblast induced motion. As anticipated, the velocity is primarily directed downward into the ground. The second peak at about 30 msec is a result of the direct ground coupling from the surface burst. At this location, it enhances the radial (horizontal) component of the motion and reverses the vertical motion. Geometry tells us that the enhancement of the horizontal motion is a characteristic of this shock at all receiver locations (except directly below the burst point). The upward reversal of vertical motion is localized very near to the free surface. At 300 msec, Figure 4.11 shows a vertical displacement of approximately 5 meters and a horizontal displacement just slightly smaller. This station is located near the edge but within the calculated crater.

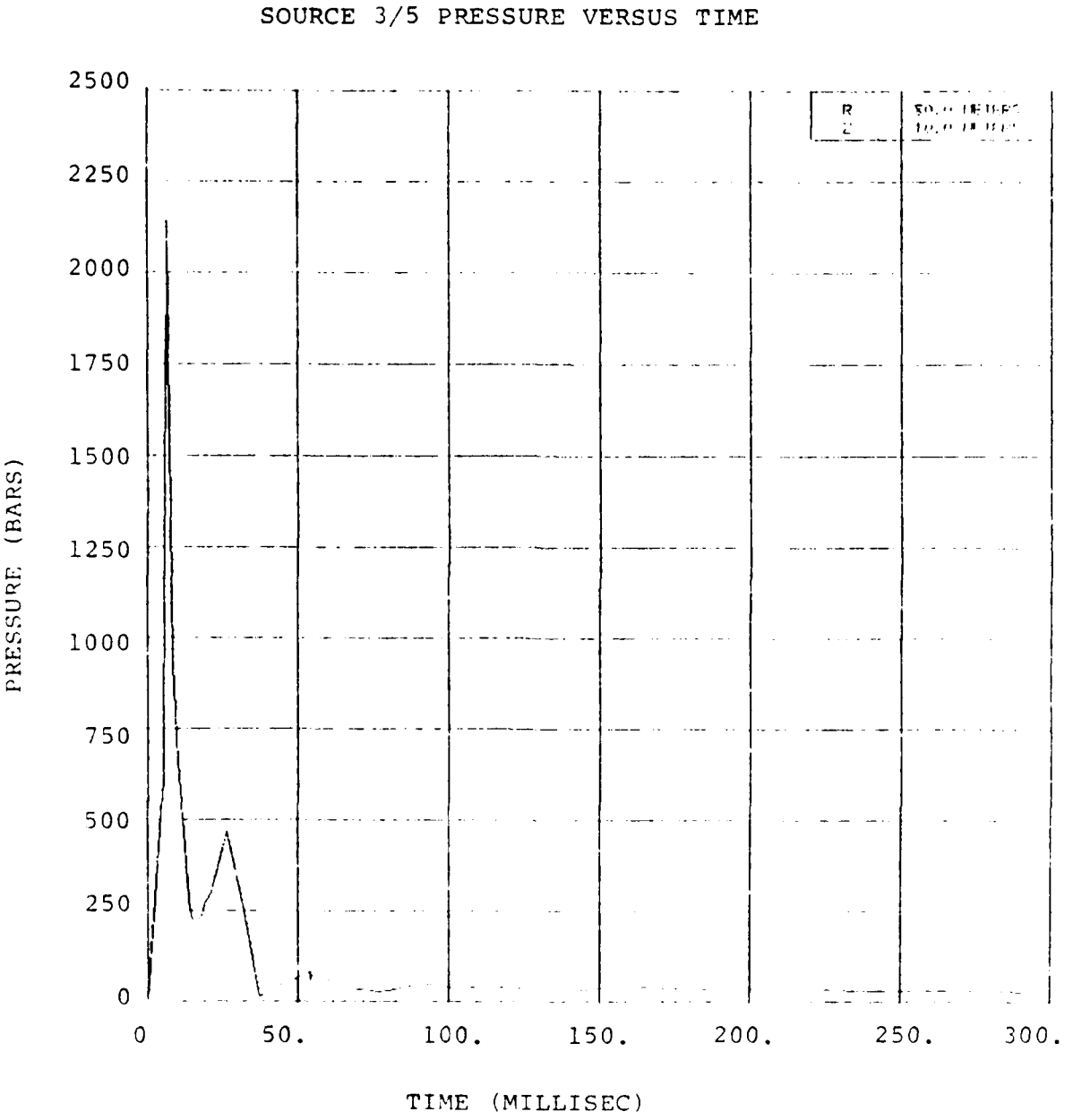

Figure 4.9 Pressure versus time at a horizontal range of 80 meters and a depth of 10 meters.

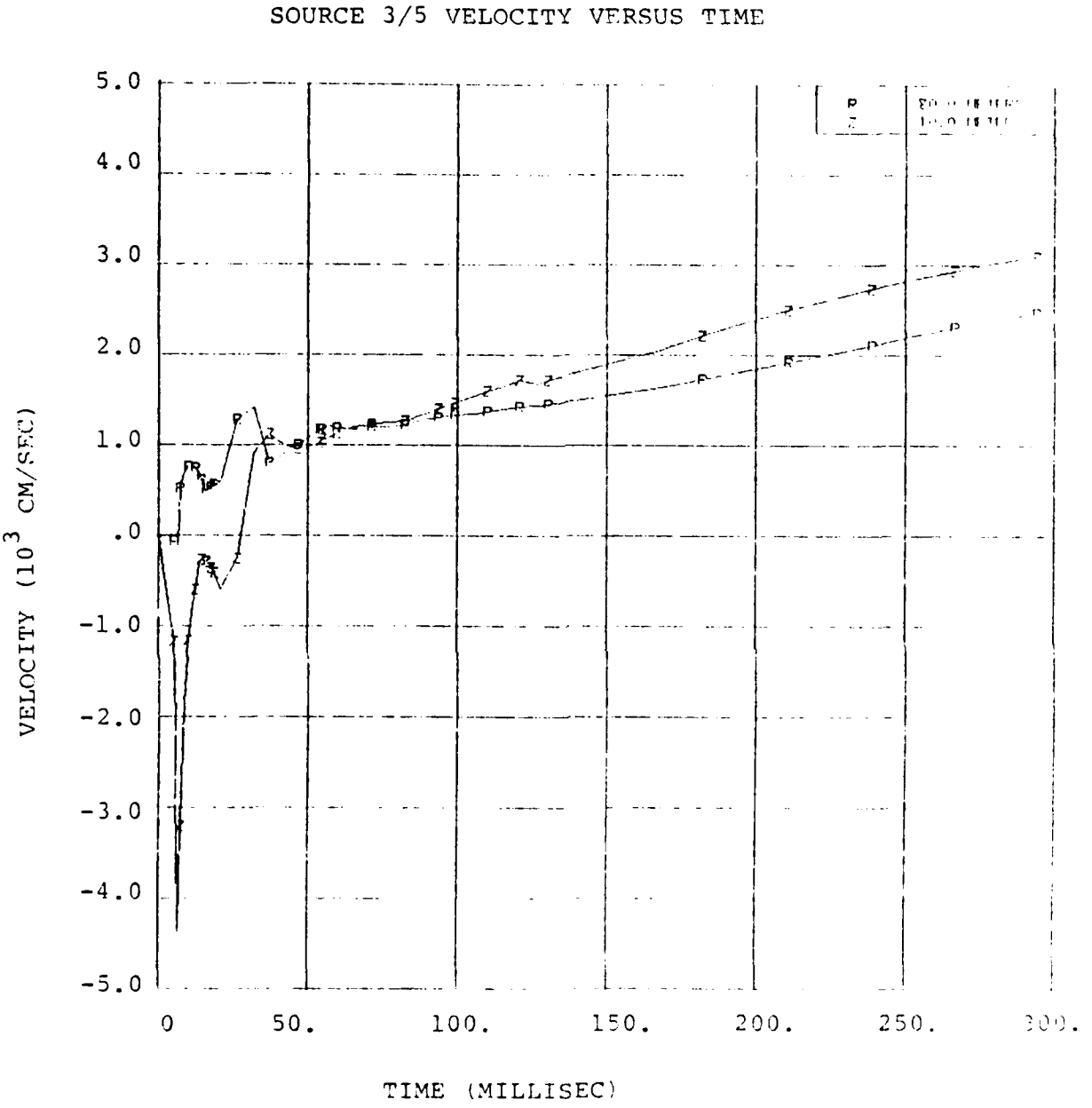

Figure 4.10 Horizontal radial (R) and vertical components (Z) of velocity at a horizontal range of 80 meters and a depth of 10 meters.

SOURCE 3/5 DISPLACEMENT VERSUS TIME

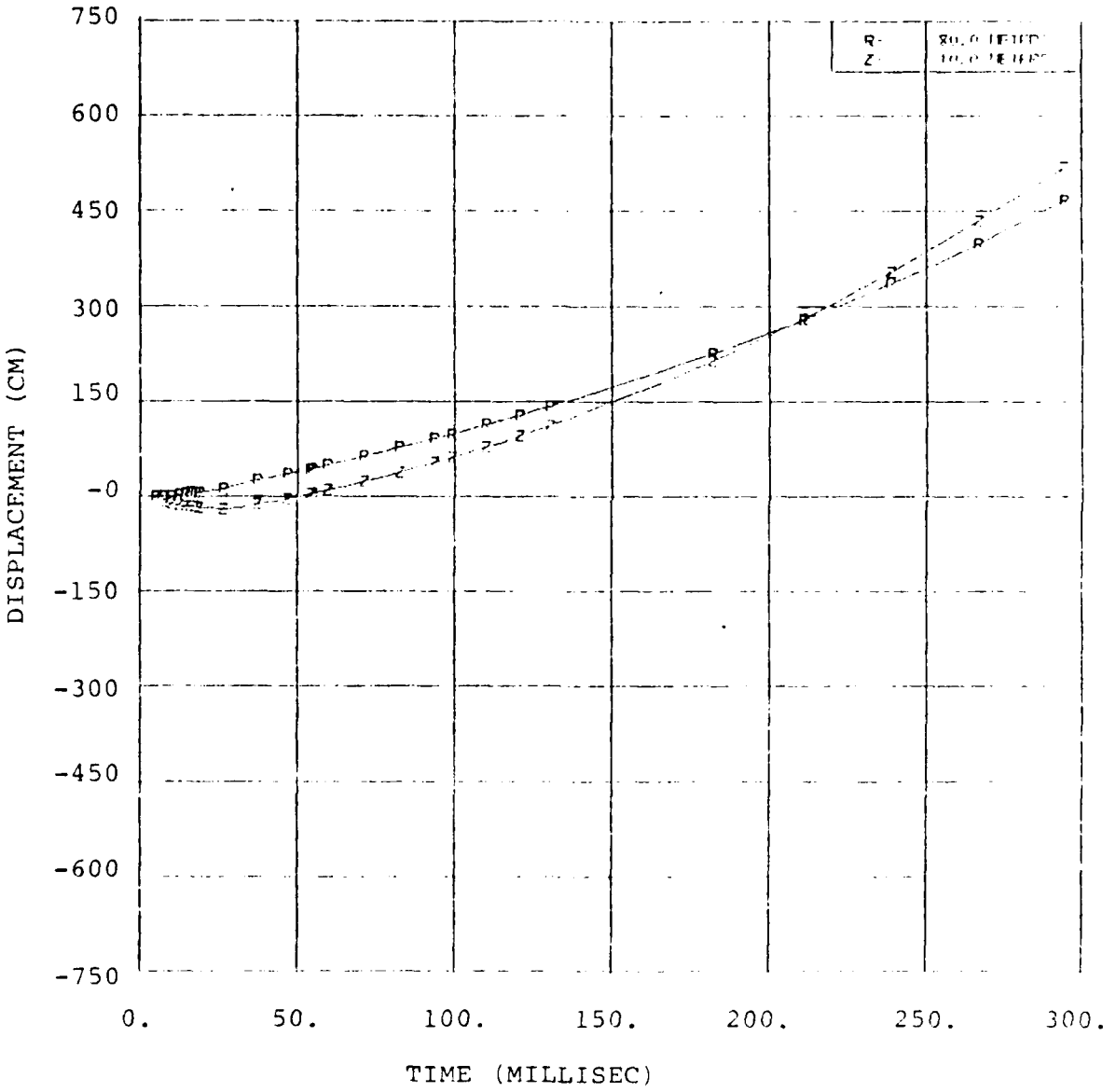

Figure 4.11 Displacement components at a horizontal range of 80 meters and a depth of 10 meters.

Figures 4.12, 4.13, and 4.14 show respectively the pressure, velocity and displacement components versus time at the same range of 80 meters but at a depth of 35 meters. The two pressure peaks are closer together in time due to the later arrival of the airblast signal from the free surface. At this depth, Figure 4.13 indicates the vertical motion is downward from the direct induced as well. Again, the primary motion due to this second arrival is outward horizontal. Although this station is only 35 meters from the free surface, the upward vertical displacement and velocity at 300 msec are approximately 7 times smaller than at a depth of 10 meters.

Figures 4.15, 4.16, and 4.17 are similar plots at the same range and a depth of 75 meters. At this depth, the two signal arrivals are close enough that it is impossible to distinguish one from the other on the pressure or velocity plots. At this station the vertical displacement is down into the ground. Note on Figure 4.15 the straight line from the origin to about 40 msec. This is plotting error which appears on many of these Figures. The pressure should be zero out to a time of approximately 30 msec. but since the dump tapes are accessed at wide intervals of time rather than saving data at each calculational cycle, the plot code has simply connected the origin to the first accessed data.

Plots of pressure, velocities, and displacements out to 300 msec have been made at many locations in order to examine carefully the nonlinear ground motion from the 1-MT surface burst. Appendix A contains a representative subset of these plots. Included are plots at horizontal ranges of 100, 120, 160, 200 and 240 meters and at depths of 20, 50, and 75 meters below the free surface. At these depths, all plots show the airblast motion arriving before the direct induced motion. Of course at some greater depth, depending on horizontal range, the direct induced arrival will be first.

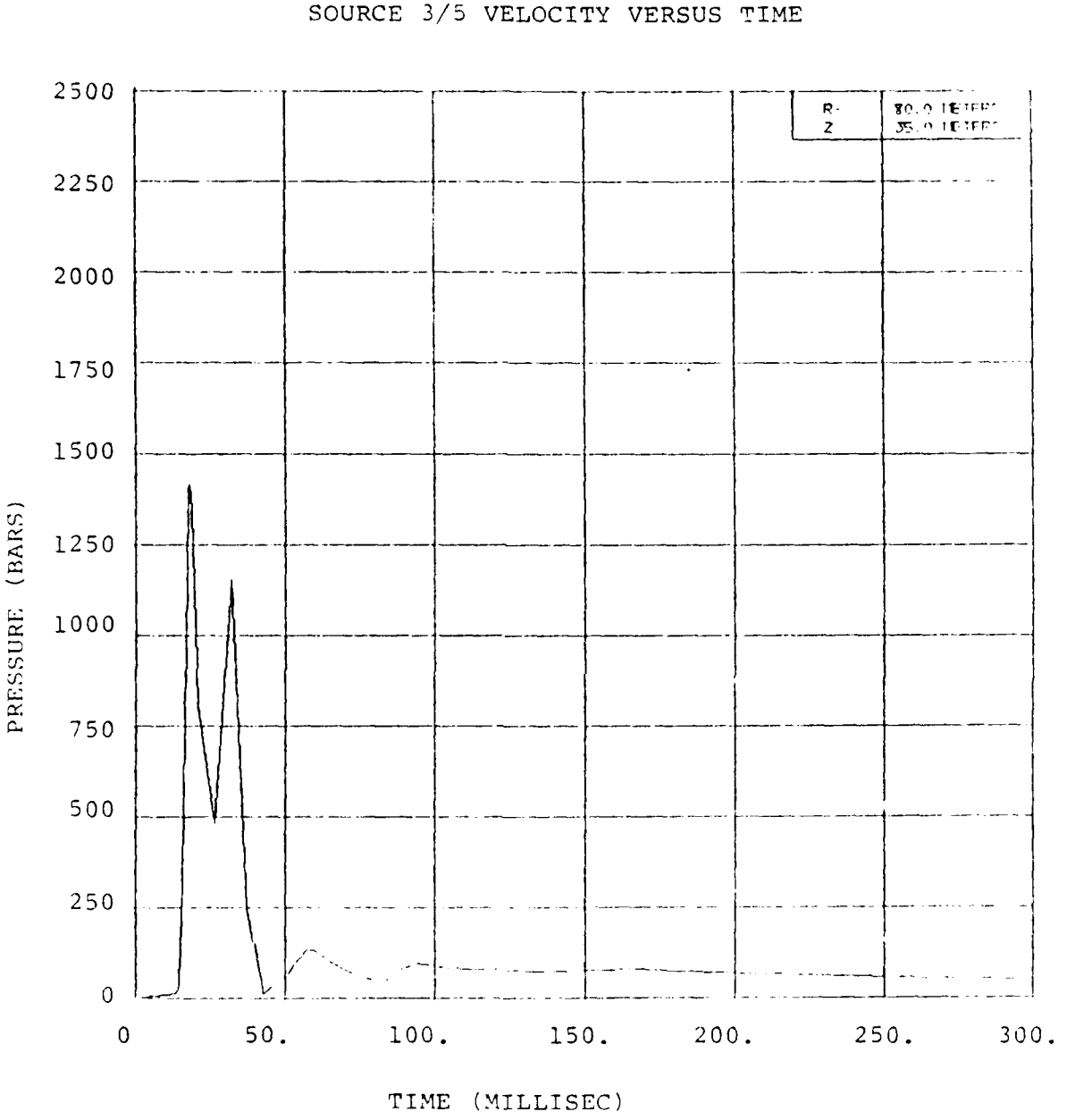

Figure 4.12 Pressure versus time at range of 80 meters and depth of 35 meters.

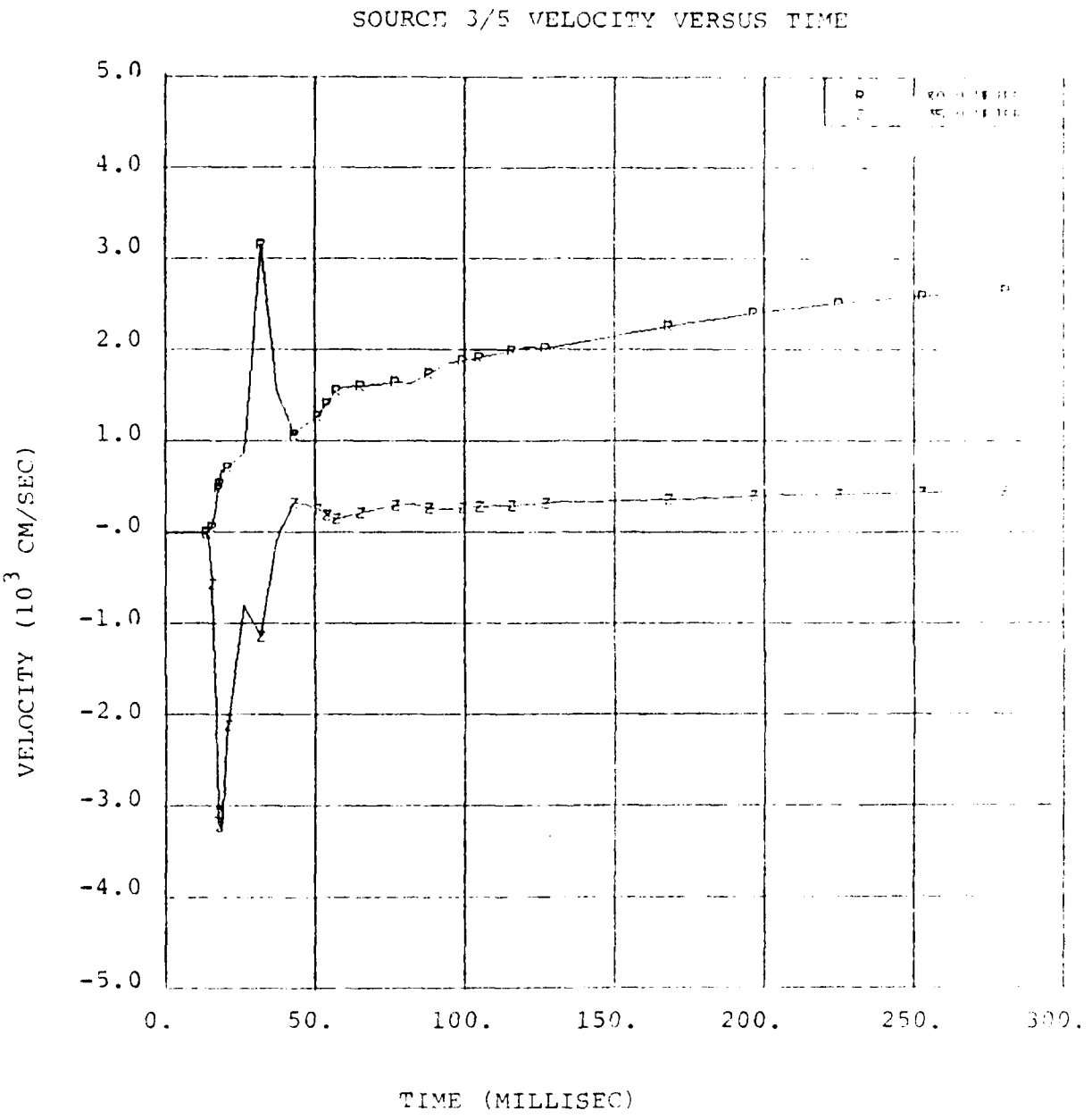

Figure 4.13 Velocities versus time at range of 80 meters and depth of 35 meters.

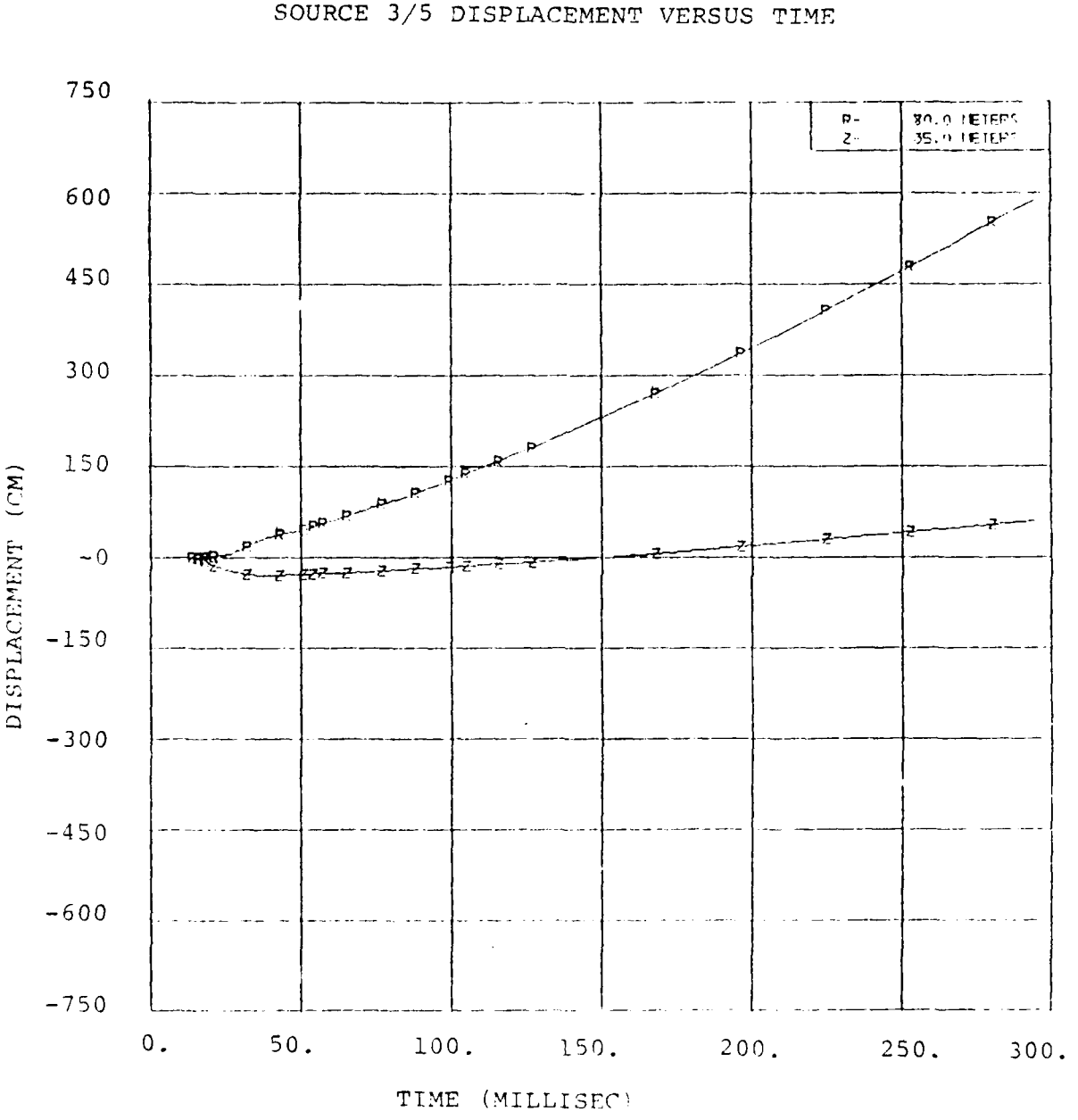

Figure 4.14 Displacements versus time at range of 80 meters and depth of 35 meters.

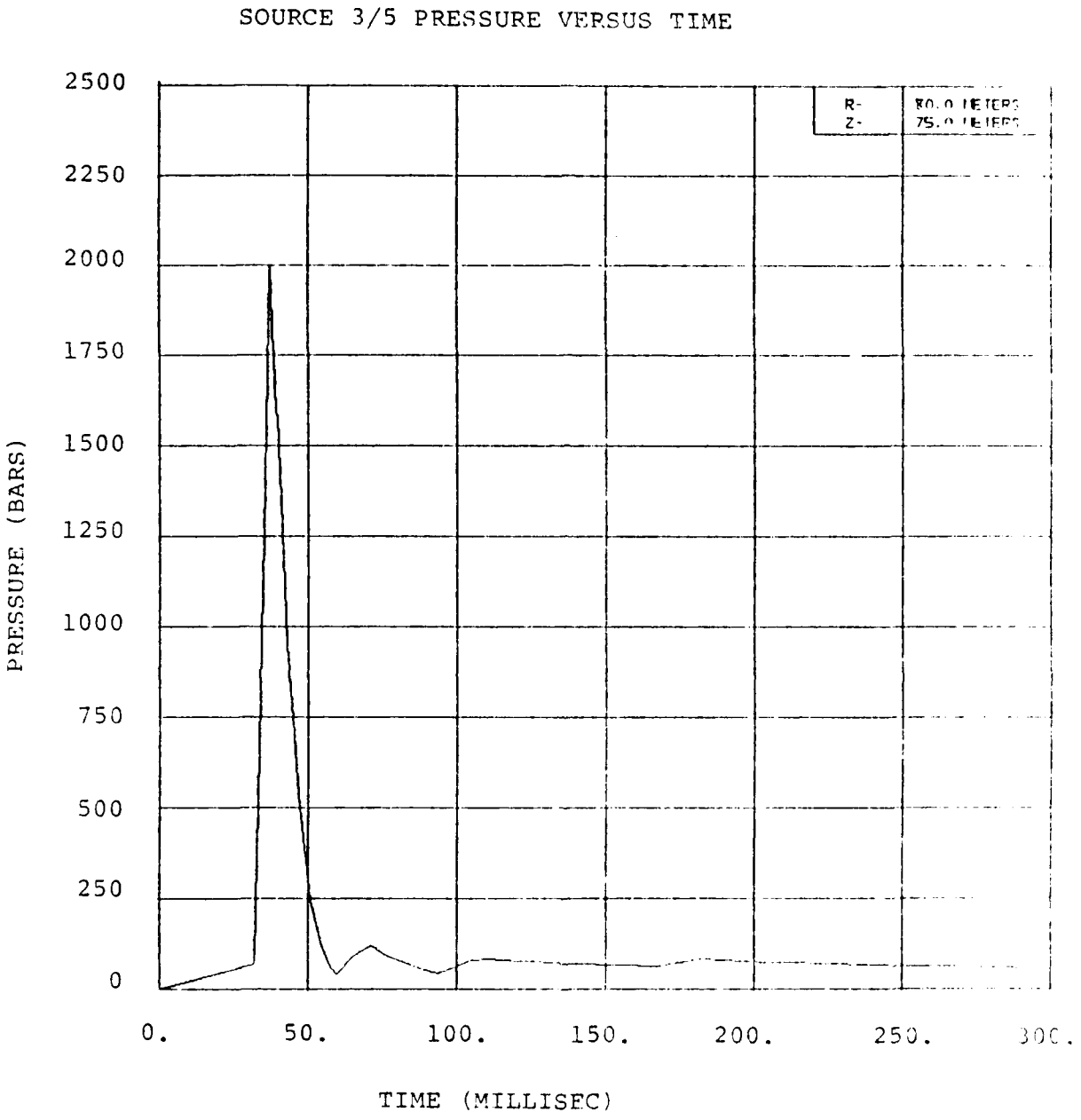

Figure 4.15 Pressure versus time at a range of 80 meters and a depth of 75 meters.

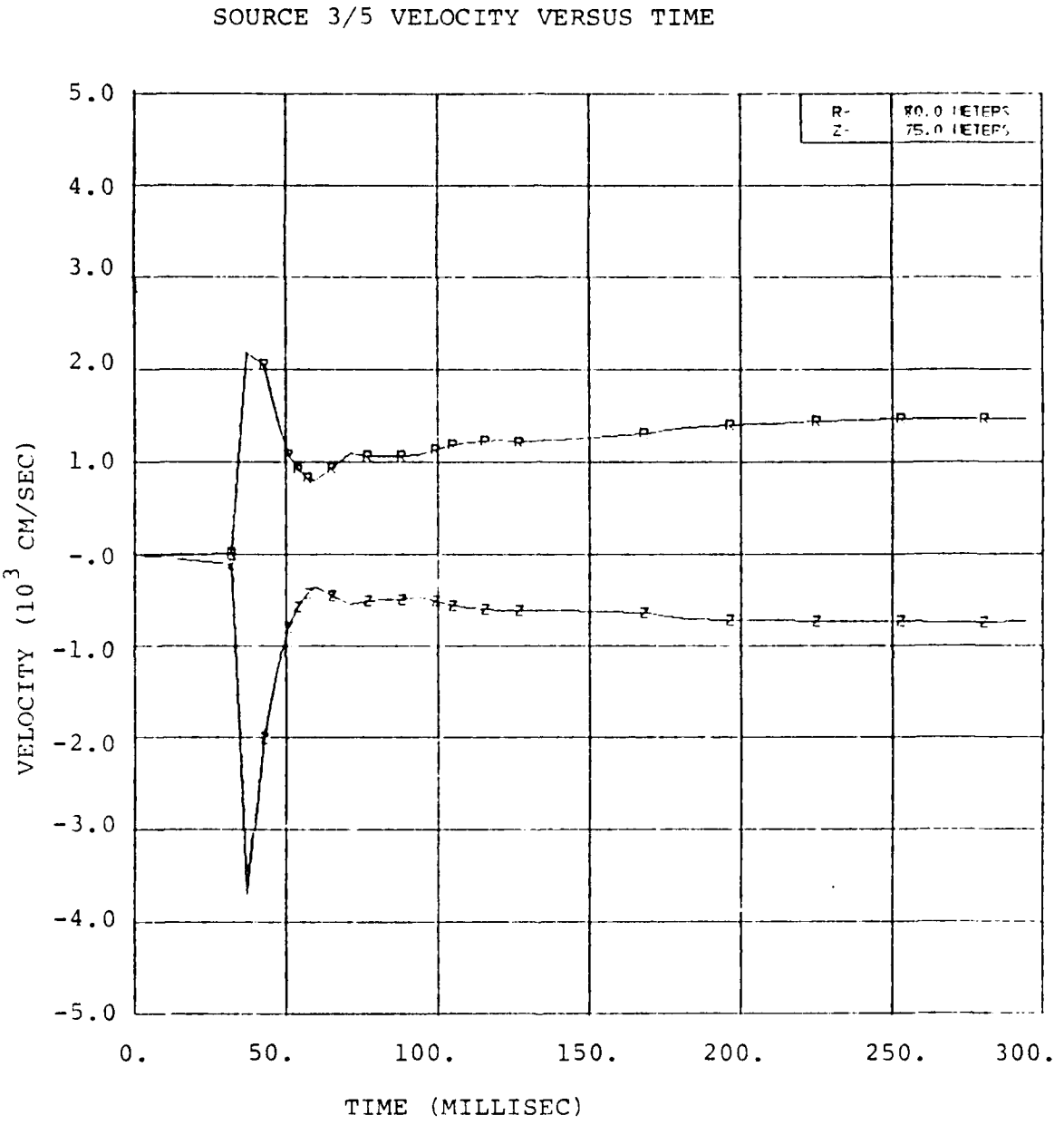

Figure 4.16 Velocities versus time at a range of 80 meters and a depth of 75 meters.

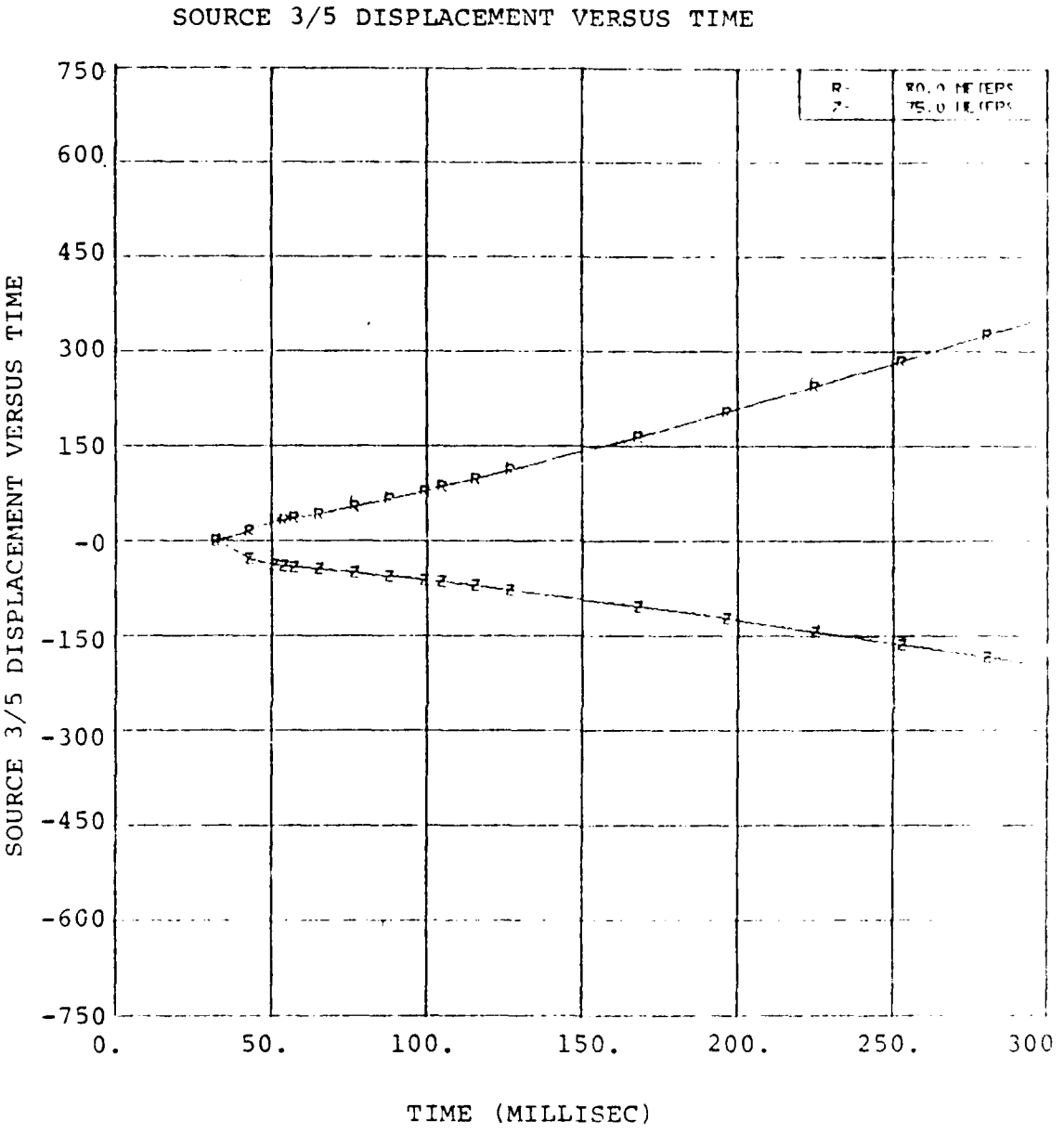

Figure 4.17 Displacements versus time at a range of 80 meters and a depth of 75 meters.

The airblast has propagated out from ground zero at speeds initially much greater than the elastic wave speed in the ground; however, it rapidly attenuated and slowed down. At 633 meters, the location of the CRAM-SAGE boundary, the airblast arrived at approximately 0.15 sec. with a peak pressure of only about 30 bars. An average airblast wave speed from the burst point to the CRAM-SAGE boundary is more than twice the elastic P-wave speed of 2000 meters per second. However, the local airblast wave speed is already 10 percent less than P-wave speed at this location and rapidly decreasing with range. This implies that at greater ranges, the ground motion due to the airblast at 633 meters will arrive before the airblast at the greater range. Thus the first motion near the free surface will be upward out of the ground, followed by a downward directed motion due to the arrival of the airblast.

Figures 4.18 and 4.19 show the elastic ground motions saved at two monitoring stations 8 meters from the free surface; the first at a range of 712 meters and the second at 815 meters. The plots show both components of displacements and velocities and three stress components versus time out to 3.26 sec. Note that in these plots the positive vertical direction is into the ground. This notation is unfortunately opposite to plots shown earlier but does represent the way the code coordinates were oriented, the earlier plots having been altered in order to show the free surface at the top of the grid for clarity rather than at the bottom. Thus, as discussed before, these plots do show the first vertical motions negative (out of the ground). Compressive stress components in these plots are shown negative. All normal stresses shown are relative to a hydrostatic overburden pressure.

Appendix B contains a representative sampling (20 plots) of the elastic ground motion monitored at the

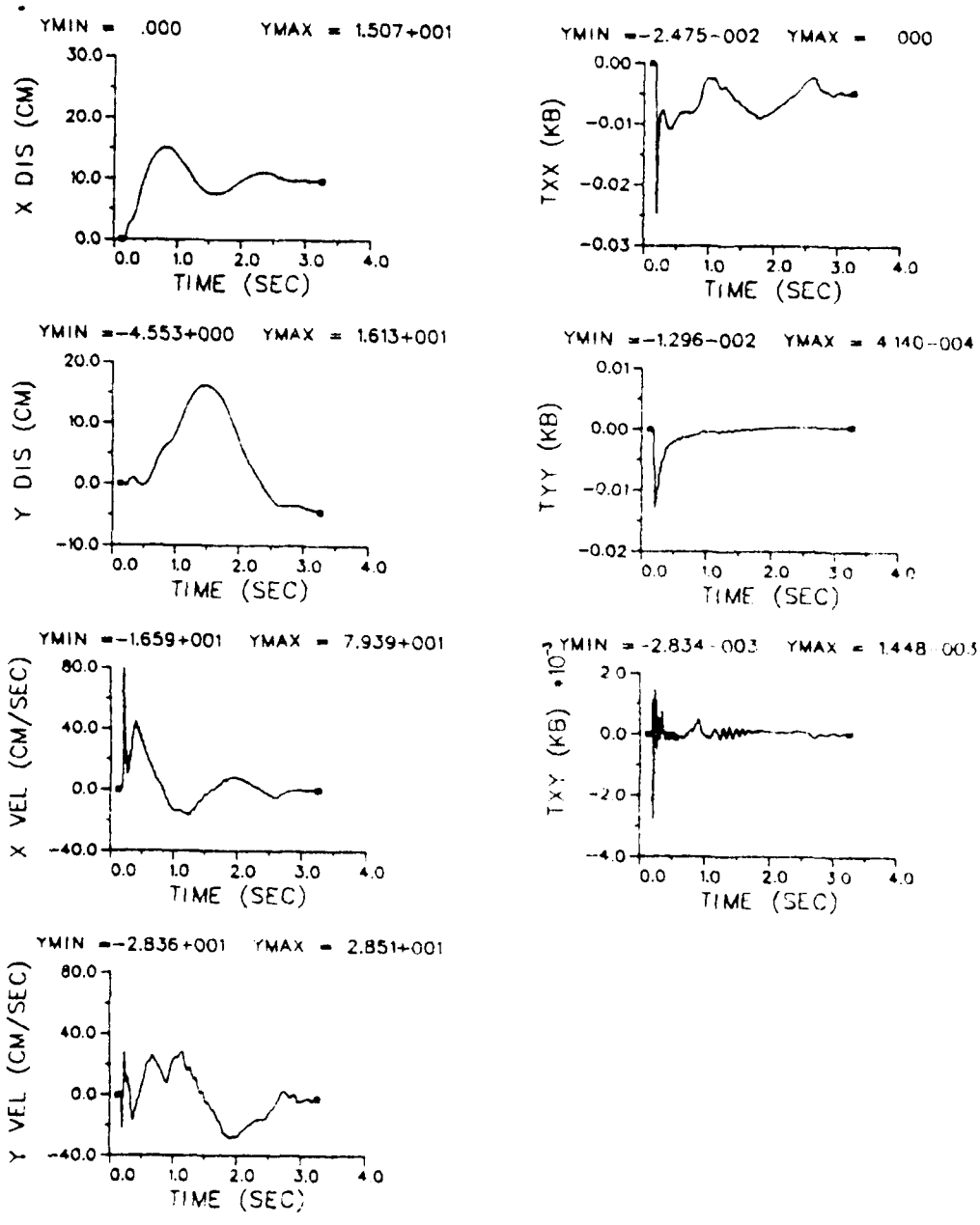

Figure 4.18. Displacements, velocities and stresses versus time 8 meters from the free surface at a range of 712 meters.

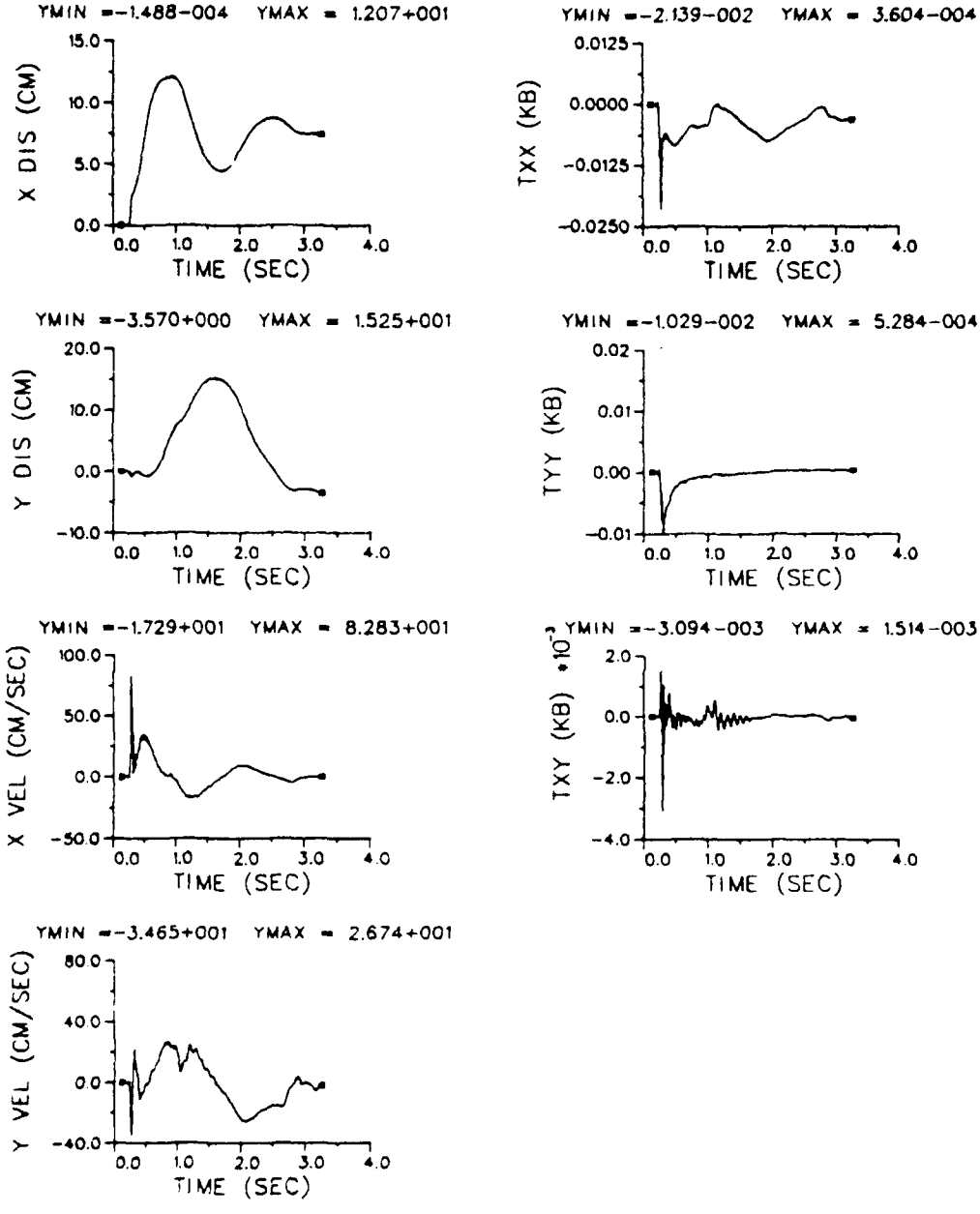

Figure 4.19. Displacements, velocities, and stresses versus time 8 meters from the free surface at a range of 815 meters.

cylindrical surfaces in SAGE shown in Figure 4.6. Since stresses in CRAM include the hydrostatic overburden pressure and those in SAGE do not, to avoid confusion, we have not published plots from CRAM stations. The CRAM results are quite similar to those of Appendix B. Since all of the data along the monitoring surfaces in both CRAM and SAGE are elastic, taking data from any of the three horizontal surfaces together with data from any of the three verticals should give the same results when propagated to the far field. Our first choice for the cylindrical monitoring surface was the middle horizontal and vertical monitoring lines of Figure 4.6 (the first lines in SAGE).

The results of Appendix B show motions at elastic stations deep below ground zero to have virtually ceased by 1.50 sec. out to ranges of approximately 400 meters. However, a long-term ground roll can be seen on the plots at all depths at larger ranges. The elastic motion due to airblast acting on the free surface at ranges beyond a monitoring surface will be subtracted from these data before proceeding with the analytical propagation of these results to ranges of interest which is the primary purpose of this effort.

Other more near source results may be of interest to the deep basing, MX and cratering communities. Figure 4.20 is a plot of peak pressure versus depth directly below ground zero. The overlay from STREAK to CRAM occurred at a pressure level of approximately 40 kbar. Figures 4.21 and 4.22 show on two different scales the contours of maximum pressure ever seen at given locations in the mesh. All contours are relative to the hydrostatic overburden. Since these contours were made by accessing computer dump tapes which are spaced many time steps apart, they are quite rough and probably miss some of the peaks. Both plots show the near surface interaction region between the direct induced spherical shock and the more planar airblast induced shock. At depth, the shape is roughly spherical.

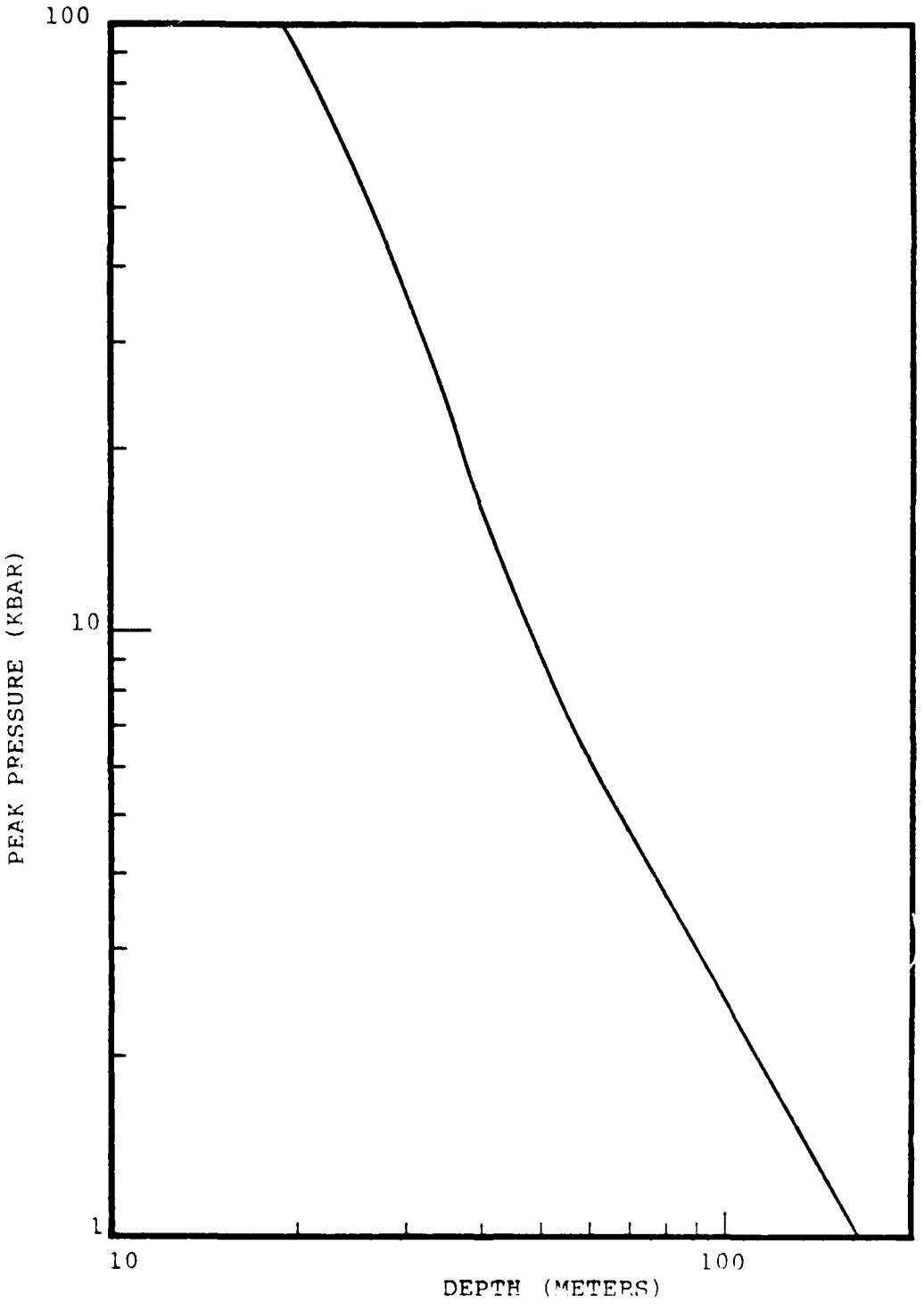

Figure 4.20 Peak pressure in ground versus depth directly below ground zero.

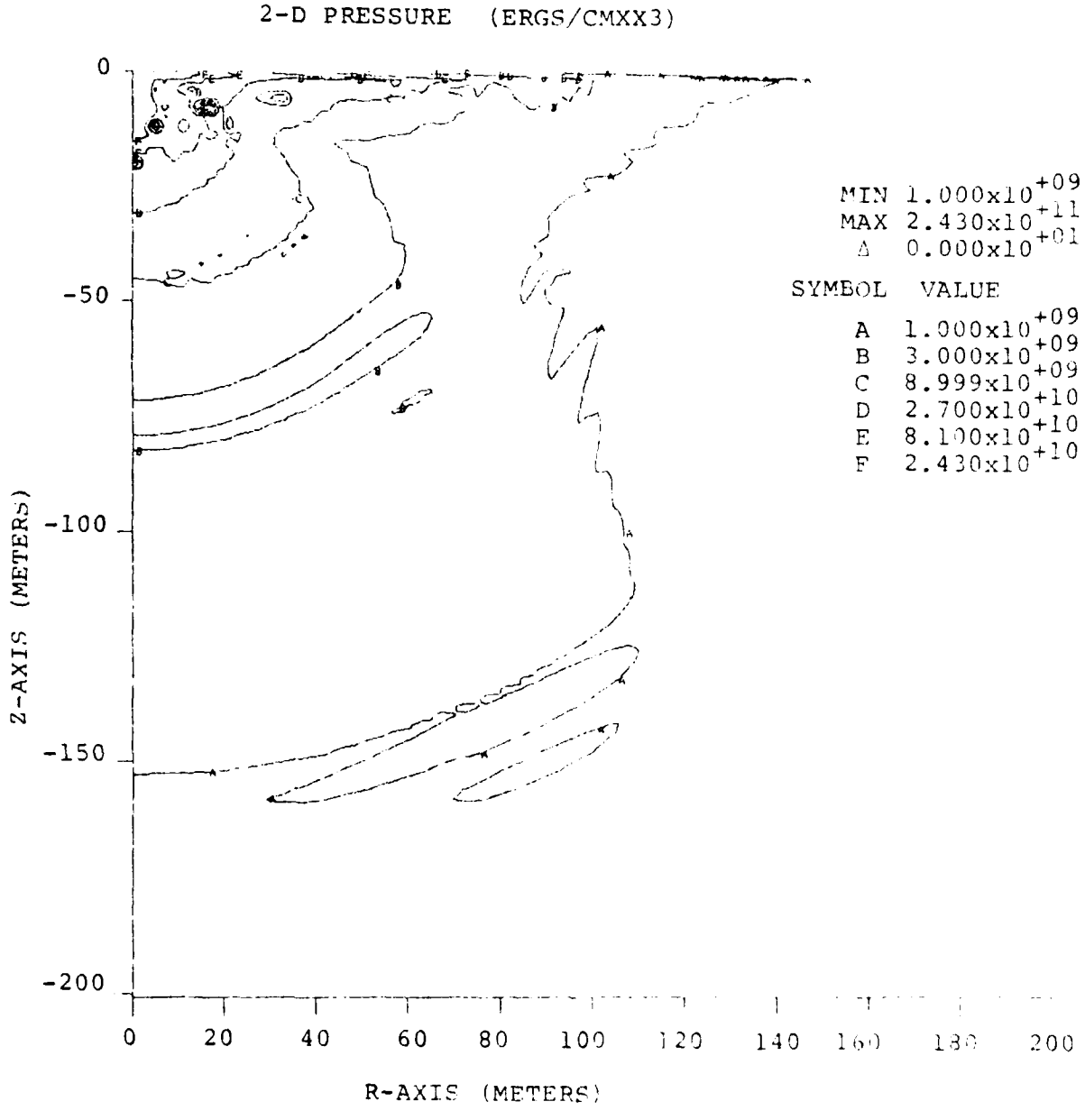

Figure 4.21 Contours of maximum pressure penetration showing immediate source region.

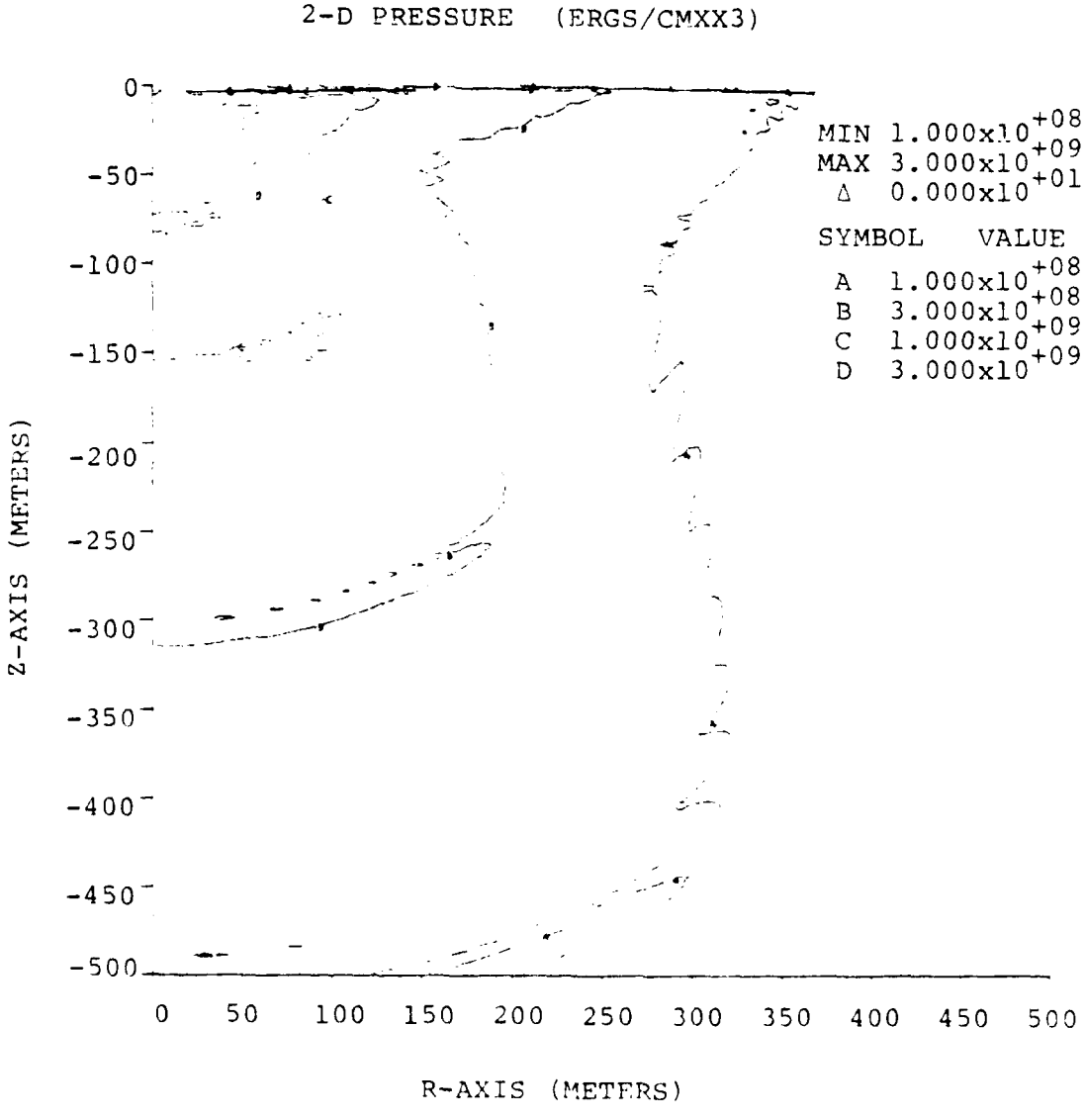

Figure 4.22. Contours of maximum pressure penetration showing stress levels less than 3 kbars.

Figure 4.3 gave the pressure contours in a portion of the mesh at a time of 10.15 msec. (As distinguished from Figures 4.21 and 4.22 which gave peak pressure contours which have no times associated with them.) Figure 4.23 shows similar pressure contours at 26.52 msec indicating the spherical shock propagation and attenuation with time. Also shown are the locations of interaction with the planar shock. In Figure 4.23, the 20 bar (A) contour at a depth of approximately 100 meters indicates the hydrostatic overburden pressure at that depth. Figure 4.24 gives the contours at 99.39 msec. Note the different contour scales and the 50 bar (B) overburden contour. Both Figures 4.23 and 4.24 show only a portion of the CRAM grid. Figure 4.25 gives these contours over the entire grid at 647 msec, late in the calculation, long after the shock waves have passed into the SAGE grid. By this time, the pressures are beginning to readjust to their final values.

4.3 CRATER FORMATION

Estimates of crater size have been made from the calculated velocity field and the amount of tensile cracking at late times. The extent and orientation of tensile cracks are shown in the CRAM grid plots of Section 4.1. There, Figure 4.5 showed tensile cracking for the first time at 51.05 msec. These cracks, located at a range of approximately 100 meters and within 40 meters of the free surface, appear to be oriented toward the upper left of the plot. Figure 4.7 showed extensive tensile cracking all around the melted blowoff materials at 321.91 msec in addition to cracks near the free surface at a range of 120 to 160 meters. Cracks are indicated in all three principal directions. These cracks were more visible in the rezoned grid at 647 msec shown in Figure 4.8.

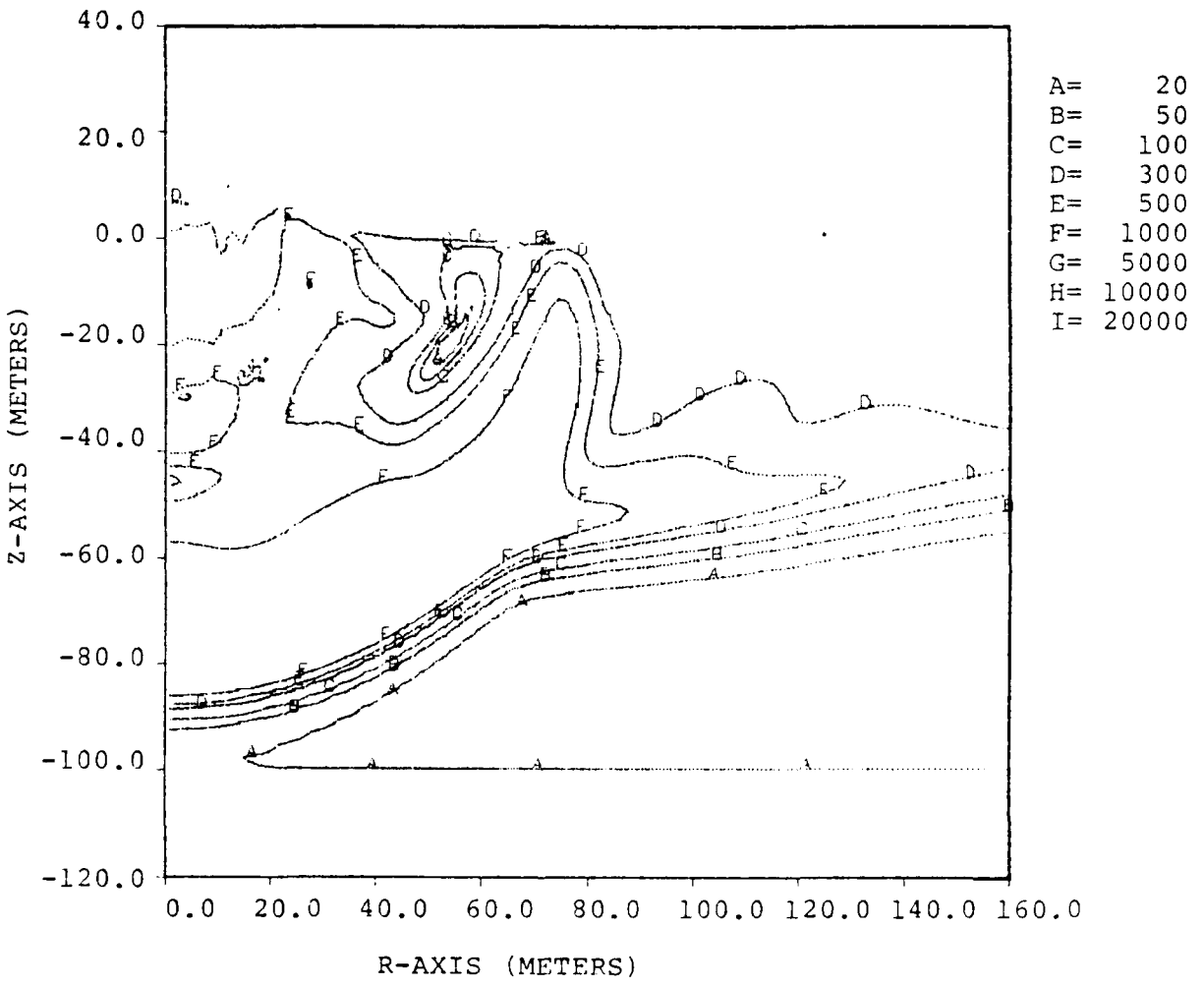

Figure 4.23. Pressure contours at 26.52 msec.

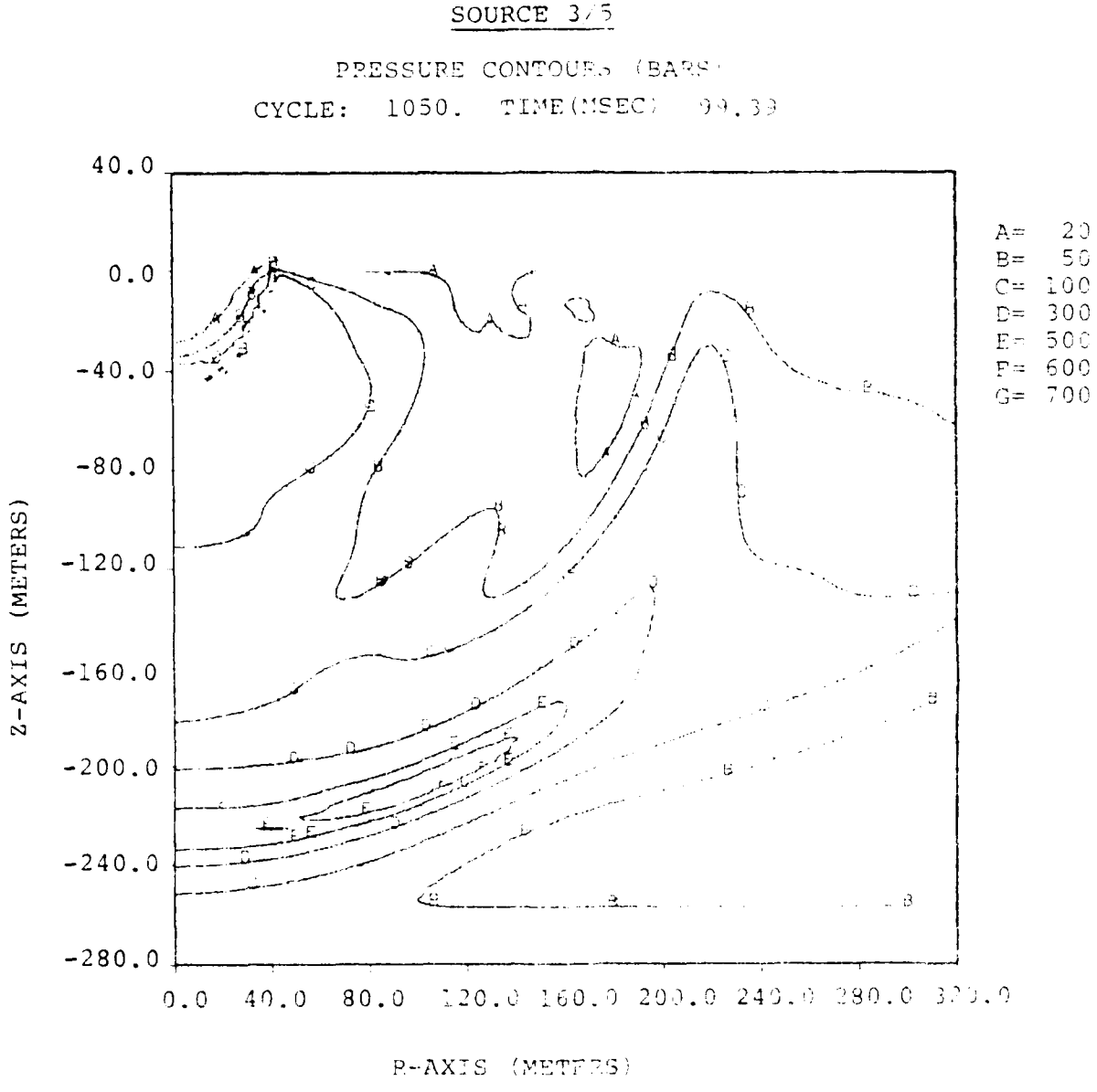

Figure 4.24. Pressure contours at 99.33 msec.

AD-A090 019 SYSTEMS SCIENCE AND SOFTWARE LA JOLLA CA F/G 18/3
NONLINEAR GROUND MOTION FROM A MEGATON NEAR SURFACE NUCLEAR EXP--ETC(U)
MAR 80 N RIMER, E J HALDA, J T CHERRY F19628-79-C-0003
UNCLASSIFIED SSS-R-80-4422 AFGL-TR-80-0167 NL

2 OF 2
AD A 090019

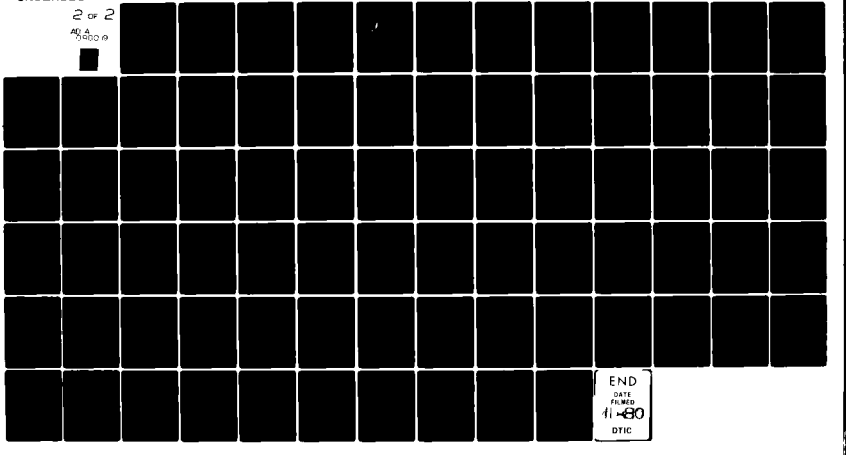

END
DATE FILMED
11-80
DTIC

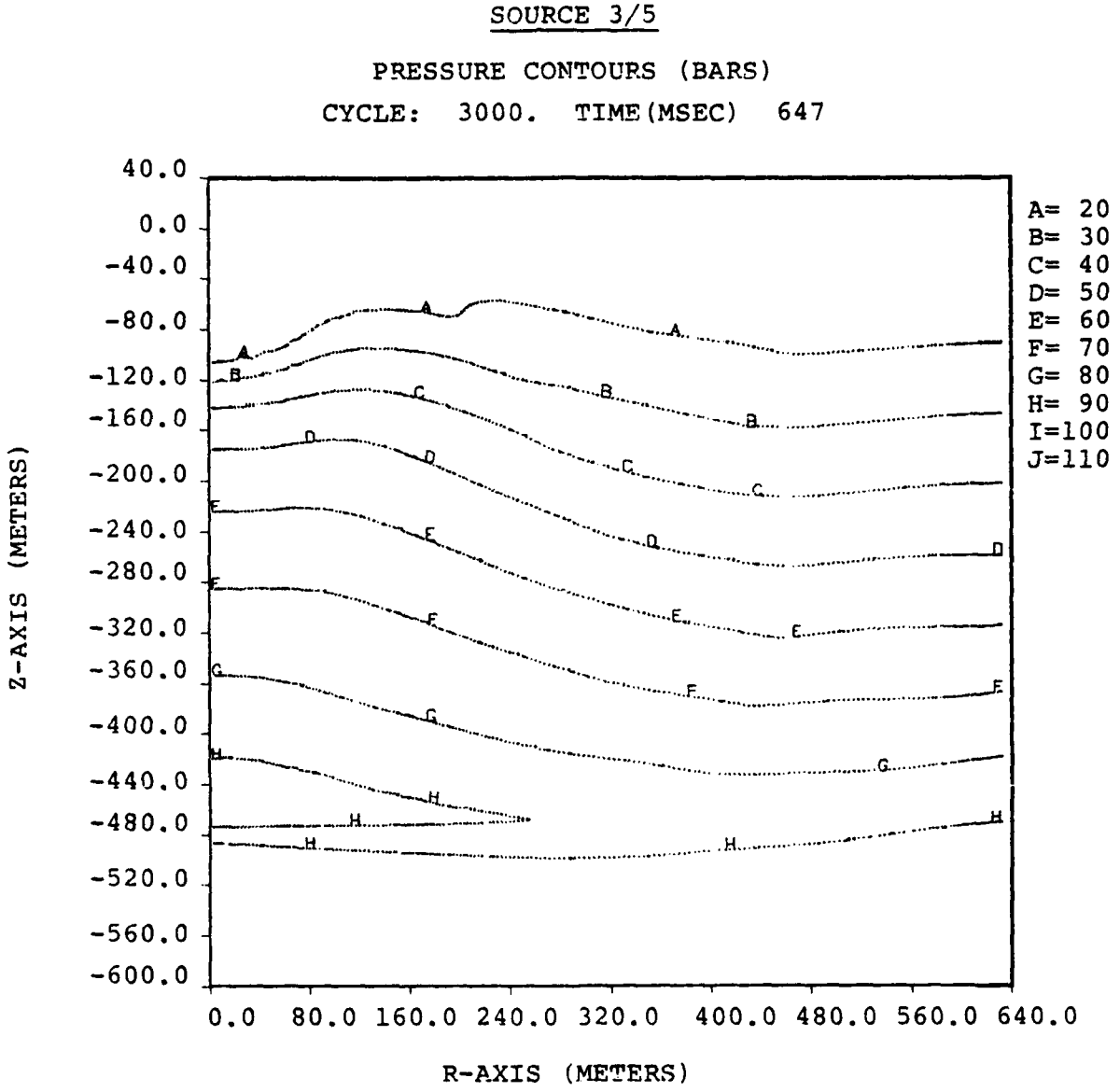

Figure 4.25. Pressure contours at 547 msec.

A good estimate of the growth of the crater with time may be made by examining the velocity vectors. Figures 4.26 through 4.30 show these velocity vectors at times of 26.52, 51.05, 99.39, 321.91 and 647 msec respectively. The location of the motion is given by the tail of the vector. Note the change in vector scale from plot to plot given at the top of these Figures.

In all plots, the largest vectors are in the cratering region. (In Figures 4.29 and 4.30, velocities in the melt region have not been plotted.) Of particular importance are the upward directed velocity vectors near the free surface at the later times which indicate the possibility of those masses being ejected from the crater.

Only those zones (masses) having sufficient upward directed kinetic energy to rise above the ground surface may be removed from the grid to form the crater. Ballistic trajectory calculations determine which of these masses fall back into the crater and which are ejected to form the lip of the crater. At a time of 755 msec, ballistic calculations were made to determine the crater size using the kinetic energy escape criteria alone and also combining this criteria with various tensile cracking criteria. We found that requiring the zone to be either melted or cracked for ejection from the crater gave only one fewer zone ejected when compared with the kinetic energy escape criterion. Based on this near agreement, we decided not to use any tensile cracking criteria in determining the crater dimensions.

Ballistic ejecta calculations were made at different times from 0.75 sec. out to approximately 1.25 sec. Very little variation in the calculated crater volumes (20 percent) were seen. Figure 4.31a shows the CRAM grid at 1.17 sec with the ejected zones removed. Figure 4.31b shows (to the same scale) a histogram of the calculated locations of the materials ballistically ejected from the crater at this time.

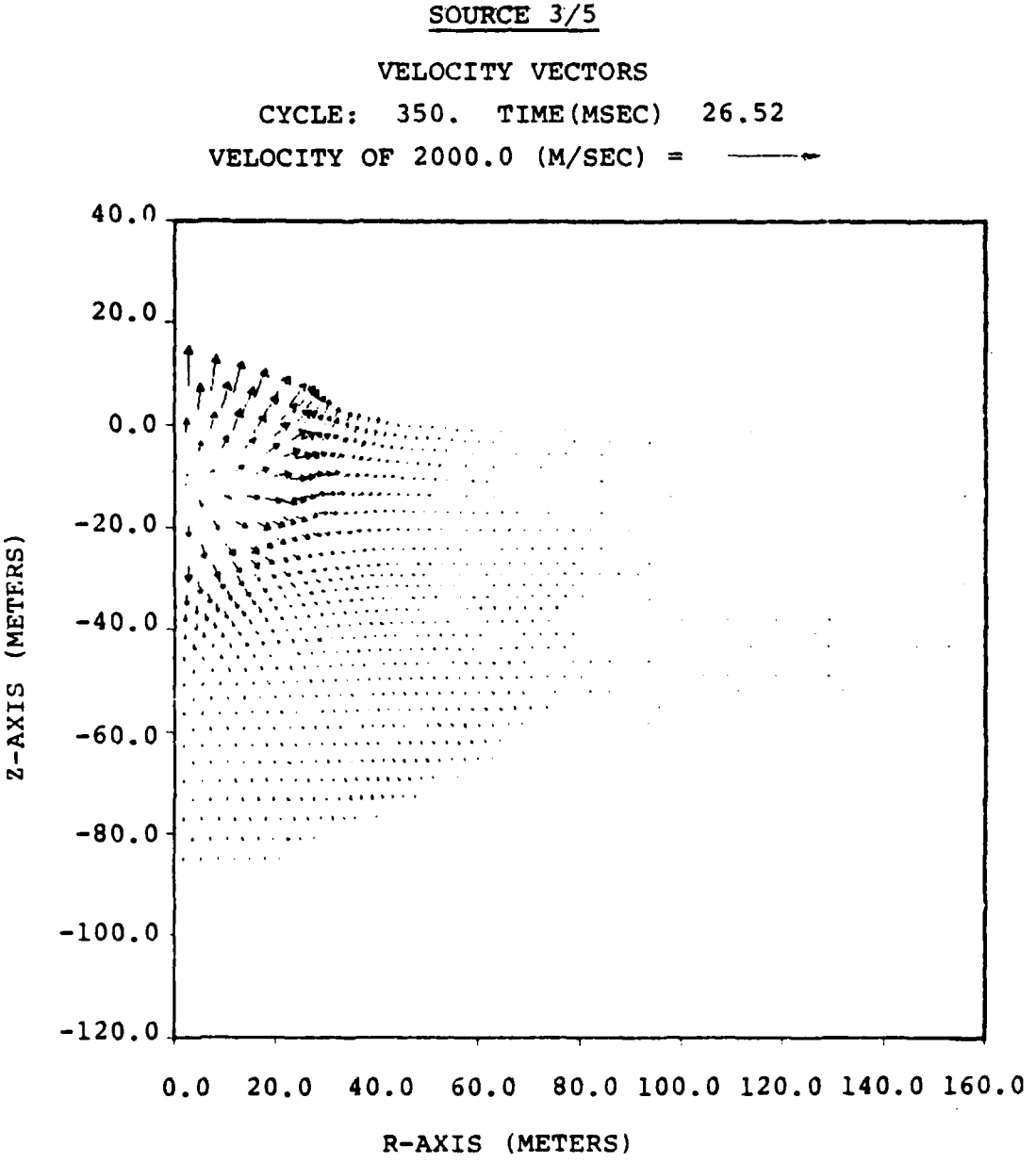

Figure 4.26. Velocity vectors at 26.52 msec.

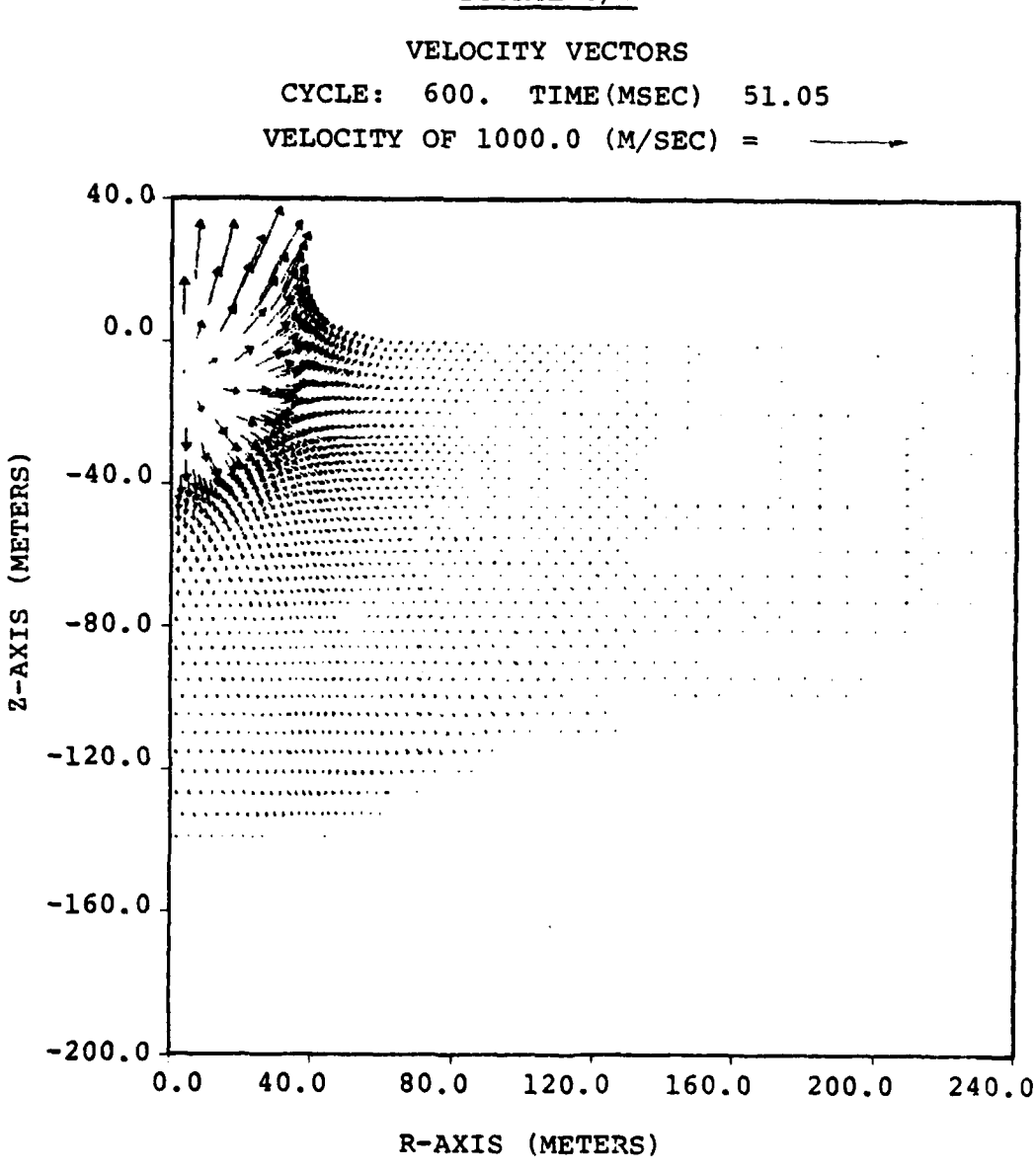

Figure 4.27. Velocity vectors at 51.05 msec.

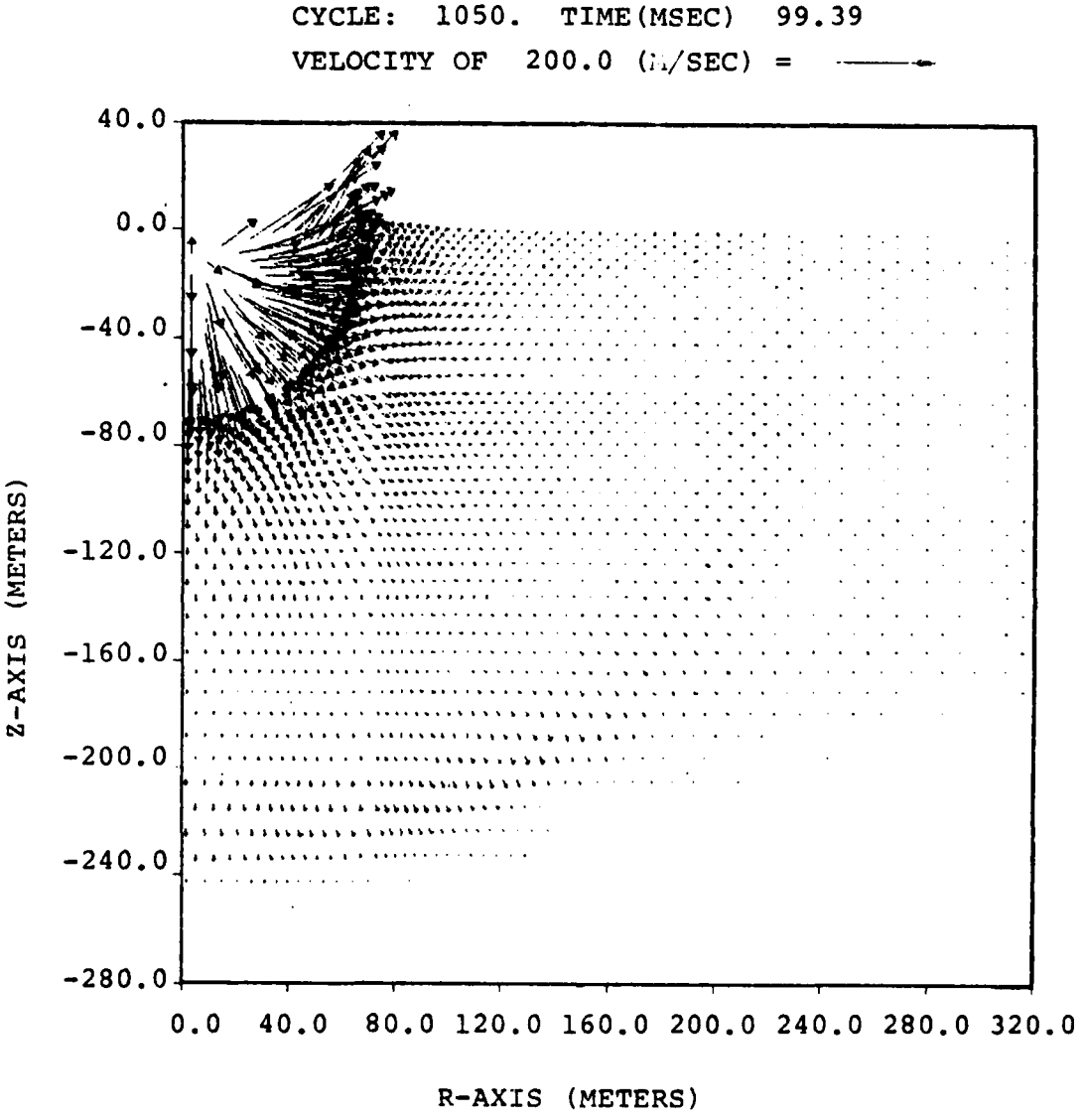

Figure 4.28. Velocity vectors at 99.39 msec.

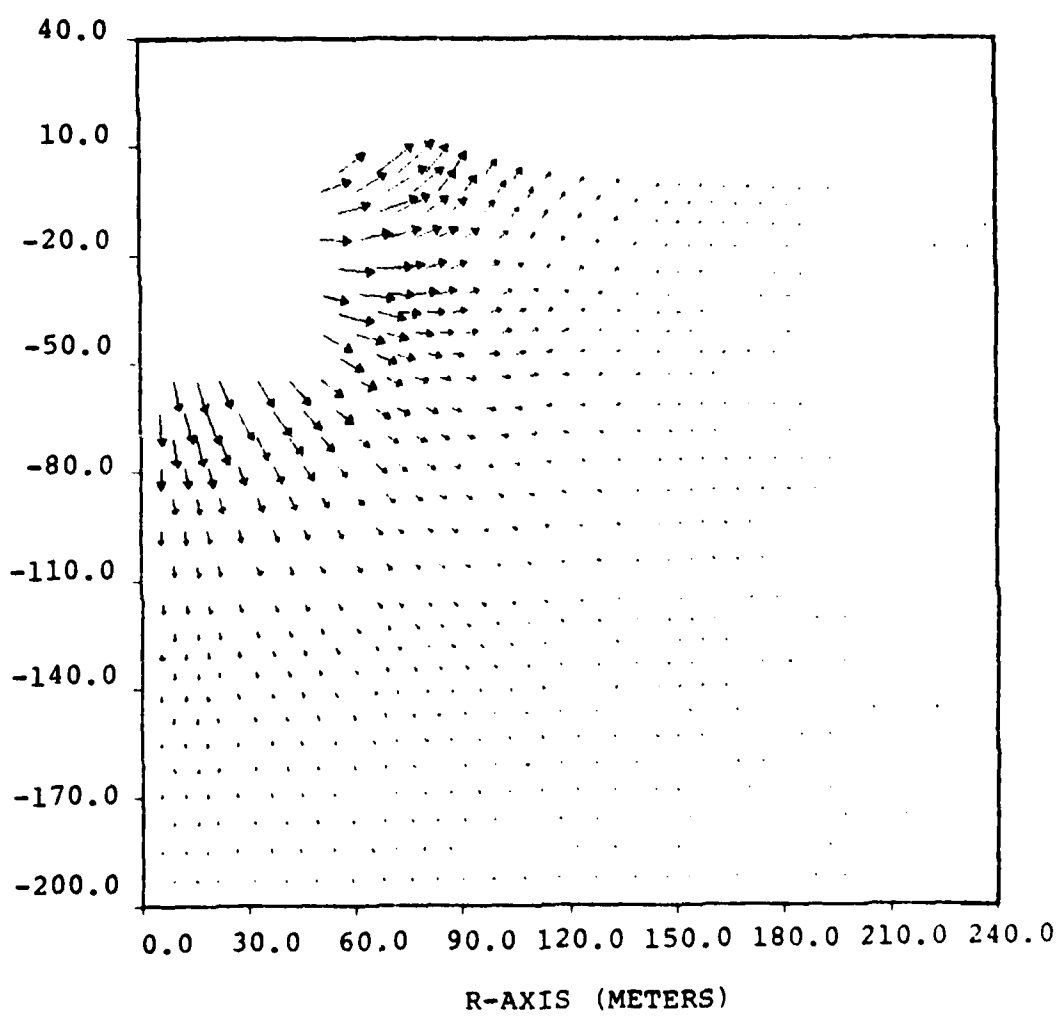

Figure 4.29. Velocity vectors of 321.91 msec.

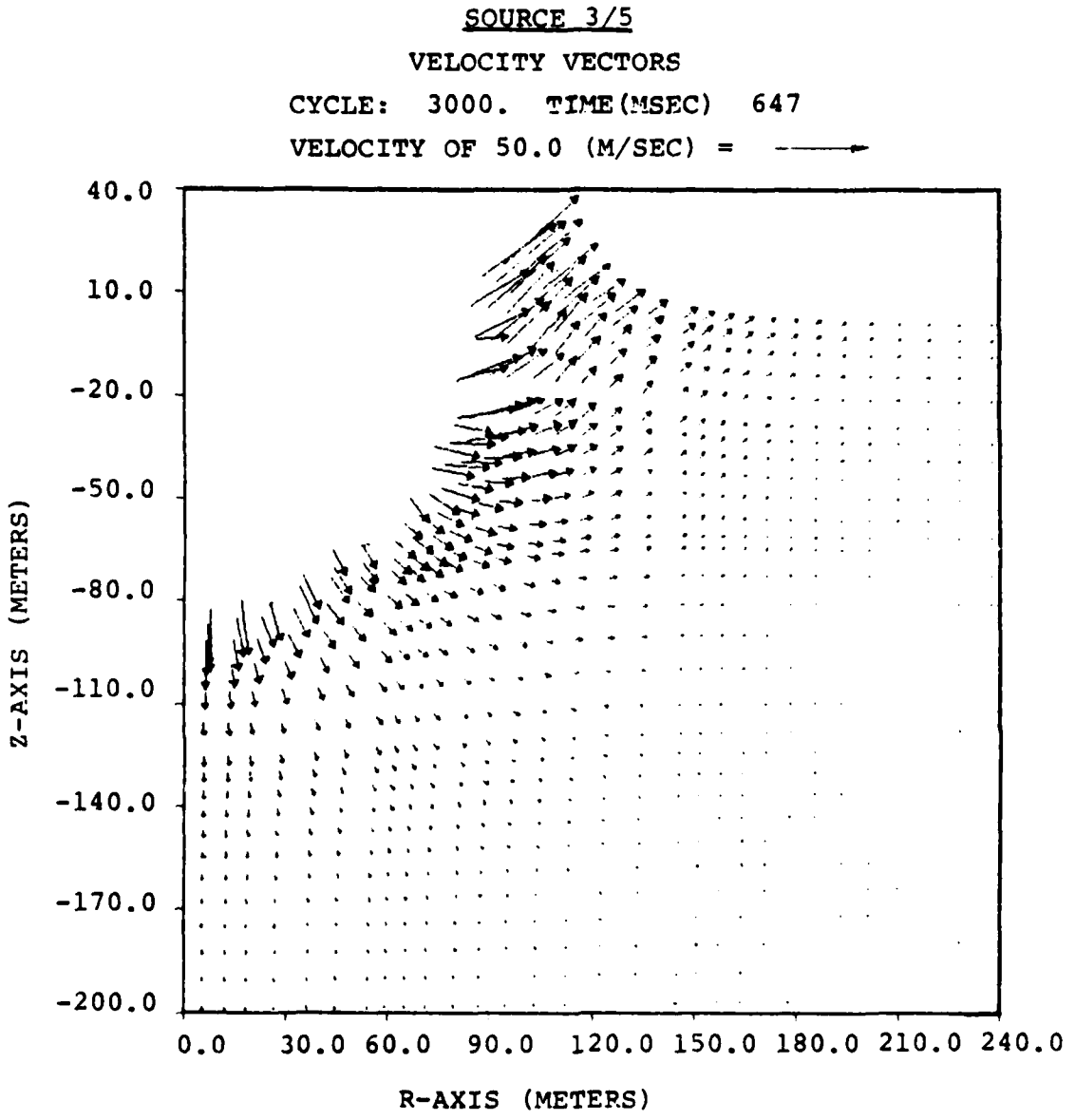

Figure 4.30. Velocity vectors at 647 msec.

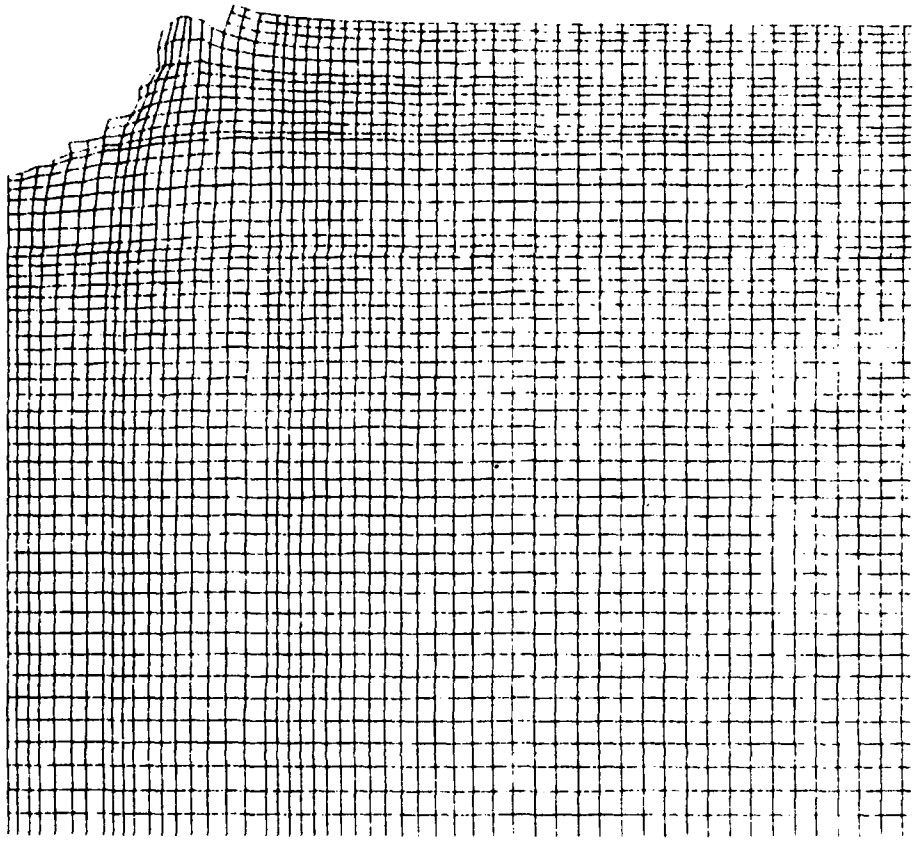

Figure 4.31a. CRAM grid at 1.17 sec with ejecta removed.

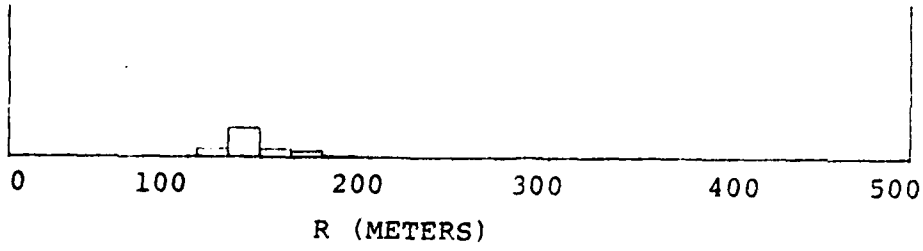

Figure 4.31b. Histogram of ejected material.

Approximate crater dimensions are a radius of 105 meters, a depth of 90 meters, and a volume of 1.04×10^6 m^3.

The calculated crater volume at 1.17 sec. corresponds to a cratering efficiency of 36.7 cubic feet per ton of explosive energy plus or minus 20 percent. Cooper (1976) has empirically estimated a cratering efficiency of 100 cubic feet per ton for wet, soft rock and 200 cubic feet per ton for wet soil. Both estimates are based on extrapolating the results of the Pacific nuclear tests in saturated coral to other geologies. The Pacific craters are unusual in both size and shape. On a scaled basis they are considerably broader and shallower than the bowl shaped craters encountered elsewhere, both experimentally and in calculations of the type presented here. A considerable segment of the cratering community hypothesize that the shape and size of the Pacific craters were due to a late time collapse of large voids in the unique structure of coral. If this hypothesis proves correct, the generic number for wet soil, the material calculated here, scaled from the Pacific tests, would be more in line with the calculations.

REFERENCES

Allen, R. T. and C. P. Knowles, "Calculation of Energy Coupling for Near-Surface Nuclear Detonations (U)," Defense Nuclear Agency Report DNA-2792F (1970) (Secret/Restrictive Data).

Allen, R. T., L. E. Bailey, and G. P. Schneyer,"Calculation of Energy Coupling for Near-Surface Nuclear Detonations(U)," Defence Nuclear Agency Report DNA-3004F (1973) (Secret/ Restricted Data)

Brode, H. L., "Review of Nuclear Weapons Effects," Annual Review of Nuclear Science, Vol. 18, pp. 153-202, 1968.

Cherry, J. T., and E. J. Halda, "Users's Manual for the SAGE Code," Systems, Science and Software Report SSS-R-79-2332, 1974.

Cherry, J. T., N. Rimer, and W. O. Wray, "Seismic Coupling from a Nuclear Explosion: The Dependence of the Reduced Displacement Potential on the Nonlinear Behavior of the Near Source Rock Environment," Systems, Science, and Software Technical Report SSS-R-76-2742. September, 1975.

Cherry, J. T. and F. L. Peterson, "Numerical Simulation of Stress Wave Propagation from Underground Nuclear Explosions," Engineering with Nuclear Explosives, AWS, USAEC, CONF-70010, 1970.

Cooper, H. F., "Estimates of Crater Dimensions for Near-Surface Explosions of Nuclear and High-Explosive Sources," Research and Development Associates Technical Report RDA-TR-2604-001, September, 1976.

Laird, D. H., "A Chemical Equilibrium Equation of State for Saturated Tuff," Systems, Science and Software Technical Report, SSS-R-75-2740, 1976.

Maenchen, G., and S. Sack, "The TENSOR Code," in Methods in Computational Physics, Vol. 3., Academic Press, New York, 1964.

Melzer, L. S., A. R. Schenker, G. D. Hulcher, and J. S. Rinehart, "Geological Influences on Nuclear Weapon Effects in Western Alluvial Valleys," Air Force Weapons Laboratory Final Report AFWL-TR-78-155, June, 1979.

REFERENCES (Continued)

Needham, C. C., M. L. Havens, and C. S. Knauth, "Nuclear Blast Standard (1 KT)," Air Force Weapons Laboratory Final Report. AFWL-TR-73-55, April, 1975.

Pyatt, K. D, Jr., "Nuclear Explosion Interaction Studies, Volume II, Methods for Analysis of Thermal Phenomena," General Atomic Final Report GA-7370, AFWL-TR-66-108, Vol. II. August, 1966.

APPENDIX A
NONLINEAR GROUND MOTION

Plots of pressure, velocities, and displacements versus time out to 300 msec at a series of locations near the free surface are presented here. Included are horizontal ranges (R) of 100, 120, 160, 200 and 240 meters and depths (Z) below the free surface of 20, 50 and 75 meters. The station location is given in the upper right hand corner of each plot. Some plots show a straight line connecting the origin to the first active piece of data, rather than a set of zeroes. This is a plotting error due to the method used in generating these plots; i.e., accessing computer dump tapes after completion of the calculation. Because only relatively large intervals of time were sampled, peak values of pressure and velocity may have been missed in these plots. For this same reason, individual plots have less wiggles than if data were available for each computational time step.

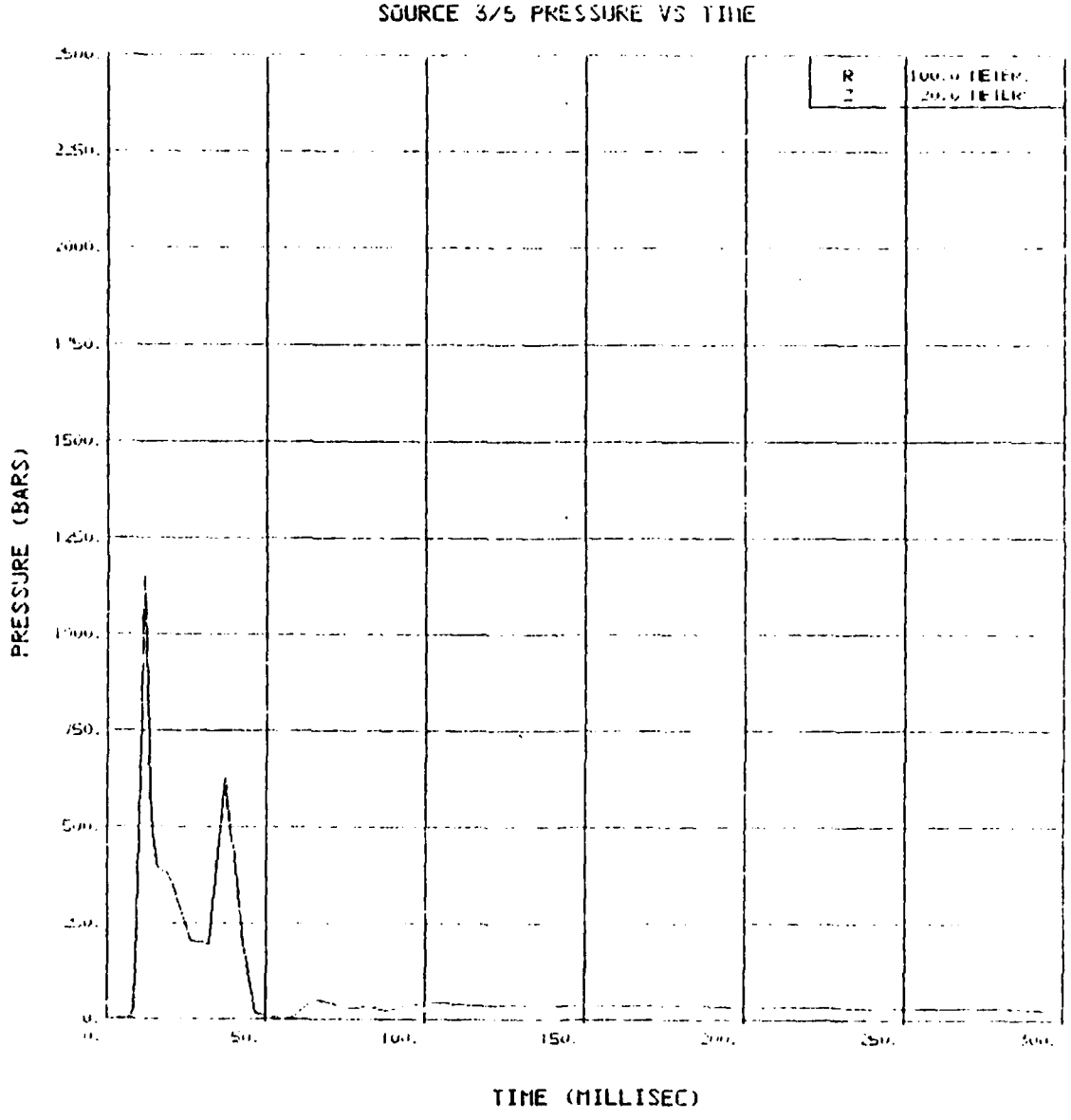
SOURCE 3/5 PRESSURE VS TIME
R
2
PRESSURE (BARS)
2250.
2000.
1750.
1500.
1250.
1000.
750.
500.
250.
0.
0.
50.
100.
150.
200.
250.
300.
TIME (MILLISEC)

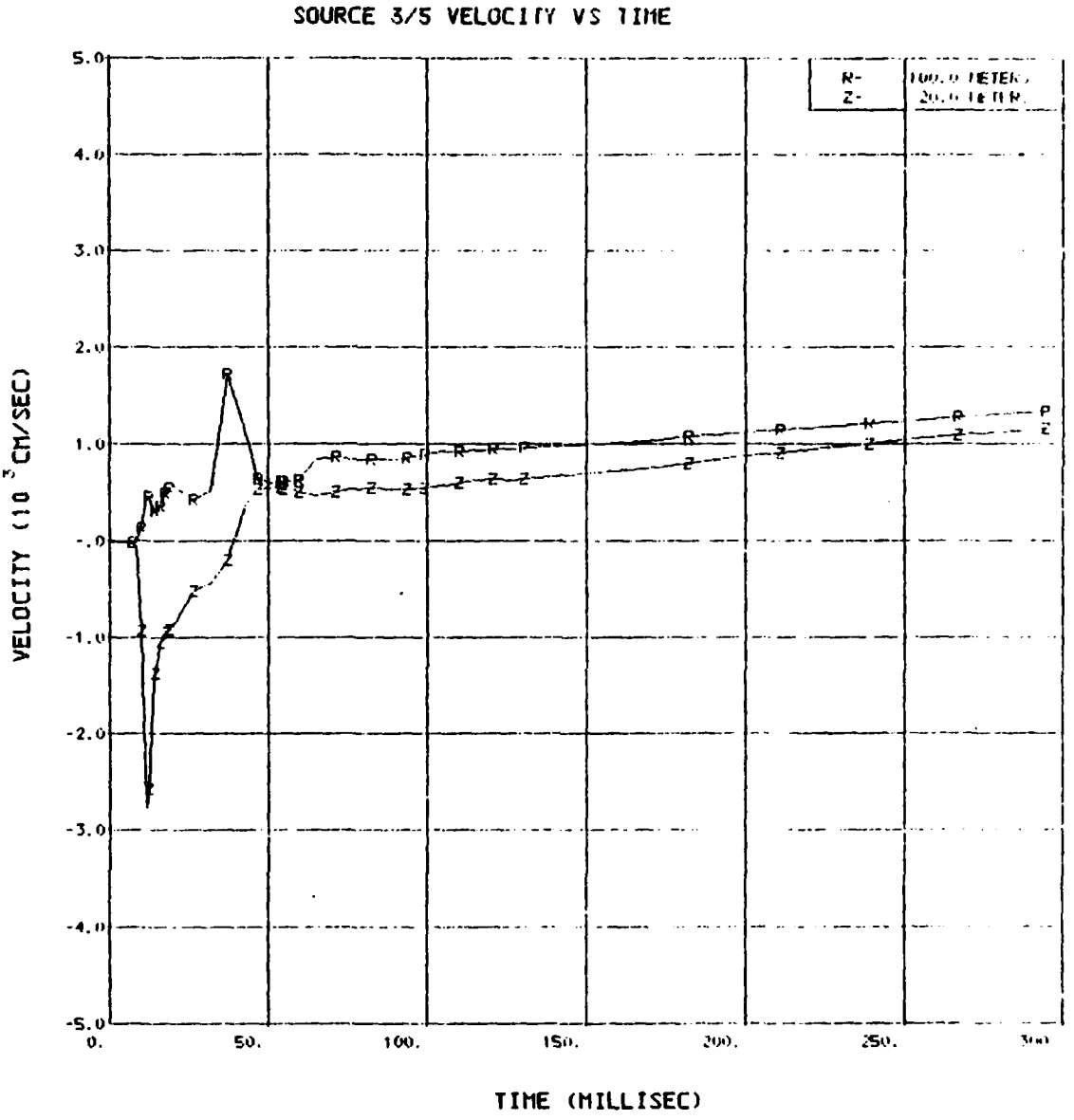
SOURCE 3/5 VELOCITY VS TIME
R-
Z-
VELOCITY (10 ³ CM/SEC)
5.0
4.0
3.0
2.0
1.0
-.0
-1.0
-2.0
-3.0
-4.0
-5.0
0.
50.
100.
150.
200.
250.
TIME (MILLISEC)

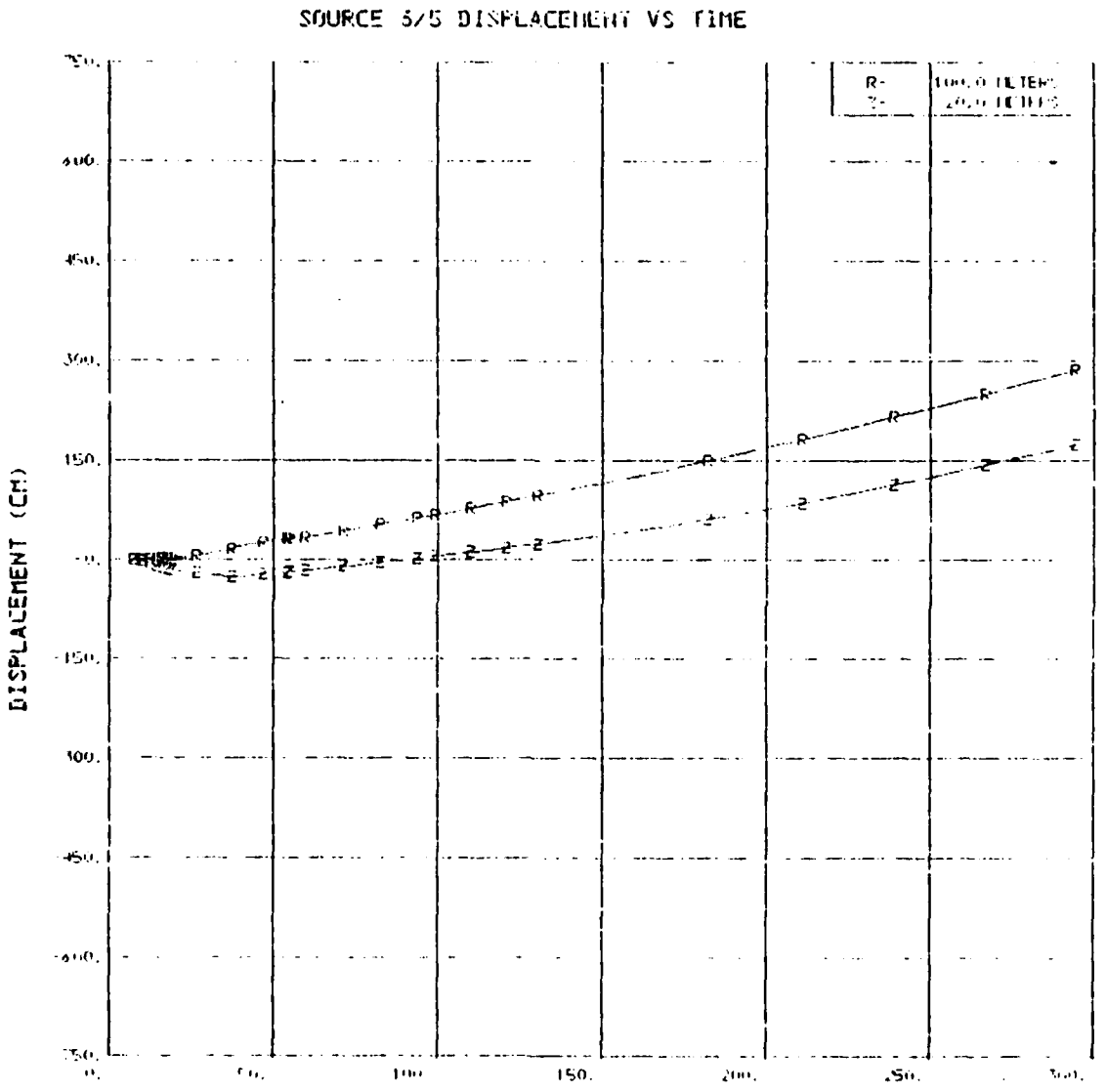
SOURCE 5/5 DISPLACEMENT VS TIME
DISPLACEMENT (CM)
TIME (MILLISEC)
R-
Z-
450.
300.
150.
-150.
-300.
-450.
-600.
-750.
0.
50.
100.
150.
200.
250.
300.

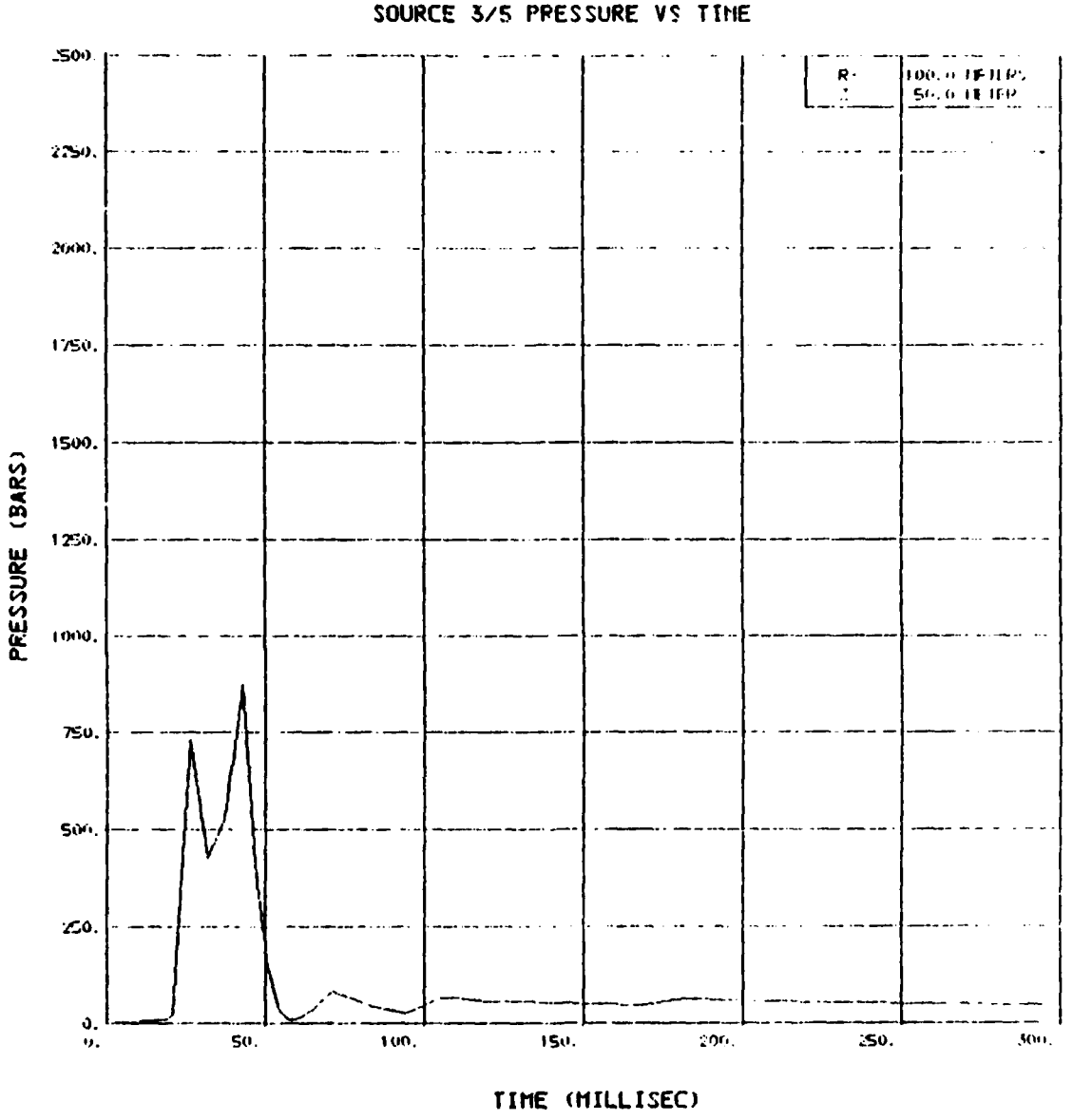
SOURCE 3/5 PRESSURE VS TIME
PRESSURE (BARS)
2500.
2250.
2000.
1750.
1500.
1250.
1000.
750.
500.
250.
0.
0.
50.
100.
150.
200.
250.
300.
TIME (MILLISEC)

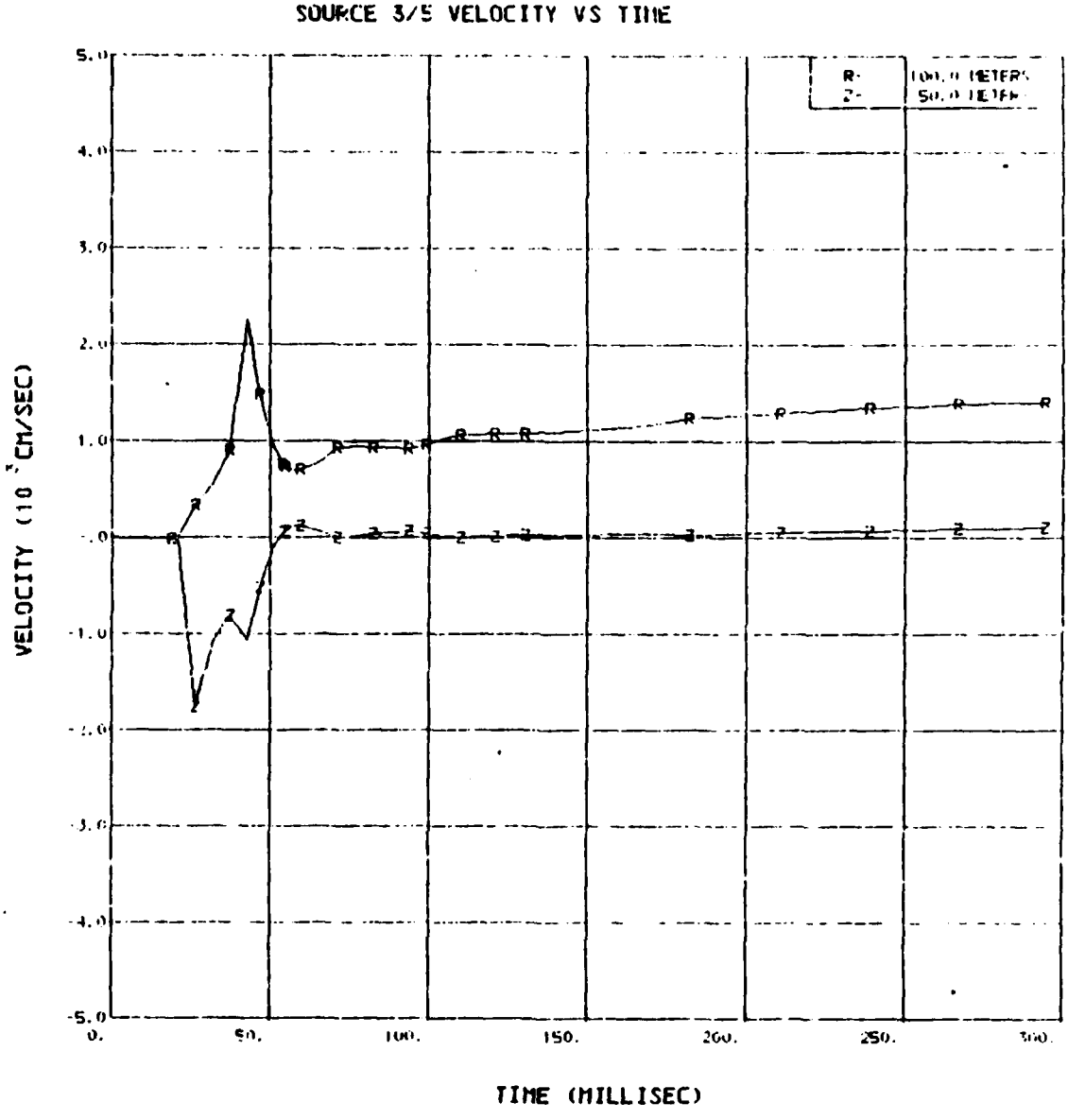
SOURCE 3/5 VELOCITY VS TIME
R-
Z-
5.0
4.0
3.0
2.0
1.0
-1.0
-2.0
-3.0
-4.0
-5.0
0.
50.
100.
150.
200.
250.
300.
VELOCITY (10 CM/SEC)
TIME (MILLISEC)

SOURCE 3/5 DISPLACEMENT VS TIME

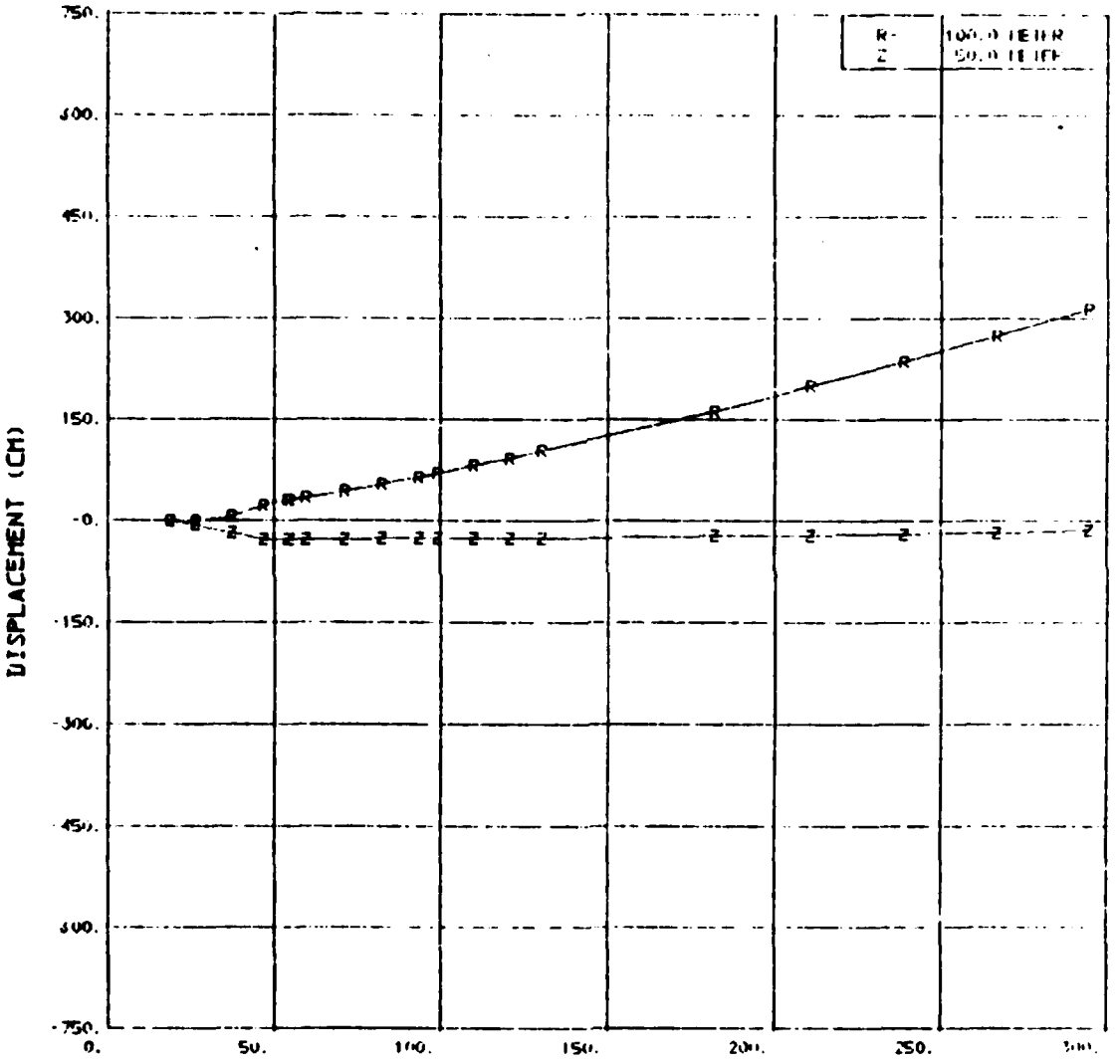

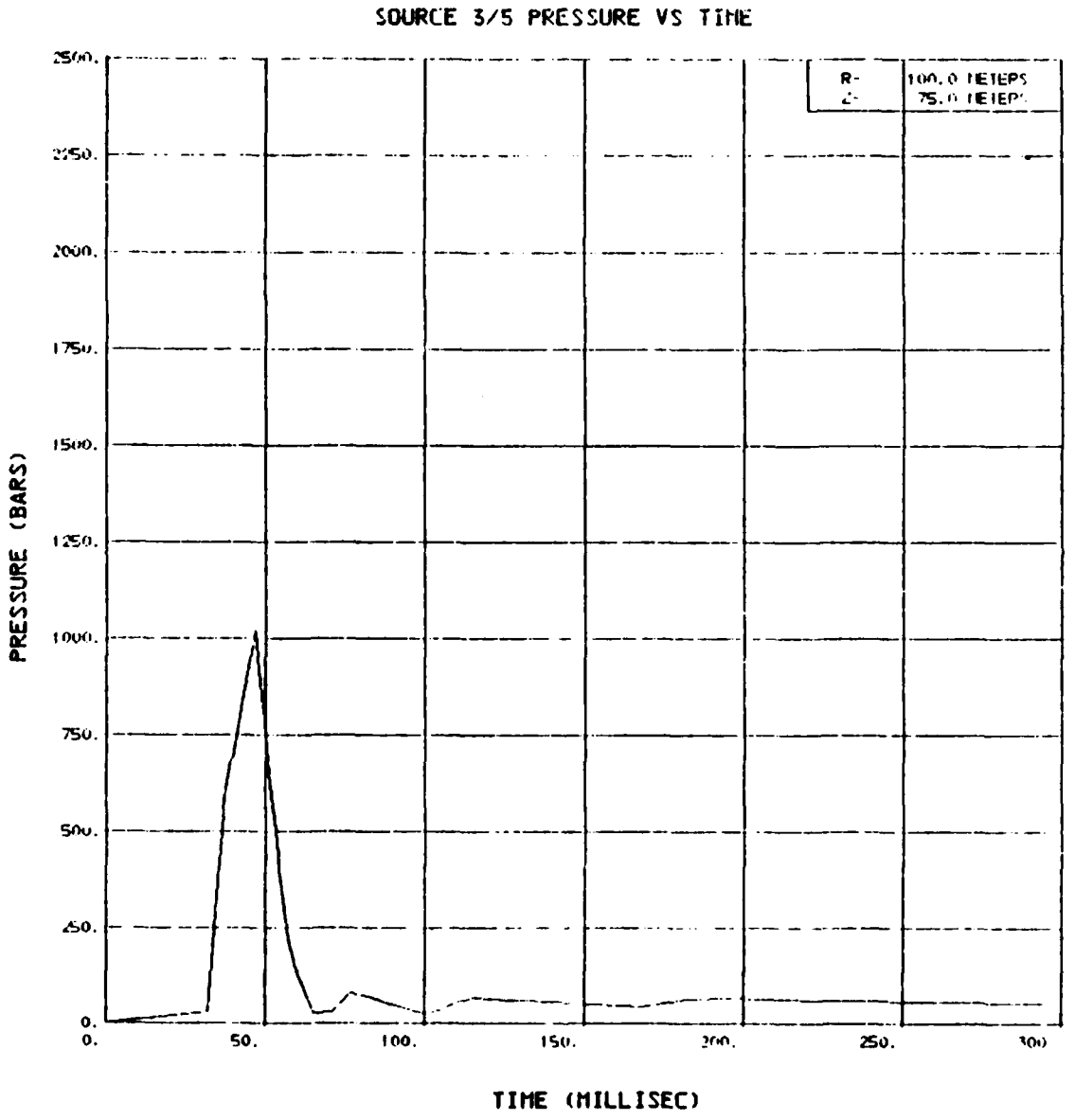
SOURCE 3/5 PRESSURE VS TIME
PRESSURE (BARS)
2500.
2250.
2000.
1750.
1500.
1250.
1000.
750.
500.
250.
0.
0.
50.
100.
150.
200.
250.
300.
TIME (MILLISEC)

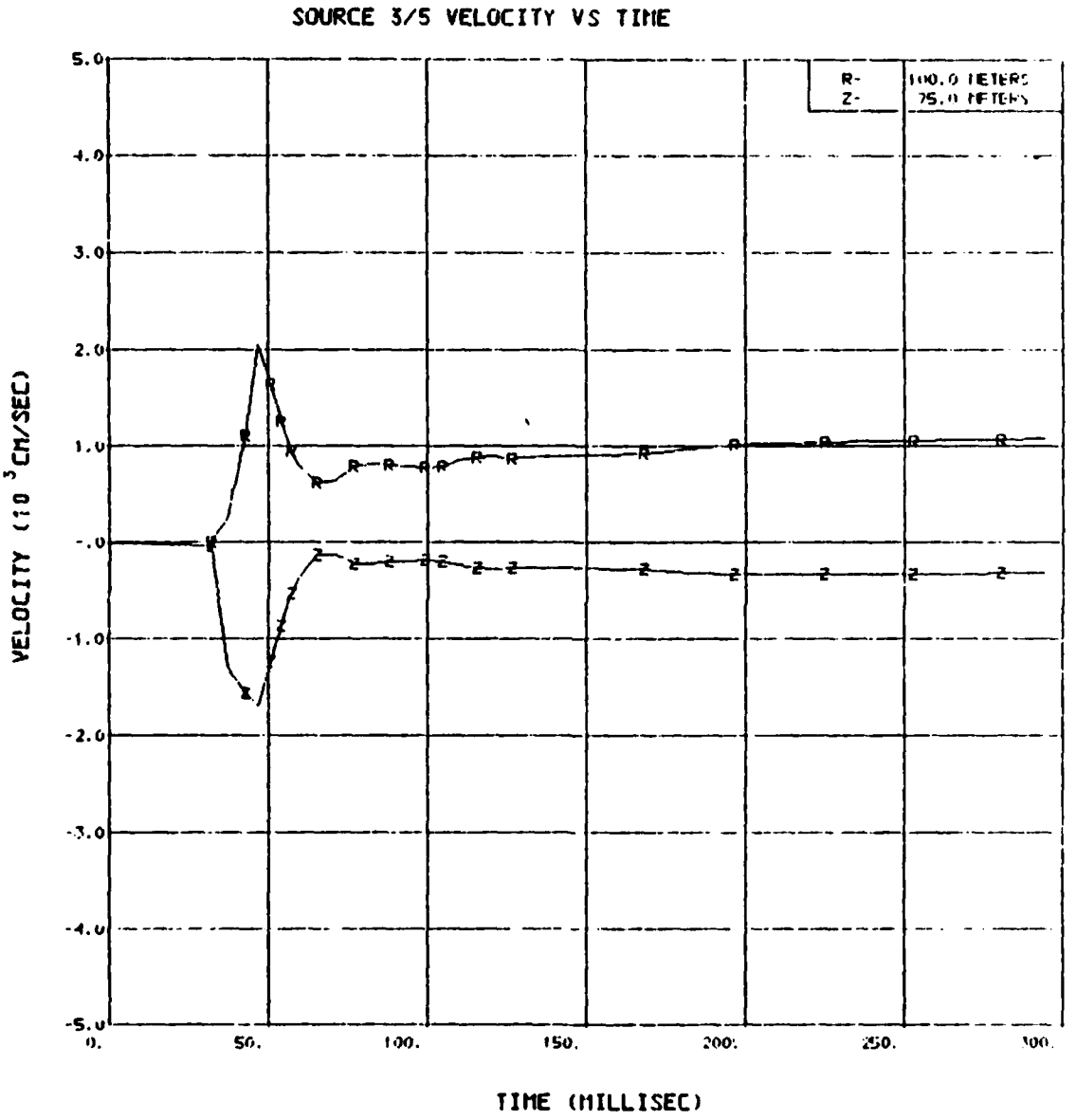
SOURCE 3/5 VELOCITY VS TIME
R-
Z-
100.0 METERS
75.0 METERS
5.0
4.0
3.0
2.0
1.0
-.0
-1.0
-2.0
-3.0
-4.0
-5.0
0.
50.
100.
150.
200.
250.
300.
VELOCITY (10 3 CM/SEC)
TIME (MILLISEC)

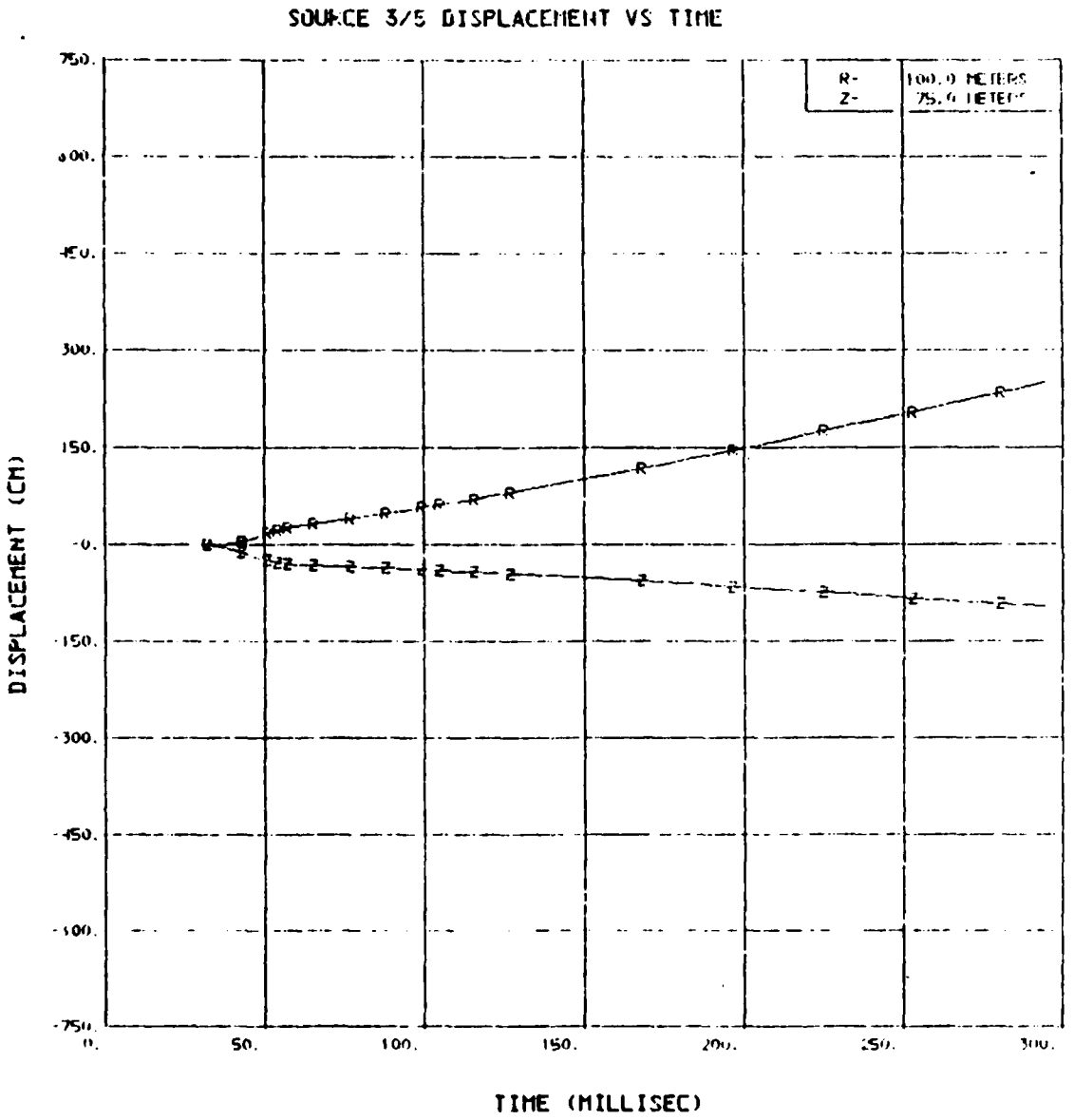
SOURCE 3/5 DISPLACEMENT VS TIME
R-
Z-
DISPLACEMENT (CM)
750.
300.
150.
0.
-150.
-300.
-450.
-600.
-750.
0.
50.
100.
150.
200.
250.
300.
TIME (MILLISEC)

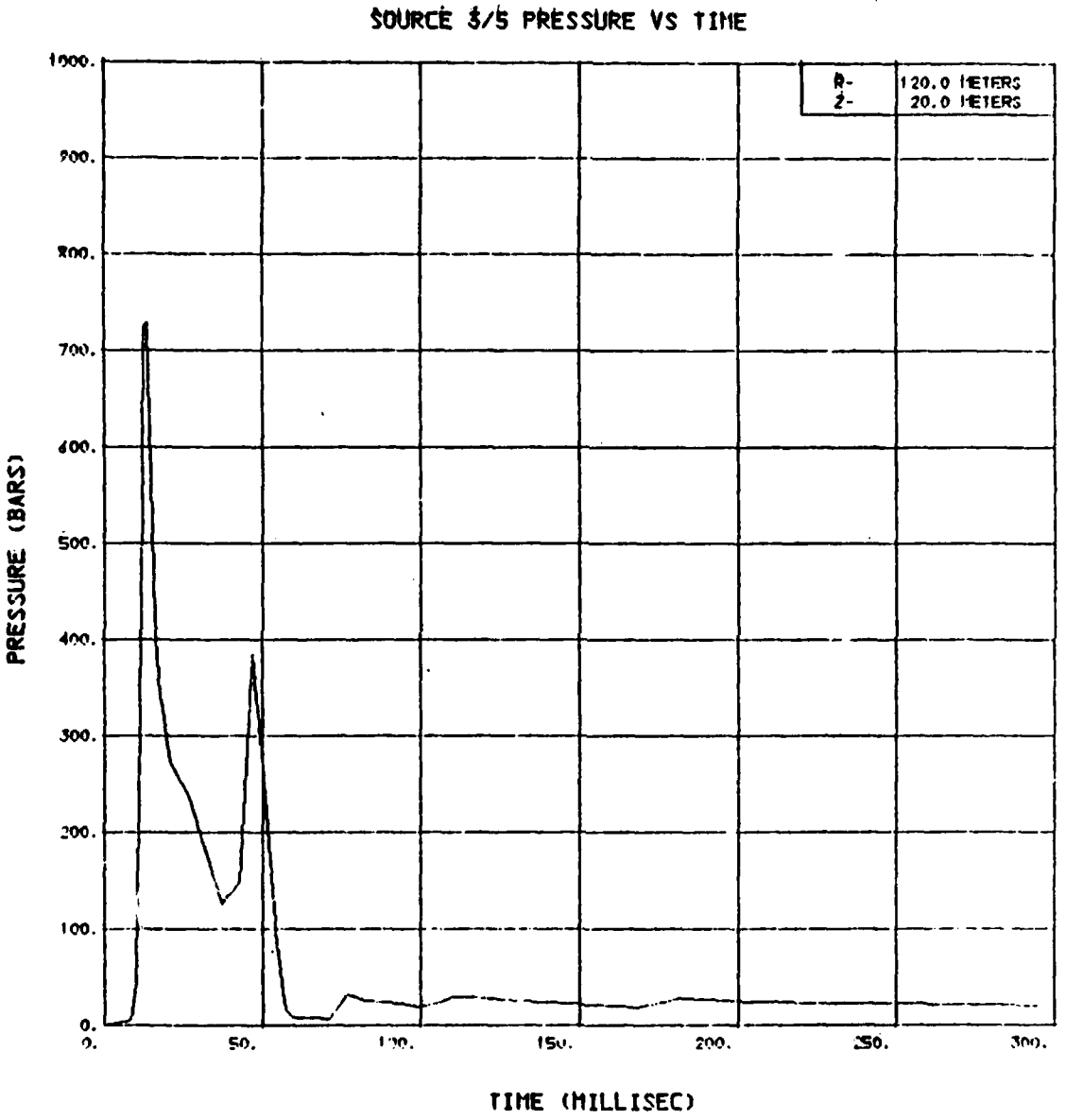
SOURCE 3/5 PRESSURE VS TIME
R- 120.0 METERS
Z- 20.0 METERS
1000.
900.
800.
700.
600.
500.
400.
300.
200.
100.
0.
PRESSURE (BARS)
0.
50.
100.
150.
200.
250.
300.
TIME (MILLISEC)

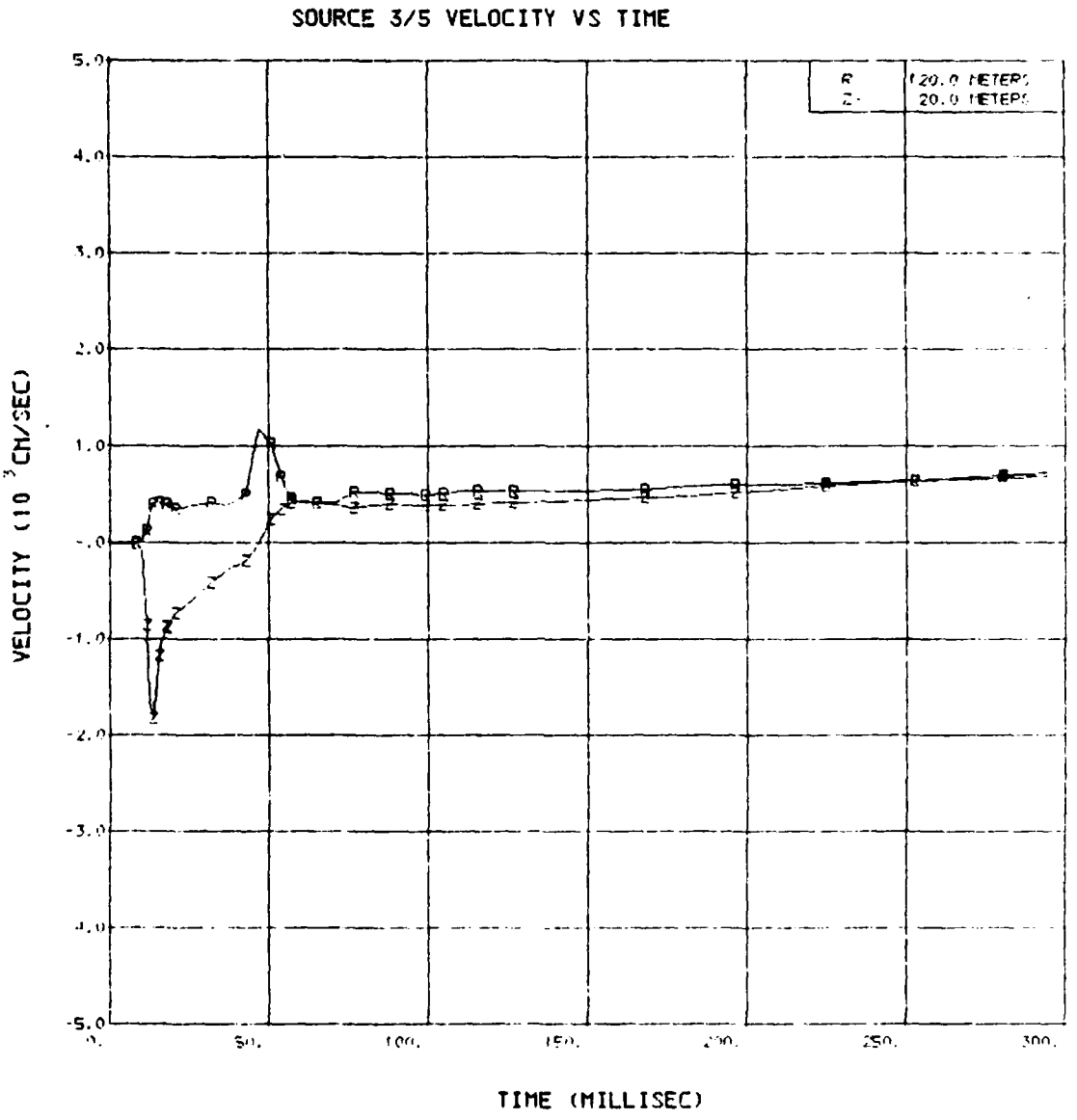
SOURCE 3/5 VELOCITY VS TIME
R 120.0 METERS
Z 20.0 METERS
5.0
4.0
3.0
2.0
1.0
-1.0
-2.0
-3.0
-4.0
-5.0
0.
50.
100.
150.
200.
250.
300.
VELOCITY (10 $^{-3}$ CM/SEC)
TIME (MILLISEC)

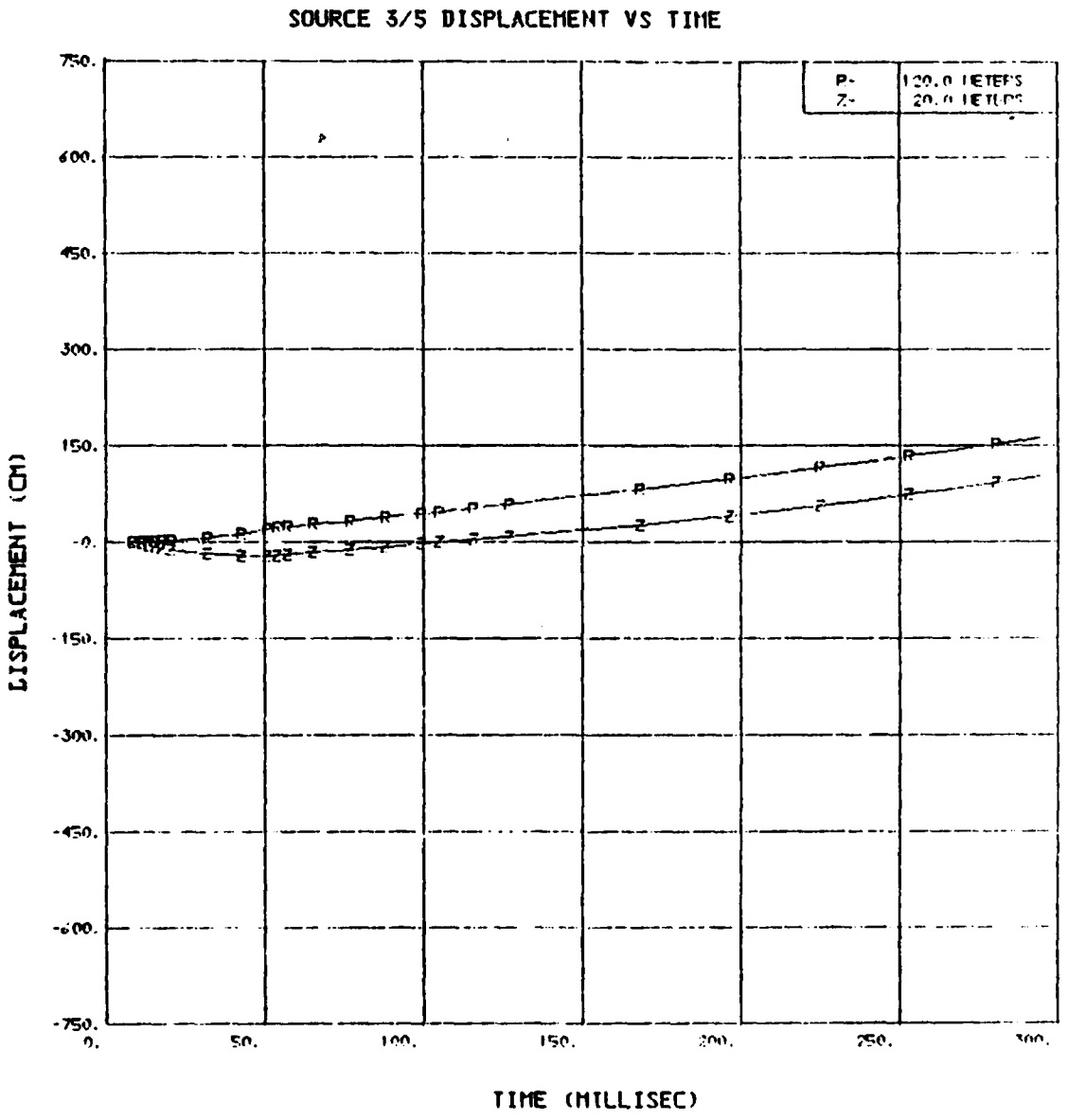
SOURCE 3/5 DISPLACEMENT VS TIME
750.
600.
450.
300.
150.
-0.
-150.
-300.
-450.
-600.
-750.
0.
50.
100.
150.
200.
250.
300.
DISPLACEMENT (CM)
TIME (MILLISEC)

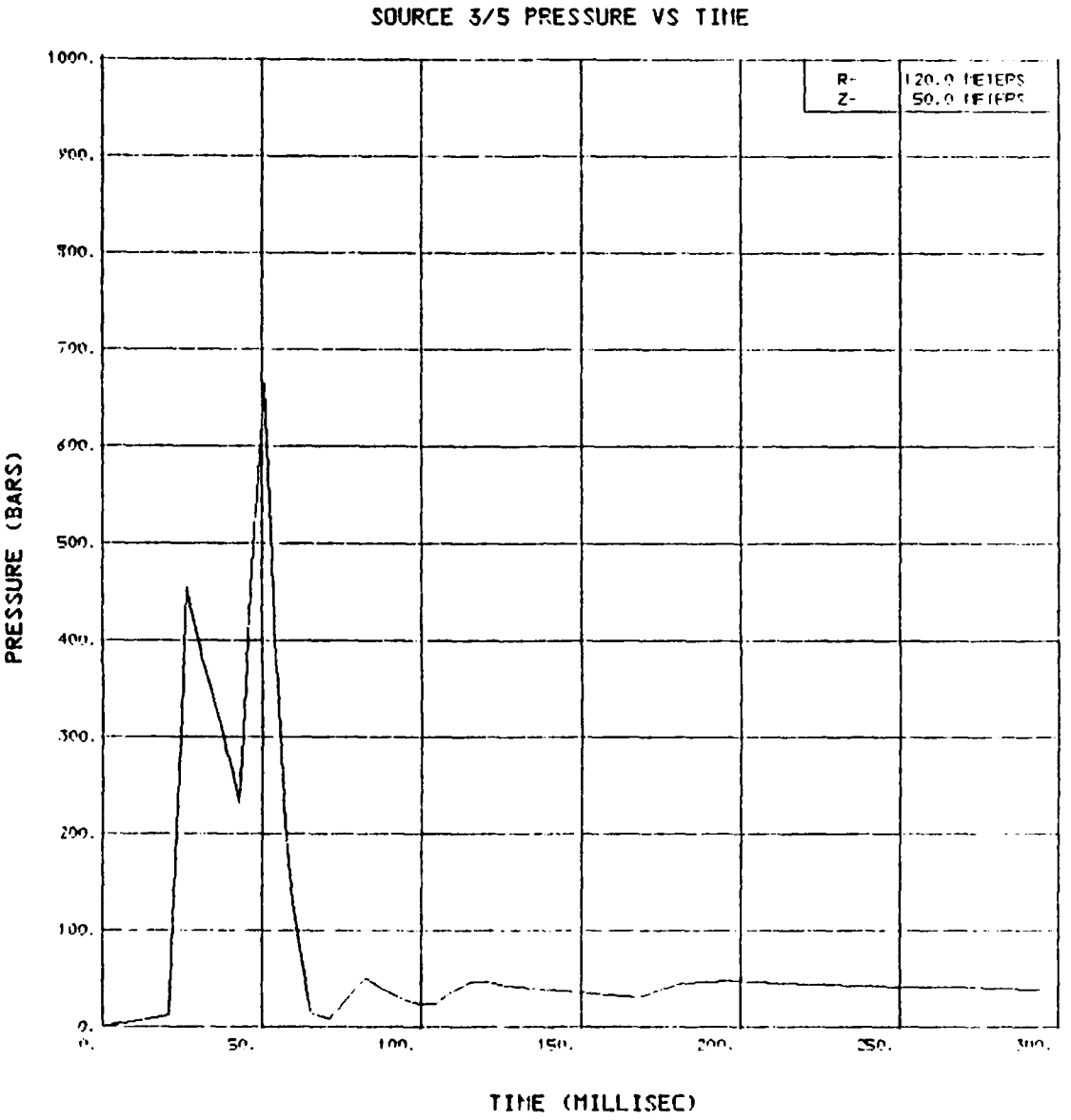
SOURCE 3/5 PRESSURE VS TIME
R-
Z-
PRESSURE (BARS)
1000.
900.
800.
700.
600.
500.
400.
300.
200.
100.
0.
0.
50.
100.
150.
200.
250.
300.
TIME (MILLISEC)

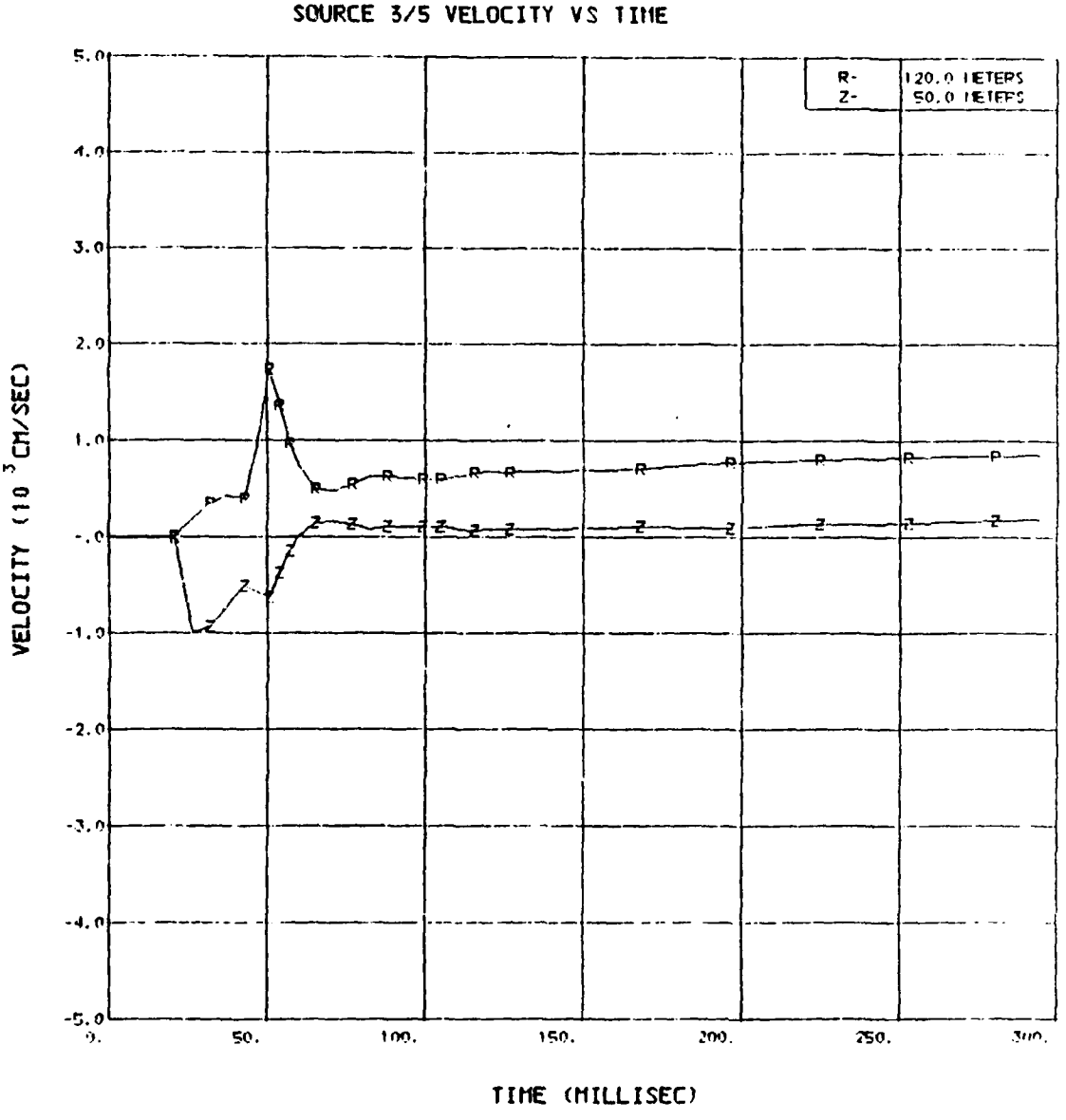
SOURCE 3/5 VELOCITY VS TIME
R- 120.0 METERS
Z- 50.0 METERS
VELOCITY (10 3 CM/SEC)
5.0
4.0
3.0
2.0
1.0
-.0
-1.0
-2.0
-3.0
-4.0
-5.0
0.
50.
100.
150.
200.
250.
300.
TIME (MILLISEC)

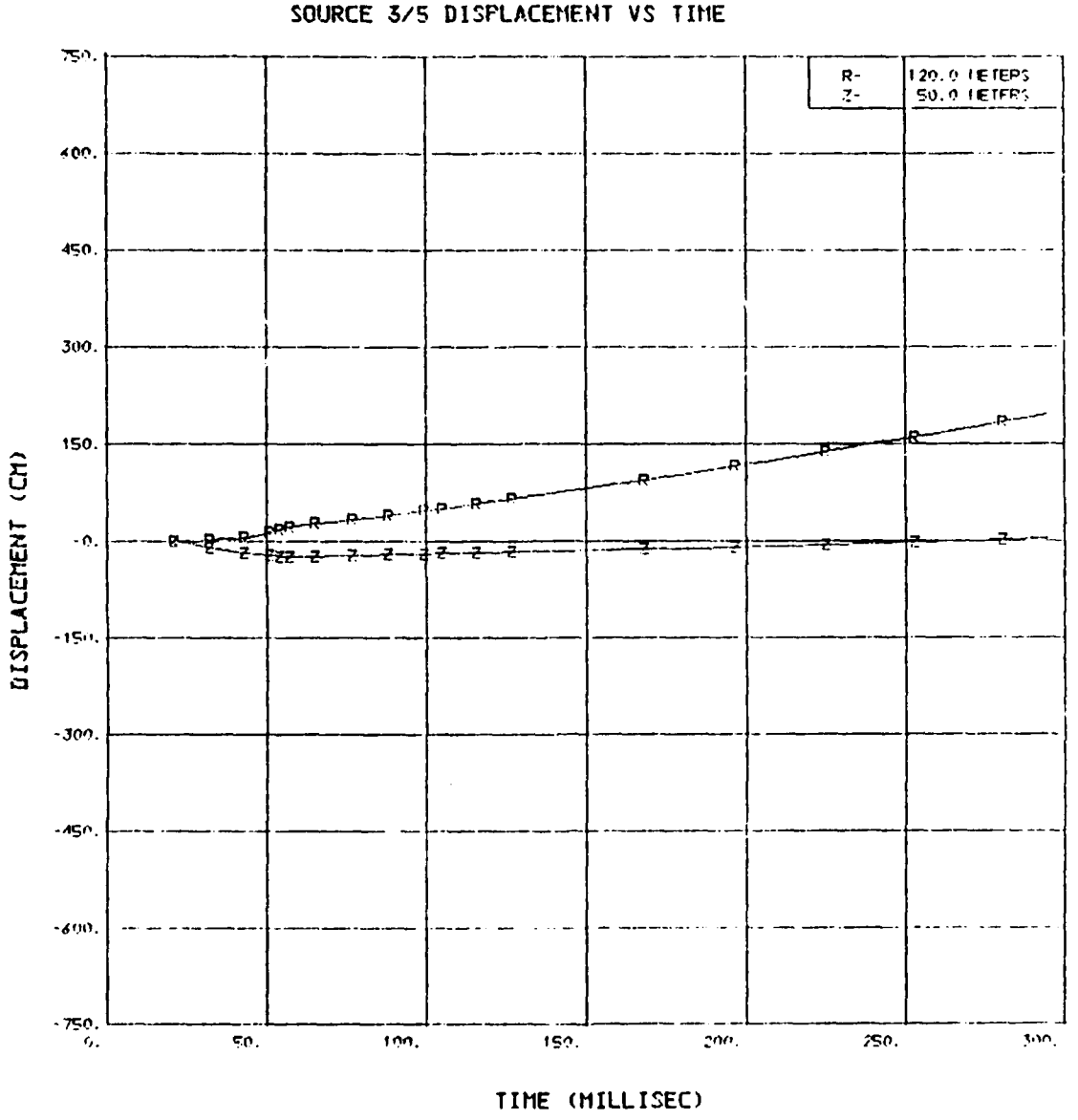
SOURCE 3/5 DISPLACEMENT VS TIME
R- 120.0 METERS
Z- 50.0 METERS
DISPLACEMENT (CM)
750.
600.
450.
300.
150.
0.
-150.
-300.
-450.
-600.
-750.
0.
50.
100.
150.
200.
250.
300.
TIME (MILLISEC)

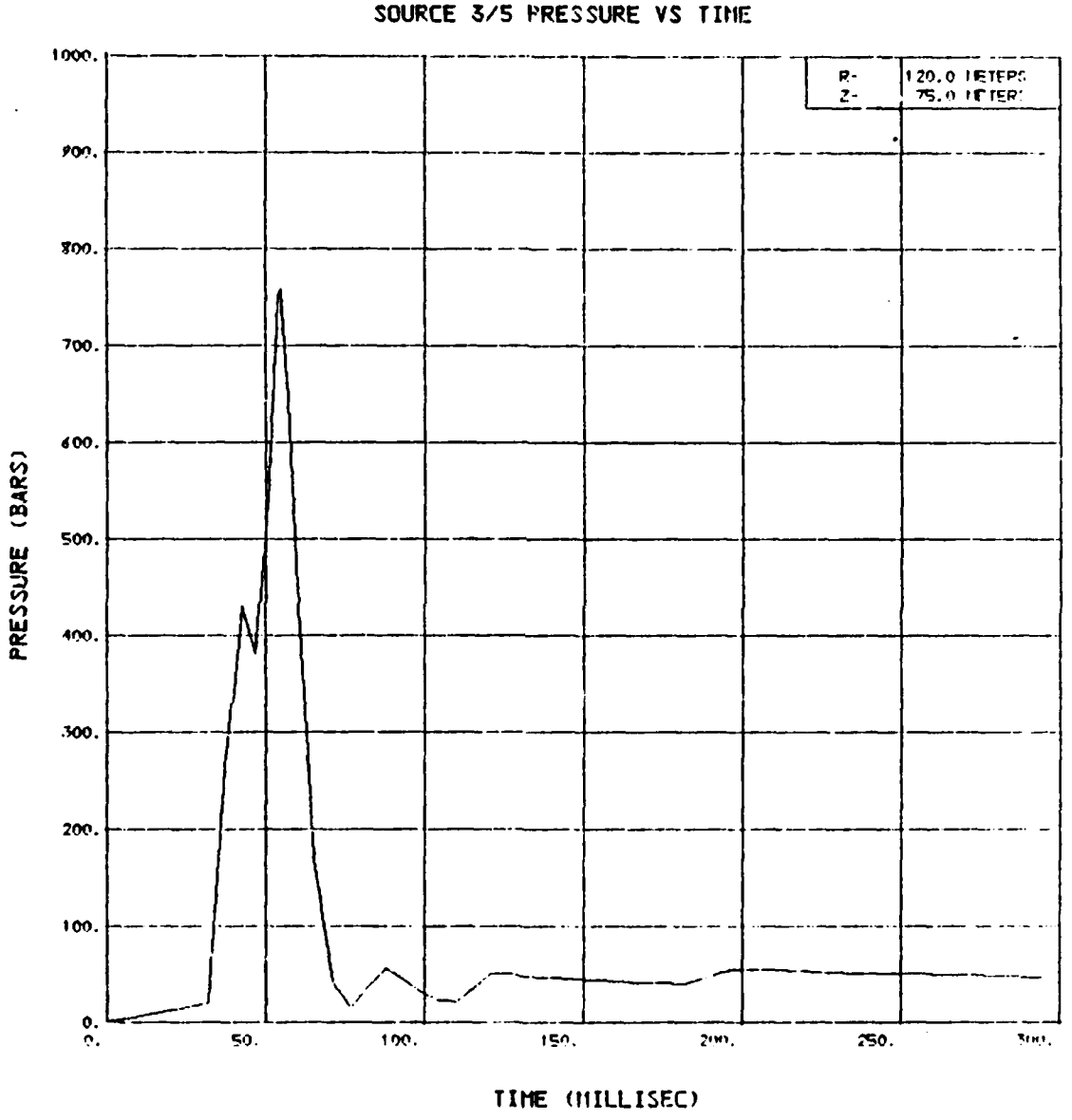
SOURCE 3/5 PRESSURE VS TIME
R-
Z-
1000.
900.
800.
700.
600.
500.
400.
300.
200.
100.
0.
PRESSURE (BARS)
0.
50.
100.
150.
250.
TIME (MILLISEC)

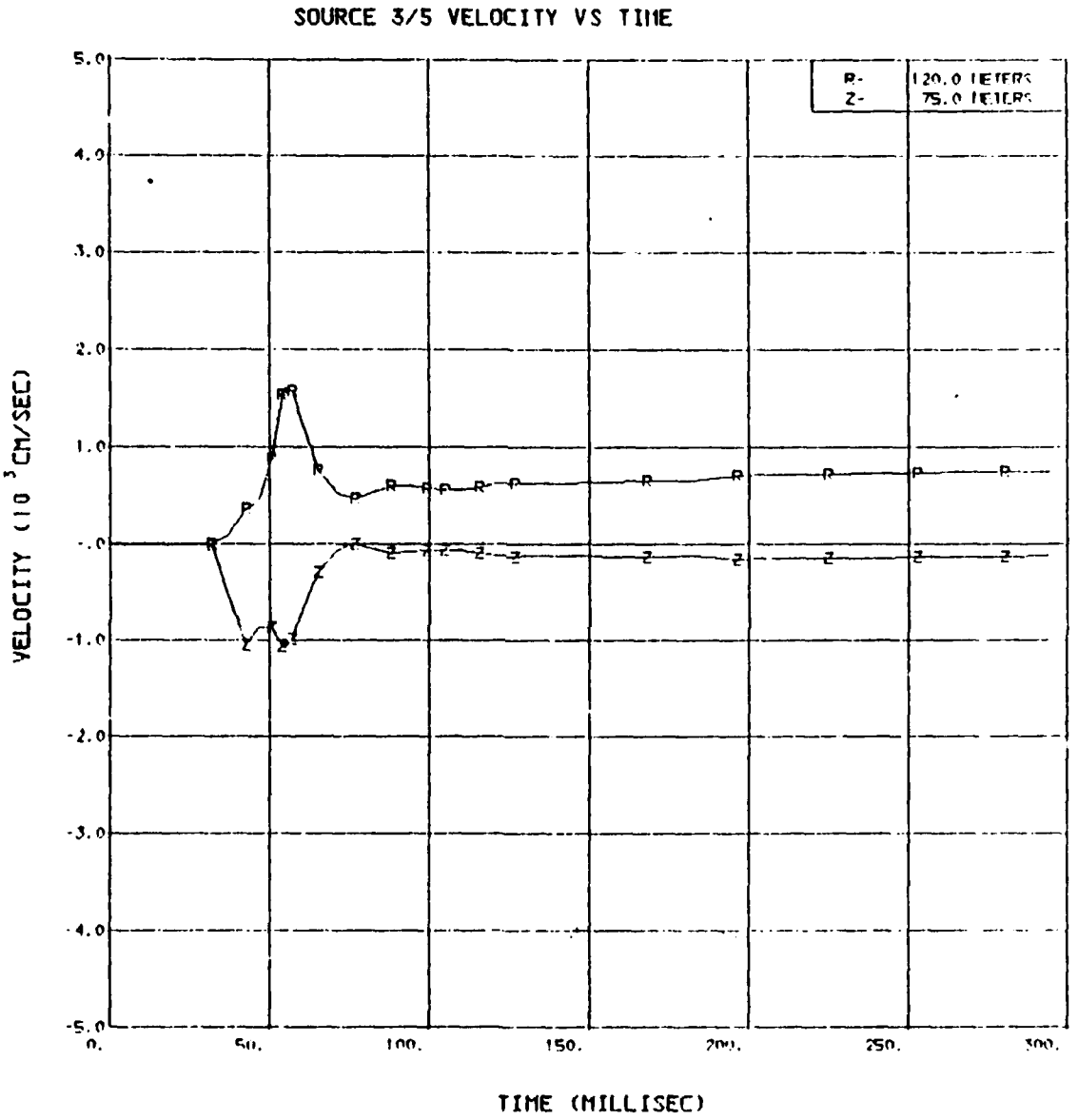
SOURCE 3/5 VELOCITY VS TIME
R- 120.0 METERS
Z- 75.0 METERS
VELOCITY (10 3 CM/SEC)
5.0
4.0
3.0
2.0
1.0
-1.0
-2.0
-3.0
-4.0
-5.0
0.
50.
100.
150.
200.
250.
300.
TIME (MILLISEC)

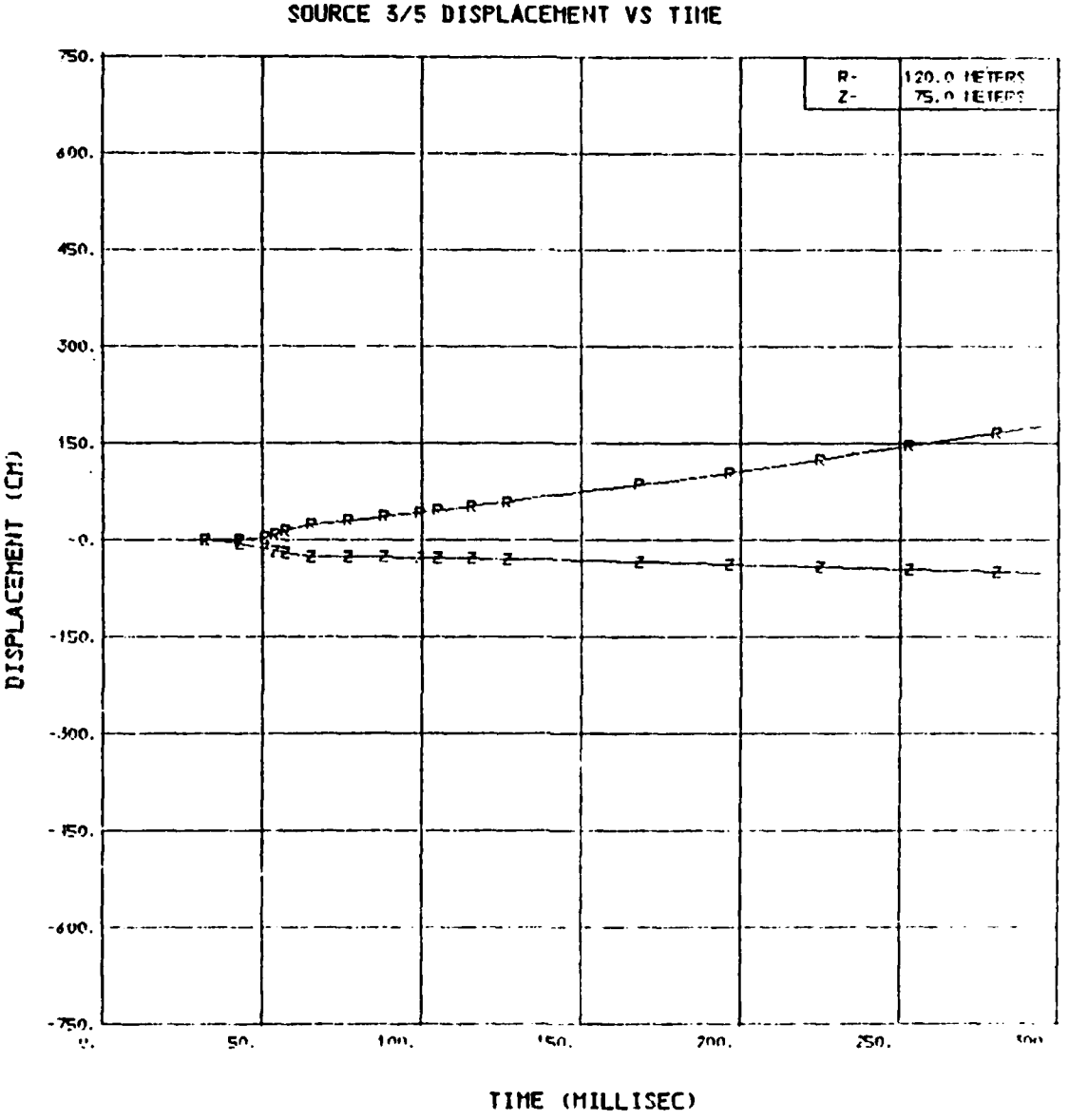
SOURCE 3/5 DISPLACEMENT VS TIME
R- 120.0 METERS
Z- 75.0 METERS
750.
600.
450.
300.
150.
-0.
-150.
-300.
-450.
-600.
-750.
0.
50.
100.
150.
200.
250.
DISPLACEMENT (CM)
TIME (MILLISEC)

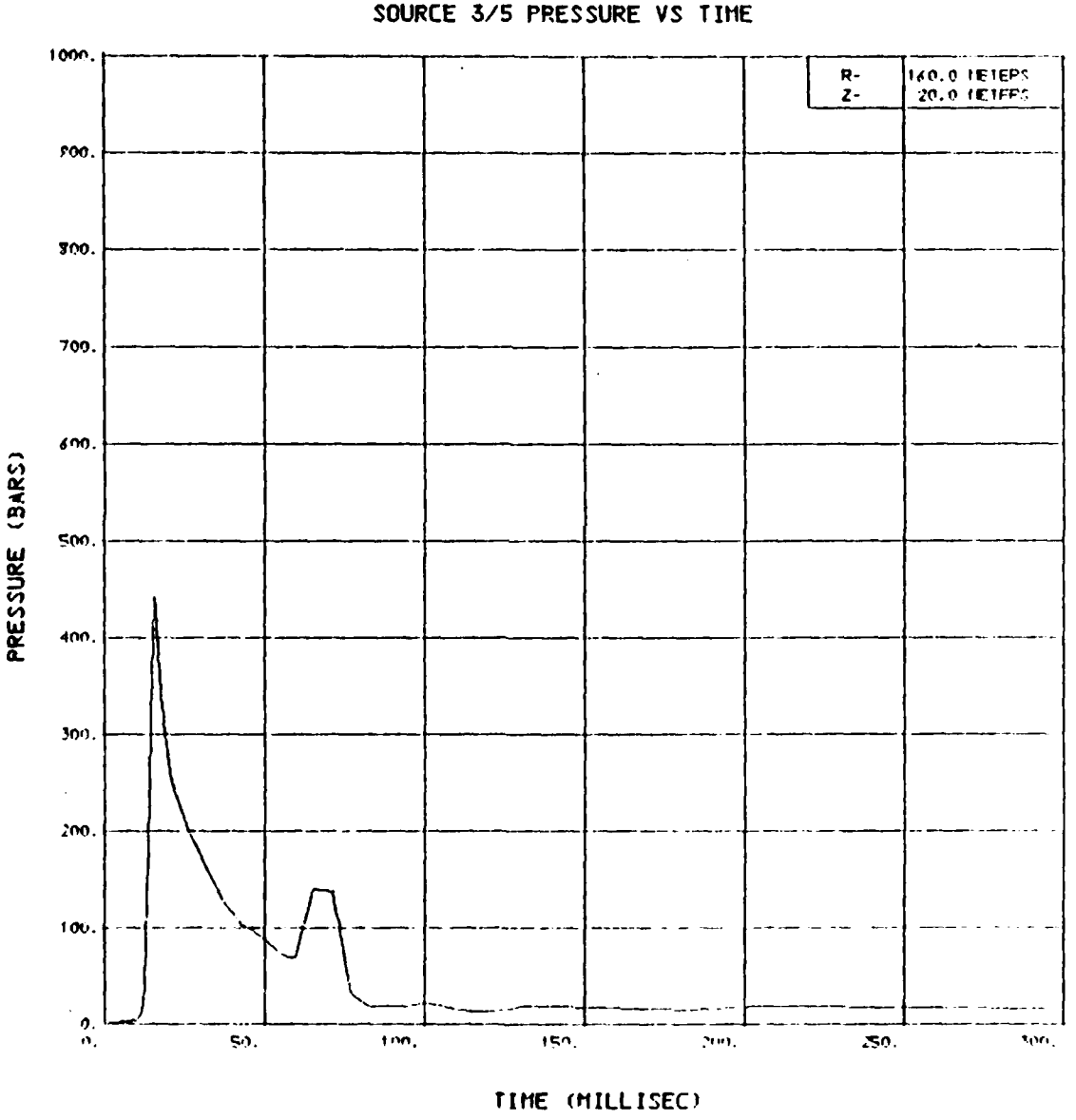
SOURCE 3/5 PRESSURE VS TIME
R-
Z-
1000.
900.
800.
700.
600.
500.
400.
300.
200.
100.
0.
PRESSURE (BARS)
0.
50.
100.
150.
200.
250.
300.
TIME (MILLISEC)

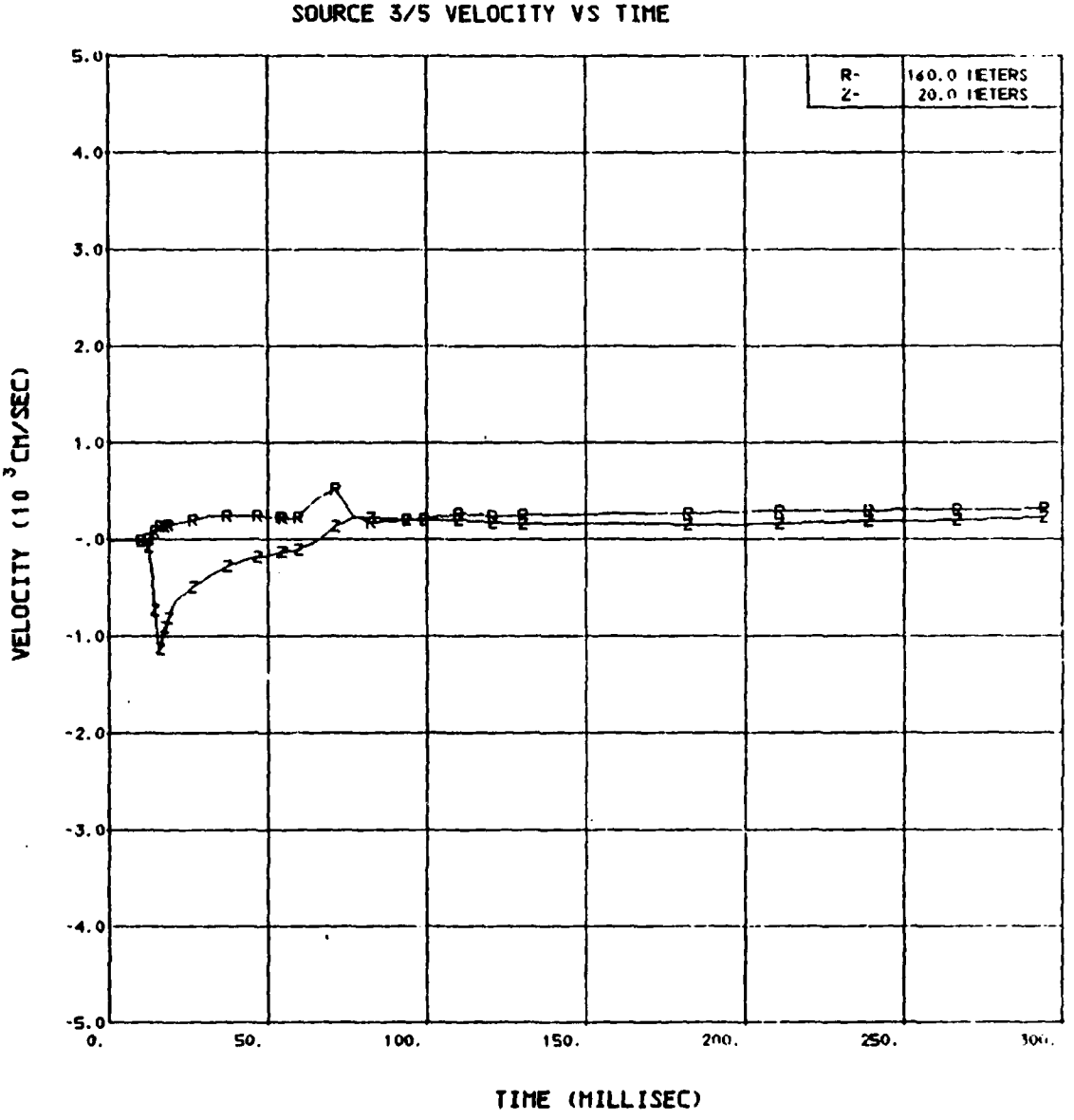
SOURCE 3/5 VELOCITY VS TIME
R- 160.0 METERS
Z- 20.0 METERS
VELOCITY (10 -3 CM/SEC)
5.0
4.0
3.0
2.0
1.0
-.0
-1.0
-2.0
-3.0
-4.0
-5.0
0.
50.
100.
150.
200.
250.
300.
TIME (MILLISEC)

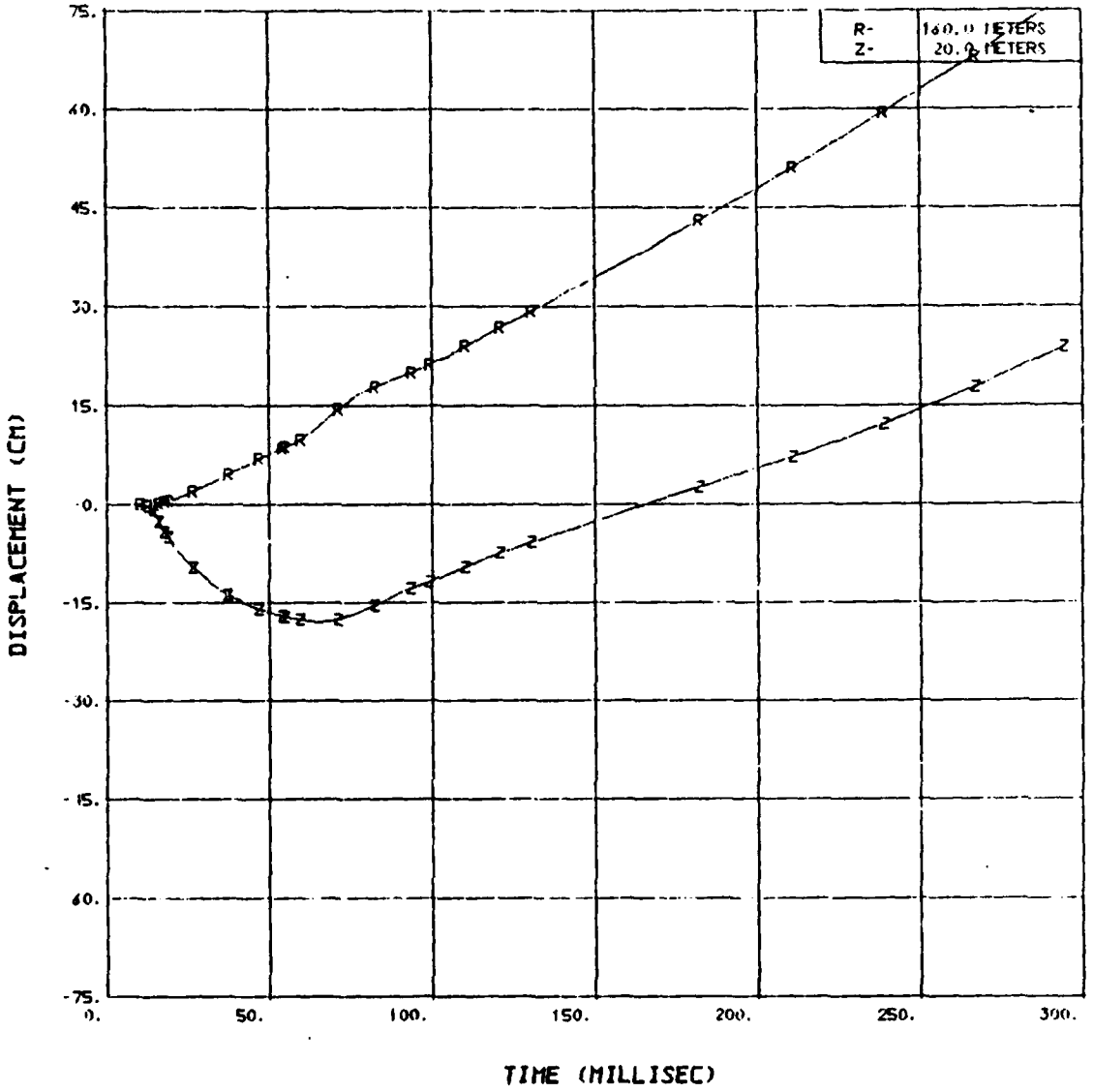
SOURCE 3/5 DISPLACEMENT VS TIME
R-
Z-
160.0 METERS
20.0 METERS
75.
60.
45.
30.
15.
0.
-15.
-30.
-45.
-60.
-75.
0.
50.
100.
150.
200.
250.
300.
DISPLACEMENT (CM)
TIME (MILLISEC)

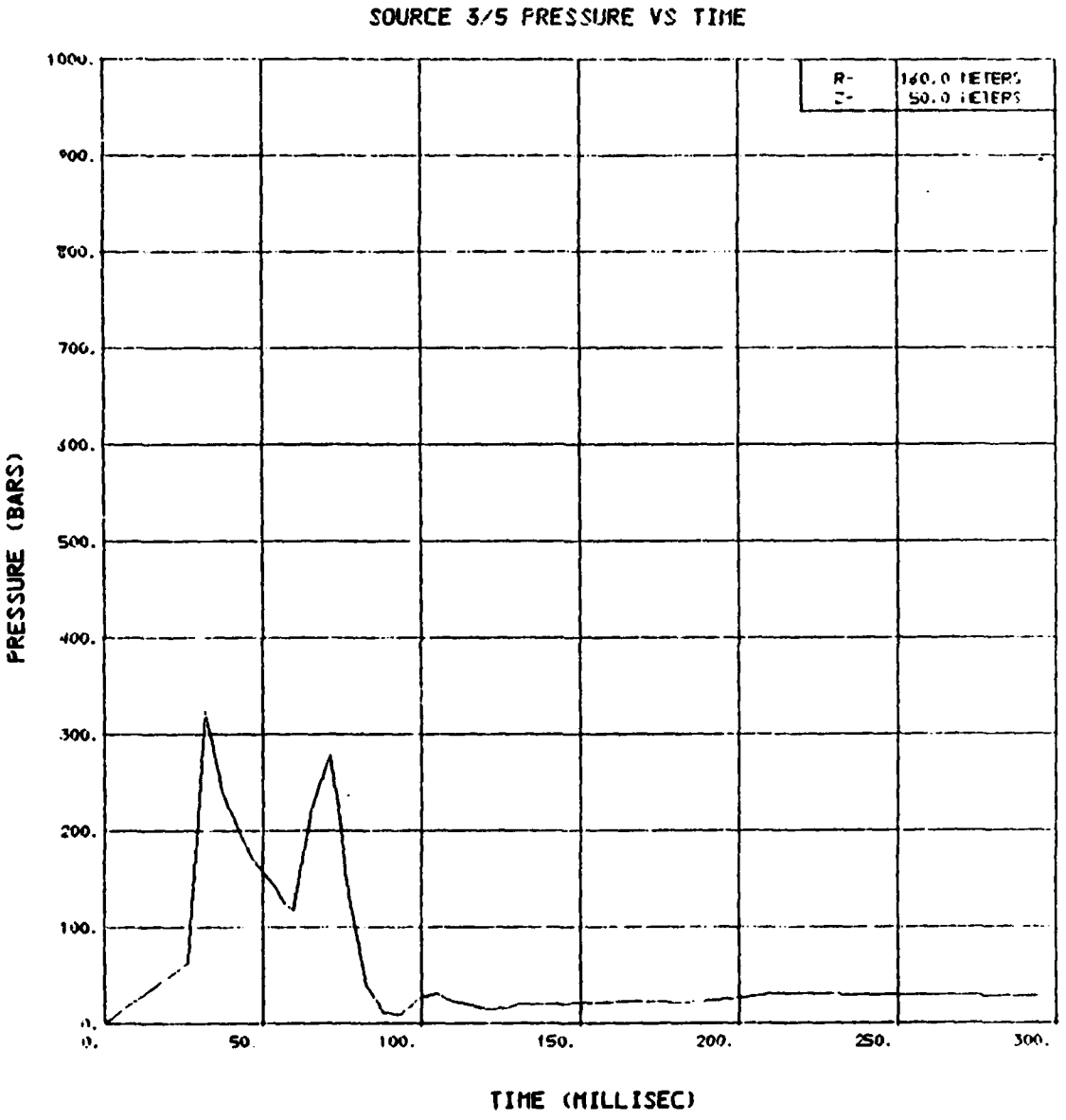
SOURCE 3/5 PRESSURE VS TIME
R- 160.0 METERS
Z- 50.0 METERS
PRESSURE (BARS)
1000.
900.
800.
700.
600.
500.
400.
300.
200.
100.
0.
0.
50.
100.
150.
200.
250.
300.
TIME (MILLISEC)

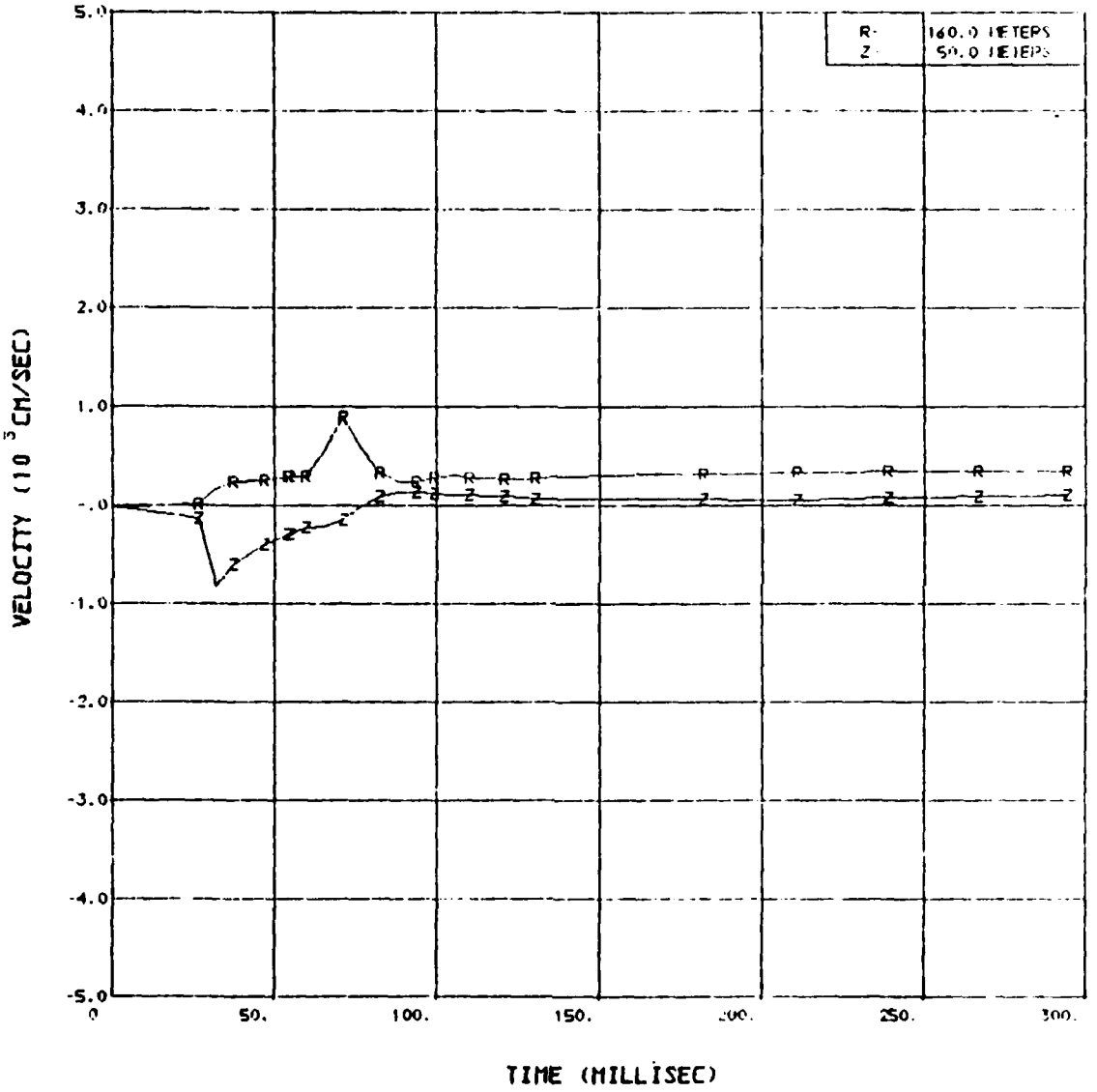
SOURCE 3/5 VELOCITY VS TIME
R
Z
160.0 METERS
50.0 METERS
VELOCITY (10 ^{3} CM/SEC)
5.0
4.0
3.0
2.0
1.0
-1.0
-2.0
-3.0
-4.0
-5.0
0
50.
100.
150.
200.
250.
300.
TIME (MILLISEC)

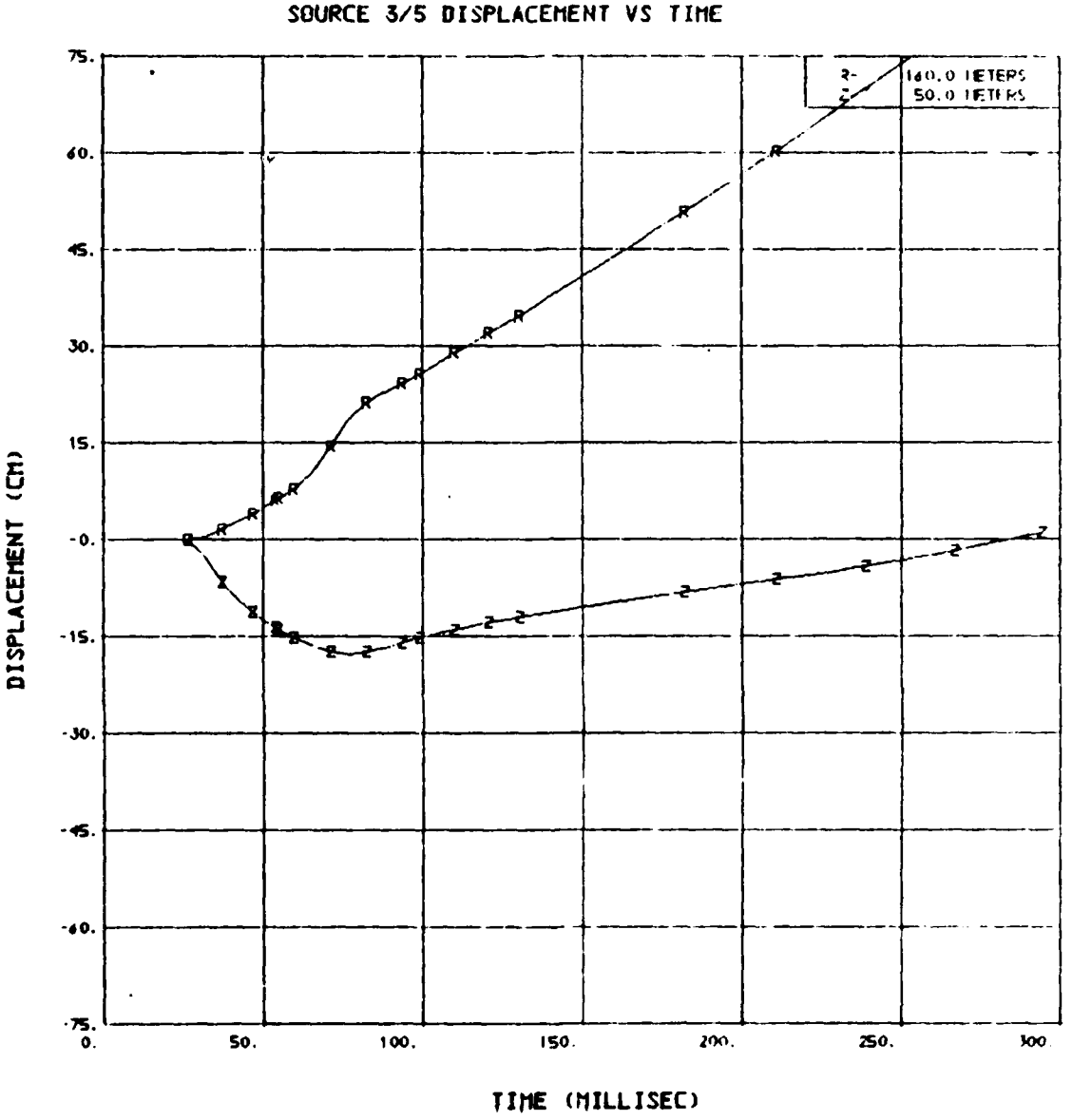
SOURCE 3/5 DISPLACEMENT VS TIME
DISPLACEMENT (CM)
TIME (MILLISEC)
75.
60.
45.
30.
15.
-0.
-15.
-30.
-45.
-60.
-75.
0.
50.
100.
150.
200.
250.
300.
R- 160.0 METERS
Z- 50.0 METERS

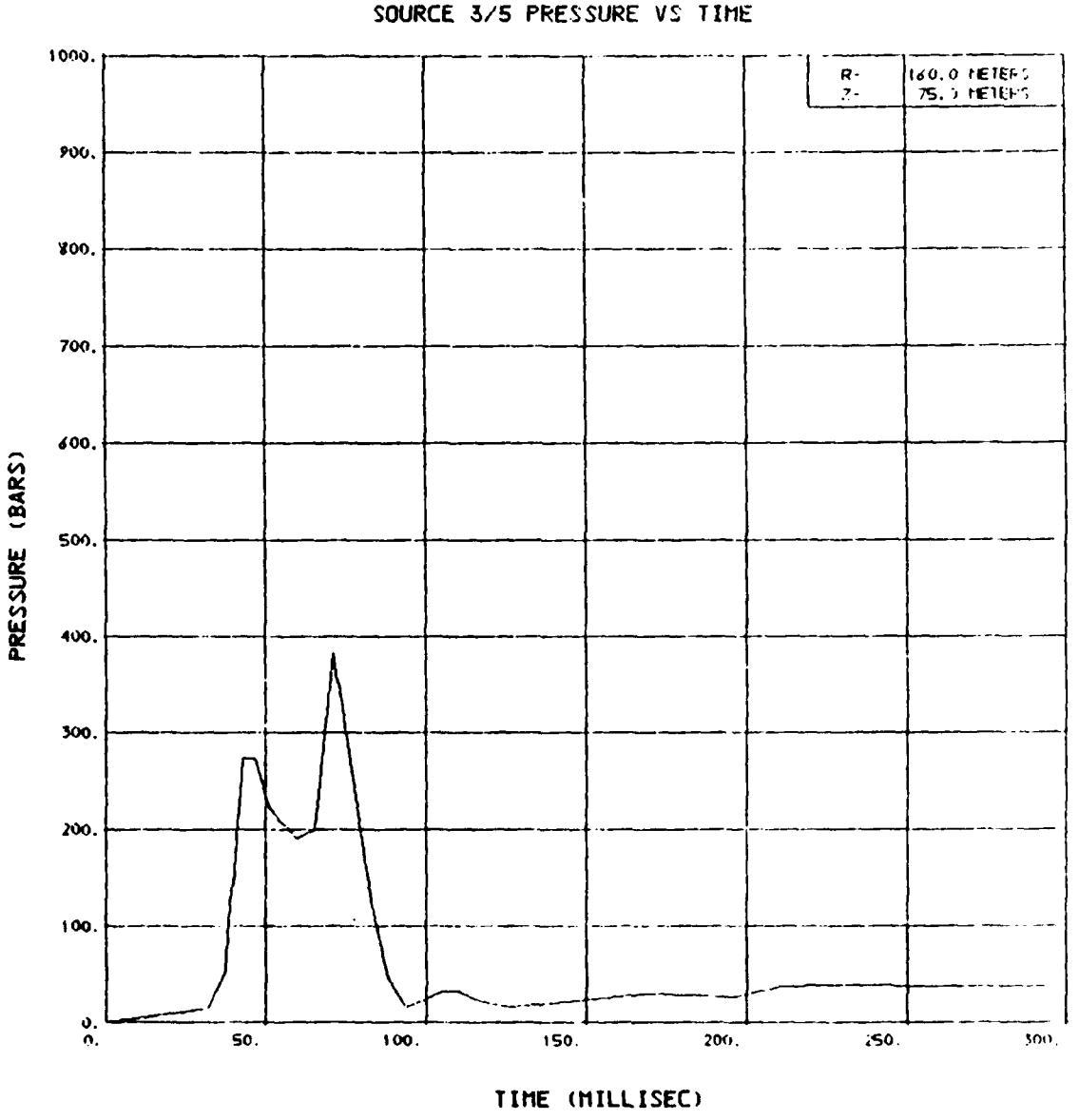
SOURCE 3/5 PRESSURE VS TIME
R-
160.0 METERS
75.0 METERS
PRESSURE (BARS)
1000.
900.
800.
700.
600.
500.
400.
300.
200.
100.
0.
0.
50.
100.
150.
200.
250.
300.
TIME (MILLISEC)

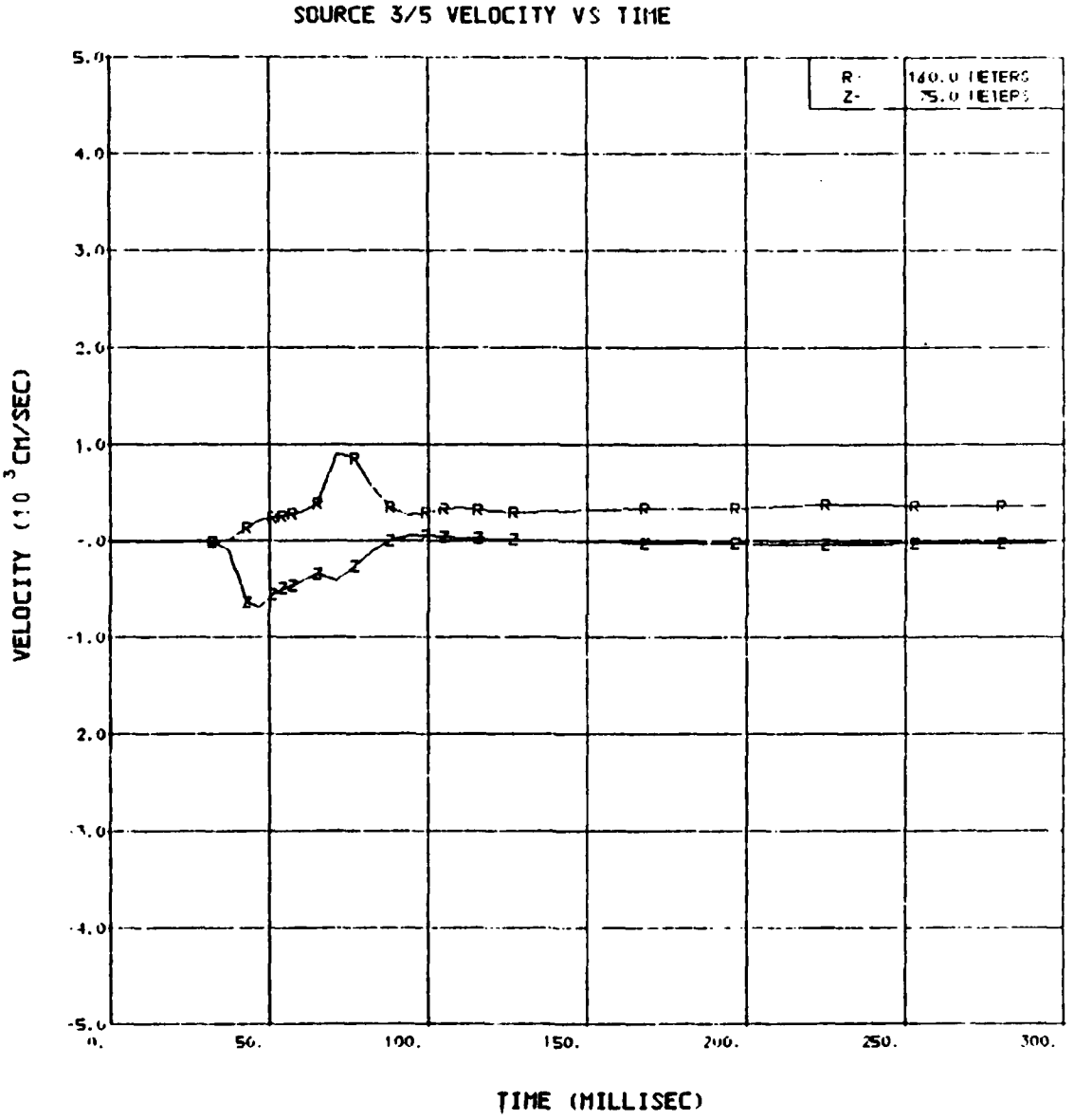
SOURCE 3/5 VELOCITY VS TIME
R-
Z-
160.0 METERS
75.0 METERS
VELOCITY (10 3 CM/SEC)
5.0
4.0
3.0
2.0
1.0
-.0
-1.0
2.0
-3.0
-4.0
-5.0
0.
50.
100.
150.
200.
250.
300.
TIME (MILLISEC)

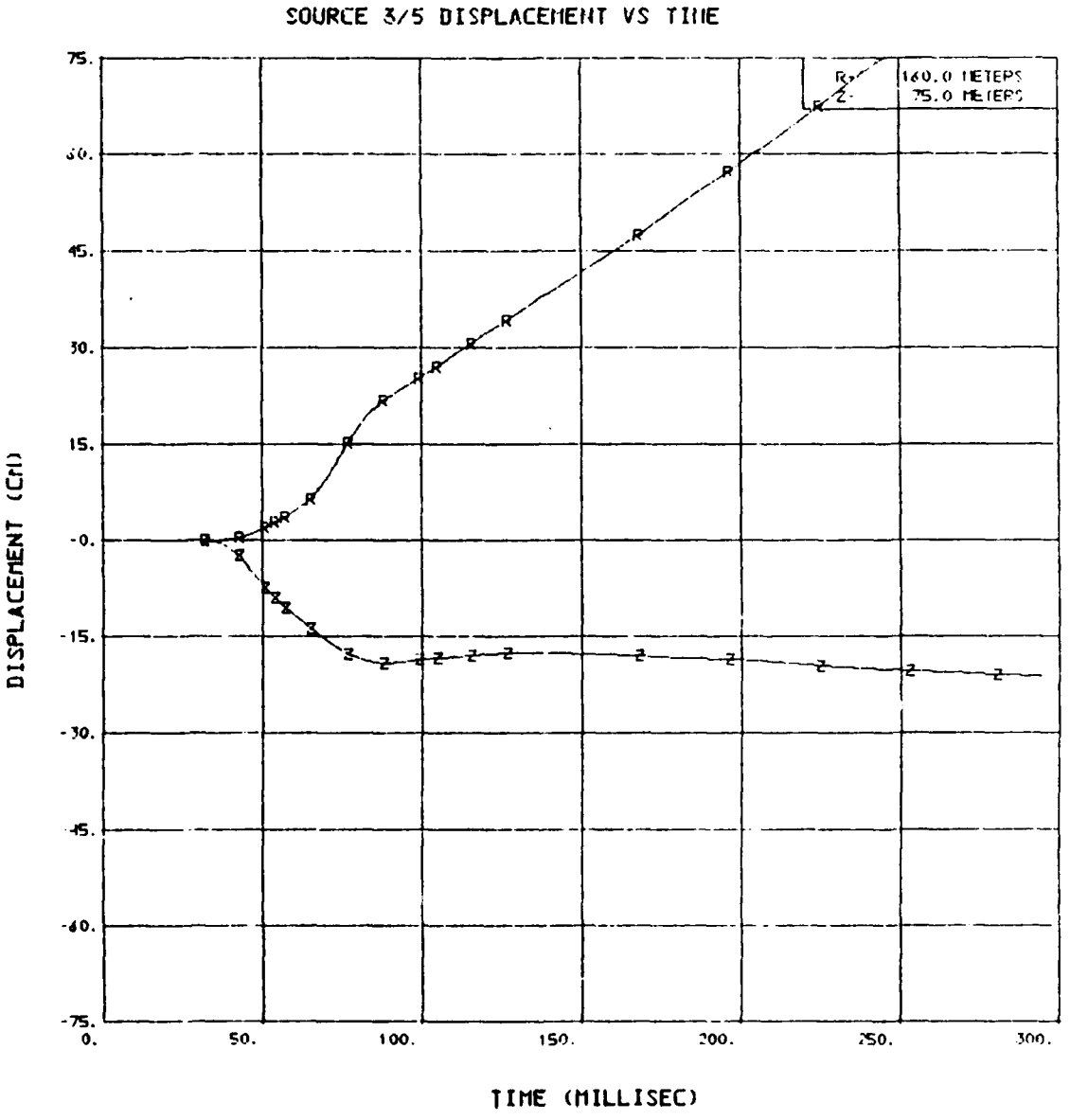
SOURCE 3/5 DISPLACEMENT VS TIME
160.0 METERS
75.0 METERS
R
Z
75.
60.
45.
30.
15.
-0.
-15.
-30.
-45.
-60.
-75.
0.
50.
100.
150.
200.
250.
300.
DISPLACEMENT (CM)
TIME (MILLISEC)

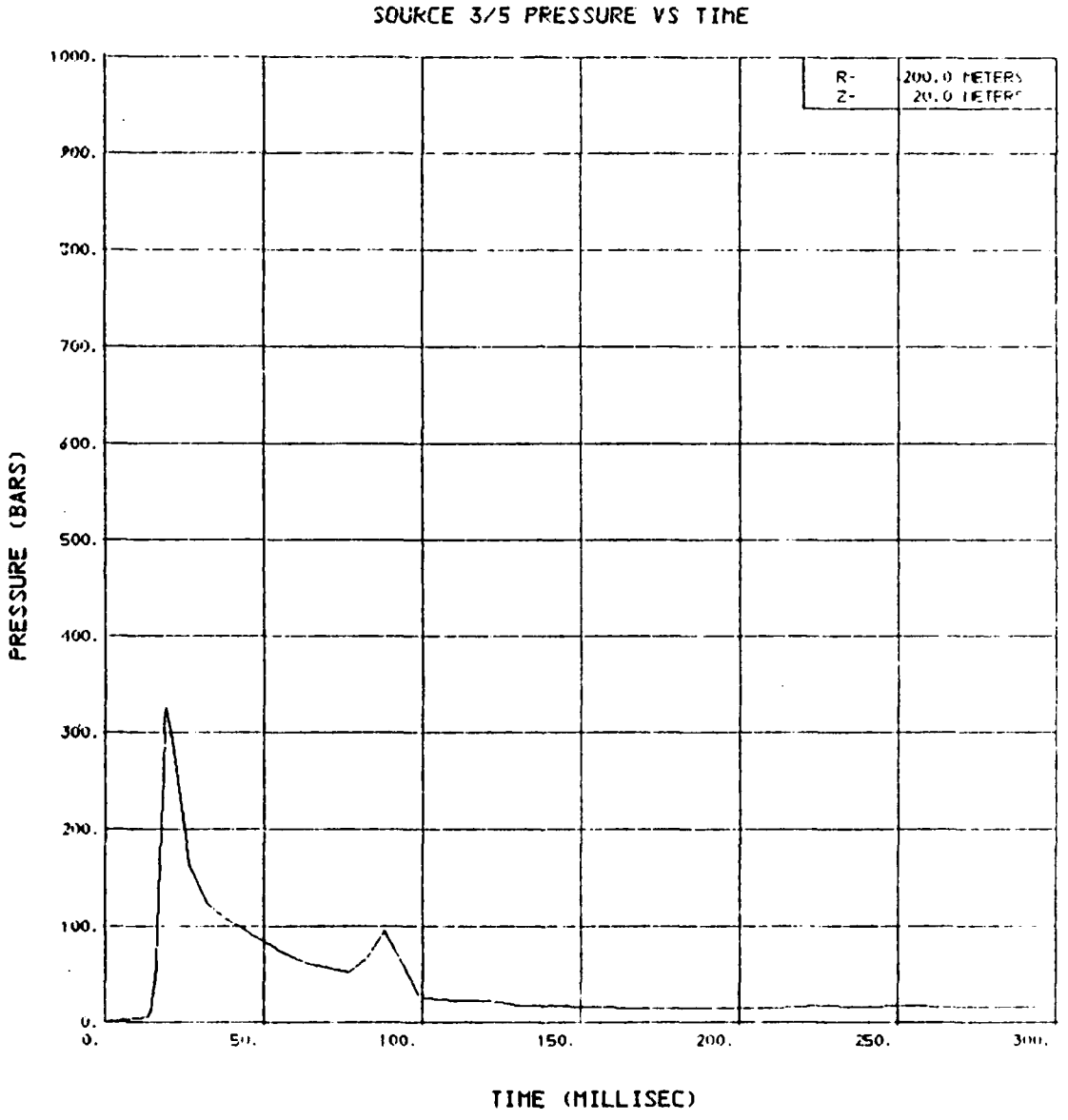
SOURCE 3/5 PRESSURE VS TIME
R- 200.0 METERS
Z- 20.0 METERS
PRESSURE (BARS)
1000.
900.
800.
700.
600.
500.
400.
300.
200.
100.
0.
0.
50.
100.
150.
200.
250.
300.
TIME (MILLISEC)

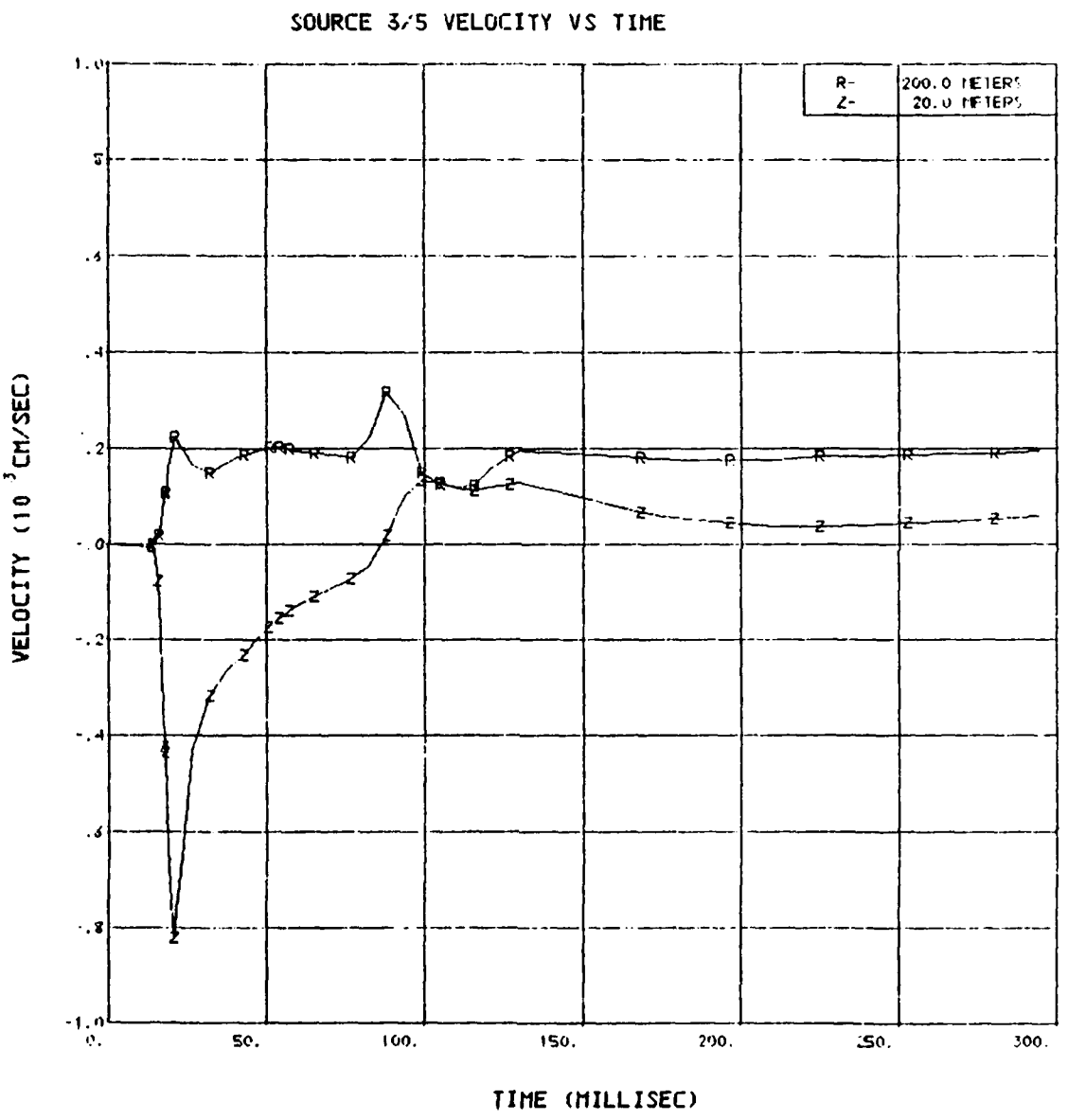
SOURCE 3/5 VELOCITY VS TIME
R-
Z-
200.0 METERS
20.0 METERS
VELOCITY (10 ^{3} CM/SEC)
1.0
.8
.6
.4
.2
.0
-.2
-.4
-.6
-.8
-1.0
0.
50.
100.
150.
200.
250.
300.
TIME (MILLISEC)

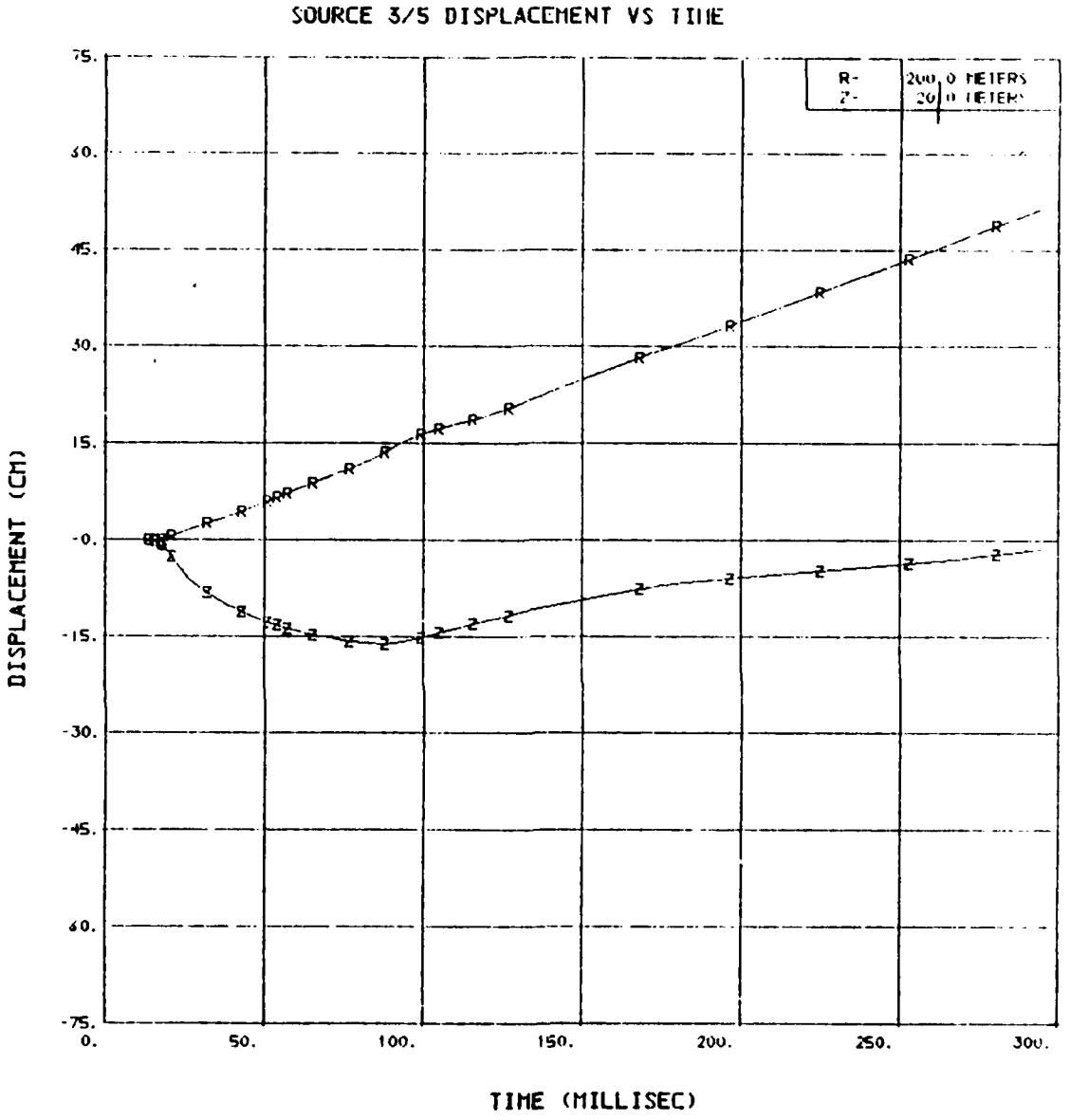
SOURCE 3/5 DISPLACEMENT VS TIME
R- 200.0 METERS
Z- 200.0 METERS
DISPLACEMENT (CM)
75.
60.
45.
30.
15.
-0.
-15.
-30.
-45.
-60.
-75.
0.
50.
100.
150.
200.
250.
300.
TIME (MILLISEC)

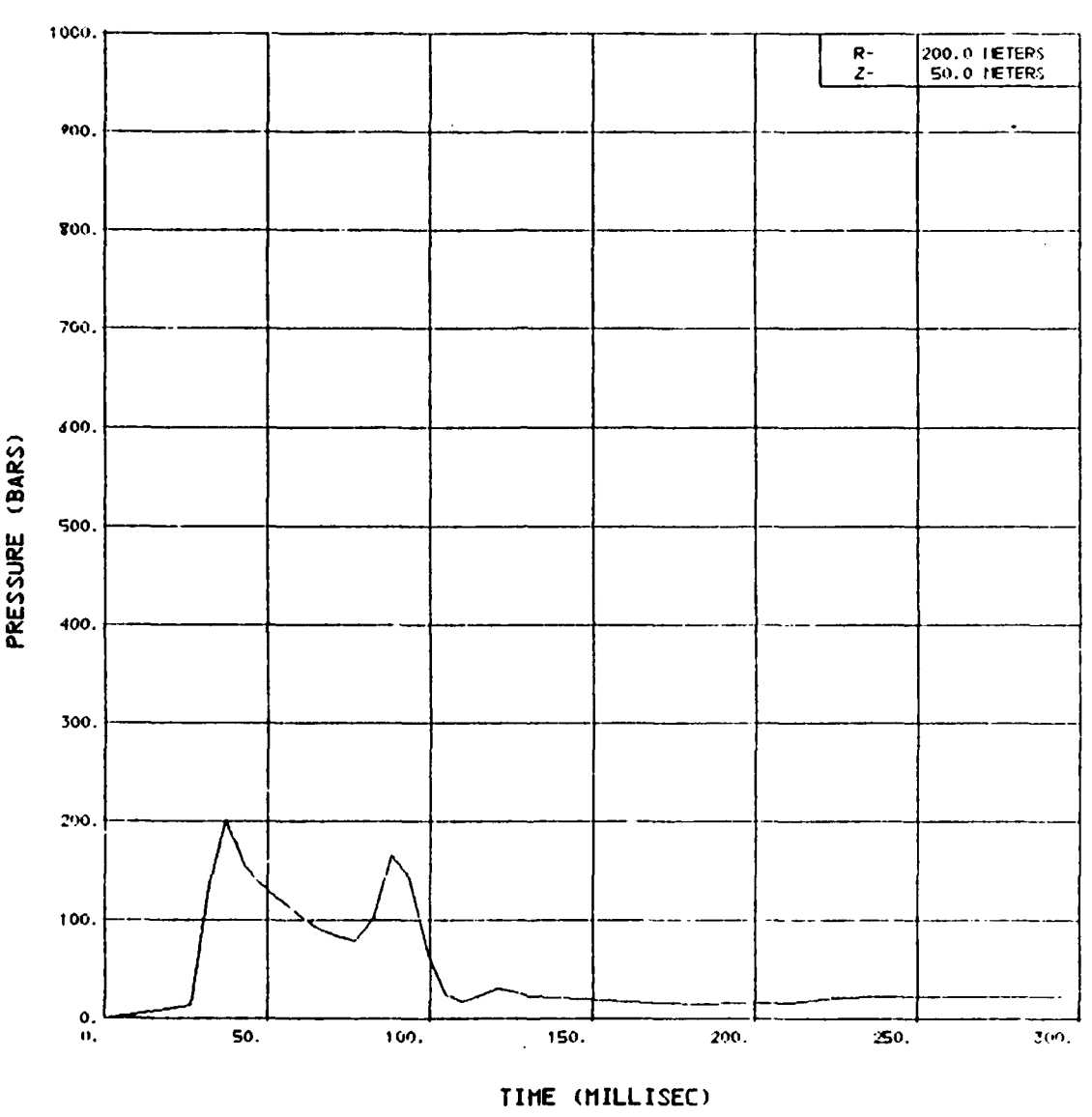
SOURCE 3/5 PRESSURE VS TIME
R- 200.0 METERS
Z- 50.0 METERS
PRESSURE (BARS)
1000.
900.
800.
700.
600.
500.
400.
300.
200.
100.
0.
0.
50.
100.
150.
200.
250.
300.
TIME (MILLISEC)

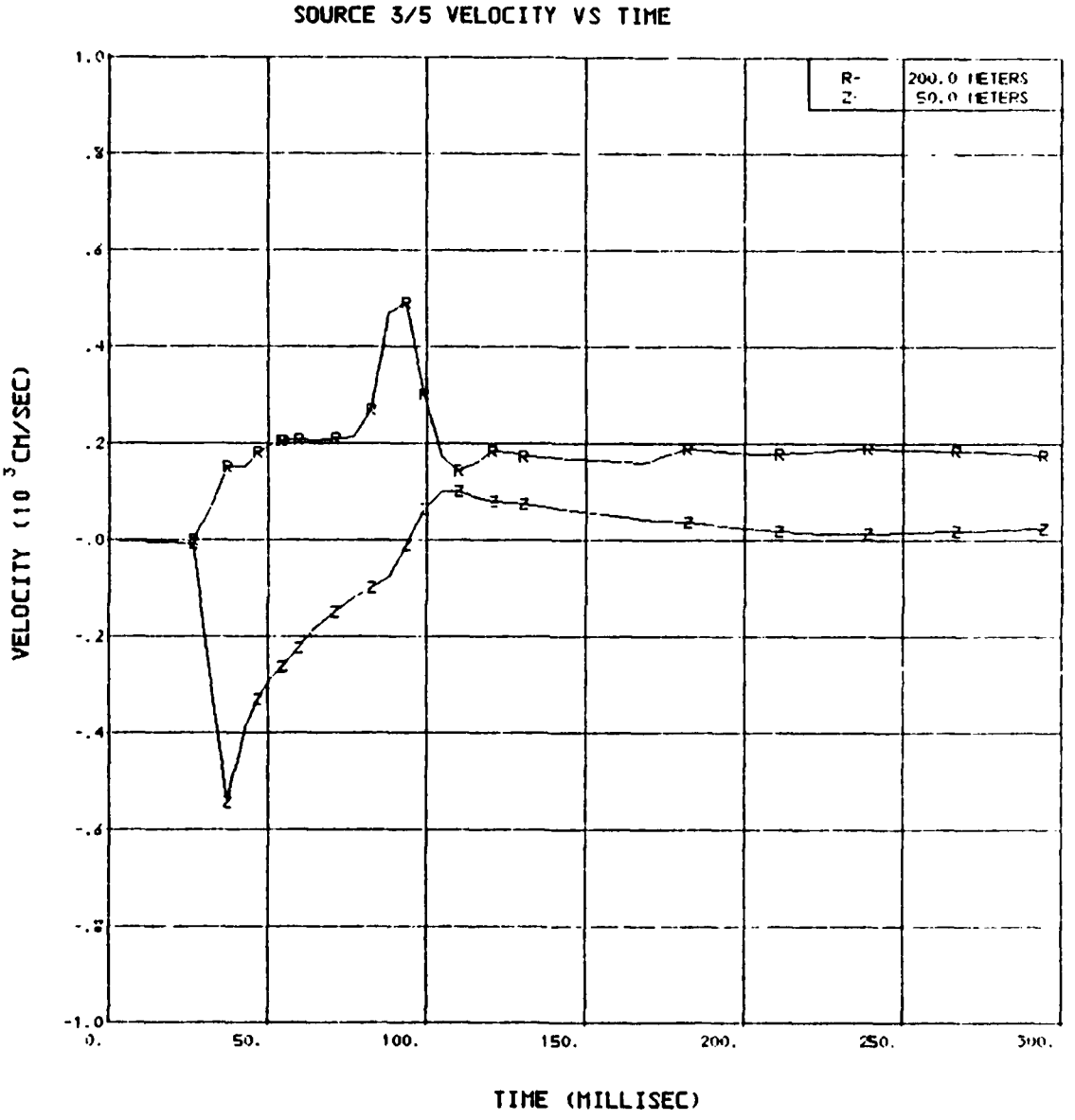
SOURCE 3/5 VELOCITY VS TIME
R- 200.0 METERS
Z- 50.0 METERS
VELOCITY (10 3 CM/SEC)
1.0
.8
.6
.4
.2
-.0
-.2
-.4
-.6
-.8
-1.0
0.
50.
100.
150.
200.
250.
300.
TIME (MILLISEC)

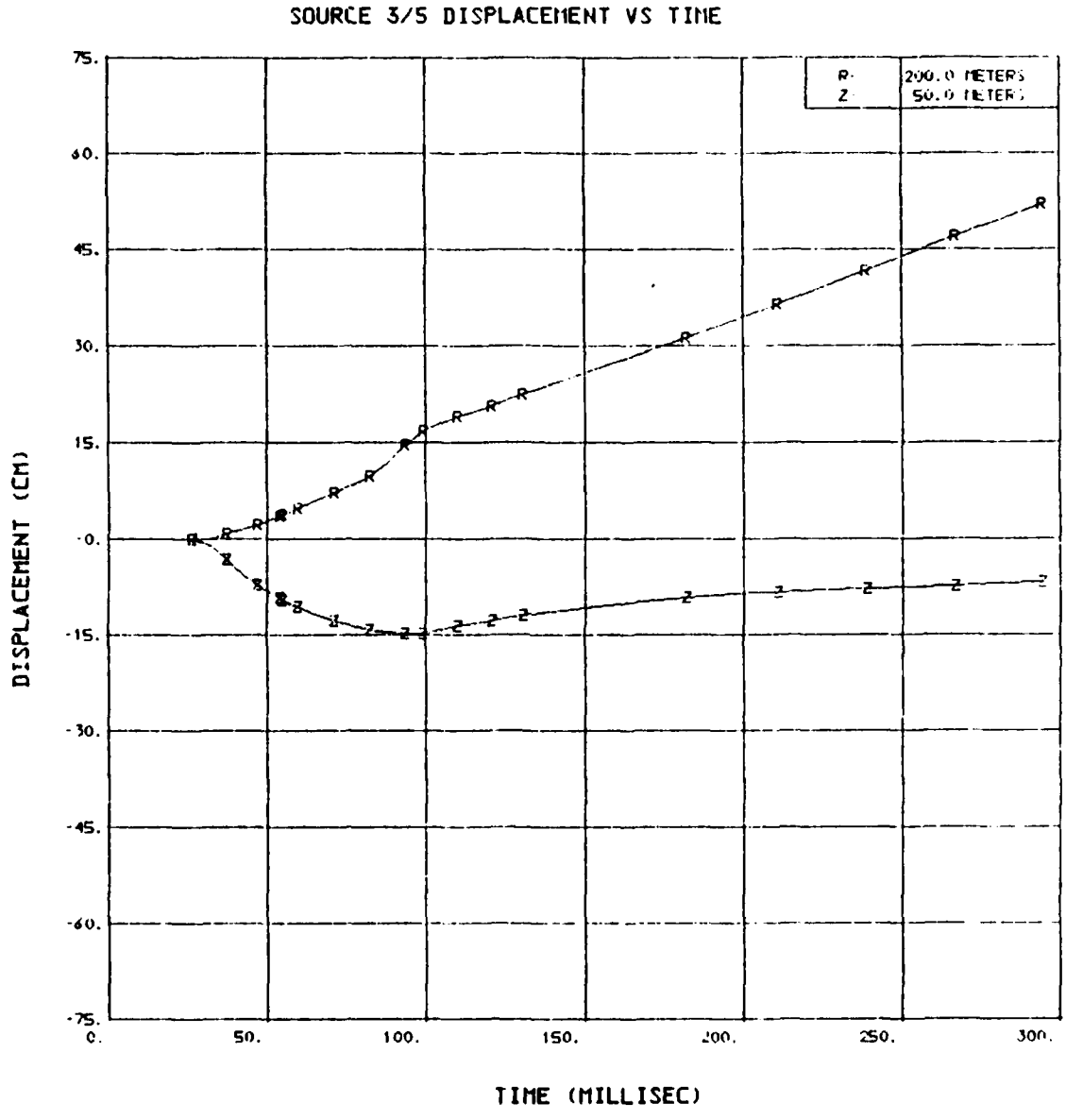
SOURCE 3/5 DISPLACEMENT VS TIME
R- 200.0 METERS
Z- 50.0 METERS
75.
60.
45.
30.
15.
0.
-15.
-30.
-45.
-60.
-75.
0.
50.
100.
150.
200.
250.
300.
DISPLACEMENT (CM)
TIME (MILLISEC)

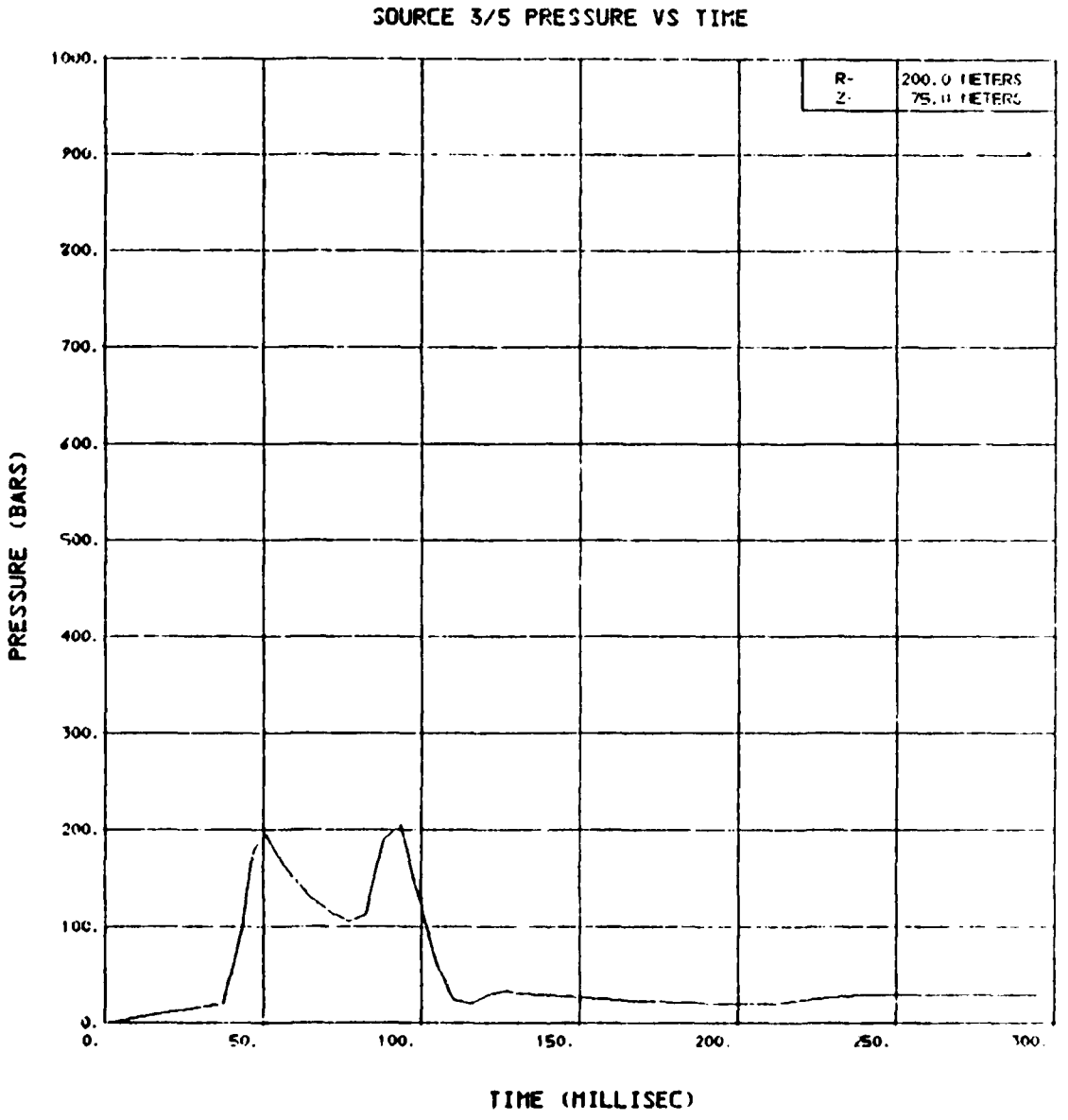
SOURCE 3/5 PRESSURE VS TIME
R-
Z-
200.0 METERS
75.0 METERS
1000.
900.
800.
700.
600.
500.
400.
300.
200.
100.
0.
0.
50.
100.
150.
200.
250.
300.
PRESSURE (BARS)
TIME (MILLISEC)

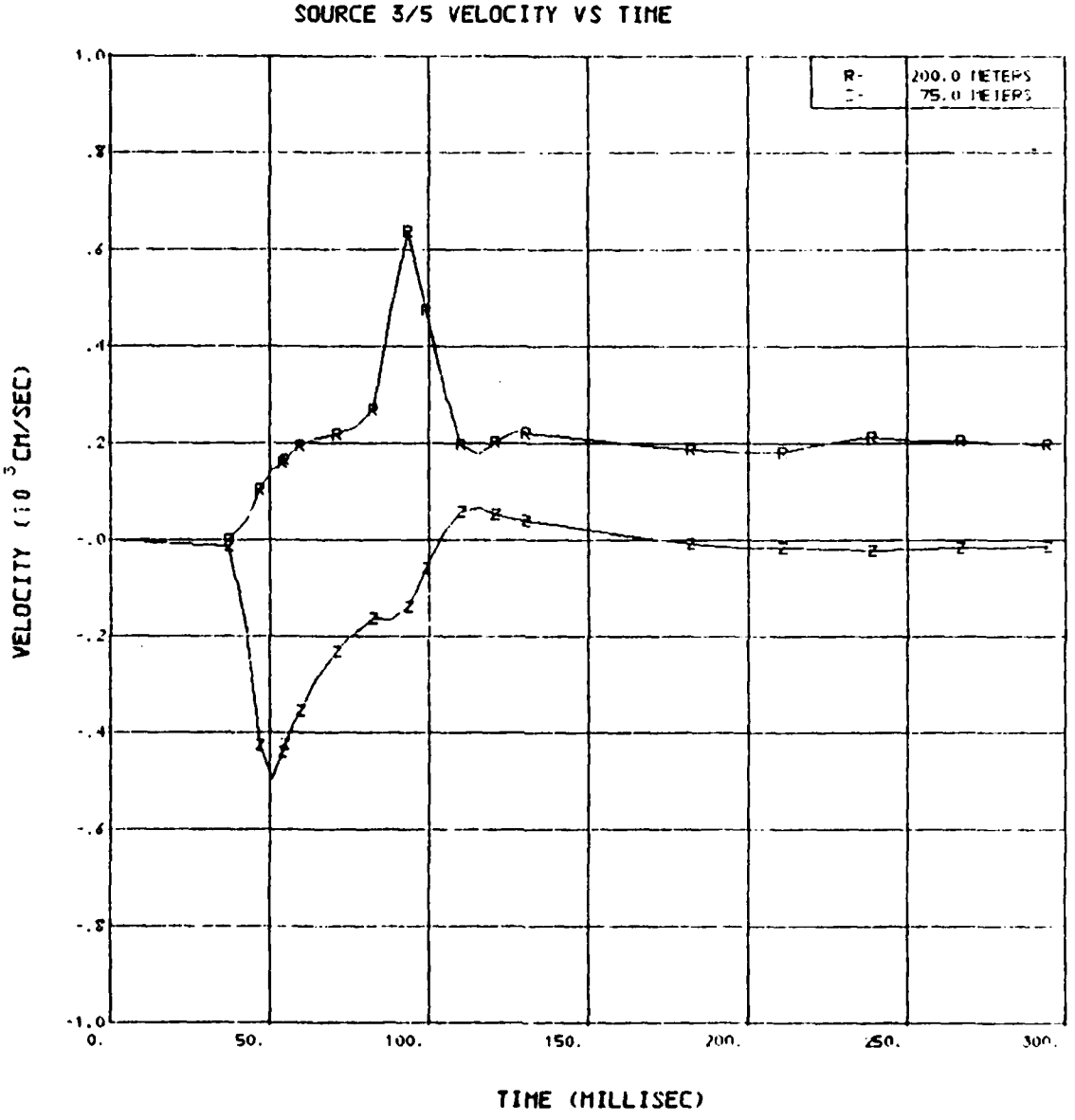
SOURCE 3/5 VELOCITY VS TIME
R- 200.0 METERS
Z- 75.0 METERS
VELOCITY (10 -3 CM/SEC)
1.0
.8
.6
.4
.2
-.0
-.2
-.4
-.6
-.8
-1.0
0.
50.
100.
150.
200.
250.
300.
TIME (MILLISEC)

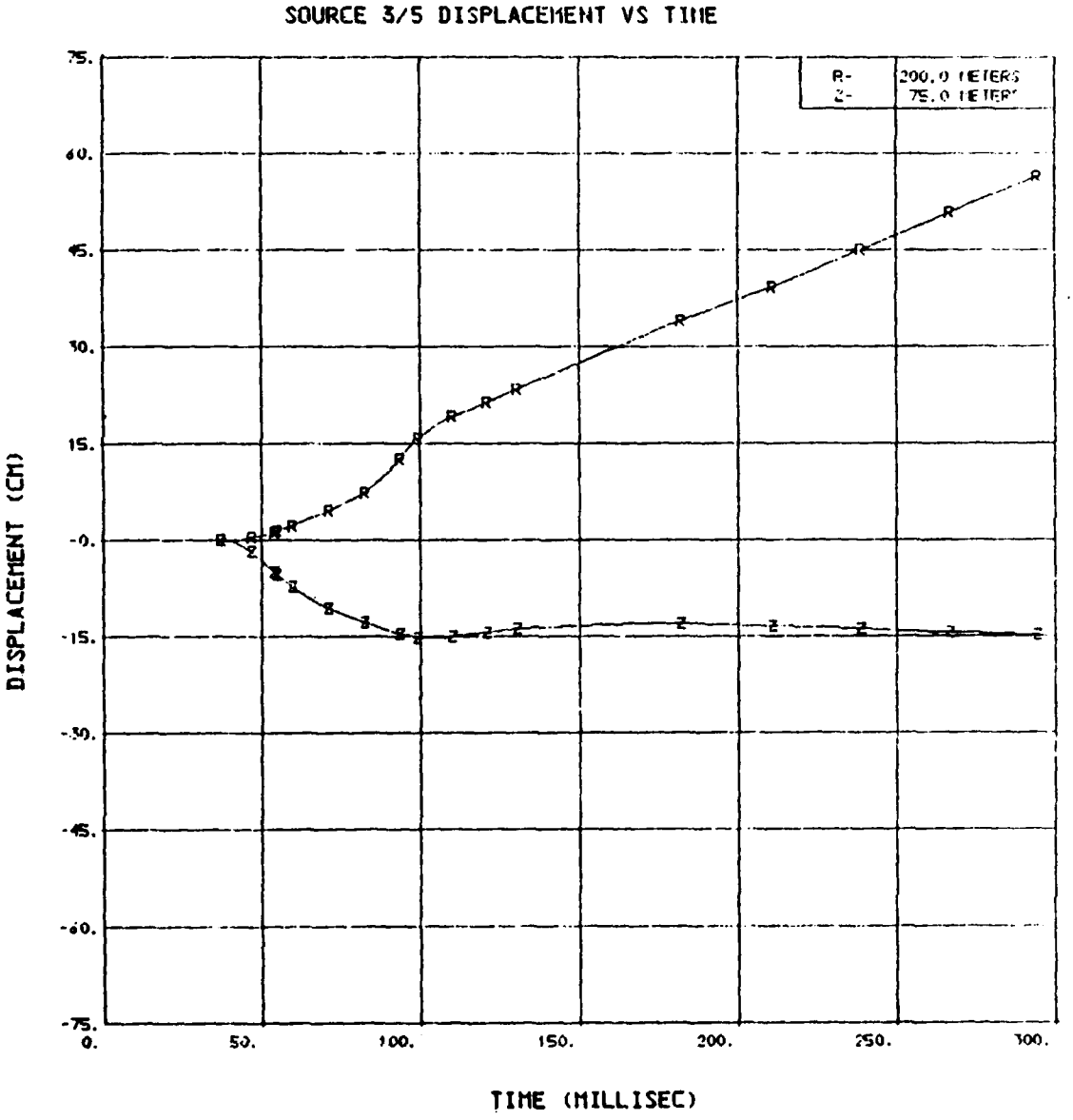
SOURCE 3/5 DISPLACEMENT VS TIME
R- 200.0 METERS
Z- 75.0 METERS
DISPLACEMENT (CM)
75.
60.
45.
30.
15.
-0.
-15.
-30.
-45.
-60.
-75.
0.
50.
100.
150.
200.
250.
300.
TIME (MILLISEC)

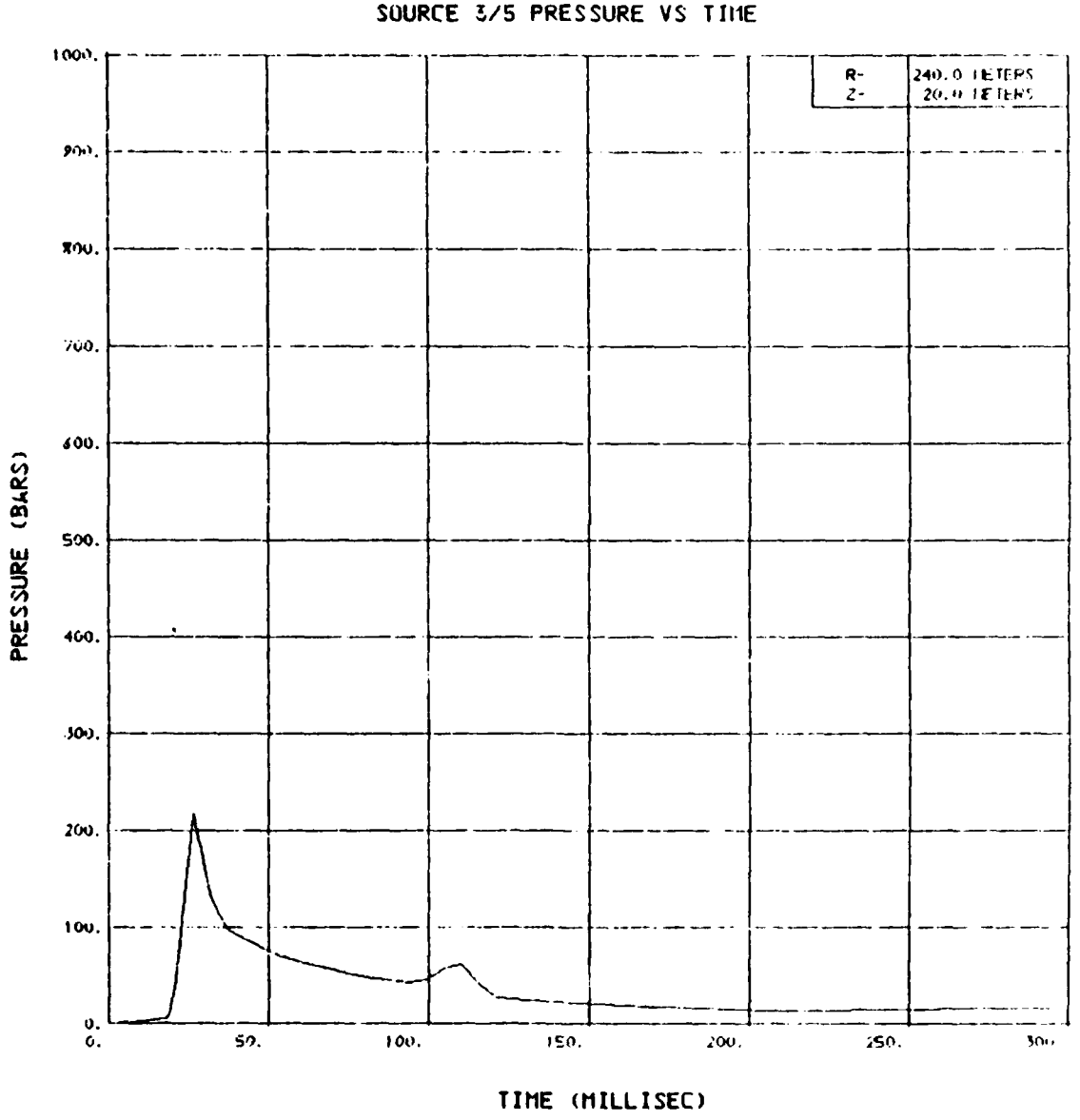
SOURCE 3/5 PRESSURE VS TIME
R- 240.0 METERS
Z- 20.0 METERS
1000.
900.
800.
700.
600.
500.
400.
300.
200.
100.
0.
0.
50.
100.
150.
200.
250.
300.
PRESSURE (BARS)
TIME (MILLISEC)

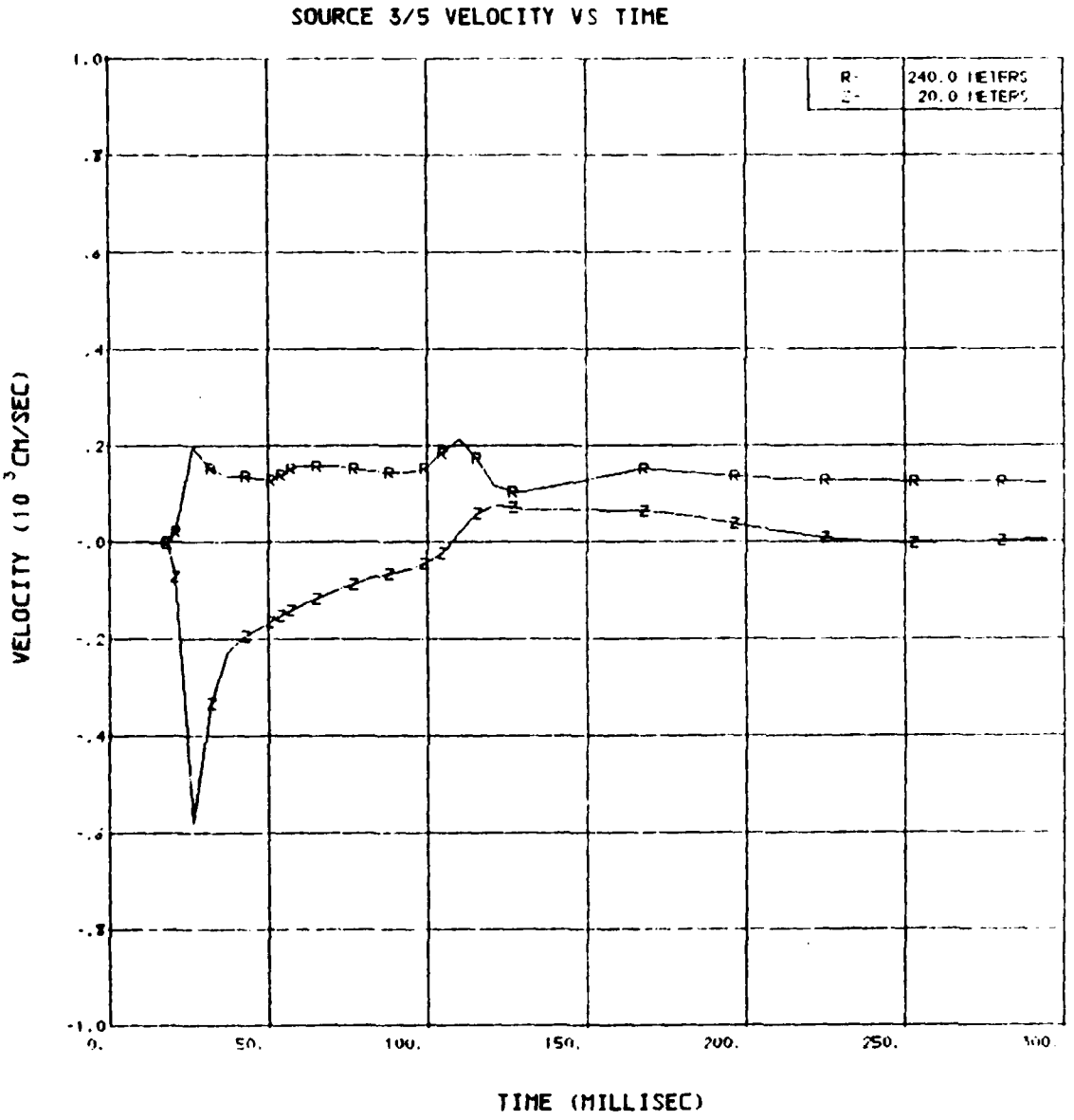
SOURCE 3/5 VELOCITY VS TIME
R- 240.0 METERS
Z- 20.0 METERS
VELOCITY (10 3 CM/SEC)
1.0
.8
.6
.4
.2
.0
-.2
-.4
-.6
-.8
-1.0
0.
50.
100.
150.
200.
250.
300.
TIME (MILLISEC)

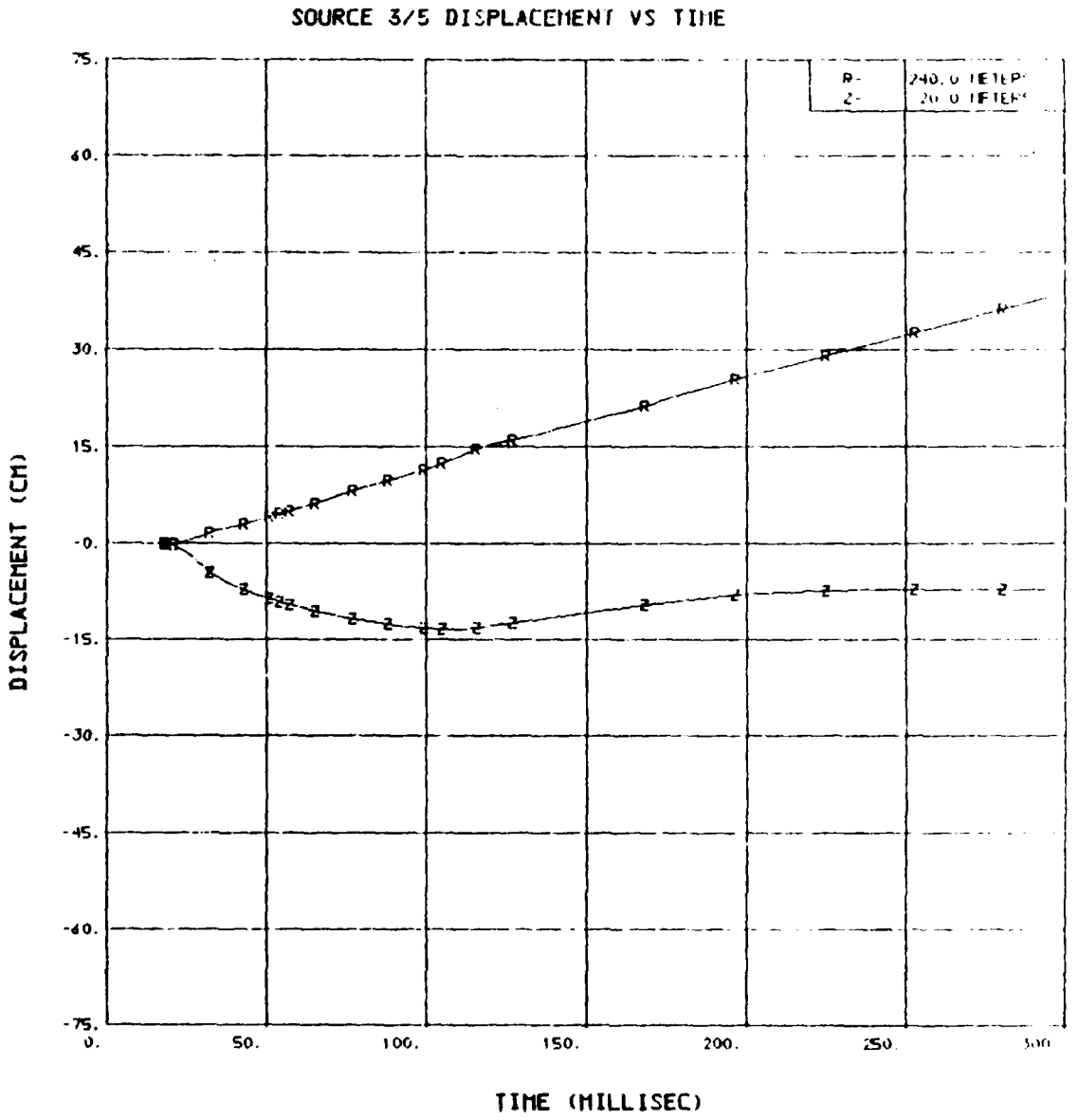
SOURCE 3/5 DISPLACEMENT VS TIME
R-
Z-
75.
60.
45.
30.
15.
-0.
-15.
-30.
-45.
-60.
-75.
0.
50.
100.
150.
200.
250.
DISPLACEMENT (CM)
TIME (MILLISEC)

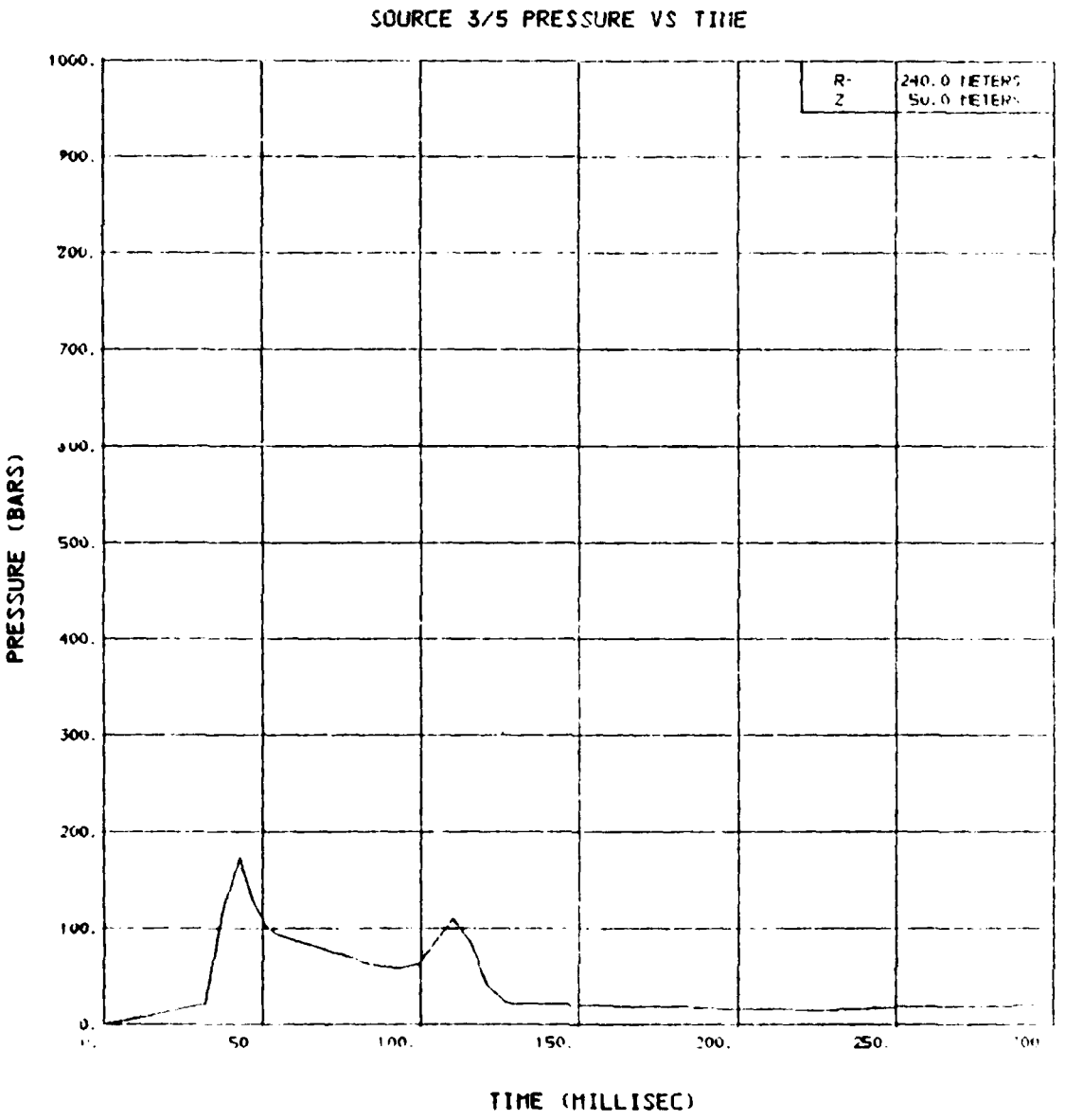
SOURCE 3/5 PRESSURE VS TIME
R-
Z
240.0 METERS
50.0 METERS
1000.
900.
200.
700.
500.
400.
300.
200.
100.
0.
50
100.
150.
200.
250.
PRESSURE (BARS)
TIME (MILLISEC)

SOURCE 3/5 VELOCITY VS TIME

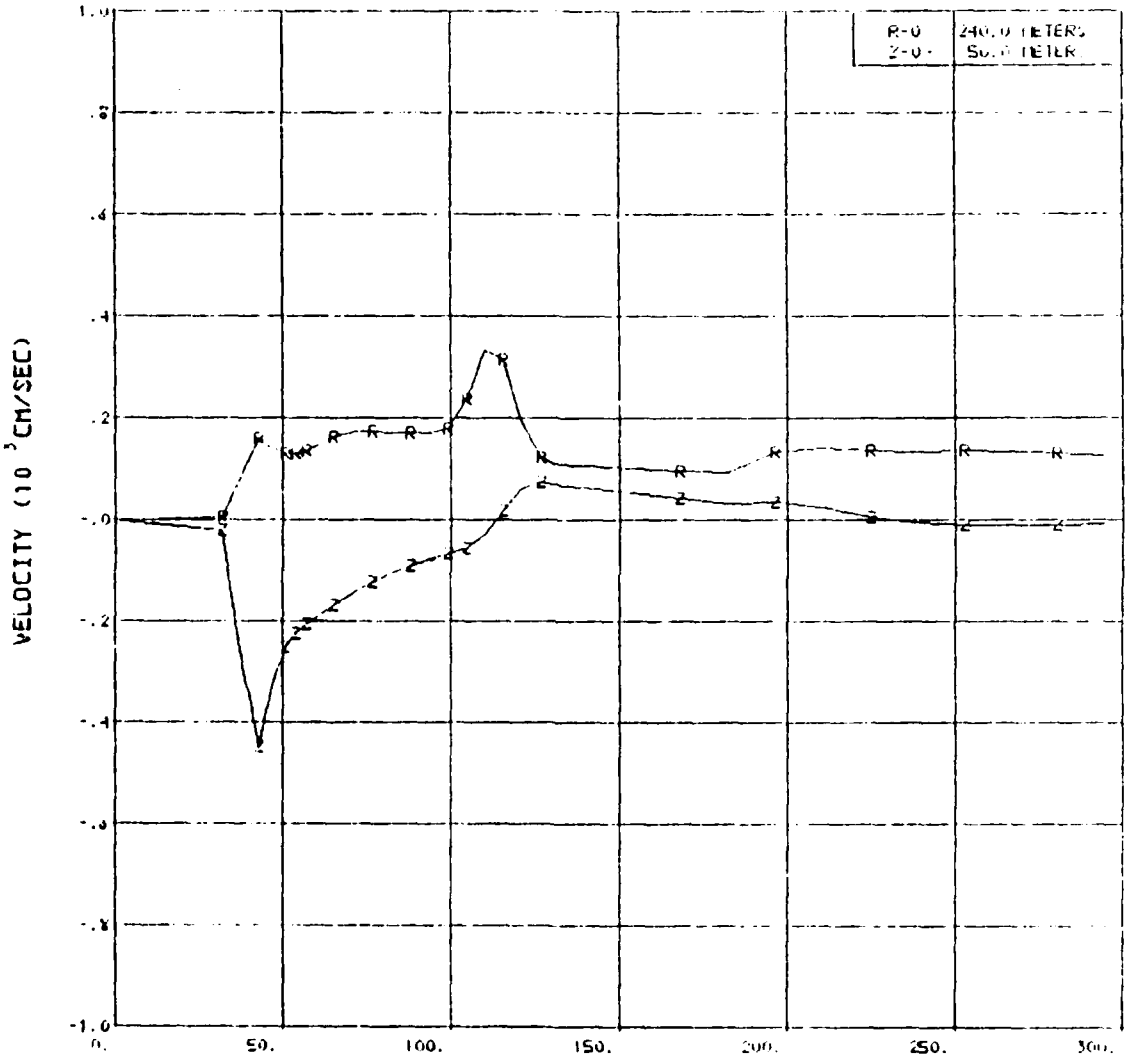

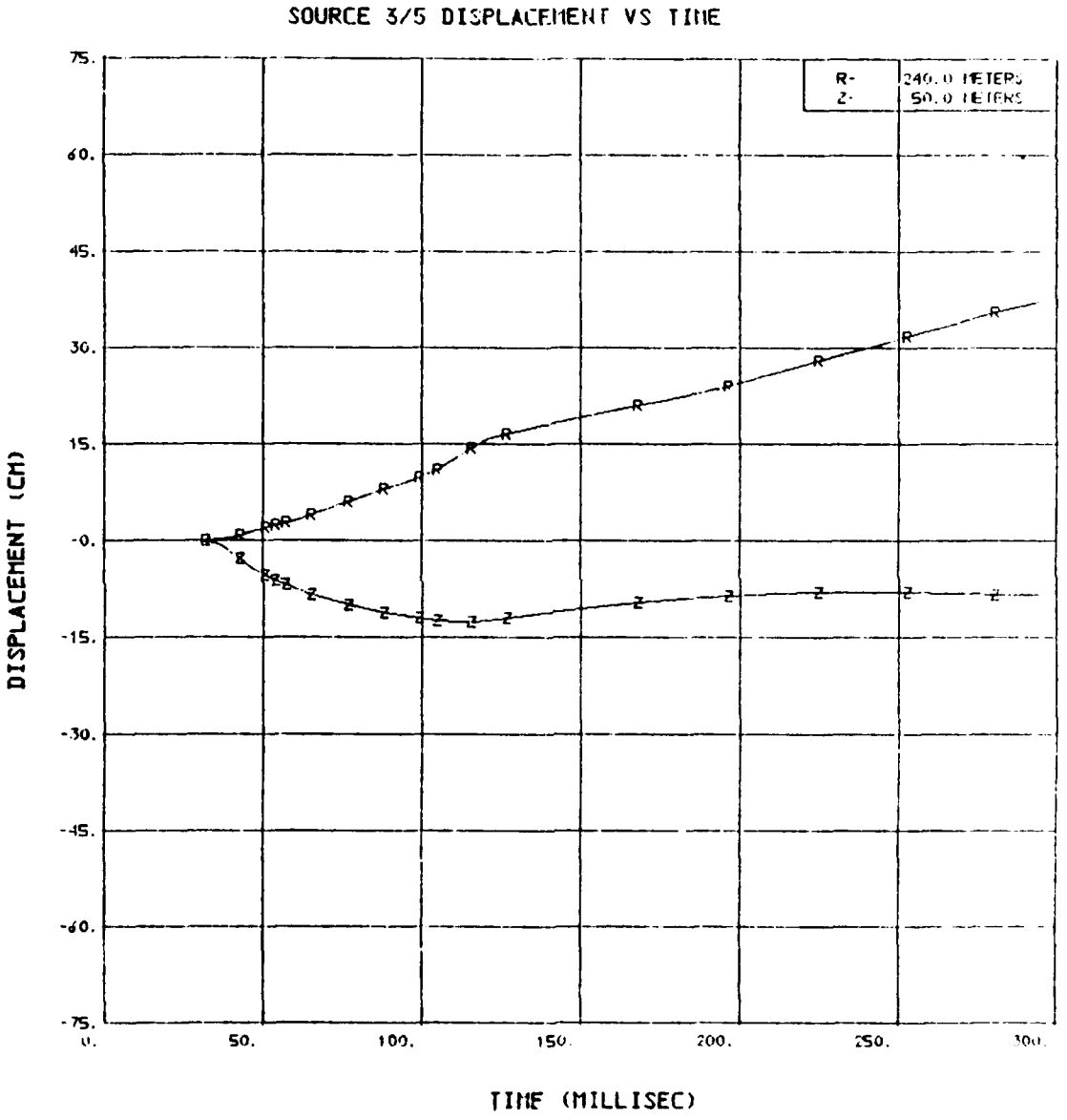
SOURCE 3/5 DISPLACEMENT VS TIME
R- 240.0 METERS
Z- 50.0 METERS
DISPLACEMENT (CM)
75.
60.
45.
30.
15.
-0.
-15.
-30.
-45.
-60.
-75.
0.
50.
100.
150.
200.
250.
300.
TIME (MILLISEC)

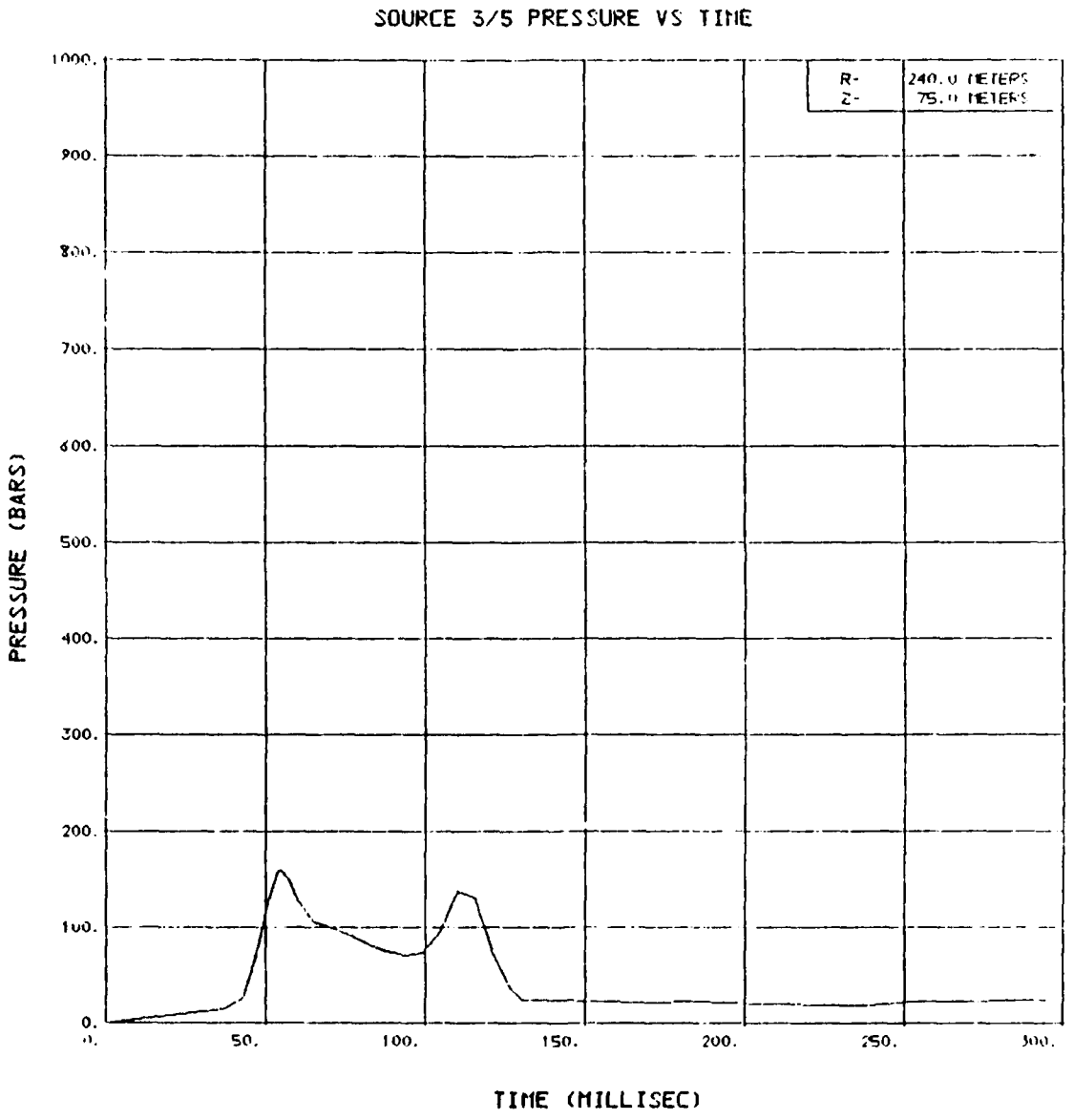
SOURCE 3/5 PRESSURE VS TIME
R- 240.0 METERS
Z- 75.0 METERS
1000.
900.
800.
700.
600.
500.
400.
300.
200.
100.
0.
PRESSURE (BARS)
0.
50.
100.
150.
200.
250.
300.
TIME (MILLISEC)

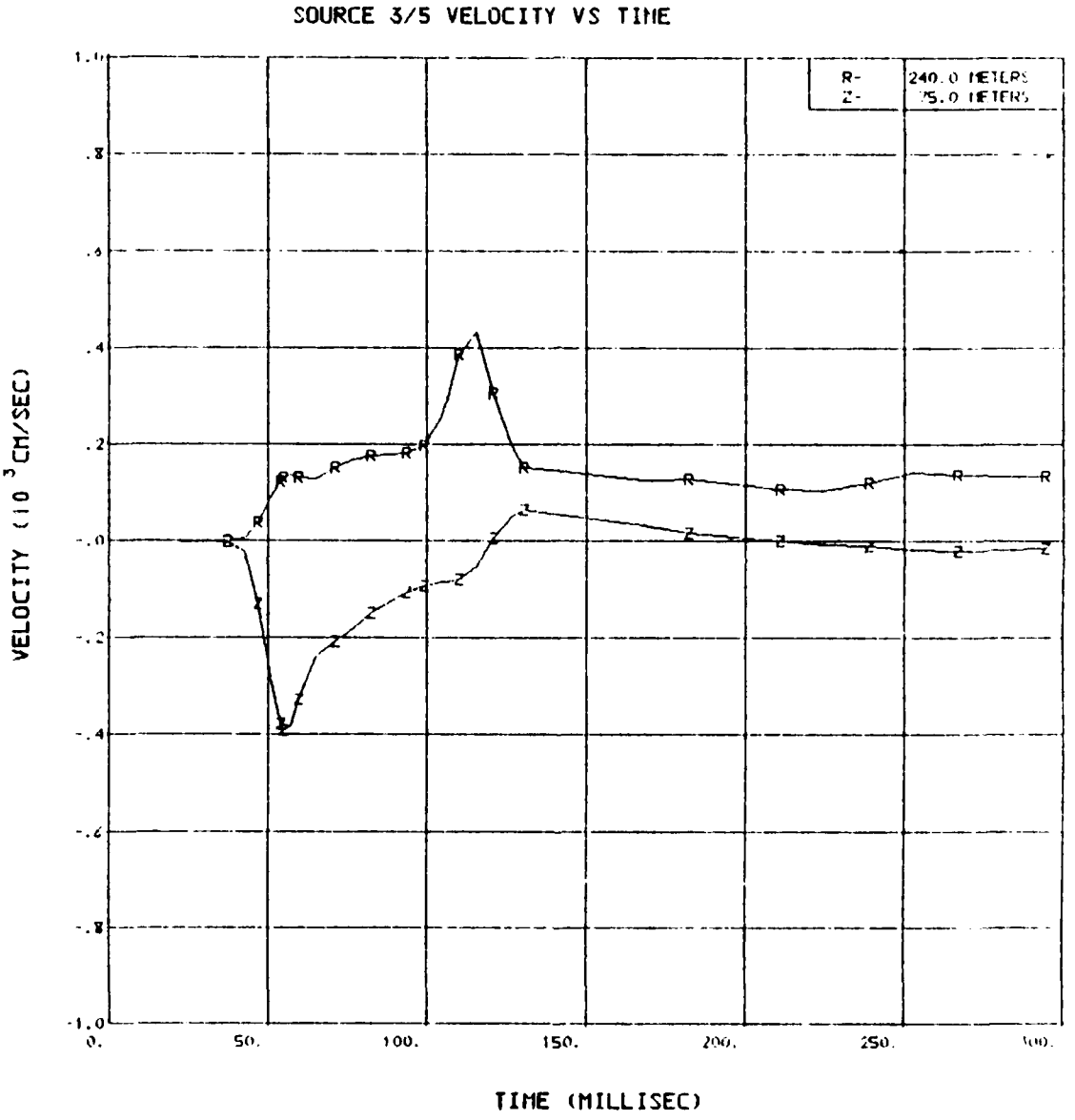
SOURCE 3/5 VELOCITY VS TIME
R- 240.0 METERS
Z- 75.0 METERS
VELOCITY (10 3 CM/SEC)
1.0
.8
.6
.4
.2
.0
-.2
-.4
-.6
-.8
-1.0
0.
50.
100.
150.
200.
250.
300.
TIME (MILLISEC)

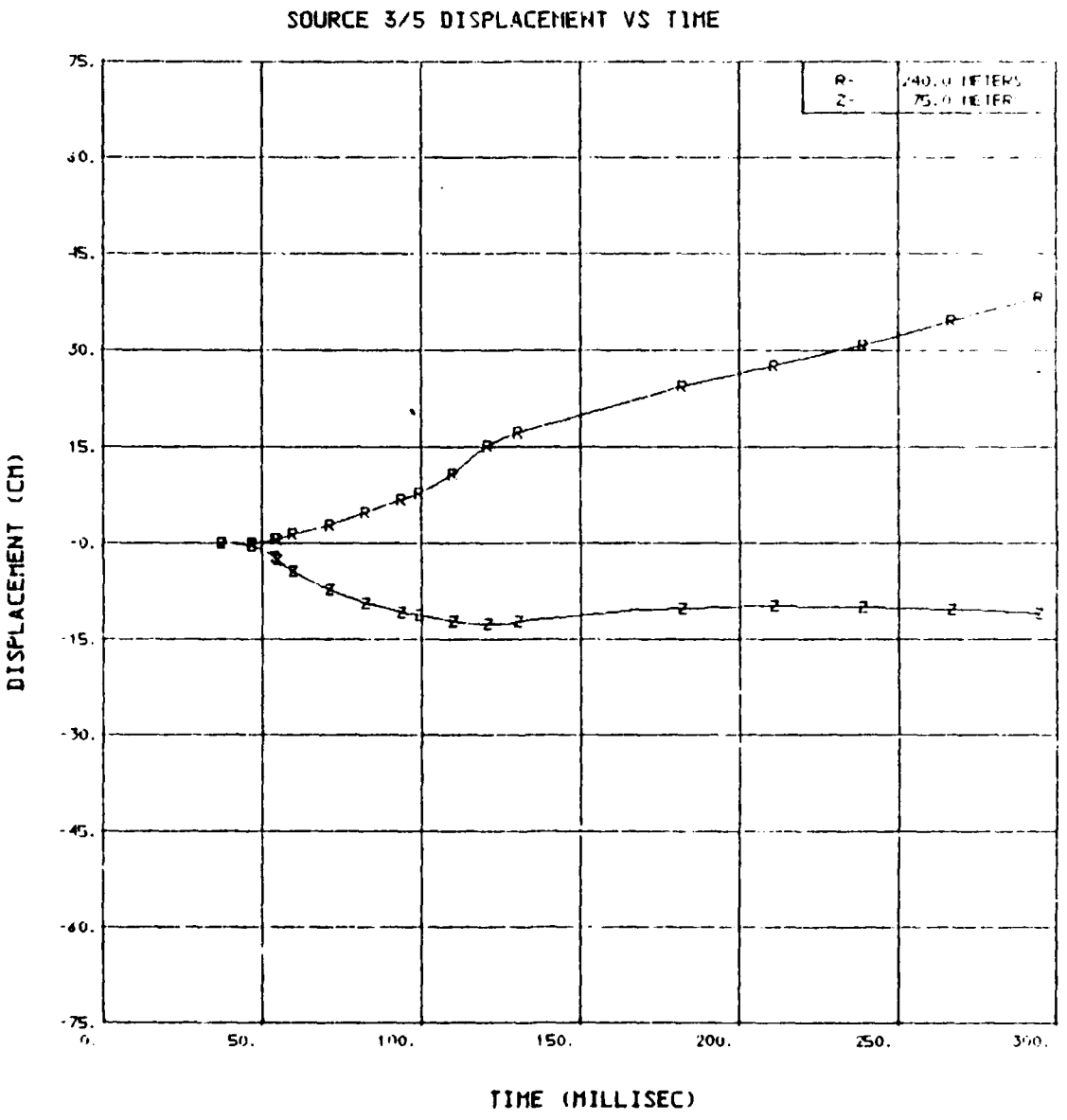
SOURCE 3/5 DISPLACEMENT VS TIME
R-
Z-
75.
60.
45.
30.
15.
-0.
-15.
-30.
-45.
-60.
-75.
0.
50.
100.
150.
200.
250.
300.
DISPLACEMENT (CM)
TIME (MILLISEC)

APPENDIX B

ELASTIC GROUND MOTIONS

Appendix B contains plots of calculated ground motions at 20 stations on cylindrical monitoring surfaces in the linear elastic SAGE code. These plots are a representative sampling of the elastic ground motion data which includes 269 stations on the monitoring surfaces in SAGE as well as 98 stations outside of the elastic radius in CRAM. The data at each station consist of horizontal (X) and vertical (Y) components of displacement and velocity, horizontal and vertical components of normal stress and shear stress. Normal stresses are relative to a hydrostatic overburden pressure, a negative stress indicating compression. The positive Y direction on these plots is down into the ground.

STATION I= 72 J= 7
X= 7.116+002 Y= 6.331+001 (METERS)

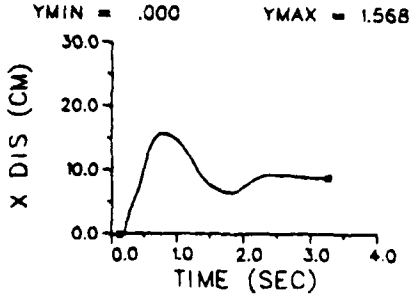

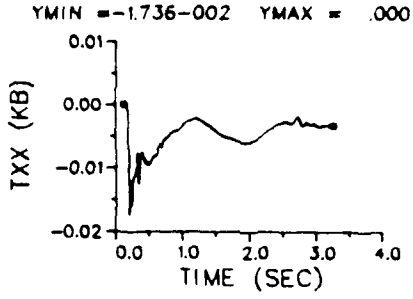

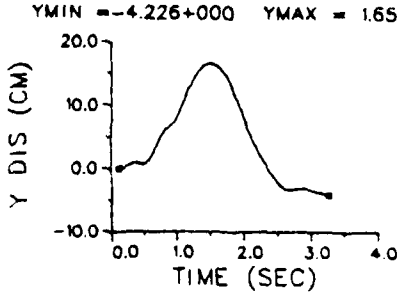

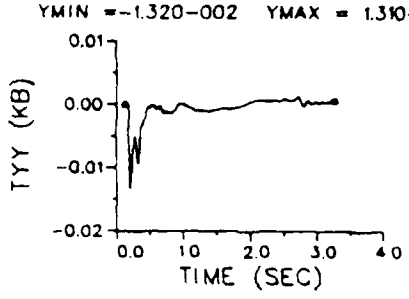

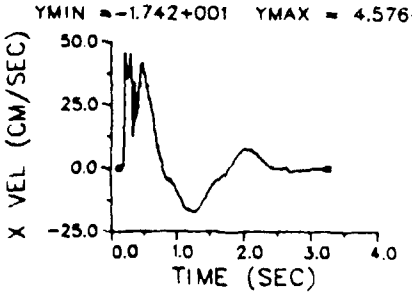

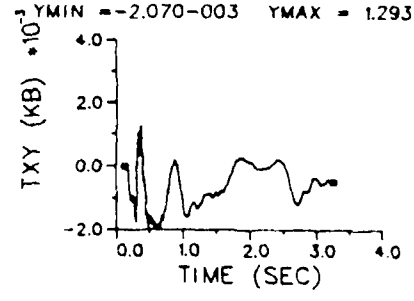

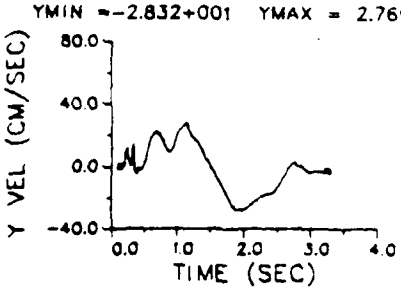

STATION I= 84 J= 7
X= 8.147+002 Y= 6.331+001 (METERS)

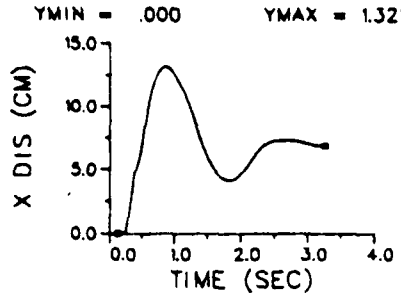

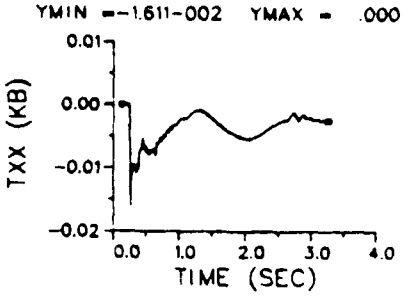

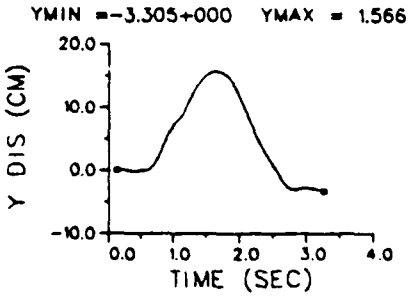

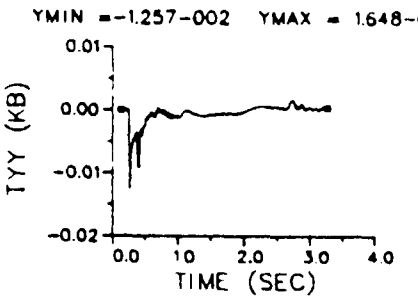

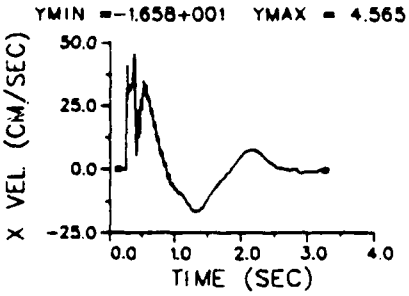

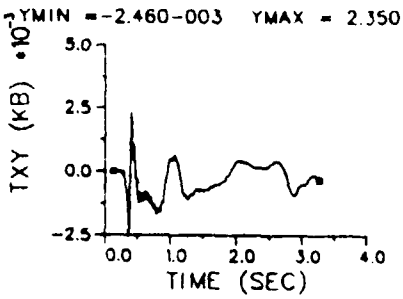

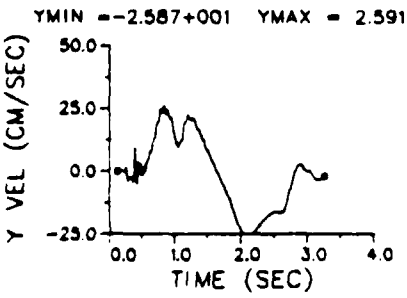

STATION I= 72 J= 12
X= 7.116+002 Y= 1.160+002 (METERS)

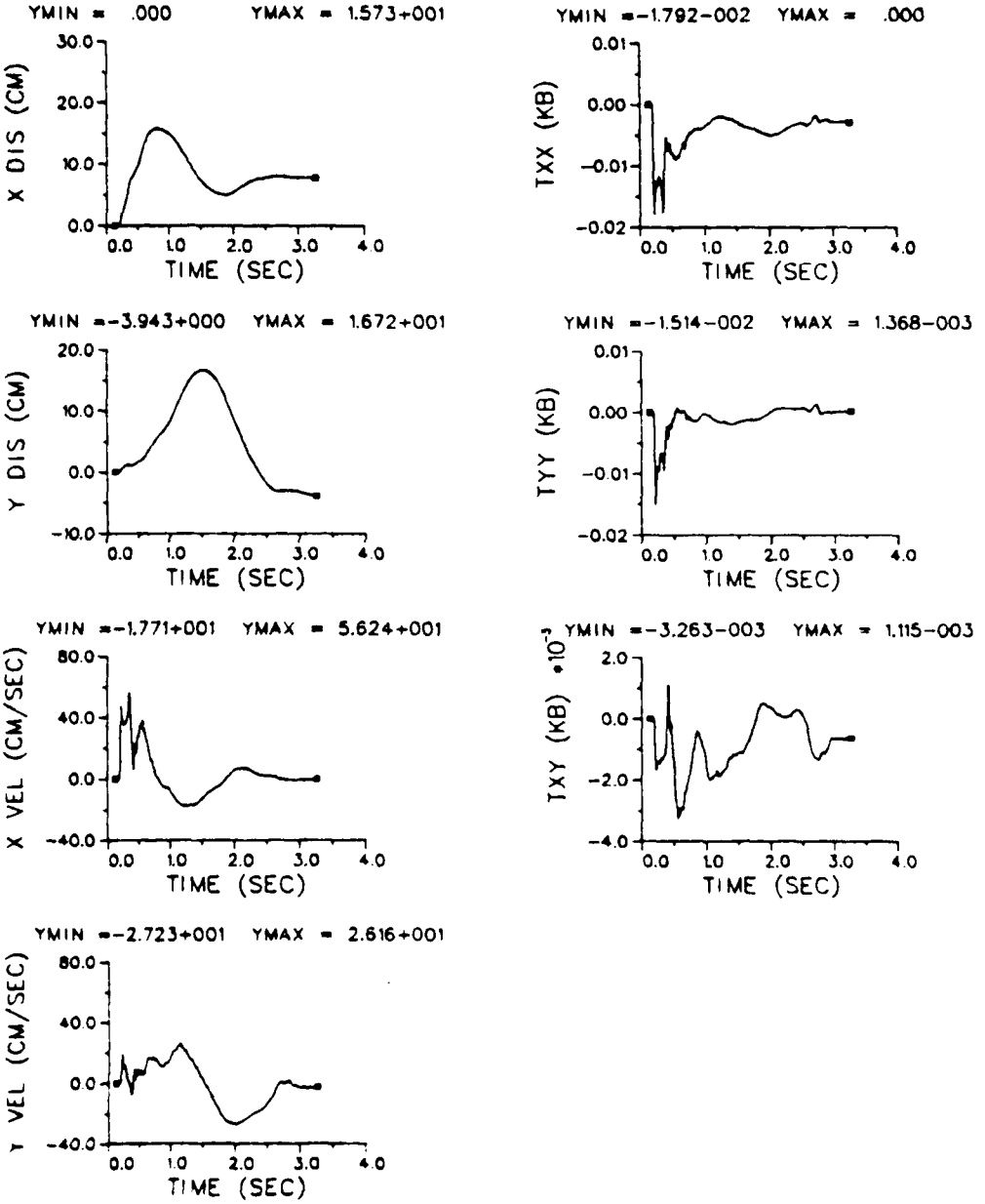

STATION I= 84 J= 12
X= 8.147+002 Y= 1.160+002 (METERS)

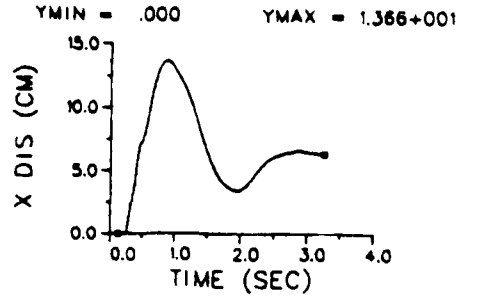

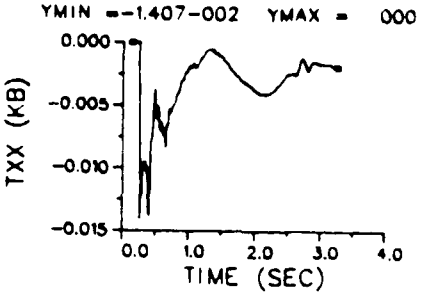

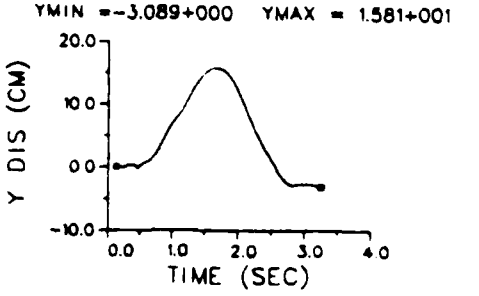

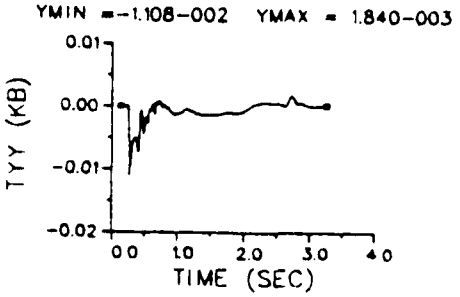

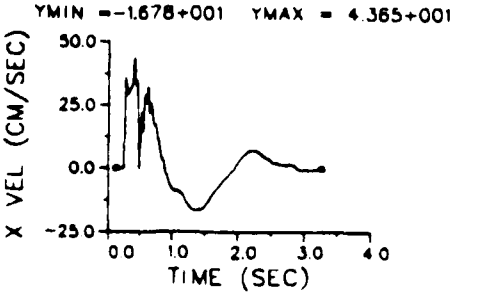

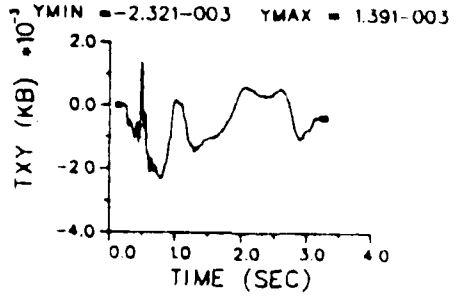

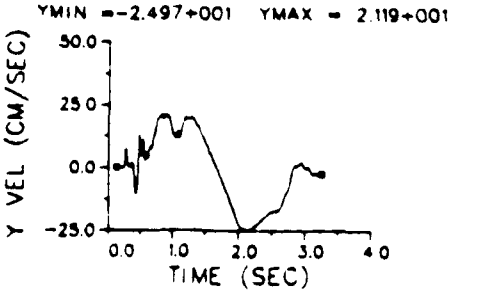

STATION I= 72 J= 22
X= 7.116+002 Y= 1.850+002 (METERS)

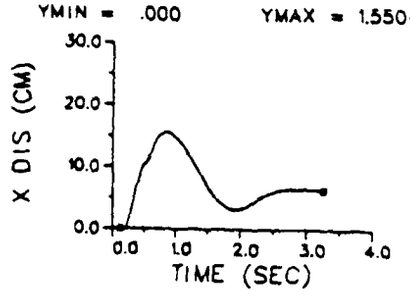

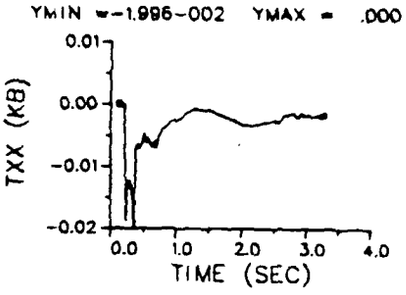

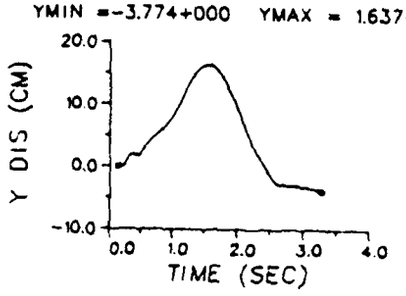

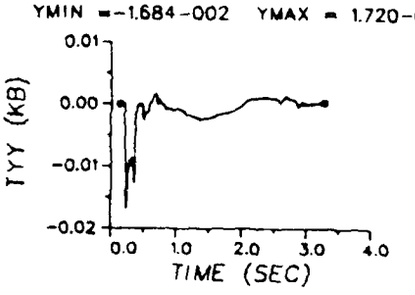

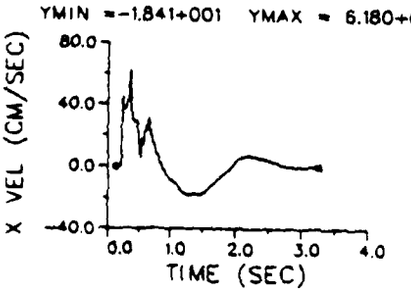

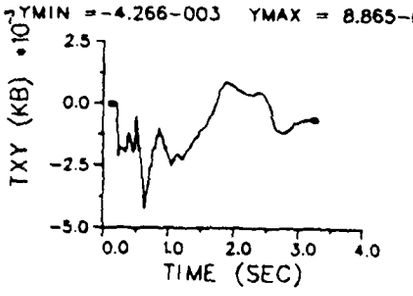

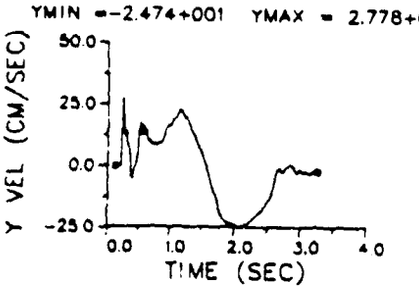

STATION I= 84 J= 22
X= 8.147+002 Y= 1.850+002 (METERS)

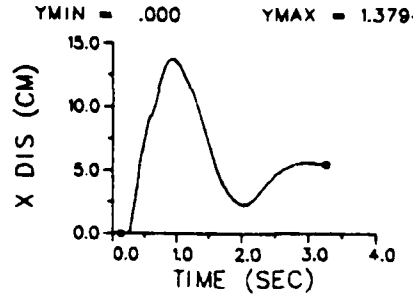

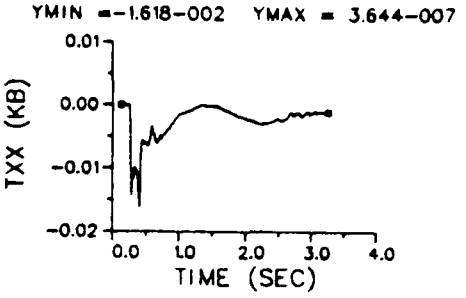

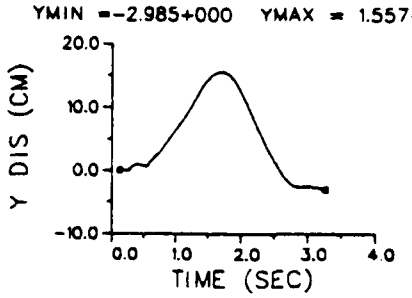

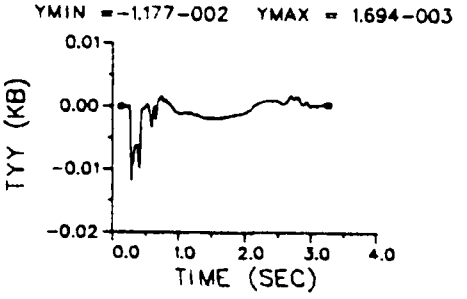

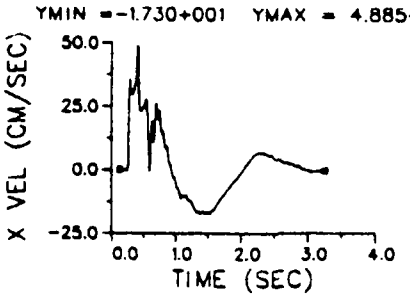

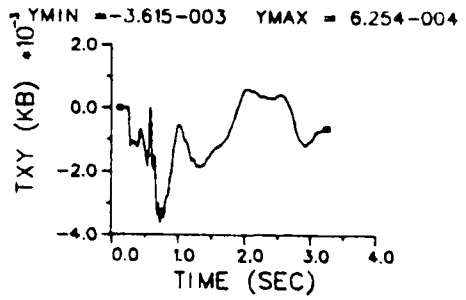

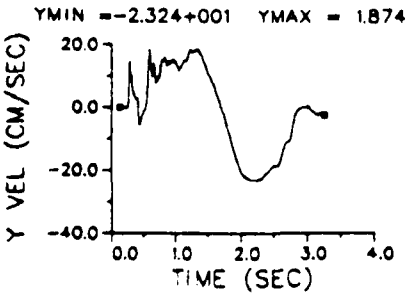

STATION I= 72 J= 32
X= 7.116+002 Y= 2.794+002 (METERS)

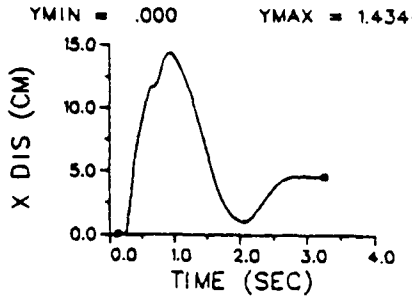

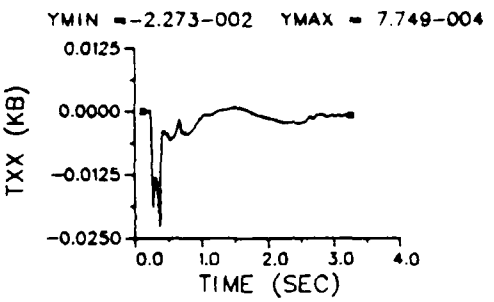

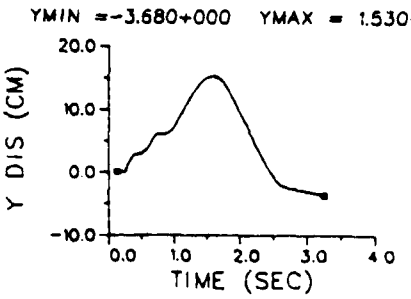

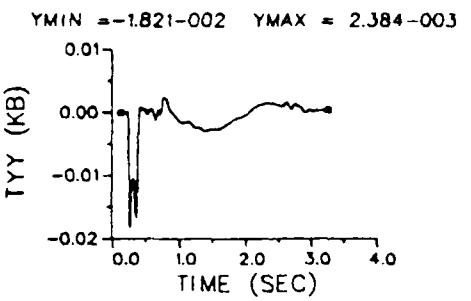

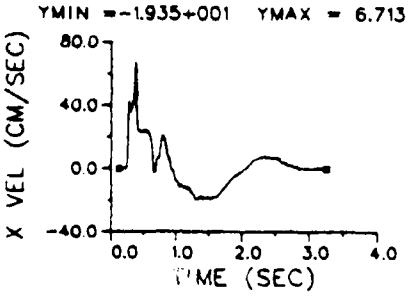

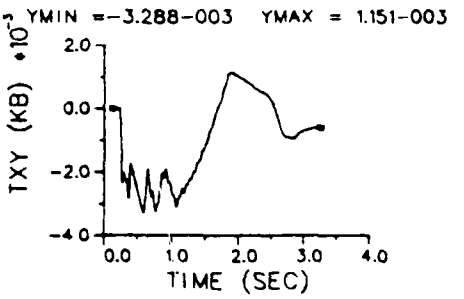

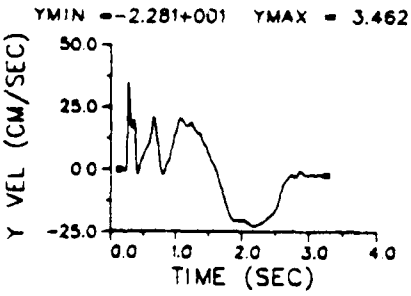

STATION I= 84 J= 32
X= 8.147+002 Y= 2.794+002 (METERS)

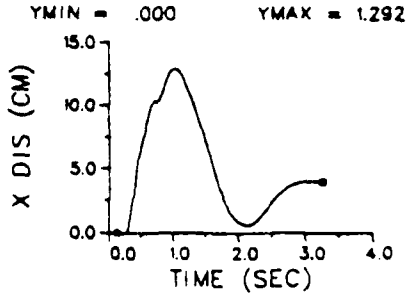

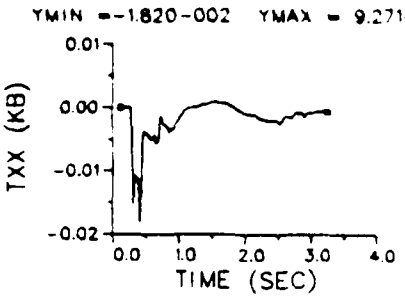

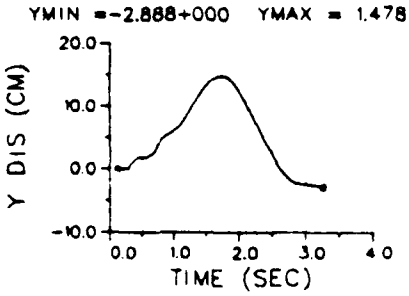

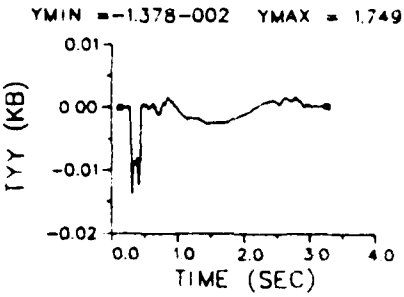

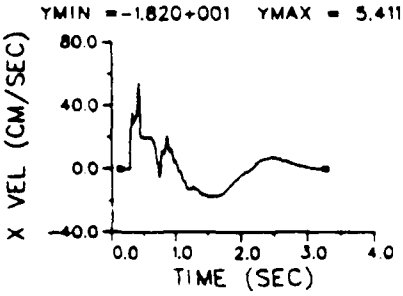

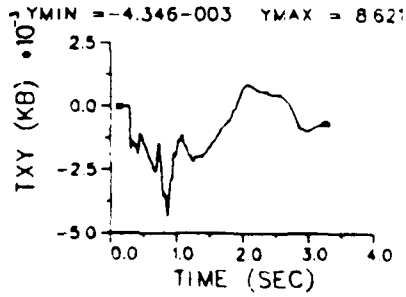

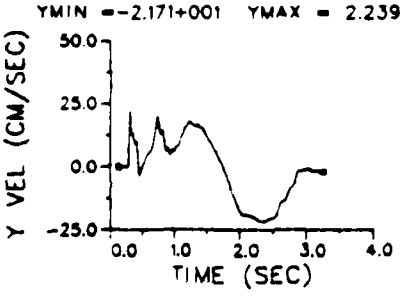

STATION I= 72 J= 42
X= 7.116+002 Y= 3.948+002 (METERS)

YMIN =-9.030-001 YMAX = 1.194+001

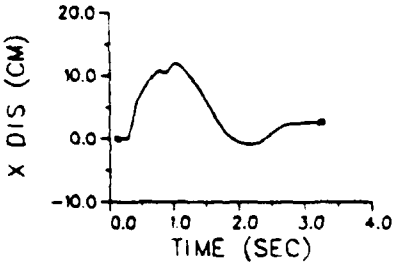

YMIN =-2.421-002 YMAX = 1.966-003

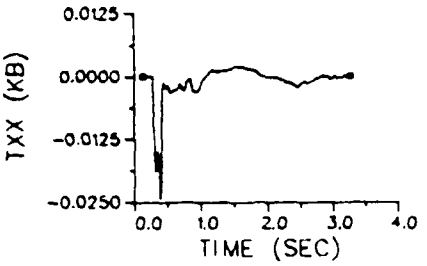

YMIN =-3.636+000 YMAX = 1.354+001

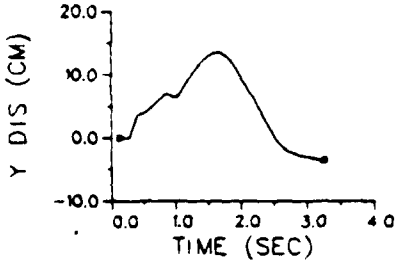

YMIN =-1.988-002 YMAX = 2.594-003

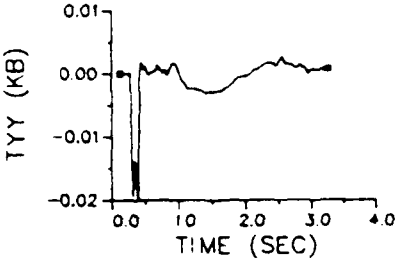

YMIN =-1.905+001 YMAX = 6.710+001

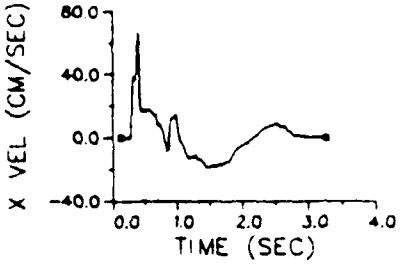

YMIN =-3.661-003 YMAX = 1.536-003

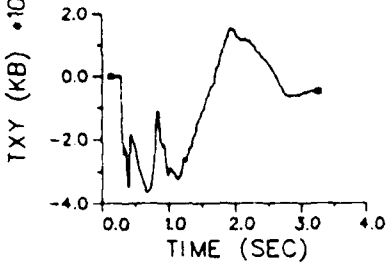

YMIN =-1.978+001 YMAX = 4.002+001

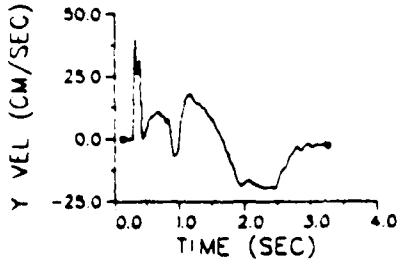

STATION I= 84 J= 42
X= 8.147+002 Y= 3.948+002 (METERS)

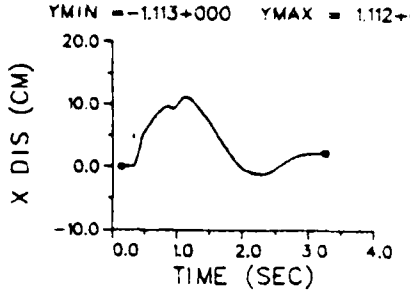

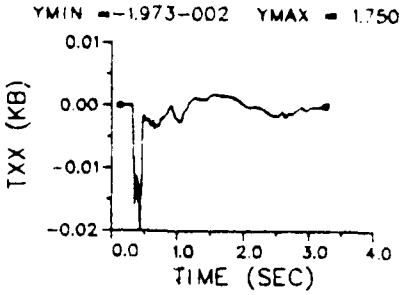

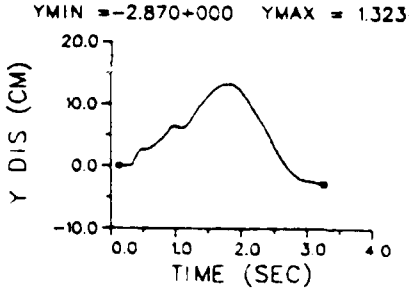

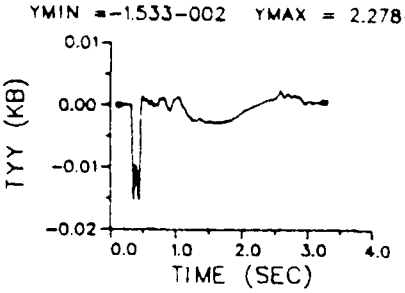

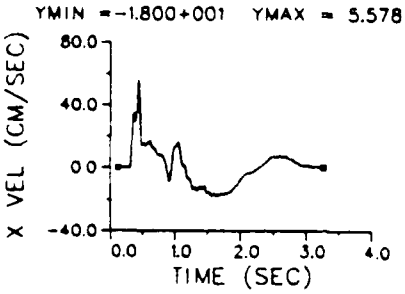

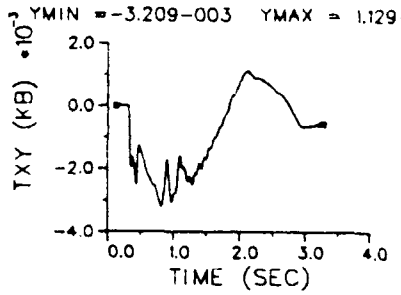

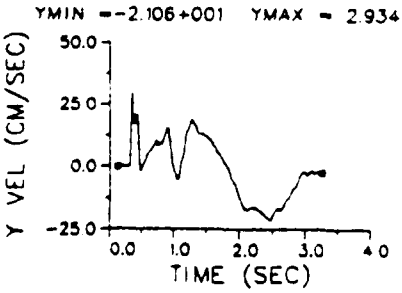

STATION I= 72 J= 51
X= 7.116+002 Y= 4.903+002 (METERS)

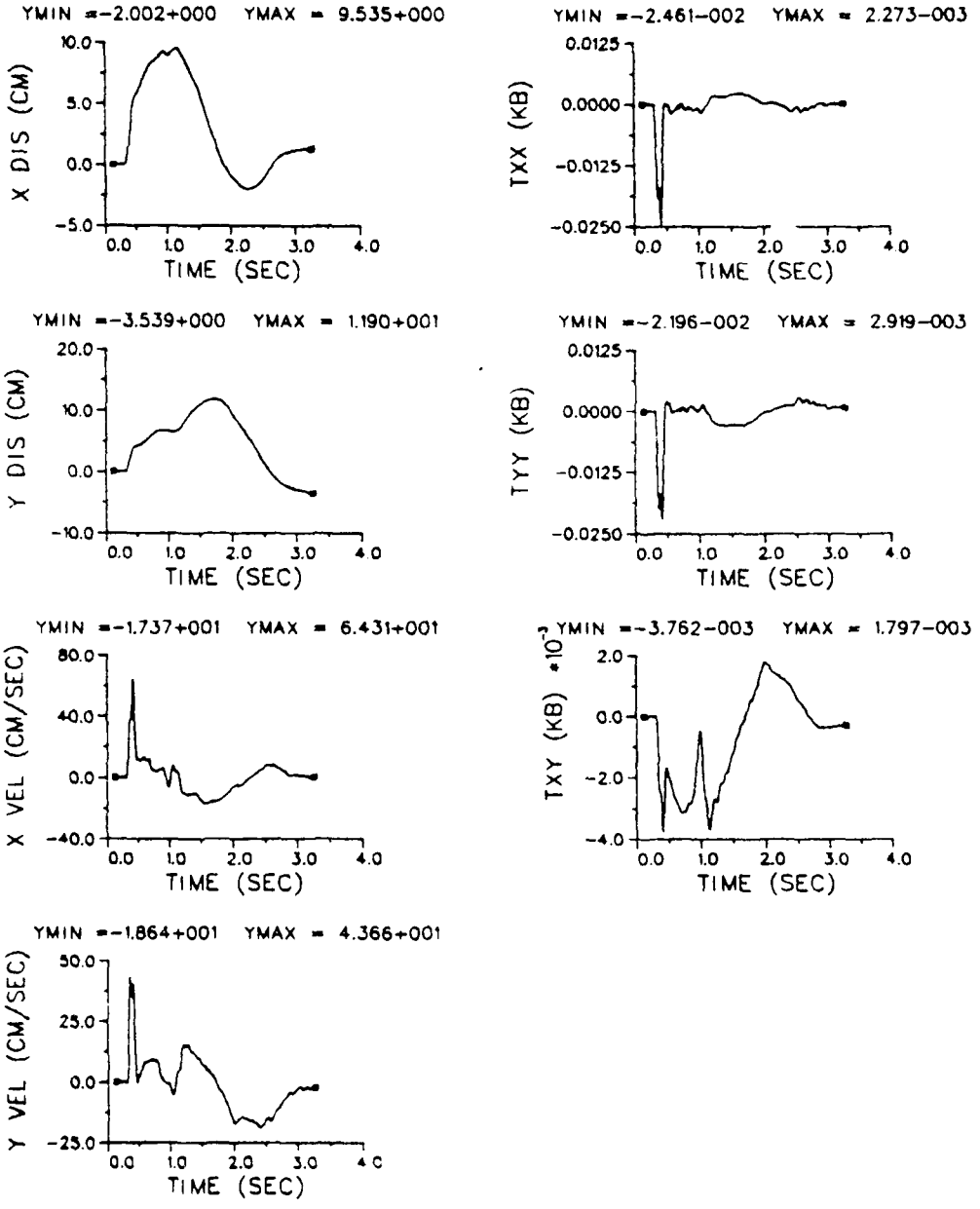

STATION I= 84 J= 51
X= 8.147+002 Y= 4.903+002 (METERS)

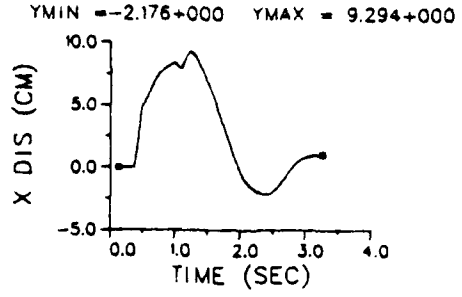

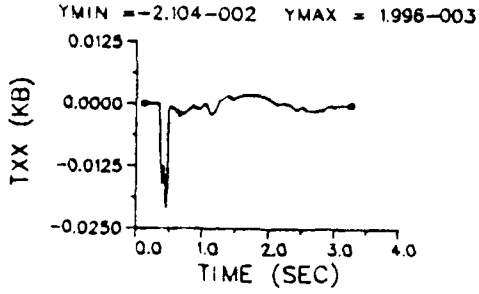

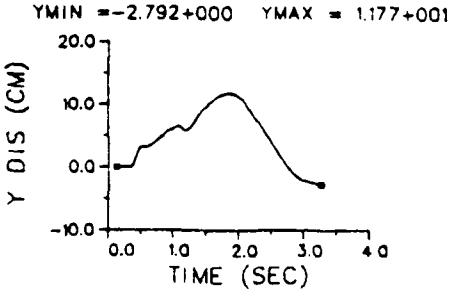

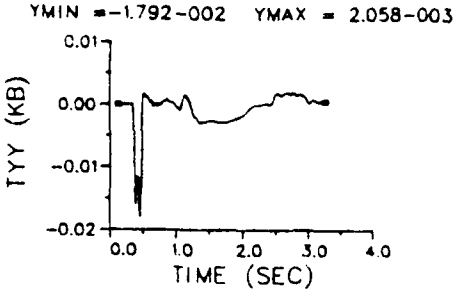

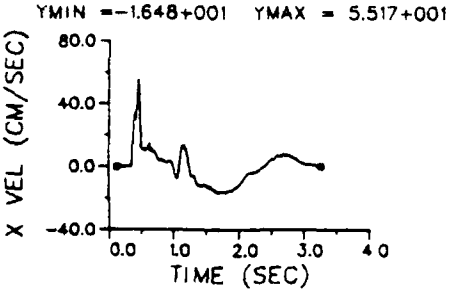

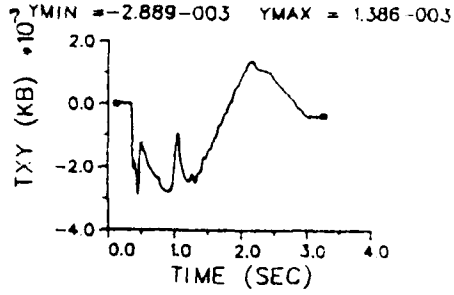

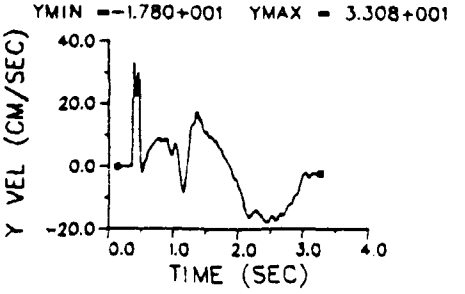

STATION I= 72 J= 61
X= 7.116+002 Y= 5.697+002 (METERS)

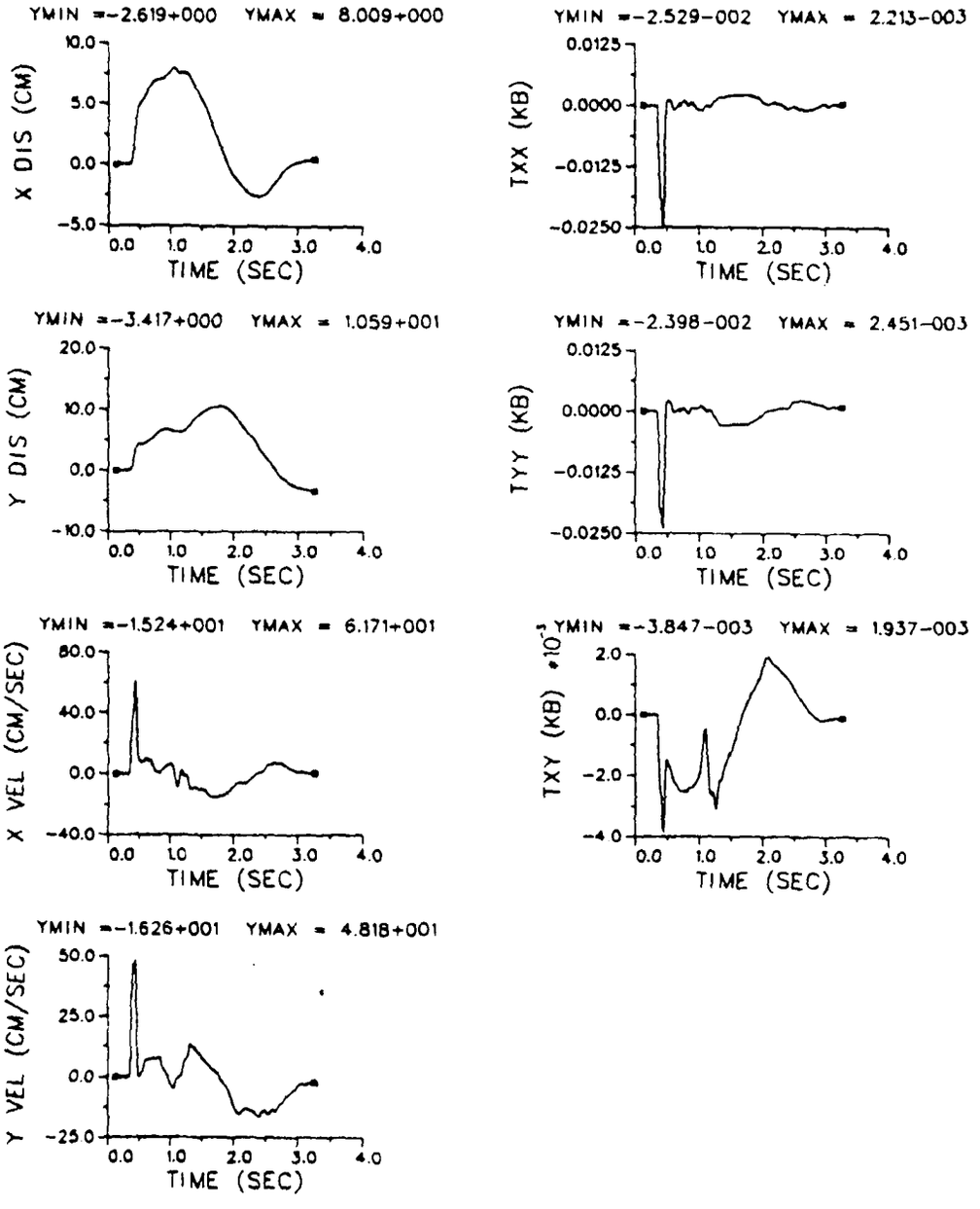

STATION I= 84 J= 61
X= 8.147+002 Y= 5.697+002 (METERS)

YMIN =-2.797+000 YMAX = 7.705+000

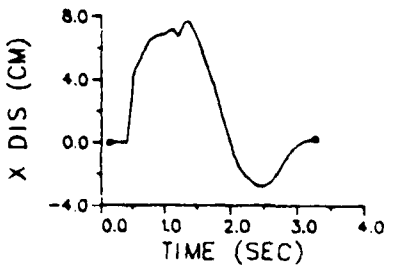

YMIN =-2.076-002 YMAX = 1.937-003

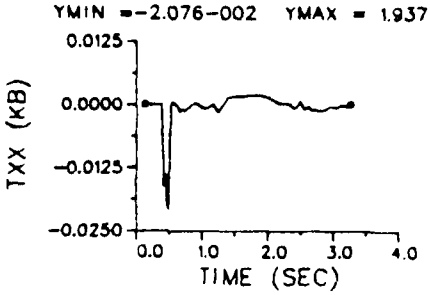

YMIN =-2.644+000 YMAX = 1.063+001

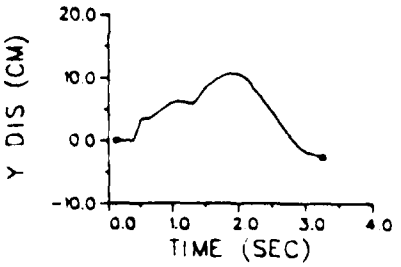

YMIN =-1.855-002 YMAX = 2.195-003

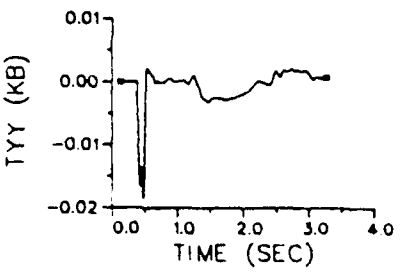

YMIN =-1.525+001 YMAX = 5.302+001

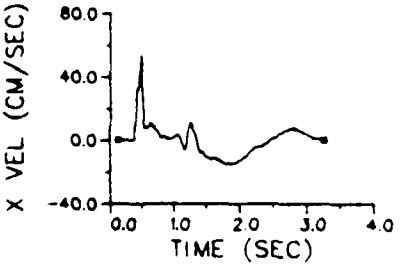

YMIN =-3.033-003 YMAX = 1.631-003

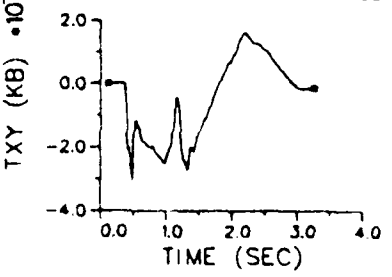

YMIN =-1.539+001 YMAX = 3.555+001

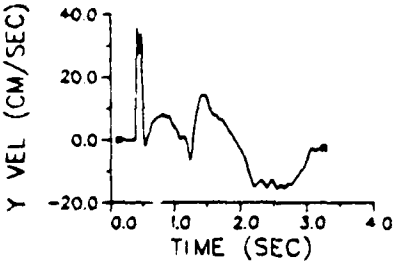

STATION I= 3 J= 62
X= 2.343+001 Y= 5.785+002 (METERS)

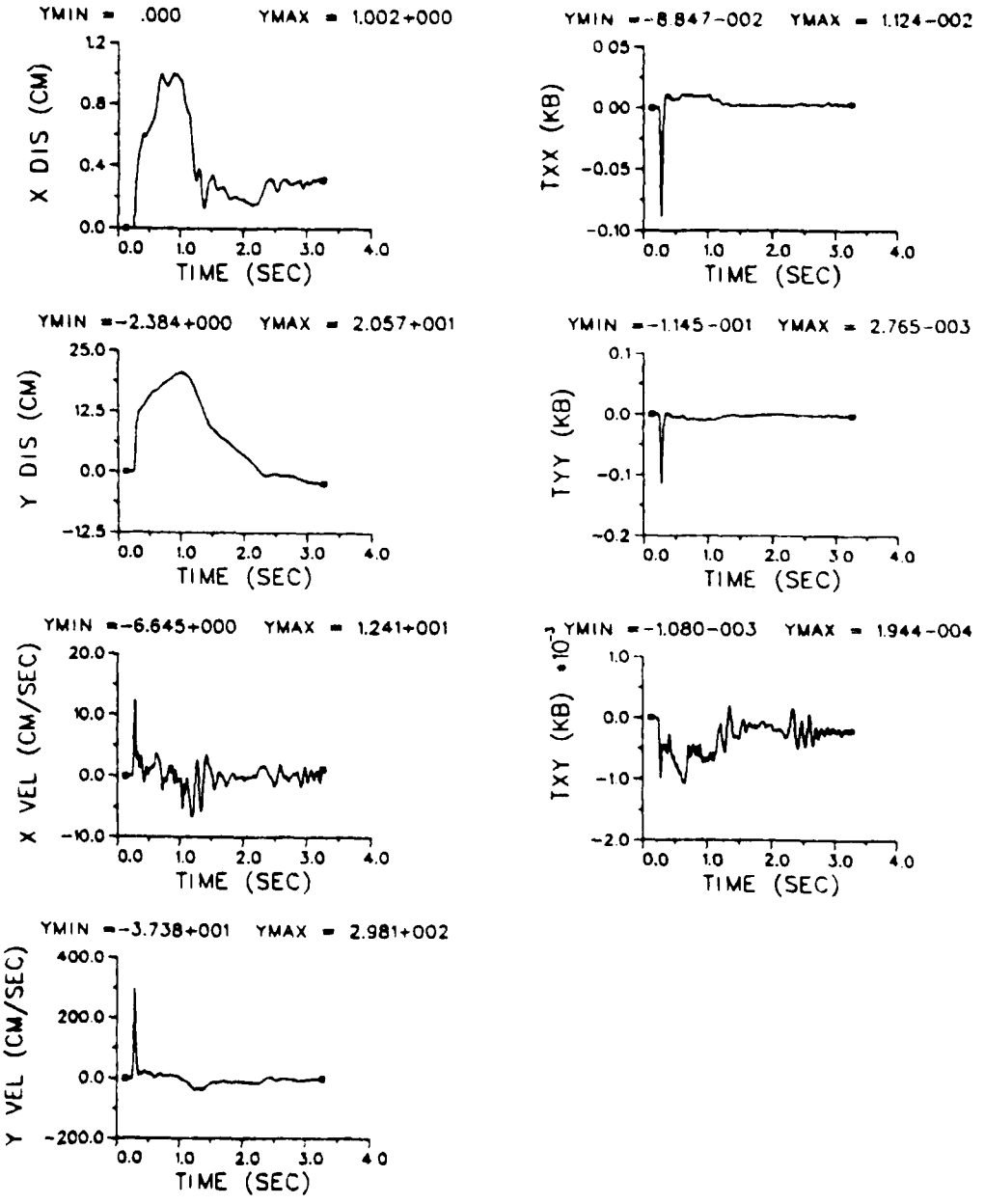

STATION I= 14 J= 62
X= 1.676+002 Y= 5.785+002 (METERS)

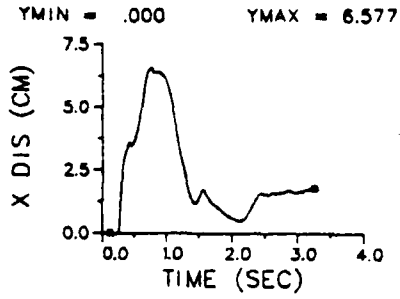

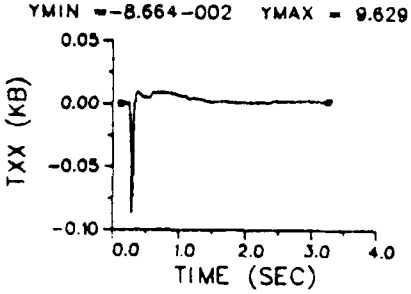

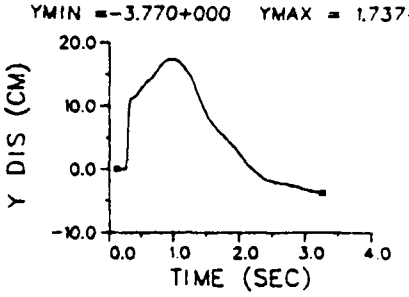

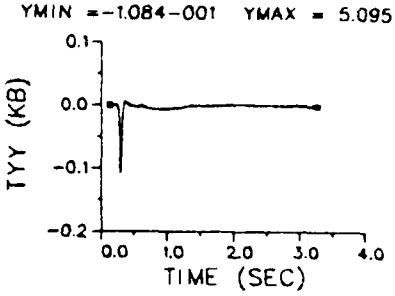

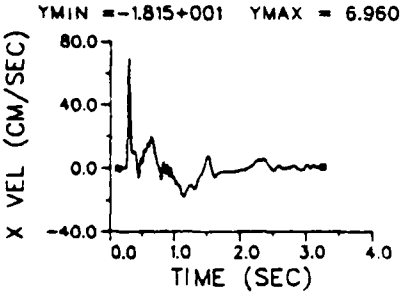

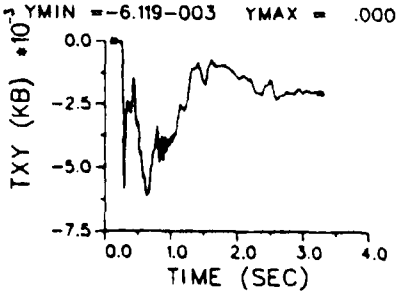

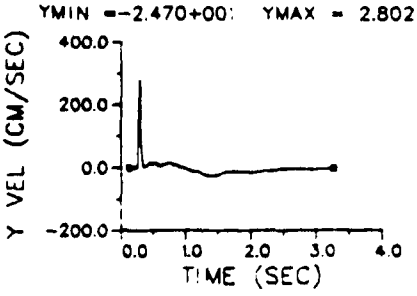

STATION I= 24 J= 62
X= 2.545+002 Y= 5.785+002 (METERS)

YMIN = .000 YMAX = 8.719+000

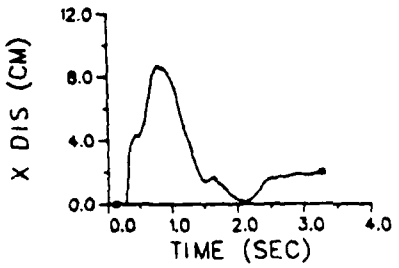

YMIN =-8.223-002 YMAX = 8.872-003

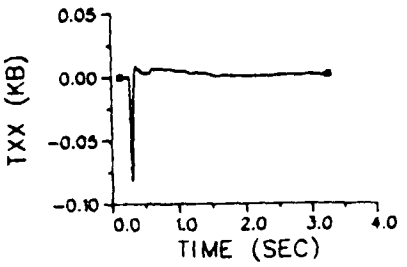

YMIN =-5.112+000 YMAX = 1.447+001

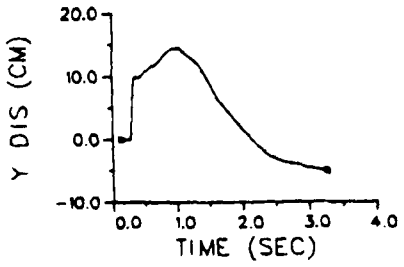

YMIN =-9.929-002 YMAX = 6.919-003

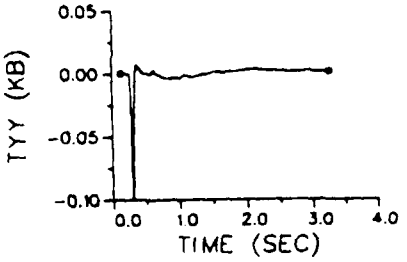

YMIN =-1.951+001 YMAX = 9.074+001

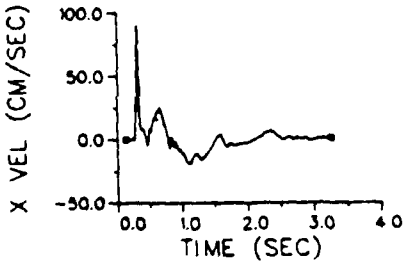

YMIN =-7.225-003 YMAX = .000

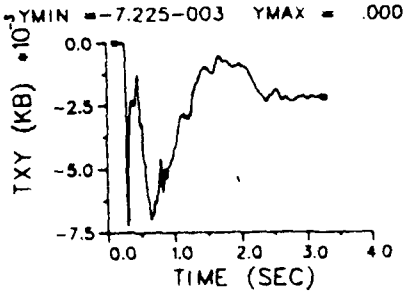

YMIN =-2.139+001 YMAX = 2.506+002

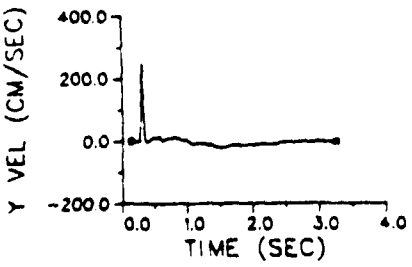

STATION I= 34 J= 62
X= 3.723+002 Y= 5.785+002 (METERS)

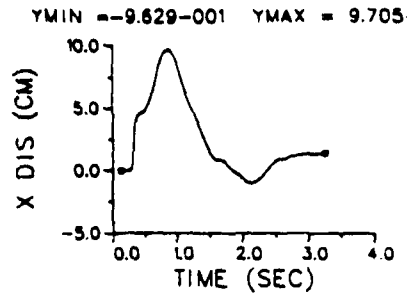

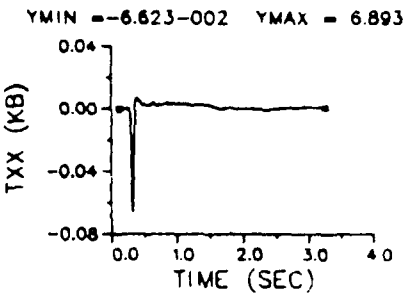

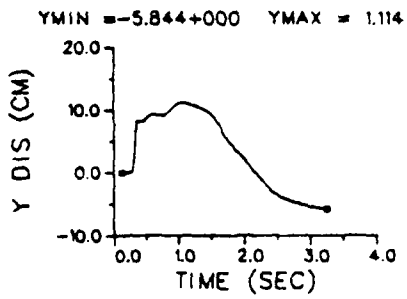

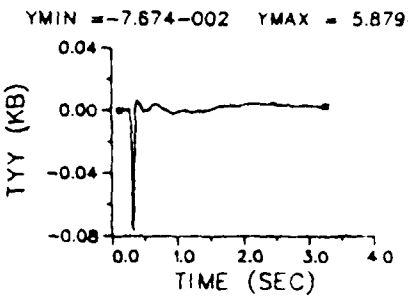

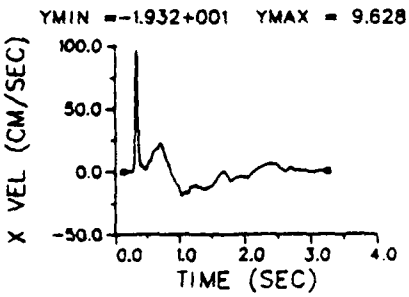

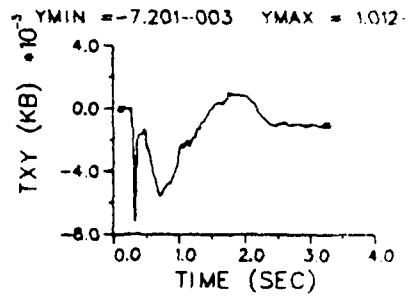

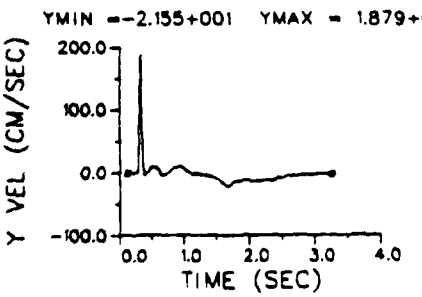

STATION I= 44 J= 62
X= 4.923+002 Y= 5.785+002 (METERS)

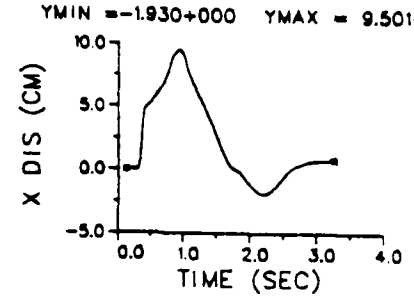

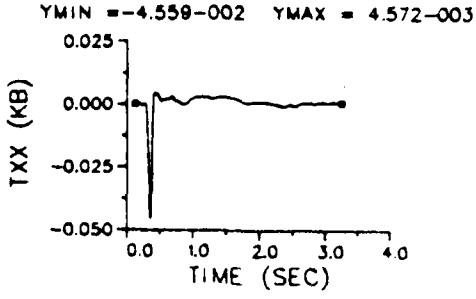

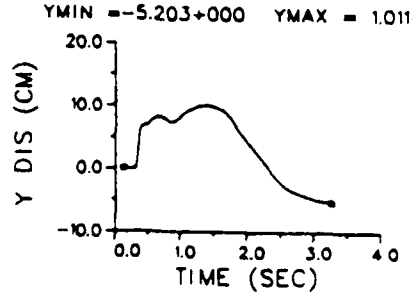

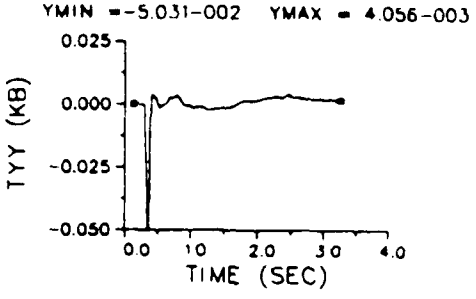

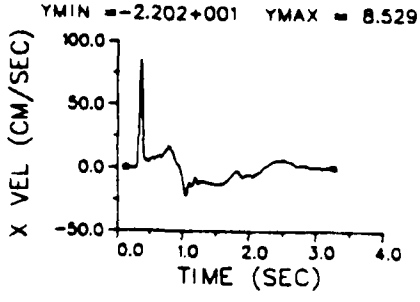

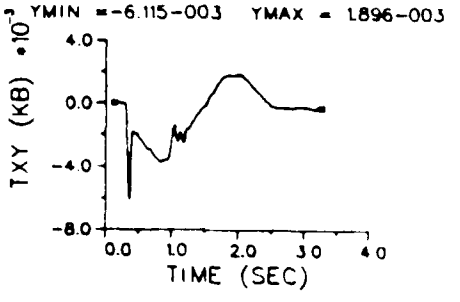

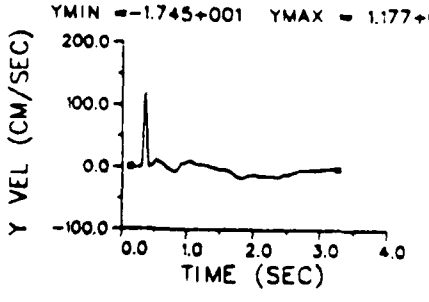

STATION I= 57 J= 62
X= 6.123+002 Y= 5.785+002 (METERS)